ACCSCIENCE PUBLISHING

Tumor Discovery

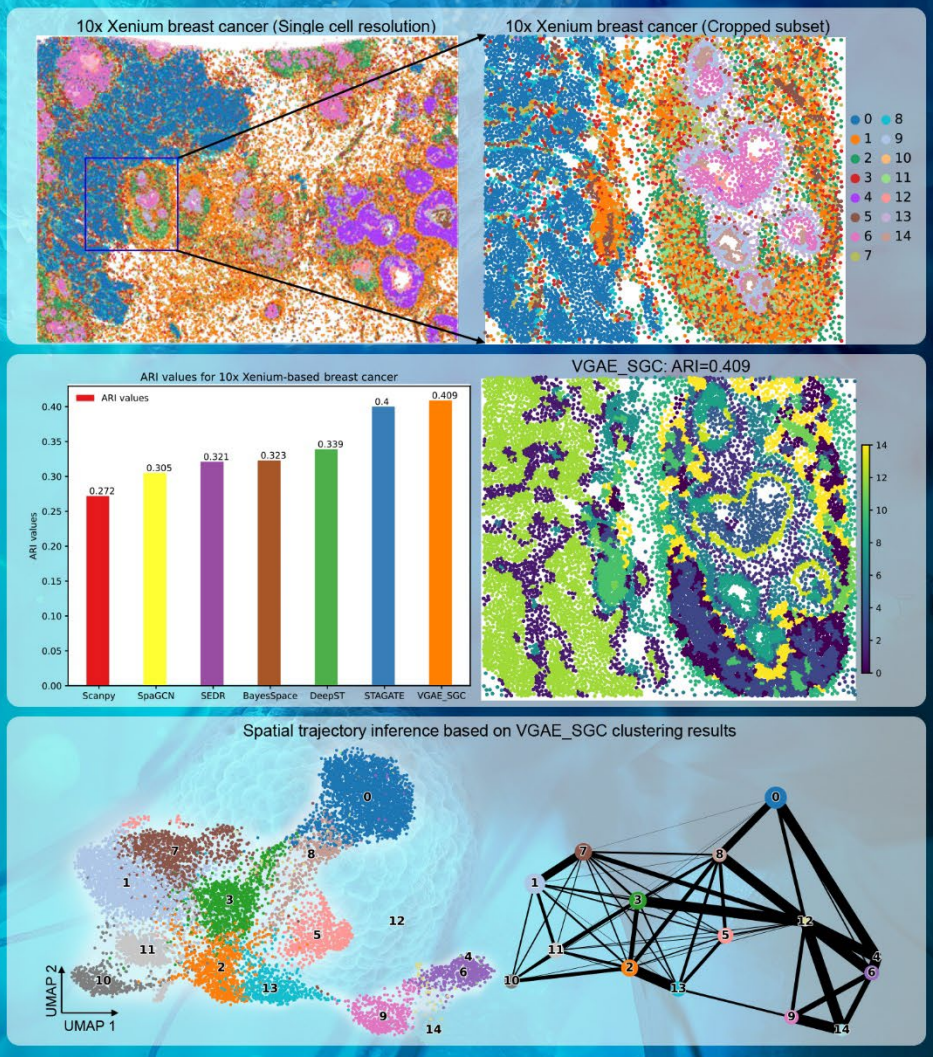

Artificial intelligence enabled spatially resolved transcriptomics reveal spatial tissue organization of multiple tumors

ISSN: 3060-8597 (Print)
ISSN: 2810-9775 (Online)
Volume 3 • Issue 1
March 2024

ACCSCIENCE PUBLISHING

Tumor Discovery

Print ISSN: 3060-8597
Online ISSN: 2810-9775

Tumor Discovery is a peer-reviewed and open-access journal that aims to present new cancer research with strong emphasis on fundamental and translational studies. *Tumor Discovery* covers topics such as etiology and pathogenesis of cancer, mechanisms and molecular pathways underlying cancer initiation and progression, tumor metastasis, etc.

Scan to access website:

Scan to submit papers:

About the Publisher

AccScience Publishing is a publishing company based in Singapore. We publish a range of high-quality, open-access, peer-reviewed journals and books from a broad spectrum of disciplines.

Contact Us

Managing Editor
td.office@accscience.sg

AccScience Publishing
8 Burn Road, #15-03 Trivex, Singapore 369977.

Volume 3 • Issue 1 • March 2024
ISSN 3060-8597 (print) ISSN 2810-9775 (online)

TUMOR DISCOVERY

ACCSCIENCE PUBLISHING

Access Science Without Barriers

TUMOR DISCOVERY

ISSN: 3060-8597 (print)
ISSN: 2810-9775 (online)

Editorial and Production Credits

Publisher: AccScience Publishing
Managing Editor: Zoe Zhang
Production Editor: Sharmila Velapasamy
Journal Development Editor: Felicia Wang
Special Issue Commissioning Editor: Hannah Zhang
Article Layout and Typeset: Sinjore Technologies (India)
Cover Design: ProPub (China)

For all advertising queries, contact td.office@accscience.sg.

Supplementary file

Supplementary files of articles can be obtained at https://accscience.com/journal/TD/3/1.

Tumor Discovery

Editorial Board

*Editorial Board Members as of March 1, 2024

ACCSCIENCE PUBLISHING

Volume 3 | Issue 1 | March 2024 |

Tumor Discovery

https://accscience.com/journal/TD

CONTENTS

ACCSCIENCE PUBLISHING

Tumor Discovery

ORIGINAL RESEARCH ARTICLE

Haplotype analysis and linkage disequilibrium of *BRCA* genes in glioblastoma: Impact on treatment response

Mohamed K. Khalifa[1], Amira M. Nageeb[2], Magdy M. Mohamed[3], Lobna R. Ezz El Arab[4], and Menha Swellam[2]*

[1]Molecular Pathology Laboratory, Children's Cancer Hospital, Cairo, Egypt

[2]Department of Biochemistry, Biotechnology Research Institute, High Throughput Molecular and Genetic Laboratory, Central Laboratories Network and the Centers of Excellence, National Research Centre, Giza, Egypt

[3]Department of Biochemistry, Faculty of Science, Ain Shams University, Cairo, Egypt

[4]Department of Clinical Oncology, Faculty of Medicine, Ain Shams University, Cairo, Egypt

Abstract

Glioblastoma (GBM) is an aggressive primary brain tumor prevalent in adults, characterized as a common malignant neoplasm of the human central nervous system with the worst survival rate among cancers. Treatment of GBM involves the addition of the alkylating agent temozolomide (TMZ) to radiotherapy, which improves overall survival by preventing replication through alkyl group-mediated DNA cross-linking. Genes related to homologous recombination (HR)-dependent DNA repair, such as the breast cancer susceptibility genes (*BRCA*), specifically *BRCA1* or *BRCA2*, contribute to cellular resistance to alkylating agents. We aimed to perform a haplotype-based study on the frequencies of *BRCA1* mutations in GBM patients compared to healthy individuals and investigate their linkage disequilibrium (LD) with the data population. Blood samples from GBM patients (n = 15) and healthy controls (n = 25) were sequenced using the Ion Torrent PGM platform to identify the *BRCA1* mutation. Subsequently, the reported variants were submitted to the LDlink tool for haplotype analysis, and their association with treatment response was assessed. Our results revealed that the *BRCA1* haplotype block consisted of seven SNPs, whose frequencies were reported with strong LD when compared to all available population data. This block was found to be represented by eight haplotypes. Five of these haplotypes were previously reported (four haplotypes were commonly reported, and one was rare), while the remaining three haplotypes were newly reported in this study. The relationship between newly reported haplotypes and response to treatment revealed that patients with these haplotypes responded to TMZ either as a complete or partial response. In addition, one haplotype in the heterozygote form was reported in the control case. In conclusion, haplotype analysis for *BRCA* genes in GBM cases can aid in predicting treatment responses and identifying cancer risk factors in individuals.

Keywords: Breast cancer susceptibility genes; Haplotype; Next-generation sequencing; Sequencing; Breast cancer

***Corresponding author:**
Menha Swellam
(menhamswellam@gmail.com)

Citation: Khalifa MK, Nageeb AM, Mohamed MM, El Arab LRE, Swellam M. Haplotype analysis and linkage disequilibrium of BRCA genes in glioblastoma: Impact on treatment response. *Tumor Discov*. 2024;3(1):1480.
https://doi.org/10.36922/td.1480

Received: August 9, 2023
Accepted: November 30, 2023
Published Online: February 15, 2024

1. Introduction

Glioblastoma (GBM) is the most prevalent primary brain tumor in adults. According to the World Health Organization, it is an aggressive, necrosis-prone, and mitotically vigorous grade IV malignant. It accounts for 45.2% of all malignant primary tumors of the brain and central nervous system (CNS). GBM is considered an inveterate disease with a 15-month median survival rate.[1] Only 5.5% of patients survive for 5 years after diagnosis.[2] GBMs are divided into primary and secondary subtypes that develop through various genetic routes, affecting individuals at different ages with varying outcomes.[3] Primary GBMs account for 80% of GBMs and are detected in people over the age of 62, while secondary GBMs occur in patients under the age of 45 and are triggered by low-grade astrocytomas or oligodendrogliomas. Secondary GBMs are more likely to occur in the frontal lobe, display less necrosis, and have a better prognosis than primary GBMs. At present, the detection of mutations in certain cancer cell genes has an extremely high predictive and prognostic value and enables the advancement of targeted therapies.

Existing treatment approaches for GBM are based on a combination of surgical methods along with radiotherapy and chemotherapy. Important variations in therapeutic techniques include the addition of temozolomide (TMZ) (alkylating chemotherapeutics) to the treatment regimen. Fractionated radiotherapy and six cycles of TMZ-based chemotherapy have been used in GBM patients.[4,5] Several clinical trials have demonstrated that long-term adjuvant TMZ chemotherapy improves progression-free survival (PFS) and 2-year survival rates in GBM patients and enhances their quality of life, but does not improve the overall survival (OS) significantly.[6] A recent randomized trial compared the results obtained from using TMZ in combination with interferon alpha and TMZ alone to evaluate the therapeutic efficacy and assess toxic consequences in high-grade glioma (grades 3 and 4). The study reported that the combination of TMZ with interferon alpha extended the survival time while maintaining tolerable toxicities compared to using TMZ alone.[7]

The breast cancer susceptibility genes (*BRCAs*) are a group of tumor suppressor genes, which includes *BRCA1 (*125,951bp) and *BRCA2 (*85,405bp).[6] *BRCA* genes are involved in cellular resistance to alkylating chemicals and are responsible for homologous recombination (HR) (a double-strand break repair process).[8-11] Mutations in these genes have been identified in several cancers, the most common of which are breast and ovarian cancer.[12] Although genomic instability may lead to a poor prognosis in GBM patients, the impaired DNA compromises pharmacological methodologies aiming to induce synthetic lethality that causes cancer cell death. This cell-killing procedure occurs only when two molecular pathways are concurrently lacking in a single cell, while an isolated defect is innocuous.[13] One category of drugs that applied in this cell-killing procedure includes inhibitors of poly (ADP-ribose) polymerase (PARP) enzyme, a significant DNA damage response constituent. PARP inhibitors (PARPis) may induce artificial lethality in tumor cells with pre-existent imperfections in the HR repair pathway, such as lethal mutations of the *BRCA1* and *BRCA2* suppressor genes.[14] Most GBM clinical experiments assessing PARPis do not assess the *BRCA* status to correlate outcomes among patient assemblies.[15] A plausible explanation for this omission could be the predictable low incidence of *BRCA* mutations in GBM compared to ovarian, breast, and pancreatic cancer.[16,17]

Germline mutations in several types of genes (tumor suppressors, oncogenes, and DNA repair genes) have been widely analyzed in genome-wide association studies.[18] The previous studies have reported that genomic variants linked to cancer often exhibit an ancestry-specific effect, termed "flip-flop," as the variant associated with cancer in an ancestral population might have no association or an opposite association as a result of linkage and epistatic effect.[19] There are few studies worldwide implicating local ancestry for cancer-causing alterations or recognizing novel ancestry-associated molecular characteristics.[20,21]

This research aims to investigate the frequency of *BRCA* mutations in GBM patients compared to healthy individuals, using sequencing technology to detect single nucleotide polymorphisms (SNPs) as well as insertions and deletions (InDels) that serve as the foundation for allele differentiation. Haplotype analysis, which contains a collection of linked SNPs, proves to be more informative than the analysis of single SNPs in determining associations with phenotypes.

2. Methods

2.1. Sample selection and inclusion criteria

On obtaining ethical approval from the Medical Ethical Committee of the National Research Centre (ID #17111) for this prospective study, 44 individuals were enrolled, divided into patients with GBM (n = 15) and healthy, normal individuals as controls. The inclusion criteria for the recruited groups were as follows: for GBM patients, they were above 18 years old, newly diagnosed using magnetic resonance imaging (MRI) and pathological examination, and their presentation was ≤2 according to the Ester Clinical Oncology Group, while for the normal

groups, they were of harmonized age and sexual category with malignancy findings. Individuals who did not meet the inclusion criteria were excluded from the study. The justification criteria for the selection of GBM patients were those who had not received any treatments (adjuvant therapy, including chemo- or radiotherapy), patients who were amenable to follow-up, and patients who had undergone surgery, and whose survival duration was above 1 month.

2.2. Medication strategy

All patients underwent MRI for analysis. Then, GBM patients were cured with clinical resection, near-total resection, or excisional biopsy. Thereafter, all patients were cured with regular therapy, which included radiotherapy (total dose of 60 Gy—administered in 30 parts over 42 days) with concomitant TMZ chemotherapy (100 mg/day for 45 days) followed by 6 cycles of TMZ treatment at a dose of 150 mg/m^2 of body surface area for days 1 – 5. All patients were followed up and assessed clinically and radiologically by MRI.

The tumor was accessed based on the radiological RANO response standards (2010)[22,23] as follows: Complete response (CR), defined as the disappearance of all identified brain injuries; partial response (PR), defined as a 50% or greater reduction of the assessable brain lesion or an objective progression of the assessable brain lesion; stable disease (SD), defined as an unchanged brain lesion (<50% reduction or <25% proliferation in the size of the assessable lesions); and progressive disease (PD), defined as ≥25% increase in the size of some or all brain injuries and/or the presence of new brain lesions.

2.3. DNA extraction

The QIAamp DNA mini blood kit (Cat. No. #51104, Qiagen, Germany) was used to extract DNA from ethylenediaminetetraacetic acid blood samples, according to the manufacturer's guidelines. The kit procedure was similar to the one established for the extraction of DNA using a spin column. For the extracted DNA, both purity and concentration were assessed using a nano-drop spectrophotometer (Quawell, Q-500, Scribner, USA) before further examination and then stored at –80°C until further estimates.

2.4. DNA library formulation and sanitization

Amplification of the target regions for *BRCA1* and *BRCA2* was carried out using the Ion AmpliSeq *BRCA1* and *BRCA2* Panel (Life Technologies Ltd., USA). This panel comprises three primer pools (167 amplicons) covering the entire coding region with 10 – 20 bp intronic neighboring sequences around the coding arrangement of the investigated genes. The amplification procedure involved a 20-µL scale using the Ion AmpliSeq Library Kit (Thermo Fisher Scientific, USA). The assay was performed using 4 µL of 5× Ion AmpliSeq HiFi Master Mix, 10 µL of 2× Ion AmpliSeq Primer Pool (every primer in a separate well for each sample), 10 ng of genomic DNA/sample (2 µL of 5 ng/µL from the test store), and lastly 4 µL of nuclease-free water. The applied thermal settings for the reaction were as follows: 99°C for 2 min, one round for triggering the enzyme activating by (99°C for 2 s, and 60°C for 4 min) for 16 cycles using a thermal cycler (SureCycler 8800, Agilent, USA). After enlargement, the primers were processed using the Fragmentase Universal Primer Assay (FuPa) Mixture and thermal conditions: 50°C for 10 min, 55°C for 10 min, and 60°C for 10 min, then ligated with two adaptors (IonCode™ Barcode Adapters, Life Technologies Ltd., USA) and the barcodes with the Ion Xpress Barcode Connectors-16 kit (Life Technologies Ltd., USA). Then, magnification was performed using the thermal conditions: 22°C for 30 min, 68°C for 5 min, and 72°C for 5 min, as indicated in the Ion AmpliSeq Library Kit user guide. Sanitization of the formulated libraries was carried out and measured by the Ion Library TaqMan Measurement Kit (Life Technologies Ltd., USA) by quantitative PCR using the real-time PCR technique (Stratagene Max3005P QPCR system, Agilent Biotechnology, USA). The QPCR was performed with the following thermal conditions: 50°C for 2 min, 95°C for 2 min, 40 rounds at 95°C for 15 s, and 60°C for 1 min. The amplified libraries were additionally subjected to template formulation.

2.5. Template formulation

The cleaned and measured libraries were assembled on molar comparable portions to achieve at least ×500 coverage for every sample. The collective collections were clonally magnified using the Ion PGM Hi-Q view OT2 kit (Life machineries, USA) on the Ion OneTouch 2 apparatus (Life Technologies Ltd., USA) according to the manufacturer's guidelines. Then, the template ion sphere particles ISP were improved using Ion PGM Enhancement Beads (Life Technologies Ltd., USA) on the Ion OneTouch ES system (Life Technologies Ltd., USA) based on the manufacturer's guidelines. Positive ISP excellence was analyzed on the Qubit 2.0 Fluorometer (Life Technologies Ltd., USA) and then sequencing was performed.

2.6. Sequencing with Ion Torrent PGM Proposal

Before starting sequencing using Ion PGM, calibration and pH amendments were carried out according to the user guide of the Ion PGM Hi-Q View Sequencing kit (Life

machineries, USA). Thereafter, using the Ion Torrent PGM platform (Ion Torrent PGM, Life Machineries, USA), all barcode-enriched samples were sequenced using the Ion 318 Chip Kit V2 BC (Life Technologies Ltd., USA). The depth of analysis was considered to be at least ×500.

2.7. Files examination

The annotations for the variations in the *BRCA1* and *BRCA2* genes were carried out using the cloud-constructed IonReporter Outfit software (version 5.4.0, Life machineries). The annotations were subsequently associated with human genome hg19 (Genome Reference Consortium GRCh37) through the Ion Torrent Server and different caller plugins, according to the criteria mentioned for the *BRCA1* and *BRCA2* panels. Investigation of alternatives was practical without prejudice, and the position arrangements for *BRCA1* and *BRCA2* were NM_007300.3 and NM_000059.3, respectively.

Haplotype analysis is the determination of the pattern of adjacent SNPs on the matching chromosome and heritability in a unit. Units may comprise a huge number of SNPs, but limited SNPs are sufficient to exclusively recognize the haplotypes in units. The HapMap is a chart of these haplotype units, and the exact SNPs that classify the haplotypes are called tag SNPs.

Linkage disequilibrium – the non-random connection of alleles at altered loci – is a sympathetic marker of the population-inherited forces that establish a genome. Due to the tremendous progress in approaches for measuring genetic differences at a fine scale, evolutionary biologists and human geneticists are progressively exploiting linkage disequilibrium to recognize past evolutionary and demographic measures, to map genes that are linked with measurable personalities and heritable illnesses, and to recognize the shared development of related groups of genes. LDlink (https://ldlink.nci.nih.gov/?tab=ldmatrix) is a set of web-based appliances to easily and proficiently interrogate LD in populations, with flexible query and communicative visualization of results.

The haplotype tables and communicating plots generated by LDlink are tailored for researchers interested in mapping common and rare disease susceptibility loci, with an emphasis on linking associated alleles and highlighting potentially functional variants.

In the present study, for the comprehensive investigation of LD and haplotype, the identified variations in both *BRCA1* and *BRCA2* were analyzed using the LDlink application. This is in contradiction to all population records, as there is currently no detailed Egyptian population database accessible.

3. Results

3.1. Clinical characteristics of the recruited individuals

A total of 44 individuals were sequenced for *BRCA* mutations, and they were categorized according to their diagnosis into 15 GBM patients and 29 healthy normal individuals as controls. Both the GBM and control groups were the same age, as there was no significant difference between their ages. In terms of gender status, there were ten females and five males in GBM, while there were 17 females and 12 males in controls.

According to the ECGO system, GBM patients were divided into two groups: those above two (9 cases, 60%) and those below or equal to two (6 cases, 40%). The sites of the primary lesion were frontal (n = 6), temporal (n = 5), and occipital (n = 4). Nine of the GBM patients who received surgical treatment underwent a biopsy, and the remaining six underwent either a total or sub-total excision. Then, ten GBM patients received radiotherapy/chemotherapy for six cycles, and three patients received the same treatment for three cycles, while the remaining patients received only radiotherapy. The GBM patients responded to the treatment strategies as follows: three GBM patients reported a CR, six GBM patients reported a PR, two showed SD, and the remaining four reported PD. The demographic and medical criteria are summarized in Table 1.

3.2. Haplotype analysis for BRCA gene mutations

In our previous study, six GBM patients were sequenced for the detection of *BRCA* gene mutations,[17] and the authors accordingly reported 13 single-nucleotide variations (SNVs) for the *BRCA1* gene using the LD matrix of the LDlink tool. Seven of these SNPs showed strong LD. Accordingly, these SNPs were separated into haplotype-like designs, and the LD matrix of the LDlink tool was used to investigate whether there was LD between the investigated SNPs compared to all data populations.

In the present study, we have sequenced *BRCA* genes in a total of 44 individuals, with 15 identified as GBM cases and the remaining as healthy controls. The primary objective was to investigate haplotype frequency in GBM cases compared to the recruited healthy individuals and to compare our findings with the data population. Accordingly, haplotype analysis and frequency assessments were carried out for the reported seven SNPs using the LDhap tool for all populations. Of these SNPs, five haplotypes were previously reported among the data population, four of them were frequently reported, one was rare, and three haplotypes were newly reported, as shown in Table 2.

Table 1. Demographic and clinical criteria for GBM (grade IV) patients

Patient ID	Gender	Age	Site of mass	ECGO	Type of surgery	Cyc.CT	Response	OS (month)
G1	Female	29	Rt. Frontal mass	2	Excision	6	CR	10
G2	Male	44	Rt. Frontal mass	1	Excision	6	PD	18
G3	Male	37	Rt. Frontal mass	1	Excision	6	PD	5
G4	Male	57	Rt. Partial mass Occipital	1	Gross total resection	6	PR	10
G5	Female	57	Rt. Frontal mass	2	Excision	3	CR	13
G6	Female	60	Rt. Frontoparietal	1	Excision	3	PD	3
G7	Female	60	Rt. Partial mass Occipital	2	Excision	6	PR	6
G8	Female	55	Rt. Partial mass Occipital	1	Excision	6	PR	7
G9	Female	38	Rt. Frontal mass Temporal	2	Partial resection	6	PR	7
G10	Female	59	Rt. Frontal mass	1	Total excision	6	PR	16
G11	Female	65	Rt. Tempropartial	2	Biopsy	2	PD	6
G12	Female	33	Lt. Frontal mass.	1	Total excision	6	CR	20
G13	Male	39	Rt. Frontal mass Temporal	1	Sub-total excision	none	SD	12
G14	Male	42	Rt. Partial mass Occipital	1	Sub-total excision	6	PR	14
G15	Female	78	Lt. Front temporal mas	2	Biopsy	none	SD	7

Abbreviations: CR: Complete response; CT: Chemotherapy; Cyc.: Cycles; Lt.: Left side; OS: Overall survival; PD: Progressive disease; PR: Partial response; Rt.: Right side; SD: Stable disease.

Table 2. Haplotype frequencies for the eight reported SNPs among enrolled individuals

SNPs Haplotypes	rs 1060915	rs 16042	rs 16941	rs 799917	rs 16940	rs 1699949	rs 3765640
Haplotype A	G	C	C	A	G	A	G
Haplotype B	A	T	T	G	A	G	A
Haplotype E	A	T	T	A	A	G	A
Haplotype F	A	C	T	A	A	A	G
Haplotype G	A	T	T	G	A	A	A
Haplotype C	G	T	C	A	G	A	G
Haplotype D	G	C	C	A	A	A	A
Haplotype H	G	C	C	G	G	A	G

Abbreviations: rs: Reference SNP cluster ID; SNPs: Single-nucleotide polymorphisms.

3.3. Correlation between haplotype analysis and clinical criteria in recruited individuals

The correlation between the detected haplotypes and the different clinical and demographic criteria for the recruited individuals (n = 44) revealed that haplotype [A] showed 1591 haplotypes in the entire data population, and its frequency was 0.3177. Among the studied groups, it was detected in 24% (7/29) of the control group, while it was detected in 13.3% (2/15) of the GBM cases. The GBM patients who were reported to possess homozygote haplotype (AA) showed PD. The haplotype [B] has a count of 955 and a frequency of 0.4525 in the data population. Among the controls, 37.9% (11/29) were homozygous for haplotype [B], and 0.68% (2/29) were heterozygous. Moreover, an individual with a family history of cancer was registered for each homo- or heterozygote haplotype. Among the GBM cases, homozygote haplotype was detected in 33.3% (5/15); four of them reported showing a PR towards TMZ, while one showed PD, while four out of 15 GBM (26.6%) were heterozygous, and their response to treatment varies from CR, PR, SD, and PD.

Haplotype [E] represented the highest haplotype count since it reported 2272 haplotypes with a frequency of 0.4537 and was, therefore, referred to as a wild haplotype across all populations. One control case was reported as homozygous (1/29), and two controls were heterozygous (2/29). Among the GBM cases, only one case was heterozygous with PD. The remaining haplotypes previously reported were [F] and [G], with a haplotype count and frequency of 89 and 0.0179, and 82 and 0.0164, respectively. Therefore,

haplotype G was considered the rare haplotype, as shown in Figure 1.

In this study, three haplotypes were detected that were newly reported and were designated as haplotypes [C], [D], and [H]; all were heterozygotes (Figure 1). GBM cases that reported heterozygotes in haplotypes [C] and [D] responded to TMZ treatment with either CR or PR. Haplotype [H] was only detected in control cases in a heterozygous form.

4. Discussion

The human genome consists of regions with strong LD and low historical recombination, termed haplotype blocks.[24] Regions of strong LD have been verified to have low haplotype multiplicity, with common haplotypes explaining the shared variation in different populations. Moreover, haplotypes can be anticipated using a subset of all existing (or known) markers (termed haplotype-tagging SNPs [htSNPs]). Hence, with the definitive haplotype block, the investigation of individual haplotypes and their familial associations could allow the indirect investigation of probable fundamental variants that may not have been genotyped. In this study, we investigated the haplotype analysis and LD among 16 GBM patients and compared them with 25 healthy controls as a first trial among Egyptian GBM patients. Moreover, these haplotypes were investigated with clinicopathological features and their response to treatment by adopting a haplotype-based method to investigate genetic discrepancies in *BRCA1*.

Previously, authors have analyzed *BRCA* gene mutations in GBM patients[25] and reported the potential role of *BRCA1* in cancer predisposition. In the present study, a total of 44 individuals were enrolled and categorized according to their clinical criteria into 15 GBM cases and 29 normal individuals as controls. The comparison of haplotype concepts between two groups can provide reliable information about the human genome[26] in GBM cases and normal individuals. At present, haplotype [A] is presented as homozygote (AA) in seven control individuals compared to two GBM cases. Although only a small number of cases were investigated in this study, reporting these haplotypes in both groups may require further investigation of a large number of GBM cases compared to normal controls, which is a study in progress. For the studied GBM cases reporting homozygous (AA) haplotypes, analyses and their association with treatment revealed their response to treatment. This may indicate the importance of using these haplotype sequences for early prediction of response to TMZ treatment among GBM patients. This finding is consistent with previously reported findings by Ding *et al.*, who reported that *BRCA1* is an effective candidate gene that induces artificial lethality with TMZ in GBM.[27] Recent strategies in the treatment landscape for tumors harboring defects in homologous repair (HR) genes (e.g., *BRCA1* and *BRCA2*) have been combined with poly (ADP-ribose) polymerase inhibitors

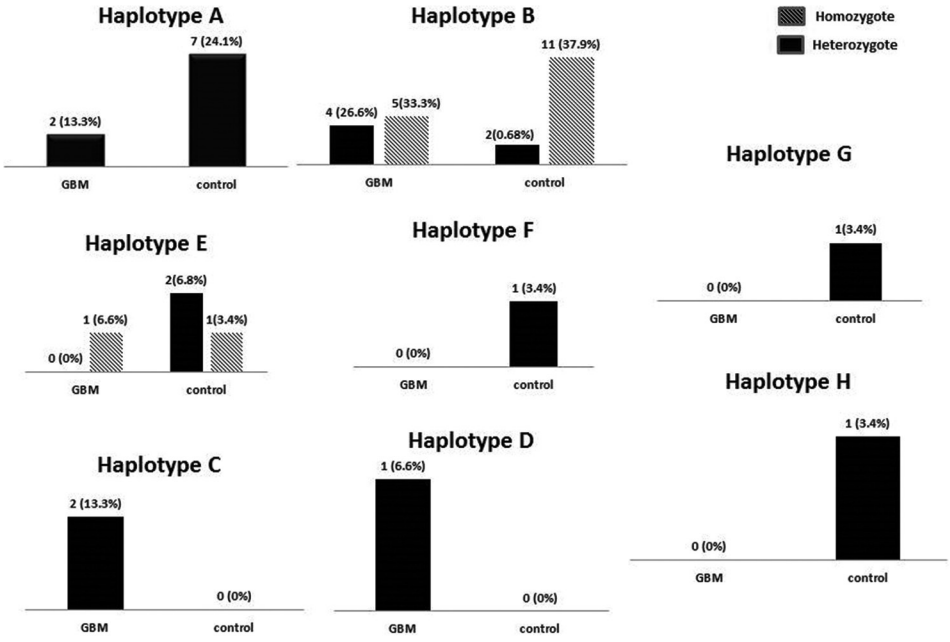

Figure 1. Frequencies and count for reported haplotypes.
Abbreviation: GBM: Glioblastoma.

(PRAPi) to improve efficacy through synergistic activity and potentially sensitize naturally PARPi-resistant tumors to PARPi. Initial combinations of PARPi and chemotherapy were delayed by major overlapping hematologic toxicity, but the latest combinations with lower toxicities and more targeted approaches are currently undergoing assessments.[28] In preclinical studies, the combination of TMZ with PRAPi has an enhanced cytotoxic effect, independent of HR,[29] as TMZ stimulates base damage, leading to the development of PARP-DNA complexes, which, in combination with effective PARP-trapping agents, enhance cytotoxicity. This has encouraged research into trials assessing this combination over different tumor histologies such as GBM,[30] colorectal cancer,[31] and breast cancer.[32] In general, the combination of TMZ and PARP inhibition was found to be well-tolerated, although efficacy was modest in most tumor subtypes.[33]

One of the assumed haplotypes includes haplotype [B], detected in homo- or heterozygous forms, which was associated with a familial history of breast cancer in the control individuals studied. This outcome was in agreement with the study of Tuazon *et al.*[34] Therefore, it will be important to carry out a future prospective study to confirm this finding in a large group of Egyptian individuals.

This paper is the first to report on the three identified haplotypes, termed haplotypes [C], [D], and [H], and all were in heterozygous form. GBM patients with haplotypes [C] and [D] responded to treatment with either CR or PR. Hence, it could be of great value to investigate the *BRCA1* haplotype among GBM patients before their treatment, as it was previously confirmed that BRCA1 protein expression may as well predict GBM survival.[35] Moreover, the newly reported haplotype [H] was only detected in healthy individuals (n = 25), which may indicate that this type of haplotype reports a lack of risk for cancer predisposition. A prospective study is currently underway to confirm this finding in a large Egyptian population.

Although GBM haplotype analysis is of great importance and the present study sheds light on this type of analysis in relation to GBM as one of the cancers worldwide, the small number of cases is one of the limitations of the study. This small number could be due to the fact that the incidence of cancer among Egyptians is not as high as breast or liver cancer. As this study is in the preliminary stage, the enrollment of a large number of cases will be considered in ongoing prospective research. Another limitation is the lack of some data for GBM patients, such as Isocitrate dehydrogenase1 (IDH1) and O6-methylguanine-DNA-methyltransferase (MGMT) status, so a comparison of haplotype variance regarding mutant IDH1 and MGMT methylation was not reported.

5. Conclusion

We build on our earlier finding that haplotype analysis among GBM patients can help predict patients who may benefit from TMZ treatment and that analyzing *BRCA1* haplotypes may identify those who are at low risk of developing cancer.

Acknowledgments

None.

Funding

The study was supported by the Science and Technology Development Fund (STDF) through Capacity Building Grant Fund (CBG) (Grant No. 4940).

Conflict of interest

The authors declare that they have no competing interests.

Author contributions

Conceptualization: Mohamed K. Khalifa, Amira M Nageeb, Menha Swellam

Formal Analysis: Mohamed K. Khalifa MS, Amira M Nageeb

Investigation: Mohamed K. Khalifa LRE, Amira M Nageeb, Lobna R. Ezz El Arab

Methodology: Mohamed K. Khalifa, Amira M Nageeb, Menha Swellam

Writing – original draft: Mohamed K. Khalifa, Amira M Nageeb, Menha Swellam

Writing – review & editing: All authors

Ethics approval and consent to participate

Ethical approval of the study was obtained from the Medical Ethical Committee of the National Research Center (ID#17111), Egypt, and all participants signed informed consent.

Consent for publication

Participants have signed their informed consent for publishing their data in this study.

Availability of data

Data used in this work are available from the corresponding author on reasonable request.

References

1. Thakkar JP, Dolecek TA, Horbinski C, *et al*. Epidemiologic and molecular prognostic review of glioblastoma. *Cancer Epidemiol Biomarkers Prev*. 2014;23(10):1985-1996.

doi: 10.1158/1055-9965.EPI-14-0275

2. Ostrom QT, Gittleman H, Xu J, *et al*. CBTRUS statistical report: Primary brain and other central nervous system tumors diagnosed in the United States in 2009-2013. *Neuro Oncol*. 2016;18(suppl_5):v1-v75.

doi: 10.1093/neuonc/now207

3. Kleihues P, Ohgaki H. Phenotype vs genotype in the evolution of astrocytic brain tumors. *Toxicol Pathol*. 2000;28(1):164-170.

doi: 10.1177/019262330002800121

4. Al-Holou WN, Hodges TR, Everson RG, *et al*. Perilesional resection of glioblastoma is independently associated with improved outcomes. *Neurosurgery*. 2020;86(1):112-121.

doi: 10.1093/neuros/nyz008

5. Stupp R, Mason WP, van den Bent MJ, *et al*. Radiotherapy plus concomitant and adjuvant temozolomide for glioblastoma. *N Engl J Med*. 2005;352(10):987-996.

doi: 10.1056/NEJMoa043330

6. Huang B, Yu Z, Liang L. Effect of long-term adjuvant temozolomide chemotherapy on primary glioblastoma patient survival. *BMC Neurol*. 2021;21:424.

doi: 10.1186/s12883-021-02461-9

7. Guo C, Yang Q, Xu P, *et al*. Adjuvant temozolomide chemotherapy with or without interferon alfa among patients with newly diagnosed high-grade gliomas: A randomized clinical trial. *JAMA Netw Open*. 2023;6(1):e2253285.

doi: 10.1001/jamanetworkopen.2022.53285

8. HGMD. Available from: https://www.hgmd.cf.ac.uk/ac/introduction.php?lang=english

9. Kondo N, Takahashi A, Ono K, Ohinishi T. DNA damage induced by alkylating agents and repair pathways. *J Nucleic Acids*. 2010;2010:543531.

doi: 10.4061/2010/543531

10. Quiros S, Roos WP, Kaina B. Rad51 and BRCA2--New molecular targets for sensitizing glioma cells to alkylating anticancer drugs. *PLoS One*. 2011;6:e27183.

doi: 10.1371/journal.pone.0027183

11. Short SC, Giampieri S, Worku M, *et al*. Rad51 inhibition is an effective means of targeting DNA repair in glioma models and CD133+ tumor-derived cells. *Neuro Oncol*. 2011;13:487-499.

doi: 10.1093/neuonc/nor010

12. Zhang N, Wu X, Yang L, *et al*. FoxM1 Inhibition sensitizes resistant glioblastoma cells to temozolomide by downregulating the expression of DNA-repair gene Rad51. *Clin Cancer Res*. 2012;18(21):5961-5971.

doi: 10.1158/1078-0432.CCR-12-0039

13. Trujillano D, Weiss MER, Schneider J, *et al*. Next-generation sequencing of the BRCA1 and BRCA2 genes for the genetic diagnostics of hereditary breast and/or ovarian cancer. *J Mol Diagn*. 2015;17:162-170.

doi: 10.1016/j.jmoldx.2014.11.004

14. Lord CJ, Ashworth A. PARP inhibitors: Synthetic lethality in the clinic. *Science*. 2017;355(6330):1152-1158.

doi: 10.1126/science.aam7344

15. Taza F, Holler A, Fu W, *et al*. Differential activity of PARP inhibitors in BRCA1-versus BRCA2-altered metastatic castration-resistant prostate cancer. *JCO Precis Oncol*. 2021;5:1200-1220.

doi: 10.1200/PO.21.00070

16. Gupta SK, Smith EJ, Mladek AC, *et al*. PARP inhibitors for sensitization of alkylation chemotherapy in glioblastoma: Impact of blood-brain barrier and molecular heterogeneity. *Front Oncol*. 2019;8:670.

doi: 10.3389/fonc.2018.00670

17. Boukerroucha M, Josse C, Segers K, *et al*. BRCA1 germline mutation and glioblastoma development: Report of cases. *BMC Cancer*. 2015;15:181.

doi: 10.1186/s12885-015-1205-1

18. Galisa SLG, Jacob PL, de Farias AA, *et al*. Haplotypes of single cancer driver genes and their local ancestry in a highly admixed long-lived population of Northeast Brazil. *Genet Mol Biol*. 2022;45(1):e20210172.

doi: 10.1590/1678-4685-GMB-2021-0172

19. Wang S, Qian F, Zheng Y, *et al*. Genetic variants demonstrating flip-flop phenomenon and breast cancer risk prediction among women of African ancestry. *Breast Cancer Res Treat*. 2018;168:703-712.

doi: 10.1007/s10549-017-4638-1

20. Carrot-Zhang J, Chambwe N, Damrauer JS, *et al*. Comprehensive analysis of genetic ancestry and its molecular correlates in cancer. *Cancer Cell*. 2020;37:639-654.e6.

doi: 10.1016/j.ccell.2020.04.012

21. Ostrom QT, Egan KM, Nabors LB, *et al*. Glioma risk associated with extent of estimated European genetic ancestry in African-Americans and Hispanics. *Int J Cancer*. 2020;146:739-748.

doi: 10.1002/ijc.32318

22. Wen PY, Macdonald DR, Reardon DA, *et al*. Updated response assessment criteria for high-grade gliomas: Response assessment in neuro-oncology working group. *J Clin Oncol*. 2010;28(11):1963-1972.

doi: 10.1200/JCO.2009.26.3541

23. Aykan NF, Özatlı T. Objective response rate assessment in oncology: Current situation and future expectations. *World J Clin Oncol*. 2020;11(2):53-73.

doi: 10.5306/wjco.v11.i2.53

24. Terkelsen T, Christensen LL, Fenton D, *et al*. Population frequencies of pathogenic alleles of BRCA1 and BRCA2: Analysis of 173 Danish breast cancer pedigrees using the BOADICEA model. *Fam Cancer*. 2019;18:381-388.

    doi: 10.1007/s10689-019-00141-9

25. Nageeb A, Mohamed M, Ezz El Arab LR, Khalifa MK, Swellam M. Next generation sequencing of BRCA genes in glioblastoma multiform Egyptian patients: A pilot Study. *Arch Physiol Biochem*. 2020;128:809-817.

    doi: 10.1080/13813455.2020.1729814

26. Massarat AR, Lamkin M, Reeve C, Williams AL, D'Antonio M, Gymrek M. Haptools: A toolkit for admixture and haplotype analysis. *Bioinformatics*. 2023;39(3):btad104.

    doi: 10.1093/bioinformatics/btad104

27. Freedman ML, Penney KL, Stram DO, *et al*. Common variation in BRCA2 and breast cancer risk: A haplotype-based analysis in the multiethnic cohort. *Hum Mol Genet*. 2004;13:2431-2441.

    doi: 10.1093/hmg/ddh270

28. Bhamidipati D, Haro-Silerio JI, Yap TA, Ngoi N. PARP inhibitors: Enhancing efficacy through rational combinations. *Br J Cancer*. 2023;129:904-916.

    doi: 10.1038/s41416-023-02326-7

29. Gill SJ, Travers J, Pshenichnaya I, *et al*. Combinations of PARP inhibitors with temozolomide drive PARP1 trapping and apoptosis in Ewing's sarcoma. *PLoS One*. 2015;10:e0140988.

    doi: 10.1371/journal.pone.0140988

30. Sim HW, McDonald KL, Lwin Z, *et al*. A randomized phase II trial of veliparib, radiotherapy, and temozolomide in patients with unmethylated MGMT glioblastoma: The VERTU study. *Neuro Oncol*. 2021;23:1736-1749.

    doi: 10.1093/neuonc/noab111

31. Pishvaian MJ, Slack RS, Jiang W, *et al*. A phase 2 study of the PARP inhibitor veliparib plus temozolomide in patients with heavily pretreated metastatic colorectal cancer. *Cancer*. 2018;124:2337-2346.

    doi: 10.1002/cncr.31309

32. Xu J, Keenan TE, Overmoyer B, *et al*. Phase II trial of veliparib and temozolomide in metastatic breast cancer patients with and without BRCA1/2 mutations. *Breast Cancer Res Treat*. 2021;189:641-651.

    doi: 10.1007/s10549-021-06292-7

33. Ding J, Wu S, Zhang C, *et al*. BRCA1 identified as a modulator of temozolomide resistance in P53 wild-type GBM using a high-throughput shRNA-based synthetic lethality screening. *Am J Cancer Res*. 2019;9(11):2428-2441.

34. De Asis Tuazon A, Lott P, Bohórquez M, *et al*. Haplotype analysis of the internationally distributed BRCA1 c.3331_3334delCAAG founder mutation reveals a common ancestral origin in Iberia. *Breast Cancer Res*. 2020;22:108.

    doi: 10.1186/s13058-020-01341-3

35. Vassilakopoulou M, Won M, Curran WJ, *et al*. BRCA1 protein expression predicts survival in glioblastoma patients from an NRG oncology RTOG cohort. *Oncology*. 2021;99(9):580-588.

    doi: 10.1159/000516168

ACCSCIENCE PUBLISHING

Tumor Discovery

ORIGINAL RESEARCH ARTICLE

Effect of 900 MHz radiofrequency electromagnetic radiation emitted from mobile phone on testicular immunity and the associated risk of testicular germ cell tumor

Fesih Ok[1]*, Mustafa Emre[2], Atil Bisgin[3], Samir Jafarguliyev[1], Ibrahim Boga[3], Salih Cetiner[4], Gulbanu Yesyet[4], Emine Bagir[5], Yildirim Bayazit[1], and Saban Doran[1]

[1]Department of Urology, Faculty of Medicine, Cukurova University, Adana, Turkey

[2]Department of Biophysics, Faculty of Medicine, Cukurova University, Adana, Turkey

[3]Department of Medical Genetics, Faculty of Medicine, Cukurova University, Adana, Turkey

[4]Central Laboratory, Faculty of Medicine, Cukurova University, Adana, Turkey

[5]Department of Pathology, Faculty of Medicine, Cukurova University, Adana, Turkey

Abstract

The emission of radiofrequency electromagnetic radiation (RF-EMR) from mobile phones has been implicated in causing inflammatory changes in the testis. Nevertheless, the direct association of these changes with the development of testicular germ cell tumors (TGCT) remains unclear. Therefore, we purposed to investigate the effect of RF-EMR exposure on inflammatory changes in the testis, cytokine gene expression levels, and the incidence of TGCT. Twenty male Wistar albino rats were randomly assigned to either the study or control groups. The study group was exposed to RF-EMR at 900 MHz, 26 V/m, and a specific absorption rate (SAR) of 0.14 W/kg for 4 h/day over 8 weeks. Histopathological analysis, vitality analysis using Annexin V, and real-time polymerase chain reaction for the analysis of interleukin 1 (IL-1), IL-4, IL-10, tumor necrosis factor-alpha, and interferon-gamma (IFN-γ) cytokine gene expressions were performed on the testicular tissue. The median testis weight (163.0 g [133.0 – 183.0] vs. 179.0 g [134.0 – 195.0], $P = 0.012$) and volume (0.95 cm^3 [0.800 – 1.400] vs. 1.100 cm^3 [1.050 – 1.500], $P = 0.031$) of the study group were significantly lower compared to the control group. The seminiferous tubule damage ($P < 0.001$) and interstitial edema ($P = 0.042$) were significantly higher in the study group. The tunica albuginea thickness was significantly reduced in the study group ($P < 0.001$). The fold changes in the expression levels of IL-4 and IFN-γ increased significantly in the study group. Our findings indicate that RF-EMR exposure causes structural, histopathological, and inflammatory toxic effects on the testis. The observed elevation in gene expression levels of IL-4 and IFN-γ cytokines following RF-EMR exposure suggests their potential role as regulators of TGCT initiation, thereby offering a viable potential therapeutic target in combination with current treatments. Nonetheless, future well-designed studies are necessary to validate our findings.

Keywords: Radiofrequency electromagnetic radiation; Testis; Inflammation; Testicular germ cell tumor

***Corresponding author:**
Fesih Ok
(drfesihok@gmail.com)

Citation: Ok F, Emre M, Bisgin A, *et al.* Effect of 900 MHz radiofrequency electromagnetic radiation emitted from mobile phone on testicular immunity and the associated risk of testicular germ cell tumor. *Tumor Discov*. 2024;3(1): 1703.
https://doi.org/10.36922/td.1703

Received: August 29, 2023
Accepted: November 30, 2023
Published Online: February 19, 2024

1. Introduction

Due to its advanced technological features, the prevalence of mobile phones has increased considerably. Investigators have suggested that the radiofrequency electromagnetic radiation (RF-EMR) emitted by mobile phones poses deleterious effects on human health.[1] Studies have demonstrated that RF-EMR from mobile devices may be associated with various adverse effects at molecular and cellular levels, including cancer, oxidative stress, increased free radicals, lipid peroxidation, DNA damage, and chromosomal abnormalities.[1] The testes and brain are among the organs most extensively investigated owing to their intense exposure to RF-EMR.[1] RF-EMR generally exerts negative effects on seminal parameters in the testes, such as sperm count, concentration, motility, and percentage of normal morphology. Moreover, it disrupts the morphological structure of the testes and boosts the permeability of the blood–testis barrier.[1]

Cytokines are physiologically produced in the testes and play essential roles in maintaining their normal function. However, cytokines also have critical roles in inducing inflammatory reactions under stress conditions. Exposure to RF-EMR leads to an increase in reactive oxygen species (ROS) and oxidative stress.[2] ROS generated by oxidative stress activates nuclear factor kappa B (NF-κB) and activator protein-1. In addition, it stimulates the transcription of genes encoding growth factors, cytokines, and extracellular matrix proteins.[1]

Testicular germ cell tumors (TGCT) are the most prevalent solid tumors in young men and commonly exhibit infiltration by T lymphocytes.[3] Tumor-infiltrating lymphocytes (TIL) and cytokine-mediated immunity are significantly associated with the development and prognosis of TGCT.[4] Klein *et al.* observed numerous B, T, and dendritic cells within germ cell neoplasia *in situ* (GCNIS) and seminoma.[4] Furthermore, a spectrum of cytokines, including pro-inflammatory cytokines (interleukin 1 beta [IL-1β], IL-6, and tumor necrosis factor-alpha [TNF-α]), anti-inflammatory cytokines (transforming growth factor-beta [TGF-β1), Th1-mediated cytokines (IL-2 and interferon-gamma [IFN-γ]), and chemokines (chemokine CXC ligand 13 [CXCL-13], chemokine CXC ligand 10 [CXCL-10], and chemokine [C-C motif] ligand [CCL-5]), were significantly presented in TGCT, suggesting the presence of a pro-tumorigenic milieu.[4] This experimental study aimed to investigate the impact of RF-EMR on inflammatory cytokine gene expression levels in the testes and its potential association with the development of TGCT.

2. Methods

2.1. Experimental design

The experimental study was conducted at the Cukurova University Health Sciences Experimental Application and Research Center. Male Wistar albino rats were utilized for the study. A total of 20 rats were categorized into study and control groups (10 rats each). Throughout the 8-week duration of the study, the rats were fed with adequate tap water and standard rat pellet chow without dietary restrictions imposed. All experimental procedures were conducted in accordance with the Institutional Animal Ethics Committee recommendations (Protocol Authorization Number: 5-2-2019).

A specialized application cage measuring 90 cm × 90 cm × 42 cm, consisting of four equal sections to accommodate rats comfortably during exposure to RF-EMR, was custom-designed (Figure 1A). The study used a radiofrequency electromagnetic field (RF-EMF) generator (GHZ2011X, Set Electronic Co. Ltd., Turkey). A monopole antenna connected to the generator emitted 900 MHz RF-EMR and was placed in the application cage. The monopole antenna was strategically positioned to evenly radiate RF-EMR at a consistent distance of 32 cm from the bodies of the rats in the study group (Figure 1B). In addition, temperature changes resulting from RF-EMR exposure were monitored using a four-channel thermometer. The specific absorption rate (SAR) value was computed based on the calculated electric field density (V/m) and power density (mW/cm^2). For the numerical determination of SAR, CST (Microwave Studio Suite [version 2018], Dassault Systèmes, Germany), an electromagnetic field solver utilizing the finite integration technique, was used (Figure 1C and D). SAR values ranged from 0.008 to 0.14 W/kg. Therefore, under identical conditions, orientation, and antenna power, a uniform SAR value of 0.14 W/kg across the whole body was

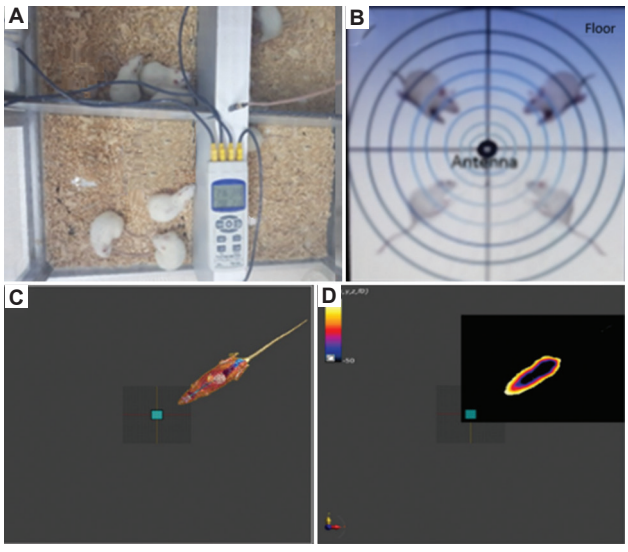

Figure 1. (A) Radiofrequency electromagnetic radiation exposure system. Monopole antenna placed in the application cage (B) and specific absorption rate distribution for the whole body in the voxel mouse model (C and D).

derived. Over the course of 8 weeks, the rats were exposed to RF-EMF at 900 MHz, 26 V/m, and SAR 0.14 W/kg for 4 h/day. At the end of the 8-week exposure period, all the rats from both the control and study groups were sacrificed, and orchiectomy procedures were performed. Testicular weight and volume were recorded, followed by storage of testis tissue for subsequent histopathological examination, DNA analysis, and apoptotic cell analysis.

2.2. Real-time polymerase chain reaction (PCR) gene expression analysis

Gene expression profiling for IL-1, IL-4, IL-10, TNF- α, and IFN-γ was conducted using primer-based designed specifically for these genes, following the protocols outlined below.

2.2.1. RNA isolation from tissue

Tissue sections with a thickness of 10 μm were collected, and the isolation protocol was performed in accordance with the manufacturer's directions (RNeasy FFPE Kit, Qiagen, Germany). Following isolation, RNA concentration was measured.

2.2.2. cDNA synthesis protocol

Ten microliters of RNA were transferred to a 0.2 ml PCR tube and incubated at 65°C for 5 min in a PCR instrument (VeritiPro Thermal Cycler, ThermoFisher Scientific, USA). A cDNA mix was prepared with 7.5 μL of RT mix and 2.5 μL of reverse transcriptase, followed by initiation of the cycle in the PCR instrument. The High-capacity cDNA Reverse Transcription Kit (ThermoFisher Scientific, USA) was used for cDNA synthesis.

2.2.3. Real-time PCR protocol

Real-time PCR experiments were performed using the GoTaq RT-PCR kit (Promega, USA) and SYBR Green chemistry (Bio-Rad, USA). The primer sequences used in this study are provided in the Appendix. Both procedures were conducted according to the manufacturer's instructions. A mixture comprising 20 μL RT-PCR mix and 5 μL cDNA was dispensed into each of the reaction tubes, which contained samples, negative control, positive control, and standards, respectively. Subsequently, the RT-PCR protocol was started in the PCR instrument. Upon completion of the RT-PCR protocol, the data obtained were analyzed using the delta cycle threshold (Ct) (comparative Ct method [ΔCt], 2-DDCt) method. Ct values for both the control and study groups were obtained from experiments performed using the qRT-PCR Rotor-Gene Q (Qiagen, Germany) device to determine changes in the expressions of IL-1, IL-4, IL-10, TNF- α, and IFN- γ genes. The changes in the expressions of the relevant genes were calculated by entering Ct data into Microsoft Excel. For statistical analyses, the Gene Globe Data Analysis Center (Qiagen, Germany) online analysis program was utilized.

2.3. Vitality determination using flow cytometry

Fresh tissue samples from both the control and study groups were cut into pieces and separated in sterile Petri dishes. They were centrifuged twice for 5 min at 400 relative centrifugal force, resulting in the suspension of cells at the end of these processes. After the final centrifugation, the cell pellet was resuspended with 100 μL of a binding solution, resulting in a 10-fold dilution, and maintained on ice. Next, 5 μL of Annexin V-FITC solution (Beckman Coulter, France) was added to the cell suspension and incubated on ice for 10 min in the dark following gentle mixing. After incubation, 400 μL of the binding solution was added, and readings were obtained using a flow cytometry device (Cytoflex, Beckman Coulter, USA). Subsequently, Annexin V-FITC-positive cells were selected, and apoptotic and necrotic cells were determined. Cells selected from the side scatter (SSC)/forward scatter (FS) graphics and analyzed in Annexin V/PI graphics.

2.4. Histopathological examination of testicular tissues

The testis resection samples intended for histopathological examination were initially fixed using 10% formaldehyde. Subsequently, five-micron-thick sections were obtained from the paraffin-embedded tissues. These tissue sections, prepared on specialized slides, were stained with hematoxylin and eosin (H&E) staining using an automated staining device (Leica ST 5020, Leica, Germany), followed by automated closure using another device (Leica ST 5030, Leica, Germany). In addition, tissue samples were subjected to histochemical analysis using Masson's trichrome method. Immunohistochemical (IHC) staining was performed on five-micron-thick sections of formalin-fixed, paraffin-embedded tissue using a SALL4 antibody (Cellmark 6E3 Mouse Monoclonal Antibody, Cell Marque, USA). The BenchMark XT visualization system with enzymatic digestion ISH protease 2 (Ventana, USA) and the iView Blue Detection Kit (Ventana, USA) were employed for visualization. Evaluation of H&E and histochemical specimens was conducted using an Olympus BX46 light microscope. Resection samples were assessed for seminiferous tubule structure, Johnson score, tunica albuginea thickness, interstitial edema, and Leydig cells. Tunica albuginea thickness and seminiferous tubule diameter were measured using the Aperio ImageScope program. Seminiferous tubule damage, interstitial edema, and Leydig cells were scored semiquantitatively on a scale ranging from 0 to 3.

2.5. Statistical analysis

The statistical analysis was conducted using IBM SPSS Statistics Version 20.0. The normal distribution of continuous variables was assessed using the Kolmogorov–Smirnov test.

Continuous variables following a normal distribution were expressed as mean ± standard deviation, and the comparison between the two groups was performed using Student's *t*-test. For continuous variables that did not fit a normal distribution, the data were reported as median (minimum–maximum), and the comparison between groups was carried out using the Mann–Whitney U test. A significance level of 0.05 was adopted for all statistical analyses.

3. Results

3.1. Testis weight and volume

The median testis weight in the study group (163.0 g [133.0 – 183.0]) was significantly lower than the control group (179.0 g [134.0 – 195.0]) ($P = 0.012$). In addition, the median testis volume in the study group (0.95 cm^3 [0.800 – 1.400]) was significantly reduced than the control group (1.100 cm^3 [1.050 – 1.500]) ($P = 0.031$). Furthermore, the median score for seminiferous tubule damage was significantly higher in the study group (1.5 vs. 0.0, $P < 0.001$). The mean tunica albuginea thickness was significantly reduced in the study group (22.3 ± 4.61 μM vs. 87.4 ± 2.67 μM) ($P < 0.001$) (Table 1).

3.2. Changes in the gene expressions of IL-1, IL-4, IL-10, TNF-α, and IFN-γ

The fold changes in the expression levels of the relevant gene in both the study and control groups were calculated using the 2-DDCt analysis and are presented in Figure 2. The delta Ct values for expression analyses of the study and control groups after real-time PCR are shown in Table 2. Notably, the expression levels of IL-4 and IFN-γ genes demonstrated statistically significant increases in fold changes within the study group (n = 10, $P < 0.01$). However, upon analyzing the interchangeability between the groups for other cytokines, no significant difference was detected ($P > 0.1$).

3.3. Vitality analysis using flow cytometry (Annexin V)

A vitality assessment was conducted using flow cytometry. The vitality rates of both groups were similar (43.6 ± 14.2% vs. 45.7 ± 15.6%, $P = 0.709$) (Figure 3).

3.4. Histopathological findings

The tunica albuginea was significantly thinner in the study group (22.3 ± 4.61 μM) than the control group (87.4 ± 2.67 μM) ($P < 0.001$). Seminiferous tubule damage, interstitial edema, and Leydig cells were evaluated semiquantitatively. Seminiferous tubule damage was significantly more pronounced in the study group (Figure 4, $P < 0.001$). While mild interstitial edema was present in the control group (Figure 5A), it was significantly more severe in the study group (Figure 5B, $P = 0.042$). Leydig cell counts were relatively higher in the control group (Figure 5C) than in the study group (Figure 5D, $P = 0.669$). In addition, tunica albuginea thickness was significantly greater in the control group (Figure 5E) than in the study group (Figure 5F) ($P < 0.001$). SALL4 staining was utilized for the detection of germ cell tumors. However, negative SALL4 IHC staining was observed in the seminiferous tubules (Figure 6).

4. Discussion

The present study aims to investigate the effects of RF-EMR on testicular health. This investigation entails the measurement of gene expressions related to inflammatory (IL-1, TNF-α, IFN-γ) and anti-inflammatory (IL-4, IL-10) cytokines in testis tissue, alongside histopathological examination. In addition, the study investigated whether

Table 1. Testis sizes and histopathologic parameters

Parameter	Study group (*n*=10)	Control group (*n*=10)	Statistical test	*p*-value
Testis weight (median [min–max] g)	163.0 (133.0 – 183.0)	179.0 (134.0 – 195.0)	Z=–2.479	0.012
Testis volume (median [min–max] cm^3)	0.95 (0.800 – 1.400)	1.100 (1.050 – 1.500)	Z=–2.174	0.031
Interstitial edema (median [min–max])	1.0 (0.0 – 3.0)	1.0 (0.0 – 1.0)	Z=–2.347	0.042
Leydig cells (median [min–max])	1.0 (1.0 – 1.0)	1.0 (1.0 – 2.0)	Z=–1.549	0.669
Johnson score (median [min–max])	10.0 (10.0 – 10.0)	10.0 (10.0 – 10.0)		N/A
Seminiferous tubule damage (median [min–max])	1.5 (0.0 – 3.0)	0.0 (0.0 – 1.0)	Z=–4.102	<0.001
Tunica albuginea thickness (mean ± SD μM)	22.3 ± 4.61	87.4 ± 2.67	F=3.145	<0.001
Seminiferous tubule diameter (mean ± SD μM)	762.5 ± 83.4	775.7 ± 37.5	F=1.919	0.637
Annexin V (mean ± SD %vitality)	43.6 ± 14.2	45.7 ± 15.6	F=0.006	0.709

Abbreviation: SD: Standard deviation.

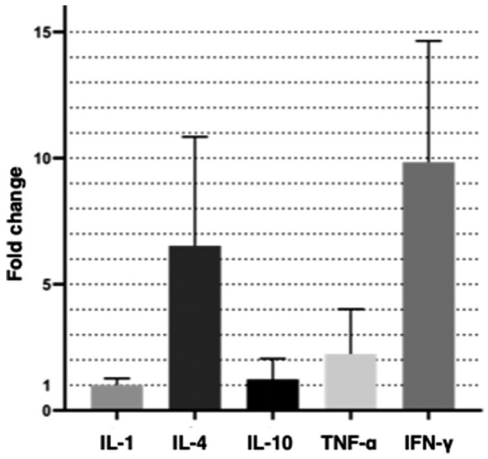

Figure 2. The fold changes in the expression levels of inflammatory cytokines. It shows that interleukin-4 and interferon-γ gene expression fold change increased significantly in the study group (n = 10).

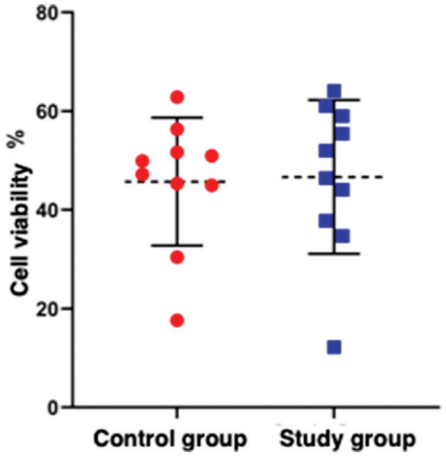

Figure 3. Vitality analysis using flow cytometry (Annexin V). It shows that the viable cell ratios were similar in the study (n = 10) and control (n = 10) groups (43.6% vs. 45.7%, P = 0.709). Student's t-test was used for statistical analysis.

changes in the immune microenvironment induced by RF-EMR exposure might foster a pro-tumorigenic environment conducive to the development of TGCTs. The findings reveal that RF-EMR exposure leads to significant increases in the gene expressions of IL-4 and IFN-γ in the testes. Furthermore, RF-EMR exposure is associated with reductions in testicular volume, weight, and tunica albuginea thickness, alongside significant increases in seminiferous tubule damage and interstitial edema.

It has been demonstrated that RF-EMR significantly weakens antioxidant enzyme activity and increases ROS formation in living organisms.[5] Increased ROS levels precipitate oxidative damage to proteins, lipids, and DNA at the cellular level.[6] Consequently, resultant free

Table 2. Delta Ct values for gene expression analysis of the study and control groups

Group	IL-1	IL-4	IL-10	TNF-α	IFN-γ
Study group					
1	−2.80	−1.00	3.90	3.90	3.89
2	−2.70	−1.80	−0.80	−0.80	−0.78
3	−2.50	0.90	1.00	1.00	0.98
4	−2.70	0.10	0.00	0.00	0.01
5	−2.10	−1.50	−0.20	−0.20	−0.24
6	−2.30	1.50	1.60	1.60	1.57
7	−2.30	−1.30	−2.70	−2.70	−2.67
8	−2.50	0.00	0.50	0.50	0.47
9	−1.80	−0.30	0.70	0.70	0.71
10	−1.80	−0.50	−0.60	−0.60	−0.65
Control group					
1	−2.40	−3.80	5.30	4.40	2.90
2	−2.70	−3.80	−0.10	−1.60	−3.30
3	−2.80	−2.60	0.00	−1.60	−3.10
4	−1.80	−1.60	1.00	1.10	−3.00
5	−2.50	−4.30	−0.90	−0.60	−3.40
6	−1.90	−3.30	−0.30	−2.20	−2.70
7	−2.50	−2.00	1.10	0.20	−3.90
8	−2.60	−2.60	−1.10	−1.00	−2.70
9	−2.30	−2.70	0.30	0.10	−3.00
10	−1.60	−1.30	0.70	−0.20	−2.40

Abbreviations: Ct: Cycle Threshold; PCR: Polymerase Chain Reaction; IL-1: Interleukin-1; TNF-α: Tumor necrosis factor-alpha; IFN-γ: Interferon-gamma.

radicals induce significant changes in the histological and morphological structures of testis and spermatogenic cells.[7] Nisbet *et al.* reported occurrences of testicular vacuolar degeneration, severe necrosis, and exfoliation of the seminiferous epithelia in rats exposed to different levels of RF-EMR ranging from 900 to 1,800 MHz.[8] Similarly, Hasan *et al.* observed histopathologically irregularly shaped testes with inhomogeneous sizes and fewer spermatogenic cell layers, resulting in enlarged lumens in the seminiferous tubules in mice exposed to RF-EMR.[7] Consistent with these findings, our study identifies significant increases in seminiferous tubule damage and interstitial edema in radiation-exposed rats, with a plausible explanation being the degenerative action of RF-EMR on the germinal epithelium and seminiferous tubule.

In a study using 32 male Wistar albino rats, Cetkin *et al.* observed significantly lower testis weight and volume in the RF-EMR exposed group.[9] Similarly, Yahyazadeh *et al.* noted considerably reduced testicular wet weight following exposure to 900 MHz RF-EMR (60 min/day for

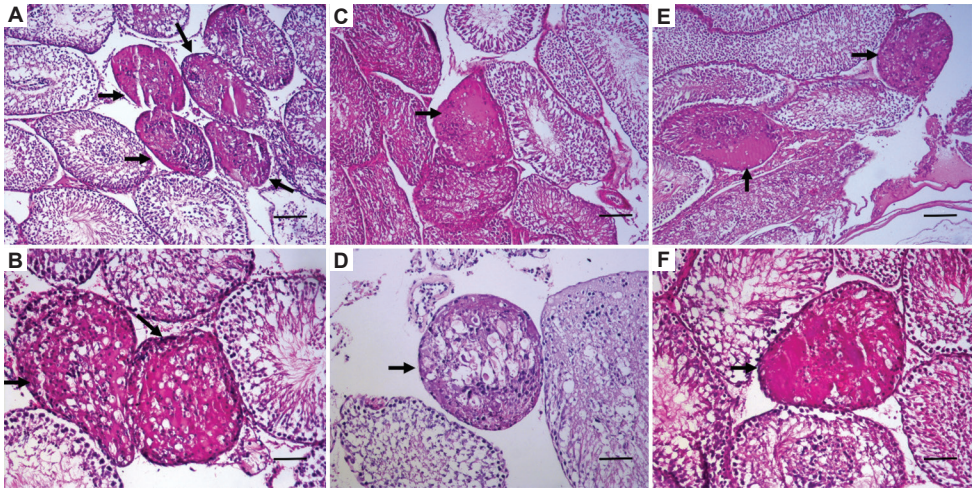

Figure 4. Disorganization, vacuolization, and edema in the seminiferous tubules. Panel A, C, and E indicate H&E magnification ×100, while panel B, D, and F indicate H&E magnification ×200. Scale bars: 100 µm. The arrows indicate disorganization, vacuolization, and edema in the seminiferous tubules. It shows the seminiferous tubule damage induced by radiofrequency electromagnetic radiation in the study group (n = 10).

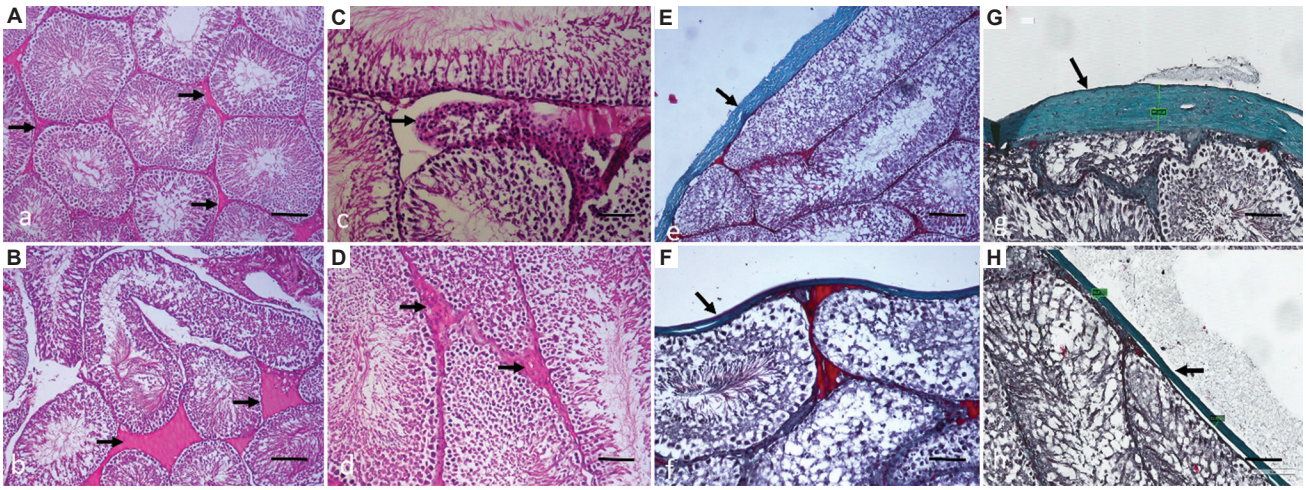

Figure 5. Mild interstitial edema in the control group (n = 10) (A); more severe in the study group (n = 10) (B) (P = 0.042). Leydig cells were relatively higher in the control group (C) than in the study group (D) (P = 0.669). Tunica albuginea thickness was significantly thinner in the study group (F) compared to the control group (E) (P < 0.001). Magnification ×100. Scale bar: 100 µm. The arrows indicate interstitial edema in panels A and B, Leydig cell intensity in panel C and D, and tunica albuginea thickness in panel E, F, G and H. Mann–Whitney U test was used for statistical analysis.

28 days).[10] Consistently, our study observed reductions in testis weight and volume in the RF-EMR exposed group. It is well-established that testicular function and weight are closely intertwined. Agarwal *et al.* reported that cell phones impair testicular function by promoting the formation of free radicals.[11] Therefore, impairments in testicular functions, such as reductions in spermatids and testosterone levels resulting from RF-EMR exposure, alongside changes in endogenous antioxidant enzymes, may contribute to decreases in testicular weights.[10] Moreover, Dasdag *et al.* reported significant reductions in tunica albuginea thickness following exposure to 2.4 GHz radiofrequency radiation,[12] corroborated by our findings of significantly reduced tunica albuginea thicknesses in the RF-EMR exposed group. These histomorphometric findings, including changes in the thickness of tunica albuginea and seminiferous tubule structures, may stem from damage to regulatory mechanisms such as the Na^+/K^+ pump, Na^+/Ca^+ and Na^+/H^+ exchangers, cytoskeleton contractility, and membrane fluidity, which govern cell volume regulation.[12]

The pathogenesis of TGCT remains unclear. This tumor's origin appears to be associated with testicular dysgenesis syndrome, probably initiated during the initial stages of embryogenesis.[13] The most prominent risk factor for TGCT is cryptorchidism, with additional risk factors including a history of TGCT, age, race, and infertility.[13] However, the

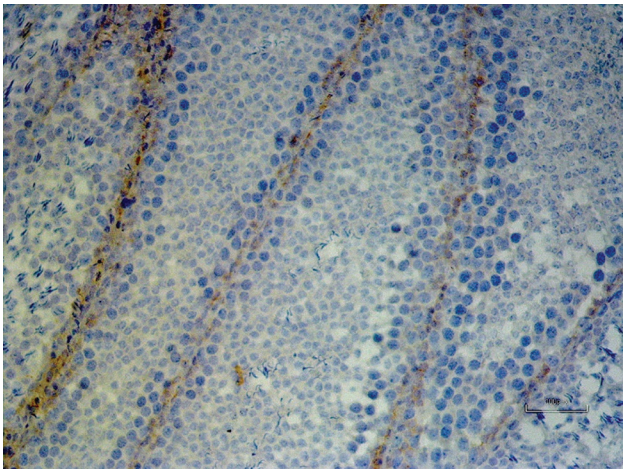

Figure 6. Negative SALL4 immunohistochemical (IHC) staining of seminiferous tubules (IHC × 200). Scale bar: 100 μm.

widely accepted view regarding the risk factors suggests that TGCT development arises from a combination of genetic, environmental, and hormonal factors.[13] There have been suggestions that mobile phones may be associated with the development of TGCT as one of the environmental factors due to their intense and close proximity to the testes.[14] However, the mechanism by which mobile phones could lead to TGCT has not been conclusively demonstrated. Nevertheless, it is acknowledged that inflammatory changes in the testes can be induced by mobile phone-related RF-EMR.[10] Regarding the immune mechanism in TGCT, previous studies have elucidated specific immune cell and cytokine characteristics.[3,4] Various pro-inflammatory cytokines have been implicated in germ cell proliferation, spermatogenetic cell differentiation, TGCT pathogenesis, metastasis, invasion, and neo-angiogenesis.[15] Building upon these data, our study suggests that the inflammation induced by RF-EMR in the testes and the associated immune response may increase the risk of TGCT.

In addition to animal experiments and clinical studies, cell culture investigations have also identified a relationship between TGCT and RF-EMR.[16] Yutong *et al*. examined N9 microglial cells exposed to 2.45 GHz EMF and observed increased levels of activated signal transducers and activators of transcription 3 (STAT3), which subsequently increased the transcription levels of inflammation-related genes, especially inducible nitric oxide synthase (iNOS) and TNF-α. They suggested that exposure to 2.45 GHz EMF could initiate inflammation and malignancy in microglia cells through signal transducer and activator of transcription 3 (STAT3) pathway.[16] STAT proteins comprise various transcription factors that mediate signal transduction from the extracellular environment to the cell nucleus. Notably, the activation of STAT3 is induced by specific cytokines, including IL-4, IFN-γ, growth factors, and oncogenes.[17] Other studies have suggested that IL-4-mediated signaling through STAT contributes to tumor development within the tumor microenvironment.[18-21] Indeed, studies have specifically indicated that dysregulated IL-4 formation is associated with various cancer types.[21,22]

IL-4 is a versatile cytokine and vital for regulating the immune system.[22] Upon IL-4 binding to its cytokine receptor, the ensuing activation of cell growth mediators, resistance to apoptosis, gene activation, and differentiation occur.[22] The significance of IL-4 as a promoter of tumor-initiating/cancer stem cell (CSC)-like cells has been demonstrated across various cancers. Elevated levels of IL-4 (generally generated by tumor-infiltrating lymphocytes) have been verified in advanced-stage prostate cancer (PC) patients.[23] *In vitro* studies with PC cell lines have demonstrated that IL-4 stimulates NF-κB and androgen receptors in a ligand-independent manner.[24] In colon cancer, CD133-positive tumor-initiating cells exhibit autocrine IL-4 signaling, leading to the upregulation of the anti-apoptotic protein Survivin, a target of the STAT-6 pathway.[25] In the pancreatic cancer cell line Capan-1, the knockdown of IL4Rα results in reduced cell growth, decreased anchorage-independent colony size, and inhibition of migration.[26] Similarly, in breast cancer cells, an antagonist of the IL-4 receptor IL4Rα was able to reduce the number of CD44+/CD24- CSC-like cells.[27] However, there is currently no study in the existing literature that conclusively proves the relationship between IL-4 and the development of TGCT. Our research revealed that exposure to RF-EMR increased IL-4 gene expression levels in rats. Although we lack robust evidence, this finding prompts the question: Could IL-4 exhibit a similar relationship with TGCT as observed with the aforementioned tumors?

The IFN-γ cytokine is predominantly generated by activated T lymphocytes and natural killer cells.[28] Although IFN-γ is effective against microbial infections, it also plays essential roles in numerous diseases, especially various types of cancers. In the past, IFN-γ was recognized solely for its antitumor properties.[28] The cytotoxic effects of IFN-γ, especially against tumor cells, have been extensively demonstrated in numerous studies. Subsequently, the pro-tumor effects of IFN- γ began to emerge. The discovery that IFN-γ promotes the expression of inhibitory molecules such as programmed cell death ligand 1 (PDL1), PDL2, indoleamine 2,3-dioxygenase 1 (IDO1), iNOS, FAS, and FAS ligand (FASL), all of which limit antitumor immunity, has raised concerns regarding the use of IFN-γ-modulating cancer immunotherapies.[29] Benci *et al*. reported that initial exposure to IFN-γ primes other factors to promote antigen presentation, T cell priming and activation, and tumor cell killing. Despite that, prolonged

exposure to IFN-γ transforms these supportive factors into adversaries, facilitating pro-tumorigenic effects via immunosuppression, angiogenesis, and tumor cell proliferation.[30] Similar to other tumors, investigations into the relationship between IFN-γ and tumor development, as well as its potential as a therapeutic target, were conducted for TGCT. Schweyer *et al.* analyzed TGCT cell lines (NTERA and NCCIT) and concluded that although they expressed and secreted IFN-γ, they were resistant to endogenous IFN-γ, as neutralization of IFN-γ with a specific antibody did not affect the proliferation and/or degree of apoptosis of the tumor cells.[28] Klein *et al.* examined the immune cellular microenvironment in testis biopsy specimens from patients with normal spermatogenesis, hypo-spermatogenesis with lymphocytic infiltration, GCNIS, and seminoma.[4] Alongside pro-inflammatory (IL-1b, IL-6, and TNF-a), anti-inflammatory (TGF-b1), Th-1-driven (IL-2) cytokines, and chemokines (CXCL-13, CXCL-10, and CCL5), high levels of IFN-γ transcripts were observed within immune cell infiltrates of GCNIS and seminoma samples.[4] Despite extensive research, the relationship between RF-EMR and the development of TGCT remains unestablished in the literature. The significant increase in the IFN-γ gene expression levels that we detected following RF-EMR exposure may potentially influence the development of TGCT.

The limitation of our work was the examination of a limited number of inflammatory markers due to budget constraints. Current budget restrictions prevented us from additional IHC analyses to observe and compare cytokine expression in tissue and protein levels using the ELISA method. However, our study boasts several strengths. Firstly, our experimental setup comprehensively examines both the IHC changes induced by RF-EMR in testicular tissue and the gene expressions of inflammatory cytokines. In addition, the identification of increased expression of IFN- γ and IL-4 genes, which have proven to influence the progression of various cancer types, provides valuable insights for further studies exploring the potential relationship between RF-EMR exposure and the development of TGCT.

5. Conclusion

RF-EMR induces structural, histopathological, and inflammatory toxic effects on testes. RF-EMR significantly reduces testes' weight and volume, increases seminiferous tubule damage and interstitial edema, and decreases tunica albuginea thickness. However, it also significantly increases the gene expression levels of IL-4 and IFN-γ, which are inflammatory cytokines that are potentially associated with TGCT development in testicular tissue. Therefore, these cytokines expressed following RF-EMR exposure may serve as regulators of TGCT initiation, offering a viable potential therapeutic target in combination with current treatment options. Nevertheless, future well-designed studies are imperative to substantiate our findings.

Acknowledgments

The author thanks the Cukurova University Scientific Research Project for all the support provided.

Funding

This work was financially supported by the Cukurova University Scientific Research Projects with grant number TSA-2019-12306.

Conflict of interest

The authors declare they have no competing interests.

Author contributions

Conceptualization: Fesih Ok, Mustafa Emre, Atil Bisgin
Formal analysis: Salih Cetiner, Emine Bagir
Investigation: Samir Jafarguliyev, Ibrahim Boga, Gulbanu Yesyet
Methodology: Yildirim Bayazit
Writing – original draft: Fesih Ok
Writing – review & editing: Yildirim Bayazit, Saban Doran

Ethics approval and consent to participate

The study received ethics approval from the Institutional Animal Ethics Committee (Protocol Authorization Number: 5-2-2019).

Consent for publication

Not applicable.

Availability of data

Data used in this work is available from the corresponding author upon reasonable request.

References

1. Bilgici B, Gun S, Avci B, Akar A, Engiz BK. What is adverse effect of wireless local area network, using 2.45 GHz, on the reproductive system? *Int J Radiat Biol*. 2018;94(11):1054-1061.

   doi: 10.1080/09553002.2018.1503430

2. Kivrak E, Yurt K, Kaplan A, Alkan I, Altun G. Effects of electromagnetic fields exposure on the antioxidant defense system. *J Microsc Ultrastruct*. 2017;5(4):167-176.

   doi: 10.1016/j.jmau.2017.07.003

3. Chovanec M, Mardiak J, Mego M. Immune mechanisms and possible immune therapy in testicular germ cell tumours.

Andrology. 2019;7(4):479-486.

doi: 10.1111/andr.12656

4. Klein B, Haggeney T, Fietz D, *et al*. Specific immune cell and cytokine characteristics of human testicular germ cell neoplasia. *Hum Reprod*. 2016;31(10):2192-2202.

doi: 10.1093/humrep/dew211

5. Gautam R, Singh KV, Nirala J, Murmu NN, Meena R, Rajamani P. Oxidative stress-mediated alterations on sperm parameters in male Wistar rats exposed to 3G mobile phone radiation. *Andrologia*. 2019;51(3):e13201.

doi: 10.1111/and.13201

6. Lu YS, Huang BT, Huang YX. Reactive oxygen species formation and apoptosis in human peripheral blood mononuclear cell induced by 900 MHz mobile phone radiation. *Oxid Med Cell Longev*. 2012;2021:740280.

doi: 10.1155/2012/740280

7. Hasan I, Amin T, Alam MR, Islam MR. Hematobiochemical and histopathological alterations of kidney and testis due to exposure of 4G cell phone radiation in mice. *Saudi J Biol Sci*. 2021;28(5):2933-2942.

doi: 10.1016/j.sjbs.2021.02.028

8. Ozlem Nisbet H, Nisbet C, Akar A, Cevik M, Onder Karayigit M. Effects of exposure to electromagnetic field (1.8/0.9 GHz) on testicular function and structure in growing rats. *Res Vet Sci*. 2012;93(2):1001-1005.

doi: 10.1016/j.rvsc.2011.10.023

9. Çetkin M, Kizilkan N, Demirel C, Bozdağ Z, Erkiliç S, Erbağci H. Quantitative changes in testicular structure and function in rat exposed to mobile phone radiation. *Andrologia*, 2017;49(10):e12761.

doi: 10.1111/and.12761

10. Yahyazadeh A, Altunkaynak BZ, Kaplan S. Biochemical, immunohistochemical and morphometrical investigation of the effect of thymoquinone on the rat testis following exposure to a 900-MHz electromagnetic field. *Acta Histochem*. 2020;122(1):151467.

doi: 10.1016/j.acthis.2019.151467

11. Agarwal A, Singh A, Hamada A, Kesari K. Cell phones and male infertility: A review of recent innovations in technology and consequences. *Int Braz J Urol*. 2011;37(4):432-454.

doi: 10.1590/s1677-55382011000400002

12. Dasdag S, Taş M, Akdag MZ, Yegin K. Effect of long-term exposure of 2.4 GHz radiofrequency radiation emitted from Wi-Fi equipment on testes functions. *Electromagn Biol Med*. 2015;34(1):37-42.

doi: 10.3109/15368378.2013.869752

13. Garolla A, De Giorgi U, Milardi D. Editorial: Testicular cancer: New insights on the origin, genetics, treatment, fertility, general health, quality of life and sexual function. *Front Endocrinol*. 2020;11:41.

doi: 10.3389/fendo.2020.00041

14. Hardell L, Carlberg M, Ohlson CG, Westberg H, Eriksson M, Hansson Mild K. Use of cellular and cordless telephones and risk of testicular cancer. *Int J Androl*. 2007;30(2):115-122.

doi: 10.1111/j.1365-2605.2006.00721.x

15. Svetlovska D, Miskovska V, Cholujova D, *et al*. Plasma cytokines correlated with disease characteristics, progression-free survival, and overall survival in testicular germ-cell tumor patients. *Clin Genitourin Cancer*. 2017;15(3):411-416.e2.

doi: 10.1016/j.clgc.2017.01.027

16. Hao Y, Yang X, Chen C, *et al*. STAT3 signalling pathway is involved in the activation of microglia induced by 2.45 GHz electromagnetic fields. *Int J Radiat Biol*. 2010;86(1):27-36.

doi: 10.3109/09553000903264507

17. Subramaniam A, Shanmugam MK, Perumal E, *et al*. Potential role of signal transducer and activator of transcription (STAT)3 signaling pathway in inflammation, survival, proliferation and invasion of hepatocellular carcinoma. *Biochim Biophys Acta*. 2013;1835(1):46-60.

doi: 10.1016/j.bbcan.2012.10.002

18. Wang X, Xin W, Zhang H, *et al*. Aberrant expression of p-STAT3 in peripheral blood CD4+ and CD8+ T cells related to hepatocellular carcinoma development. *Mol Med Rep.* 2014;10(5):2649-2656.

doi: 10.3892/mmr.2014.2510

19. Nappo G, Handle F, Santer FR, *et al*. The immunosuppressive cytokine interleukin-4 increases the clonogenic potential of prostate stem-like cells by activation of STAT6 signalling. *Oncogenesis*. 2017;6(5):e342.

doi: 10.1038/oncsis.2017.23

20. Erb HHH, Guggenberger F, Santer FR, Culig Z. Interleukin-4 induces a $CD44_{high}$/$CD49b_{high}$ PC3 subpopulation with tumor-initiating characteristics. *J Cell Biochem*. 2018;119(5):4103-4112.

doi: 10.1002/jcb.26607

21. Erb HHH, Culig Z, Stope MB. IL-4 Counteracts the cytotoxic effects of peripheral blood mononuclear cells on hormone-sensitive prostate cancer cells. *In Vivo*. 2021;35(4):1973-1977.

doi: 10.21873/invivo.12465

22. Nelms K, Keegan AD, Zamorano J, Ryan JJ, Paul WE. The IL-4 receptor: Signaling mechanisms and biologic functions. *Annu Rev Immunol*. 1999;17:701-738.

doi: 10.1146/annurev.immunol.17.1.701

23. Goldstein R, Hanley C, Morris J, *et al*. Clinical investigation of the role of interleukin-4 and interleukin-13 in the evolution of prostate cancer. *Cancers* (*Basel*). 2011;3(4):4281-4293.

doi: 10.3390/cancers3044281

24. Lee SO, Lou W, Nadiminty N, Lin X, Gao AC. Requirement for NF-(kappa)B in interleukin-4-induced androgen receptor activation in prostate cancer cells. *Prostate*. 2005;64(2):160-167.

doi: 10.1002/pros.20218

25. Di Stefano AB, Lovino F, Lombardo Y, *et al*. Survivin is regulated by interleukin-4 in colon cancer stem cells. *J Cell Physiol*. 2010;225(2):555-561.

doi: 10.1002/jcp.22238

26. Traub B, Sun L, Ma Y, *et al*. Endogenously expressed IL-4Rα promotes the malignant phenotype of human pancreatic cancer *in vitro* and in *vivo*. *Int J Mol Sci*. 2017;18(4):716.

doi: 10.3390/ijms18040716

27. Gaggianesi M, Turdo A, Chinnici Z, *et al*. IL4 primes the dynamics of breast cancer progression via DUSP4 inhibition. *Cancer Res*. 2017;77(12):3268-3279.

doi: 10.1158/0008-5472.CAN-16-3126

28. Schweyer S, Soruri A, Peters J, *et al*. Malignant germ cell tumours of the testis express interferon-gamma, but are resistant to endogenous interferon-gamma. *Br J Cancer*. 2003;89(5):915-921.

doi: 10.1038/sj.bjc.6601209

29. Gocher AM,Workman CJ, Vignali DA. Interferon-γ: Teammate or opponent in the tumour microenvironment? *Nat Rev Immunol*. 2022;22(3):158-172.

doi: 10.1038/s41577-021-00566-3

30. Benci JL,Xu B, Qiu Y, *et al*. Tumor interferon signaling regulates a multigenic resistance program to immune checkpoint blockade. *Cell*. 2016;167(6):1540-1554.e12.

doi: 10.1016/j.cell.2016.11.022

Appendix

Table 1. Primers sequences used for PCR.

Gene name	Primer sequence
Il-1 (NM_008361)	
Il-1-F	TGGACCTTCCAGGATGAGGACA
Il-1-R	GTTCATCTCGGAGCCTGTAGTG
Il-4 (NM_021283)	
IL-4-F	ATCATCGGCATTTTGAACGAGGTC
IL-4-R	ACCTTGGAAGCCCTACAGACGA
Il-10 (NM_010548)	
Il-10-F	CGGGAAGACAATAACTGCACCC
Il-10-R	CGGTTAGCAGTATGTTGTCCAGC
TNF-α (NM_013693)	
TNF-α-F	GGTGCCTATGTCTCAGCCTCTT
TNF-α-R	GCCATAGAACTGATGAGAGGGAG
IFN-γ (NM_008337)	
IFN-γ-F	CAGCAACAGCAAGGCGAAAAAGG
IFN-γ-R	TTTCCGCTTCCTGAGGCTGGAT

Abbreviations: IL-1: Interleukin-1; TNF-α: Tumor necrosis factor-alpha; IFN-γ: Interferon-gamma; PCR: Polymerase chain reaction.

ACCSCIENCE PUBLISHING

Tumor Discovery

ORIGINAL RESEARCH ARTICLE

Artificial intelligence enabled spatially resolved transcriptomics reveal spatial tissue organization of multiple tumors

Teng Liu[1,2†], Jinxin Ye[3†], Chunnan Hu[1†], Zongbo Zhang[1], Zhuomiao Ye[2], Jiangnan Liao[2], and Mingzhu Yin[1,2*]

[1]Department of Clinical Research Center (CRC), Clinical Pathology Center (CPC), Cancer Early Detection and Treatment Center (CEDTC) and Translational Medicine Research Center (TMRC), Chongqing University Three Gorges Hospital, Chongqing University, Wanzhou, Chongqing, China

[2]Department of Chongqing Technical Innovation Center for Quality Evaluation and Identification of Authentic Medicinal Herbs, Chongqing University Three Gorges Hospital, Chongqing University, Wanzhou, Chongqing, China

[3]Physics and Technique Department of Radiation Oncology, Cancer treatment institute, Chongqing University Three Gorges Hospital, Chongqing University, Wanzhou, Chongqing, China

Abstract

Spatially resolved transcriptomics was honored as the Method of the Year 2020 by Nature Methods. This approach allows biologists to precisely discern mRNA expression at the cellular level within structurally preserved tissues. Leveraging artificial intelligence in spatial transcriptomic analysis enhances the understanding of cellular-level biological interactions and offers novel insights into intricate tissues, such as tumor microenvironments. Nevertheless, numerous existing clustering algorithms employing deep learning exhibit the potential for enhancement. In this paper, we focus on graph deep learning-based spatial domain identification for spatial transcriptomics (ST) data from multiple tumors. This identification enables the recognition of cell subpopulations in distinct spatial coordinates, aiding further studies on tumor progression, such as cell-cell communication, pseudo-time trajectory inference, and single-cell deconvolution. Initially, the gene expression profiles and spatial location information were transformed into a gene feature matrix and a cell adjacency matrix. A variational graph autoencoder was then applied to extract features and reduce the dimensions of these two matrices. Following training in the constructed graph neural networks, the latent embeddings of ST data were generated and could be leveraged for spatial domain identification. Through a comparison with established methods, our approach demonstrated superior clustering accuracy. The utilization of accurately segmented spatial regions enables downstream analyses of multiple tumors, encompassing the trajectory of tumor evolution, and facilitating differential gene expression analysis across various cell types.

Keywords: Spatial transcriptomics; Artificial intelligence; Graph neural network; Spatial domain identification; Tumor progression

†*These authors contributed equally to this work.*

***Corresponding author:**
Mingzhu Yin
(yinminzhu@cqu.edu.cn)

Citation: Liu T, Ye J, Hu C, *et al.* Artificial intelligence enabled spatially resolved transcriptomics reveal spatial tissue organization of multiple tumors. *Tumor Discov*. 2024;3(1):2049.
https://doi.org/10.36922/td.2049

Received: October 16, 2023
Accepted: December 15, 2023
Published Online: March 6, 2024

1. Introduction

Spatiotemporal molecular medicine involves comprehending medicine across various dimensions, layers, perspectives, and dynamics through the integration of spatialization and temporalization of clinical phonemes with spatiotemporal molecular omics.[1] This emerging discipline strives to elucidate the pathogenesis, epidemiology, historical context, patient symptoms and signs, clinical measurements, and therapeutic approaches. Spatially resolved transcriptomics plays a crucial role in connecting and correlating information between histological sections and molecular profiles, such as cell-cell interactions, transcription factor distribution, spatial positioning, and mRNA expression within the cell through artificial intelligence, computerized programming, and visualization techniques.[2] Spatial transcriptomics (ST) technologies document transcriptomic expression data and their respective two-dimensional tissue locations at spatial resolution.[3] In the past decade, various ST technologies have been introduced to capture mRNA molecules and their locations, each differing in resolution, sensitivity, sequencing depth, and scale. Some notable technologies include seqFISH+,[4] MERFISH,[5] omsFISH,[6] 10× Visium,[7] Slide-seqV2,[8] 10× Xenium,[9] and Stereo-seq.[10]

Partitioning spatial domains in a tumor's spatial transcriptome data can shed light on the composition of the tumor microenvironment and the localized development of tumor cells. The primary goal of spatial clustering is to segment tumor tissues into distinct cell subpopulations, facilitating downstream analyses of differential gene expression, biological function grouping, and cell-cell communication.[11] Conventional methods classify cell types based on gene expression profiles using algorithms such as K-means and Louvain.[12] Giotto[13] identifies spatial domains through the construction of a hidden Markov random field model, leveraging both the feature matrix and spatial coordinates. stLearn[14] utilizes a standard Louvain clustering workflow to handle the cell adjacency matrix, subsequently using spatial positions to identify subgroups within broader clusters. BayesSpace[15] employs a fully Bayesian statistical model to enhance resolution and conduct clustering analysis, promoting the categorization of nearby spots into the same group based on a predefined spatial prior. Despite the potential of spatial location information to enhance clustering accuracy, the aforementioned spatial clustering algorithms have yet to achieve optimal performance.[16]

Graph deep learning (GDL) has emerged as a promising approach for integrating gene expression profiles and spatial location information to address spatial clustering tasks.[17] Numerous studies have proposed graph neural network (GNN) architectures aimed at reducing the dimensionality of ST data and identifying spatial regions. Notably, SpaGCN[18] presents a comprehensive framework that partitions data based on the aggregation of gene expression, histology, and spatial location. In the cell clustering for ST data technique, a sequence of graph convolutional networks is embedded within the deep graph infomax module to derive embeddings for cell nodes.[19] STAGATE[20] devises a graph attention autoencoder framework for spatial domain identification. This approach constructs a cell-type-aware spatial neighbor network to characterize the spatial similarity at domain boundaries. Similarly, GraphST[21] utilizes a graph self-supervised contrastive learning mechanism for the unified analysis of ST data, encompassing spatial clustering, multisample integration, and cell-type deconvolution. The contrastive learning framework within the spatial clustering module enables the acquisition of informative and discriminative spot representations by minimizing the embedding distance between spatially adjacent spots. All the algorithms mentioned above can be improved in terms of clustering performance.

Motivated by the successful application of diverse artificial intelligence algorithms in analyzing ST datasets, this paper introduces a variational graph autoencoder (VGAE) enriched with multiple layers of GNNs for identifying spatial domains in tumor tissues (Figure 1). Initially, gene expression profiles and spatial location information are transformed into a gene feature matrix and a cell adjacency matrix, respectively. The VGAE consists of two primary components: an encoder and a decoder. The encoder employs GNNs to extract matrix features, reduce the feature dimensions, and generate latent embeddings. In contrast, the decoder reconstructs two matrices based on these latent embeddings. Clustering methods were, then, applied to latent embeddings to detect spatial domains within the tumor tissue. Various loss functions are utilized to enhance the quality and performance of the latent embeddings by minimizing the overall errors, including the reconstruction error and Kullback-Leibler (KL) divergence error. The presented spatial clustering method is compared with existing approaches to demonstrate its effectiveness. Additional details are provided in the "Methods" section. In addition, we employ this clustering framework on different tumor tissues to investigate their respective tumor microenvironments.

2. Methods

2.1. VGAE

The VGAE is a machine learning model that is primarily utilized in the domains of graph representation learning

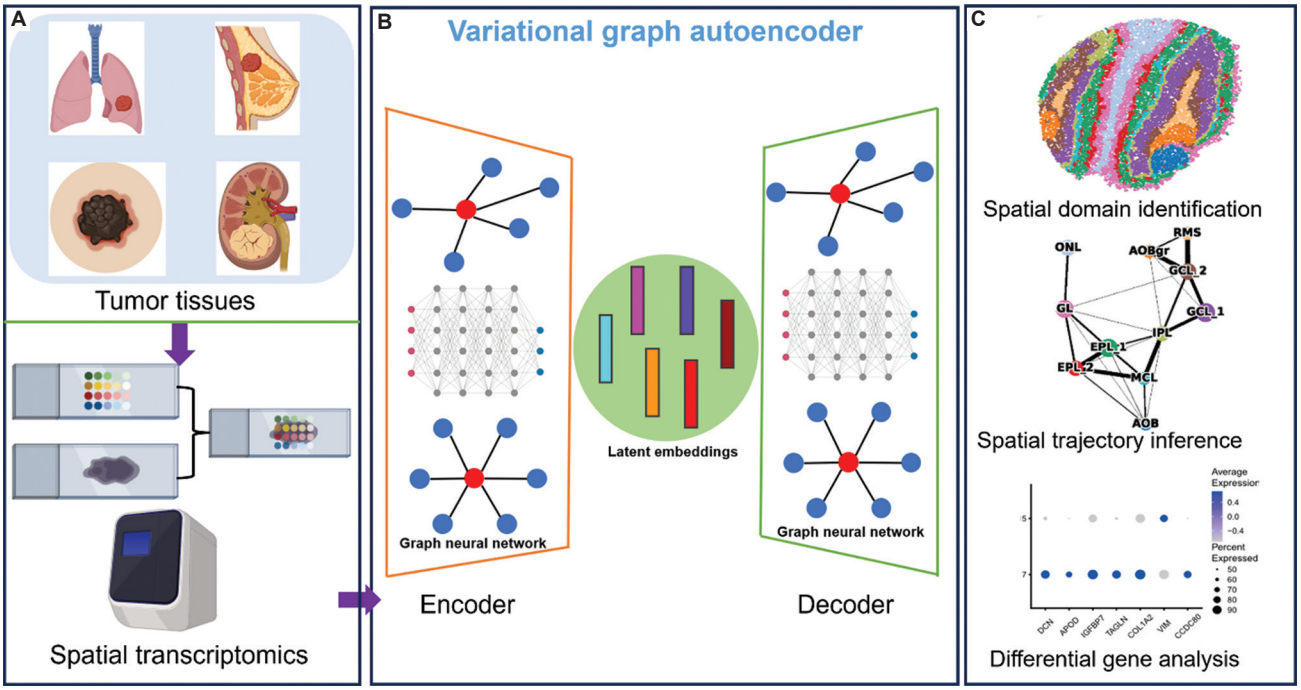

Figure 1. The proposed variational graph autoencoder-based spatial clustering framework. (A) Diverse spatial transcriptomics (ST) technologies are employed to generate distinct ST datasets of tumor tissues; (B) the ST data can be effectively processed using a graph deep learning framework to obtain latent embeddings that encapsulate meaningful and informative features; (C) these learned latent embeddings find application in various downstream analysis tasks, including spatial clustering, spatial trajectory analysis, and identification of differential genes.

and generative modeling. It amalgamates principles from variational autoencoders and GNNs, facilitating efficient acquisition and generation of representations for data organized in graph structures. The primary goal of VGAE lies in acquiring low-dimensional, continuous latent embeddings for spatial spots within the ST data. These latent embeddings can encapsulate meaningful and informative features, preserving both the structural and functional attributes inherent in spatial transcriptome datasets. In the encoding process, the initial GNN layer (Equation I) determines a lower-dimensional feature matrix, denoted as $\tilde{X}$, based on the given feature matrix X and the adjacency matrix A:[22]

$$\tilde{X} = GNN(X, A) = \mathrm{Re}LU(\tilde{A}XW_0)$$

$$\tilde{A} = D^{-\frac{1}{2}}AD^{-\frac{1}{2}} \quad \text{(I)}$$

Where $\tilde{A}$ represents the symmetrically normalized adjacency matrix, signifies the rectified linear activation function, and W_0 stands for the weight parameter for this layer of the GNN. Subsequently, the second layer (Equation II) produces the mean and variance vectors of the feature matrix utilizing the weight parameters W_1:

$$\mu = GNN_{\mu}(X, A) = \tilde{A}\tilde{X}W_1$$

$$\log\sigma^2 = GNN_{\sigma}(X, A) = \tilde{A}\tilde{X}W_1 \quad \text{(II)}$$

The mean and variance vectors share the same weight parameters. Finally, the latent embeddings are determined by the reparameterization trick[22] according to these two values (Equation III):

$$Z = \mu + \sigma\varepsilon \quad \text{(III)}$$

where ε belongs to the standard normal distribution, ε ∈ Norm (0,1). Within the VGAE module, the incoming and predictive graphs are denoted by probability distributions, specifically q(Z|X, A) and p(A|Z). Since the decoder involves an inner product operation, the reconstruction of the adjacency matrix is formulated as an inner product (Equation IV):

$$p(A \mid Z) = \sigma(Z \cdot Z^T) \quad \text{(IV)}$$

The loss function encompasses two types of errors: reconstruction loss and a regularization term. The reconstruction loss encourages the decoded output to closely resemble the original input, while the regularization term promotes the learned latent distribution to align with the prior. The formulation of this loss function is as follows (Equation V):

$$L = L_{\text{recon}} + L_{KL}$$

$$L = \mathrm{E}_{q(Z|\mathrm{X},\mathrm{A})}[\log p(A \mid Z)] - KL(q(Z \mid X, A) \,||\, p(Z)) \qquad \text{(V)}$$

The term KL(.) denotes the Kullback-Leibler divergence between two probability distributions. Training VGAE to minimize this objective function enables the model to learn a probabilistic mapping of spots to a latent space, facilitating meaningful and informative representations of the structure and features of the ST data. The downstream clustering methods partition the latent embeddings to detect spatial domains. Subsequently, the resulting clustering labels are compared with the ground-truth to assess accuracy and performance.

2.2. GNN

In the VGAE model, the encoder utilizes two layers of GNNs to extract features and reduce dimensions. GNNs facilitate the processing of ST data by enabling spots to learn from and communicate with neighboring spots. Each spot aggregates information from its neighbors, subsequently updating its own representation based on this aggregated data. The Pytorch_pyG package[23] in Python offers multiple implementations of GNNs. Existing spatial clustering architectures typically incorporate only a single GNN. In this study, we opt for the simple graph convolution (SGC) ConvNet[24] to construct the encoder.

The SGC ConvNet highlights issues of model complexity and redundant computations within GDL. To address these defects, SGC ConvNet aims to minimize collapsing weight matrices and nonlinearities between successive layers. This streamlined linear model demonstrated comparable or even superior performance at both theoretical and experimental levels. Notably, the convolution kernel in SGC is redefined as a linear function (Equation VI):

$$\check{Y}_{SGC} = soft\max\left(S...SSX\Theta^{(1)}\Theta^{(2)}...\Theta^{(K)}\right) = soft\max\left(S^K X\Theta\right) \qquad \text{(VI)}$$

where S is the normalized adjacent matrix, X is the feature matrix, Θ is the weight matrix, and softmax indicates the normalized exponential function.

2.3. ST datasets

Various types of ST data from tumors were utilized to evaluate the proposed spatial clustering architecture. These datasets were generated using diverse ST technologies, resulting in variations in resolution, spot counts, and gene profiles. Specifically, the human dorsolateral prefrontal cortex (DLPFC) ST data was obtained from the 10× Visium platform, and the spatialLIBD project conducted an extensive study utilizing this data, encompassing spot-level information, layer-level data, and spatial marker genes.[25] The project comprises a total of 12 samples, each dissection covering six neuronal layers plus white matter. Consequently, eight samples were categorized into seven clusters, while the remaining four were grouped into five (ground-truth, cortical layers one to six, white matter). For validation of the GNN algorithm, sample 151673 was chosen as a representative due to its specificity. This sample entails 3,639 spots and 33,538 genes, with provided spot annotations.

The second ST dataset originates from human breast cancer tissue and is available through the 10× Visium dataset repository. This dataset holds significant value for the analysis of heterogeneous tumor and immune microenvironments, given its substantial intratumoral and intertumoral variations. To facilitate clustering estimation, the sample is divided into 20 regions using the SEDR[26] package, relying on pathological features and gene expression. These annotated regions provide the foundation for clustering evaluation. In total, this dataset encompasses 3798 spots and 36,601 genes.

The 10× Xenium technology represents a novel approach integrating single-cell, spatial, and *in situ* analysis of FFPE tissue. Notably, breast cancer tumor datasets associated with this technology were reprocessed and republished on December 6, 2022.[9] Leveraging its non-destructive workflow, Xenium spatially aligns RNA, protein, and histological data within a unified image. This feature empowers us to discern cell types and their corresponding gene expression profiles at a single-cell resolution. In the breast cancer tumor dataset, a remarkable seventeen distinct cell types have been identified, amounting to 164,079 cells and utilizing a 313-plex gene panel. To alleviate computational load, this manuscript employs a segmented version of this data for clustering comparison, comprising 15 cell types, 11,996 cells, and the 313 gene panel.

2.4. Data pre-processing and hyperparameters

In this article, data pre-processing and VGAE training are conducted within a Python virtual environment using PyTorch_pyG, Squidpy, and Scanpy toolkits. Initially, gene expression profiles undergo normalization and log transformation using Scanpy.[27] Users also have the option to select "SCTransform" for gene expression normalization. Three thousand highly variable genes are selected to construct the feature matrix. Subsequently, the scikit-learn toolkit[28] employs a nearest-neighbor search technique to calculate the adjacency matrix. The neighbors for each spot are determined using either the k-nearest neighbor or radius-nearest neighbor modes. Specifically, for the 10×

Visium technology, the radius-nearest neighbor mode is used to ensure each spot is in proximity to approximately five neighbors. Conversely, the k-nearest neighbor mode is employed to guarantee that each spot has precisely five neighbors for the 10× Xenium method.

On generating the feature and adjacency matrices, we utilize the VGAE module embedded with SGC ConvNets to learn latent embeddings through model training. This step is implemented in Python using PyTorch_pyG. The relevant hyperparameters are defined as follows: input channels are 3000 (representing the number of highly variable genes), hidden channels are 128, and output channels are 128. The learning rate is set to 1e-6, the number of epochs is 5000, the weight decay factor is 1e-4, gradient clipping is set at five, and the random seed is fixed at zero for all experiments. The model architecture comprises four hidden layers, and the activation function used outside each layer is the exponential linear unit function.

After generating the latent representations in the embedding space, we employ the K-means method as the downstream clustering approach for identifying spatial domains. The clustering process is facilitated using the scikit-learn package. The number of clusters in the K-means corresponds to the ground truth. The hardware utilized in this study includes an Intel (R) Core (TM) i9-12900F CPU at 2.40 GHz, 64 GB of memory, and a GeForce RTX 3090Ti GPU. To effectively run the GNN-based spatial clustering algorithms, the maximum number of spots should be below 20,000. Consequently, for the ST data from the 10× Xenium technology, we utilize a cropped subset of the data, ensuring it remains below this threshold. Given that this subset encompasses all genes and groups, it does not compromise the spatial clustering experiments.

2.5. Spatial clustering metrics

On acquiring the prediction labels using K-means, we employ the adjusted Rand index (ARI) to assess the similarity between these predicted labels and the ground truth. The ARI is a commonly utilized metric for evaluating clustering algorithms. It is calculated using the scikit-learn toolkit by comparing the two vectors. Assuming that $P = \{P_1, P_2, \ldots P_M\}$ and $G = \{G_1, G_2, \ldots G_M\}$ represent the predicted and ground-truth label sets, the ARI is defined as follows (Equation VII):

$$ARI = \frac{\sum_{i,j}\binom{n_{ij}}{2} - \left[\sum_i \binom{n_{i.}}{2}\sum_j \binom{n_{.j}}{2}\right] / \binom{n}{2}}{\frac{1}{2}\left[\sum_i \binom{n_{i.}}{2} + \sum_j \binom{n_{.j}}{2}\right] - \left[\sum_i \binom{n_{i.}}{2}\sum_j \binom{n_{.j}}{2}\right] / \binom{n}{2}} \quad \text{(VII)}$$

Where c is the number of cell types, n_i and n_j denote the number of spots belonging to P_i *and* G_j, and n_{ij} implies the number of spots located in P_i and G_j. A higher ARI indicates a greater similarity between the two groups, with all ARI values ranging from zero to one.

If the ground truth for the ST data is not available, the Silhouette Coefficient (SC) score and Davies-Bouldin (DB) score[29] are employed to assess the clustering performance. The SC score is computed based on the mean intra-cluster distance and mean nearest-cluster distance for the predicted labels, ranging from minus one to one. It signifies the dispersion level between clusters, and a higher SC score indicates better clustering accuracy. The DB score represents the average similarity measure of each cluster with the most similar cluster, ranging from zero to positive infinity. A lower DB index is preferred. These metrics are calculated using the scikit-learn package.

3. Results and discussion

3.1. Evaluating the clustering accuracy on human dorsolateral pre-frontal cortex data

We named our proposed spatial clustering method VGAE_SGC. To demonstrate its accuracy and effectiveness, we compared this method with six benchmark approaches: BayesSpace,[15] SpaGCN,[18] STAGATE,[20] SEDR,[26] Scanpy,[27] and DeepST.[30] The evaluation was performed on the ST data using sample 151673 from the human DLPFC dataset, and we calculated and compared the average ARI values across 12 samples. In the ground truth of sample 151,673, there were seven marked groups (six cortical layers and one white matter).

The VGAE_SGC approach exhibited the highest average ARI of 0.542 (Figure 2A). In addition, STAGATE and DeepST achieved ARI values exceeding 0.50. The ground truth of sample 151673 is illustrated in Figure 2B, with the spatial domain identification results closely aligned with this ground truth (ARI = 0.5253, Figure 2C). The spatial clustering results of the six compared methods are presented in Figure 2D, displaying ARI values lower than 0.50 for this sample. Through this comparison with the ground truth, we established the clustering accuracy of our proposed method. Subsequently, we validated this method using tumor ST datasets to assess its spatial clustering capabilities.

3.2. Deciphering multiple regions of human breast cancer from low-resolution technology

The analysis involved seven distinct clustering methods applied to the human breast cancer dataset obtained from 10× Visium. This ST dataset, manually annotated using the SEDR package, comprises 20 regions encompassing four

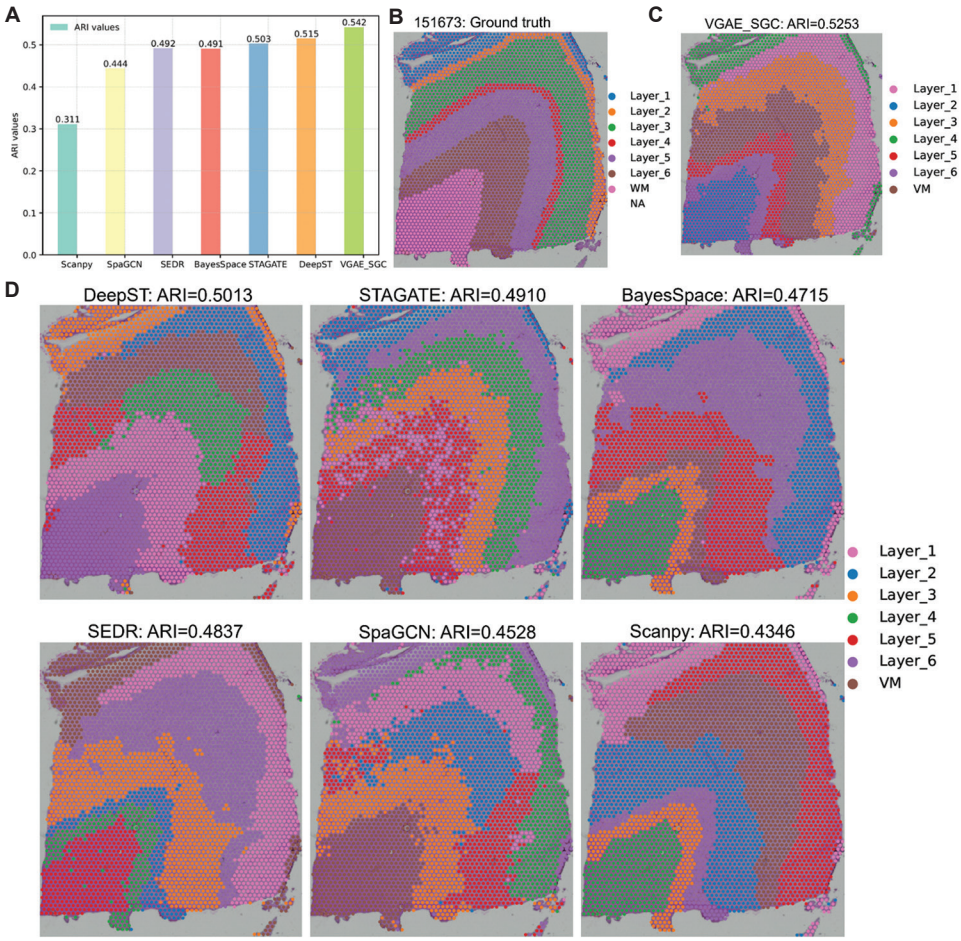

Figure 2. The spatial clustering results of seven compared methods on human DLPFC data; (A) the average adjusted Rand index (ARI) values in seven methods for twelve samples; (B) the ground truth of sample 15,1673 of this spatial transcriptomics (ST) data; (C) the spatial domain identification results of the proposed method VGAE_SGC; and (D) the spatial clustering results of six benchmarking methods for comparison.
Abbreviation: DLPFC: Dorsolateral pre-frontal cortex.

morphotypes: DCIS/LCIS, IDC, tumor edge, and healthy areas (Figure 3A). All seven approaches yielded ARI values exceeding 0.50, with VGAE_SGC achieving the highest ARI of 0.603 (Figure 3B). Figure 3C illustrates the spatial clustering outcomes of the top three methods. Notably, in the case of VGAE_SGC, several clusters (0, 10, 1, 13, 7, and 14) were closely aligned with the ground truth. These findings underscore the efficacy of VGAE_SGC in identifying cell subpopulations and effectively detecting the tumor microenvironment.

We performed a comprehensive downstream analysis of the spatial clustering results obtained from VGAE_SGC. Specifically, the IDC_5 region was divided into two distinct clusters, denoted as clusters 2 and 11, within VGAE_SGC. We, further, scrutinized the rationale behind the segmentation of the cell types. The differential gene expression profiles for clusters 2 and 11 are depicted in Figure 3D, revealing *COX6C* for cluster 2, and *ADIRF* and *HLA-B* for cluster 11. This analysis suggests disparate gene profiles for the two groups, which are indicative of distinct cell types. To elucidate the biological functions associated with these clusters, we conducted a gene set enrichment analysis of these differentially expressed genes. The enriched pathways for these clusters predominantly pertained to antigen processing and presentation (Figure 3E).

3.3. Partitioning tumor regions for the single-cell-resolution human breast cancer data

Finally, we validated our proposed spatial clustering framework, VGAE_SGC, using an alternative single-cell-resolution ST dataset. This dataset was produced utilizing the advanced 10x Xenium technology and pertains to breast cancer tissue, as shown in Figure 4A. The initial ST dataset boasts a high resolution, comprising 164,079 spots and 313 genes. To alleviate the computational demands, we segmented this primary dataset into a cropped subset,

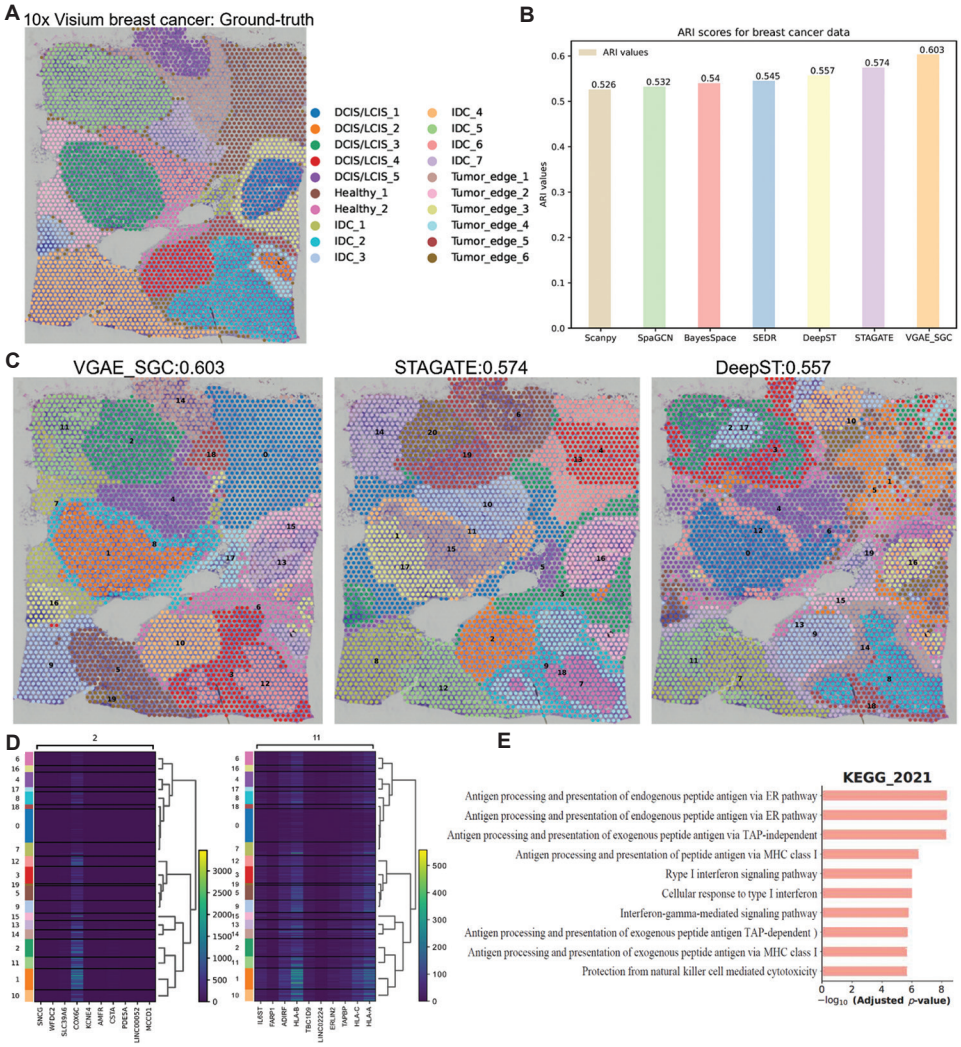

Figure 3. The spatial clustering and downstream analysis results on human breast cancer from 10× Visium platform: (A) The ground truth of breast cancer data labeled by SEDR package; (B) the adjusted Rand index (ARI) values of seven compared methods on this spatial transcriptomics (ST) data; (C) the spatial domain identification results of DeepST, STAGATE, and VGAE_SGC on the breast cancer data; (D) the differential gene analysis between group 2 or 11 and other clusters; and (E) the gene set enrichment analysis of differential genes in groups 2 and 11.

specifically encompassing 15 cell types with 11,996 cells and the same set of 313 genes (Figure 4A).

We conducted a comparative analysis of the clustering accuracy across the seven methods using the aforementioned cropped ST data. Notably, VGAE_SGC and STAGATE exhibit proximity in performance, outperforming the remaining methods, as shown in Figure 4B. Figure 4C portrays the spatial distribution of spots in the VGAE_SGC case, revealing that clusters 0, 1, 6, and 9 aligned with the annotated labels, as shown in Figure 4A. In addition to conducting differential gene and biological function analyses, we employed VGAE_SGC's clustering groups to infer the spatial development trajectory (Figure 4D). Initially, we present a uniform manifold approximation and projection (UMAP) plot illustrating VGAE_SGC's clustering results. Subsequently, we utilized the *scanpy.tl.paga* function within Scanpy to construct the spatial evolutionary trajectory, highlighting that group 0 represents regular cells and cluster 5 corresponds to tumor cells in breast cancer.

VGAE_SGC excelled in discerning cellular compartmentalization and diverse cellular subpopulations within spatial transcriptomic data. It also demonstrates proficiency in detecting the tumor microenvironment, which is crucial for uncovering neo-cells, elucidating carcinogenesis mechanisms, and advancing cancer treatments. However, it is essential to acknowledge the limitations of this approach. Notably, we did not leverage

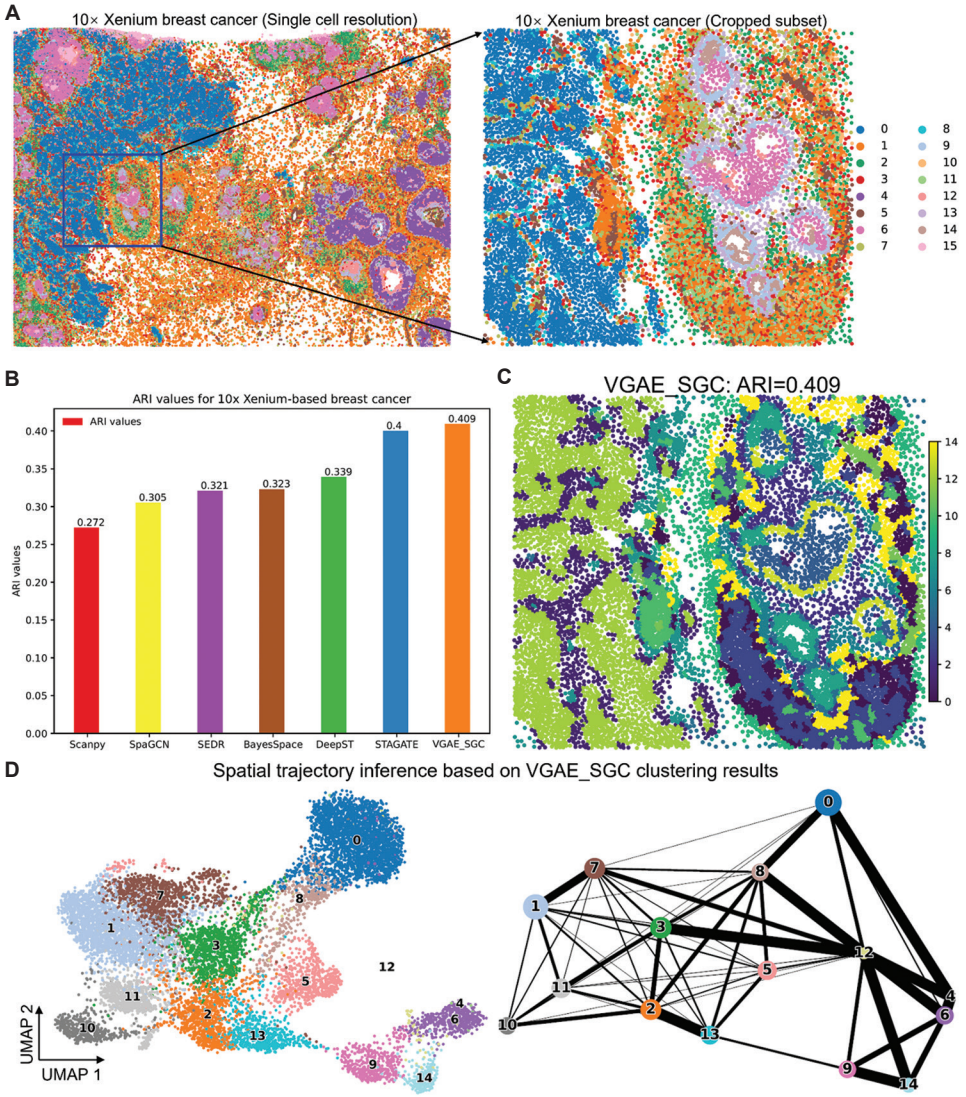

Figure 4. The proposed spatial clustering method, VGAE_SGC, undergoes validation using single-cell resolution breast cancer spatial transcriptomics (ST) data: (A) The primary breast cancer dataset is obtained through the 10× Xenium technology. To enhance computational efficiency, a cropped subset of this ST data is utilized in this study; (B) the adjusted Rand index (ARI) values for seven compared approaches are computed using the cropped ST data; (C) the spatial distribution of spots in the VGAE_SGC method yields an ARI value of 0.409; and (D) the reduced-dimension graph illustrates VGAE_SGC's spatial clustering outcomes and its associated inferred spatial evolutionary trajectory.

extensive single-cell data, which is a significant factor in optimizing the performance of our algorithm.

4. Conclusion

This article explores the utilization of artificial intelligence algorithms for spatial clustering tasks in spatially resolved transcriptomics. Specifically, we introduced a VGAE enhanced with SGC ConvNets to delineate spatial domains in ST data from various tumor tissues. The clustering accuracy of our architecture is demonstrated through comparisons with several existing clustering methodologies. We validated our proposed method, VGAE_SGC, using breast cancer datasets with varying resolutions. In addition, we delineated various downstream analysis tasks predicted for spatial clustering outcomes, including differential gene expression analysis, identification of biological functions, and inference of spatial developmental trajectories. Unsupervised learning modules face challenges in accurately identifying spatial regions within an organization. However, future research can focus on integrating methods to enhance the clustering results. Approaches such as contrastive and

semi-supervised methods, generative adversarial neural networks, and graph-based deep learning have shown promise for improving the accuracy and effectiveness of spatial clustering in organizational analysis.

Acknowledgments

We thank BioRender (biorender.com) for providing technical support in drawing the figures.

Funding

This work was supported in part by the National Key R&D Programs (NKPs) of China (Grant No. 2022YFC3601800) [M.Y.]; the Science and Technology Research Program of Chongqing Municipal Education Commission (Grant No. KJZD-K202300105) [T.L.]; Chongqing medical scientific research project (Joint project of Chongqing Health Commission and Science and Technology Bureau) (Grant No. 2024QNXM004) [T.L.].

Conflict of interest

The authors declare that they have no competing interests.

Author contributions

Conceptualization: Mingzhu Yin
Formal analysis: Jiangnan Liao
Investigation: Jinxin Ye, Chunlan Hu
Methodology: Teng Liu, Zongbo Zhang
Writing – original draft: Teng Liu, Zhuomiao Ye
Writing – review & editing: Jinxin Ye, Mingzhu Yin

Ethics approval and consent to participate

Not applicable.

Consent for publication

Not applicable.

Availability of data

The data can be downloaded from the provided links. Human DLPFC: the primary source: https://www.nature.com/articles/s41593-020-00787-0; the pre-processed source: https://github.com/LieberInstitute/spatialLIBD); Human breast cancer: the primary source: https://www.10xgenomics.com/resources/datasets/human-breast-cancer-block-a-section-1-1-standard-1-1-0; the pre-processed source: https://github.com/JinmiaoChenLab/SEDR_analyses/); and Human breast cancer from 10x Xenium: the primary source: https://www.10xgenomics.com/products/xenium-in-situ/preview-dataset-human-breast; https://squidpy.readthedocs.io/en/stable/notebooks/tutorials/tutorial_xenium.html

References

1. Wang X, Fan J. Spatiotemporal molecular medicine: A new era of clinical and translational medicine. *Clin Transl Med*. 2021;11(1):e294.

   doi: 10.1002/ctm2.294

2. Wang X. Clinical trans-omics: An integration of clinical phenomes with molecular multiomics. *Cell Biol. Toxicol.* 2018;34:163-166.

   doi: 10.1007/s10565-018-9431-3

3. Rao A, Barkley D, França GS, *et al*. Exploring tissue architecture using spatial transcriptomics. *Nature*. 2021;596:211-220.

   doi: 10.1038/s41586-021-03634-9

4. Eng CHL, Lawson M, Zhu Q, *et al*. Transcriptome-scale super-resolved imaging in tissues by RNA seqFISH+. *Nature*. 2019;568:235-239.

   doi: 10.1038/s41586-019-1049-y

5. Chen KH, Boettiger AN, Moffitt JR, *et al*. RNA imaging. Spatially resolved, highly multiplexed RNA profiling in single cells. *Science*. 2015;348:aaa6090.

   doi: 10.1016/B978-0-12-822824-1.00002-X

6. Codeluppi S, Borm LE, Zeisel A, *et al*. Spatial organization of the somatosensory cortex revealed by osmFISH. *Nat Methods*. 2018;15:932-935.

   doi: 10.1038/s41592-018-0175-z

7. Ghorbani S, Jelinek E, Jain R, *et al*. Versican promotes T helper 17 cytotoxic inflammation and impedes oligodendrocyte precursor cell remyelination. *Nat Commun*. 2022;13:2445.

   doi: 10.1038/s41467-022-30032-0

8. Stickels RR, Murray E, Kumar P, *et al*. Highly sensitive spatial transcriptomics at near-cellular resolution with Slide-seqV2. *Nat Biotechnol*. 2021;39:313-319.

   doi: 10.1038/s41587-020-0739-1

9. Janesick A, Shelansky R, Gottscho AD, *et al*. High resolution mapping of the tumor microenvironment using integrated single-cell, spatial and in situ analysis. *Nat Commun*. 2023;14:8353.

   doi: 10.1038/s41467-023-43458-x

10. Chen A, Liao S, Cheng M, *et al*. Spatiotemporal transcriptomic atlas of mouse organogenesis using DNA nanoball-patterned arrays. *Cell*. 2022;185:1777-1792.e21.

    doi: 10.1016/j.cell.2022.04.003

11. Williams CG, Lee HJ, Asatsuma T, *et al*. An introduction to spatial transcriptomics for biomedical research. *Genome Med*. 2022;14:68.

    doi: 10.1186/s13073-022-01075-1

12. Bu Z, Li HJ, Zhang C, *et al*. Graph K-means based on leader identification, dynamic game, and opinion dynamics. *IEEE Trans Knowl Data Eng*. 2020;32:1348-1361.

doi: 10.1109/TKDE.2019.2903712

13. Dries R, Zhu Q, Dong R, *et al*. Giotto: A toolbox for integrative analysis and visualization of spatial expression data. *Genome Biol*. 2021;22:78.

doi: 10.1186/s13059-021-02286-2

14. Pham D, Tan X, Balderson B, *et al*. Robust mapping of spatiotemporal trajectories and cell–cell interactions in healthy and diseased tissues. *Nat Commun*. 2023;14:7739.

doi: 10.1038/s41467-023-43120-6

15. Zhao E, Stone MR, Ren X, *et al*. Spatial transcriptomics at subspot resolution with BayesSpace. *Nat Biotechnol*. 2021;39:1375-1384.

doi: 10.1038/s41587-021-00935-2

16. Liu Y, Wang T, Duggan B, Sharpnack M, Huang K, Zhang J, *et al*. SPCS: A spatial and pattern combined smoothing method for spatial transcriptomic expression. *Brief Bioinform*. 2022;23:bbac116.

doi: 10.1093/bib/bbac116

17. Wu Z, Pan S, Chen F, *et al*. A comprehensive survey on graph neural networks. *IEEE Trans Neural Netw Learn Syst*. 2021;32:4-24.

doi: 10.1109/TNNLS.2020.2978386

18. Hu J, Li X, Coleman K, *et al*. 2021. SpaGCN: Integrating gene expression, spatial location and histology to identify spatial domains and spatially variable genes by graph convolutional network. *Nat Methods*. 18:1342-1351.

doi: 10.1038/s41592-021-01255-8

19. Li J, Chen S, Pan X, *et al*. Cell clustering for spatial transcriptomics data with graph neural networks. *Nat Comput Sci*. 2022;2:399-408.

doi: 10.1038/s43588-022-00266-5

20. Dong K, Zhang S. Deciphering spatial domains from spatially resolved transcriptomics with an adaptive graph attention auto-encoder. *Nat Commun*. 2022;13:1739.

doi: 10.1038/s41467-022-29439-6

21. Long Y, Ang KS, Li M, *et al*. Spatially informed clustering, integration, and deconvolution of spatial transcriptomics with GraphST. *Nat Commun*. 2023;14:1155.

doi: 10.1038/s41467-023-36796-3

22. Thomas NK, Welling, M. Variational Graph Auto-Encoders. [arXiv Preprint] arXiv. 2016;2:1611.07308.

doi: 10.48550/arXiv.1611.07308

23. Fey M, Lenssen JE. Fast graph representation learning with pytorch geometric. [arXiv Preprint] arXiv. 2019;1903.02428.

doi: 10.48550/arXiv.1903.02428

24. Wu F, Souza A, Zhang T, *et al*. Simplifying Graph Convolutional Networks. In: *International Conference on Machine Learning*. Vol. 97. New York: PMLR; 2019. p. 6861-6871.

doi: 10.48550/arXiv.1902.07153

25. Pardo B, Spangler A, Weber LM, *et al*. SpatialLIBD: An R/Bioconductor package to visualize spatially-resolved transcriptomics data. *BMC Genomics*. 2022;23(1):1-5.

doi: 10.1186/s12864-022-08601-w

26. Xu H, Fu H, Long Y, *et al*. Unsupervised spatially embedded deep representation of spatial transcriptomics. *Genome Med*. 2024;16:12.

doi: 10.1186/s13073-024-01283-x

27. Wolf FA, Angerer P, Theis FJ. SCANPY: Large-scale single-cell gene expression data analysis. *Genome Biol*. 2018;19:15.

doi: 10.1186/s13059-017-1382-0

28. Pedregosa F, Varoquaux G, Gramfort A, *et al*. Scikit-learn: Machine learning in python. *J Mach Learn Res*. 2011;12:2825-2830.

29. Addagarla SK, Amalanathan A. Probabilistic unsupervised machine learning approach for a similar image recommender system for e-commerce. *Symmetry*. 2020;12:1783.

doi: 10.3390/sym12111783

30. Xu C, Jin X, Wei S, *et al*. DeepST: Identifying spatial domains in spatial transcriptomics by deep learning. *Nucleic Acids Res*. 2022;50:e131.

doi: 10.1093/nar/gkac901

ACCSCIENCE PUBLISHING

Tumor Discovery

ORIGINAL RESEARCH ARTICLE

Profiling energy metabolism in normal bladder tissue and non-muscle-invasive bladder cancer cases of different histological grades

Guilherme Prado Costa[1,2], Petra Karla Böckelmann[1], Renato Prado Costa[2], Carlos Hermann Schaal[2], Fernando César Sala[2], André Pereira Vanni[2], Leandro Luiz Lopes de Freitas[3], João Carlos Cardoso Alonso[1,4], Gabriela Cardoso de Arruda Camargo[1], Gabriela de Oliveira[1], Bianca Ribeiro de Souza[5], Athanase Billis[3], and Wagner José Fávaro[1]*

[1]Laboratory of Urogenital Carcinogenesis and Immunotherapy (LCURGIN), Universidade Estadual de Campinas (UNICAMP), Campinas City, São Paulo State, Brazil

[2]Department of Urology, Amaral Carvalho Hospital (HAC), Jaú City, São Paulo State, Brazil

[3]Department of Pathology, Medical School, Universidade Estadual de Campinas (UNICAMP), Campinas City, São Paulo State, Brazil

[4]Department of Urology, Paulínia Municipal Hospital, Paulínia City, São Paulo State, Brazil

[5]Department of Obstetrics and Gynecology, OVCARE, University of British Columbia, Vancouver, British Columbia, Canada

Abstract

Bladder cancer (BC) stands as the second most common urinary tract malignancy. Recent years have witnessed a growing interest in investigating energy metabolism to help with better understanding the energy sources harnessed by tumor cells. The aims of the present study are to feature and compare cell energy metabolism profiles among different histological grades of non-muscle-invasive BC (NMIBC) by adjusting their bioenergetic cellular indexes based on the specific tumor types. Forty urinary bladder tissue samples from patients both with and without a diagnosis of urothelial lesions were collected. Subsequently, samples were categorized into four groups comprising ten samples each, namely: normal (no urothelial lesions) group, low-grade pTa group, high-grade pTa group, and high-grade pT1 group. These tissue samples were examined by means of immunohistochemistry and Western blotting to assess proteins involved in cell energy metabolism. Based on the current findings, the normal and low-grade pTa groups presented clear preference for the oxidative phosphorylation pathway; consequently, they recorded high bioenergetic cellular index. On the other hand, both the high-grade pTa and pT1 groups presented proclivity towards the glycolytic pathway. These observations, mainly those associated with the bioenergetic cellular index, hold promising clinical relevance in the management of BC. Given the often aggressive and potentially debilitating nature of treatments applied to this neoplasia type, the current study offers invaluable insights on this topic and emphasizes changes in the bioenergetic cellular index at different NMIBC grades, which could serve as potential markers for both the diagnosis and prognosis of NMIBC patients.

Keywords: Bladder cancer; Energy metabolism; Bioenergetic cellular index; Cancer metabolism

***Corresponding author:**
Wagner José Fávaro
(favarowj@unicamp.br)

Citation: Costa GP, Böckelmann PK, Costa RP, *et al*. Profiling energy metabolism in normal bladder tissue and non-muscle-invasive bladder cancer cases of different histological grades. *Tumor Discov*. 2024:3(1):2290. https://doi.org/10.36922/td.2290

Received: November 22, 2023
Accepted: January 9, 2024
Published Online: March 19, 2024

1. Introduction

Bladder cancer (BC) emerges as a significant global public health concern due to the elevated morbidity and mortality rates.[1] Notably, BC tends to be recurrent and aggressive in terms of progression, even in cases at localized disease stages.[1,2] Patients diagnosed with BC often require multiple intravesical treatments, while advanced and metastatic cases are treated with intricate surgical and systemic interventions. Consequently, BC imposes a substantial burden on health-care resources, resulting in significant economic costs.[1,3]

Non-muscle-invasive BC (NMIBC) accounts for the majority of bladder tumor cases, comprising 70 – 75% of the cases. NMIBC is characterized by the confinement of tumor to the urothelium as papillary tumor (pTa) or carcinoma *in situ* (pTis or CIS) without stromal invasion or with limited invasion into the lamina propria (pT1).[4,5] This cancer type encompasses a diverse group of tumors, with progression rates to the muscle-invasive phenotype ranging from 0.8% to 50% within 5 years,[6,7] as indicated by previous studies. Notably, significant risk factors for NMIBC progression include the concurrent presence of CIS, high tumor grade, and T1 stage.[6,7] In addition, factors such as multiplicity, tumor size ≥3 cm, and a history of relapse are also considered risk factors for this disease.[6,7]

Low-grade Ta tumors present relapse rates up to 50%, and they only progress in 5% of cases. Conversely, high-grade T1 tumors show relapse rates exceeding 80%, and over 50% of cases progress within the initial 3 years.[8,9] Chromosomal changes stemming from DNA strand oxidation. Chromosomal changes resulting from DNA strand oxidation affect the functions of oncogenes and tumor suppressor genes, as well as trigger different biological behaviors in low- and high-grade BC. Notably, low-grade BC tends to manifest as superficial, papillary, and indolent tumors, whereas high-grade BC are prone to relapse and to progress into invasive muscle tissue.[8] Moreover, other prognostic factors, such as tumor size, multifocality, papillary versus sessile appearance, and lymphovascular invasion hold clinical significance.[10] These behavioral variations may be intricately linked to cell energy metabolism profiles presented by different histological grades of NMIBC. Analyzing and understanding metabolic adaptation strategies adopted by neoplastic cells to meet the high cell growth and proliferation demands within each histological grade of NMIBC is a promising approach to acquiring more comprehensive knowledge on their behavior.

Cancer onset and advancement are intricately linked to changes in cell metabolism, which provide energy to support cell growth and fast proliferation.[11] These metabolic adaptations encompass increased oxygen consumption, nutrient depletion, as well as the generation of reactive nitrogen and oxygen intermediates. The Warburg effect is a prominent metabolic phenomenon observed in cancer cells.[11,12] This effect involves preference for aerobic glycolysis and lactate fermentation over oxidative phosphorylation, even in the presence of abundant oxygen and fully functional mitochondria. This metabolic shift serves the essential purpose of meeting the increased energy demands necessary for the synthesis of lipids, proteins, and nucleic acids of the cancer cells. Thus, Warburg effect stands out as a pivotal feature of BC cancer cells, as well as of different solid tumor types.[11]

Metabolic activity in normal cells primarily relies on oxidative phosphorylation, which is a highly efficient process that generates abundant adenosine triphosphate (ATP) in comparison to glycolysis. Glucose is converted into pyruvate through glycolysis within the cytosol in physiologically normal cells, and subsequently, it is turned into carbon dioxide in the mitochondria, mainly under aerobic conditions.[11,13] However, glycolysis takes precedence under anaerobic conditions, and it results in limited pyruvate supply to the oxygen-consuming mitochondria.[11,13] This metabolic shift is featured by high glucose consumption and by lactate production, regardless of oxygen availability.[11,13-16]

Several key proteins participating in both the oxidative phosphorylation and glycolysis pathways can be utilized as markers to assess the activity of these metabolic processes. Glucose transporter-1 (GLUT1), phosphofructokinase (PFK), glyceraldehyde 3-phosphate dehydrogenase (GAPDH), and lactate dehydrogenase A (LDH-A) are used as glycolytic pathway markers. Moreover, pyruvate dehydrogenase (PDH), citrate synthase (CS), short chain 3-hydroxyacyl-CoA dehydrogenase (HADHSC), mitochondrial ATP synthase F1-beta-subunit (β-F1-ATP synthase), and heat shock protein 60 (hsp60) are used as oxidative phosphorylation pathway markers.

Several previous studies have focused on investigating the mitochondrial energy metabolism of neoplastic cells and assessed the β-catalytic subunit concentration within the H+-ATP synthase complex as oxidative phosphorylation marker. These studies have also investigated hsp60 as marker of mitochondrial structural proteins, in association with GAPDH, which was used as glycolytic pathway marker. These data make it feasible to calculate the bioenergetic cellular index (IBEC) through the following equation:[17-19]

$$\mathrm{IBEC} = \frac{\beta - \mathrm{F1} - \mathrm{ATPase}}{\mathrm{hsp60\,x\,GAPDH}} \quad (1)$$

In light of the foregoing, the aims of the current study were to feature and compare the cell energy metabolism profiles among normal bladder tissue and NMIBC tissues with different histological grades (low-grade pTa, high-grade pTa, and high-grade pT1). The present research adjusted the IBEC to these specific tumor types in order to establish a clinically relevant criterion with prognostic significance to classify this neoplasia.

2. Materials and methods

2.1. Human samples

This retrospective study analyzed 40 urinary bladder tissue samples from patients (median age of 62 years) both with and without a diagnosis of urothelial lesions by maintaining male-to-female ratio of 2:1. Tissue specimens were obtained at the Urology Service at Amaral Carvalho Hospital, Jaú City, Brazil. Ten bladder tissue samples were sourced from autopsies of patients without a diagnosis of urothelial injury or urological disease. In addition, the remaining 30 bladder tissue samples were obtained from patients who underwent transurethral resection of the bladder tumor (TURBT).

Histopathological diagnoses were meticulously assessed by a senior uropathologist in accordance with the classification consensus put forth by the International Society of Urological Pathology/World Health Organization.[20] The categorization process lied in splitting the samples into three different groups, with each comprising ten samples, namely normal (no urothelial lesions) group, low-grade pTa group, high-grade pTa group, and high-grade pT1 group. Subsequently, these tissue samples were subjected to rigorous analyses using techniques encompassing immunohistochemistry and Western blotting.

All procedures herein were conducted in full compliance with the ethical standards set forth by the Ethics and Research Committee of Amaral Carvalho Hospital, Jaú City, Brazil (CAAE number: 47475815.9.0000.5434).

2.2. Immunohistochemical analysis

The same set of bladder samples (n = 10 per group), which had been previously used for histopathological analysis, was also used for immunolabeling procedures. These tissue samples were cut into 5 μm-thick sections. Antigen retrieval was achieved by subjecting the aforementioned sections to three 5-min heating cycles in 10 mM citrate buffer at pH 6.0, in standard microwave oven. Subsequently, sections were incubated in peroxidase blocker (EasyPath EP12-20523, Sao Paulo, Brazil) and this procedure was followed by incubation in 5% goat serum blocking solution (EasyPath EP12-20523, Sao Paulo, Brazil) at room temperature for 10 min.

Specific antigens corresponding to (GLUT1; rabbit polyclonal antibody, sc7903, Santa Cruz Biotechnology, USA), (PFK; mouse monoclonal antibody, LS-C173559, LifeSpan BioSciences, Inc., USA), (GAPDH; rabbit polyclonal antibody, ab37168, abcam, USA), (LDH; mouse monoclonal antibody, sc137243, Santa Cruz Biotechnology, USA), (PDH; rabbit polyclonal antibody, GTX104040, GeneTex, USA), (CS; mouse monoclonal antibody, sc390693, Santa Cruz Biotechnology, USA), (HADHSC; rabbit polyclonal antibody, sc 292196, Santa Cruz Biotechnology, USA), mitochondrial ATP synthase F1-beta-subunit (β-F1-ATP synthase [ATPase]; rabbit polyclonal antibody, sc134962, Santa Cruz Biotechnology, USA), and (hsp60; mouse monoclonal antibody, sc376240, Santa Cruz Biotechnology, USA) were identified by reacting the tissue specimens with specific primary antibodies, which were diluted in 1% bovine serum albumin (BSA) and stored overnight at 4°C. Bound antibodies were detected based on using EasyLink One kit (EasyPath EP-12-20504, Sao Paulo, Brazil). Subsequently, sections were slightly counterstained with Harris' hematoxylin and visualized in Leica DM2500 microscope equipped with DFC295 camera (Leica, Munich, Germany).[21]

The rate of positively stained cells was assessed in ten fields for each antibody, under high magnification (×400), to assess antigen immunoreactivity intensity within urothelial cells in ImageJ software (https://imagej.nih.gov/ij/). Quantitative data were analyzed in two different manners, namely total immunoreactivity and immunoreactivity intensity. Total immunoreactivity was calculated as complement of the negative rate of urothelial cells observed for a given antibody, subtracted from 100%. In other words, it represented the total number of urothelial cells in the field that presented immunoreactivity to the assessed antibody. Immunoreactivity intensity was assessed based on categorizing the observed immunoreactivity within urothelial cells by taking into consideration intensity criteria. These categories were established in ImageJ software, at scale ranging from 0 to 3 wherein: 0 (no immunoreactivity) means 0% positive urothelial cells, 1 (weak immunoreactivity) indicates 1 – 35% positive urothelial cells, 2 (moderate immunoreactivity) represents 36 – 70% urothelial cells, and 3 (intense immunoreactivity) features >70% positive urothelial cells.[22]

2.3. Western blotting

Urinary bladder samples were collected from all 40 patients and subjected to immunoblotting analysis performed according to the established protocols.[21] In total, 70 μg protein was loaded into each well on the SDS-polyacrylamide gel for electrophoresis. Subsequently, proteins were transferred to nitrocellulose membranes,

which, in turn, were blocked with 3% BSA solution diluted in TBS-T buffer to mitigate non-specific protein binding. Nitrocellulose membranes were incubated overnight with primary antibodies (diluted 1:1000 in 1% BSA), such as GLUT1, PFK, GAPDH, LDH, PDH, CS, HADHSC, β-F1-ATP synthase (ATPase), and hsp60, at 4°C. On completing the primary antibody incubation, membranes were further incubated with secondary HRP-conjugated antibodies (diluted 1:3000 ratio in 1% BSA; MilliporeSigma, USA) for 2 h. Immunoreactive bands were visualized through incubation with 3,3'-diaminobenzidine chromogen (Sigma Chemical Co., St Louis, USA). Immunoblots were run in duplicate, and the samples were grouped into sets comprising 10 samples per group, for each repetition.

Semi-quantitative densitometry analysis was applied to the bands in NIH ImageJ 1.47v software (National Institute of Health, USA, available at: http://rsb.info.nih.gov/ij/), and it was followed by statistical analyses. Results are expressed as mean ± standard deviation of band intensities in comparison to β-actin (which was used as endogenous positive control) labeling intensity.[21]

2.4. IBEC

The IBEC was calculated from several parameters determined based on the established protocols using Equation 1.[17,18,23]

2.5. Statistical analysis

Quantitative results are expressed as mean ± standard deviation, whenever appropriate. Comparison of immunohistochemical and Western blotting data among the investigated groups were analyzed using one-way analysis of variance, followed by Tukey test, at 1% significance level (P <0.01). IBEC assessment was performed using Student's t-test for paired samples.

3. Results

3.1. Patients' baseline demographic and general features

The study included 40 patients who were divided into four groups, with each comprising 10 patients. The median age of the patients was 62.5 years, and the male-to-female ratio was 2:1. With respect to BC risk factors, 70.0% (28/40) of patients were smokers. Prior TURBT was observed in 12.5% (5/40) of patients, whereas Bacillus Calmette–Guérin (BCG) therapy had been administered in only 2.5% of cases. This study only included cases whose specimens were of the same tumor stage and grade as the corresponding specimens assessed during the prior TURBT. The median size observed for low-grade pTa tumors was 3.0 cm, whereas that observed for high-grade pTa tumors was 3.0 cm, and the one for high-grade pT1 tumors was 4.0 cm (Table 1).

Each sample collected from urinary bladders was classified based on their histopathological grade. After the classification procedure, the samples were divided into four groups based on histopathological grade, namely, normal (no urothelial lesions) group, low-grade pTa group, high-grade pTa group, and high-grade pT1 group. Samples belonging to the low-grade pTa group showed extensive papillary lesions. Urothelial cells presented overall orderly appearance with minimal variability in their architecture and cytological features, lack of nuclear hyperchromasia, and infrequent miotic figures (Figure 1A and B). High-grade pTa group samples also presented extensive papillary lesions but featured disorderly arranged urothelial cells, significant cell pleomorphism, nuclear hyperchromasia, and several mitotic figures (Figure 1C and D). On the other hand, the high-grade pT1 group samples presented basement membrane rupture with consequent invasion of neoplastic urothelial cells arranged in cords or nests on the lamina propria. Neoplastic urothelial cells presented eosinophilic cytoplasm and a large number of hyperchromatic nuclei and mitotic figures (Figure 1E and F).

3.2. The oxidative phosphorylation pathway prevailed in normal bladder tissue and low-grade pTa bladder tumor

Intense immunoreactivity was observed for β-F1-ATP synthase (ATPase), HADHSC, PDH, and CS, within the

Table 1. Baseline characteristics

	No lesions	Non-muscle-invasive bladder cancer		
	Normal	Low-grade pTa	High-grade pTa	High-grade pT1
Patients (n)	10	10	10	10
Male/Female	7/3	8/2	7/3	8/2
Age (years in median)	61	56	62	71
Smoking (yes/no)	3/7	8/2	8/2	9/1
Previous TURBT (yes/no)	0/10	1/9	2/8	2/8
Previous BCG (yes/no)	0/10	0/10	0/10	1/9
Lesion size (median)	0	3.0 cm	3.0 cm	4.0 cm

Abbreviations: BCG: Bacillus Calmette–Guérin; TURBT: Transurethral resection of the bladder tumor.

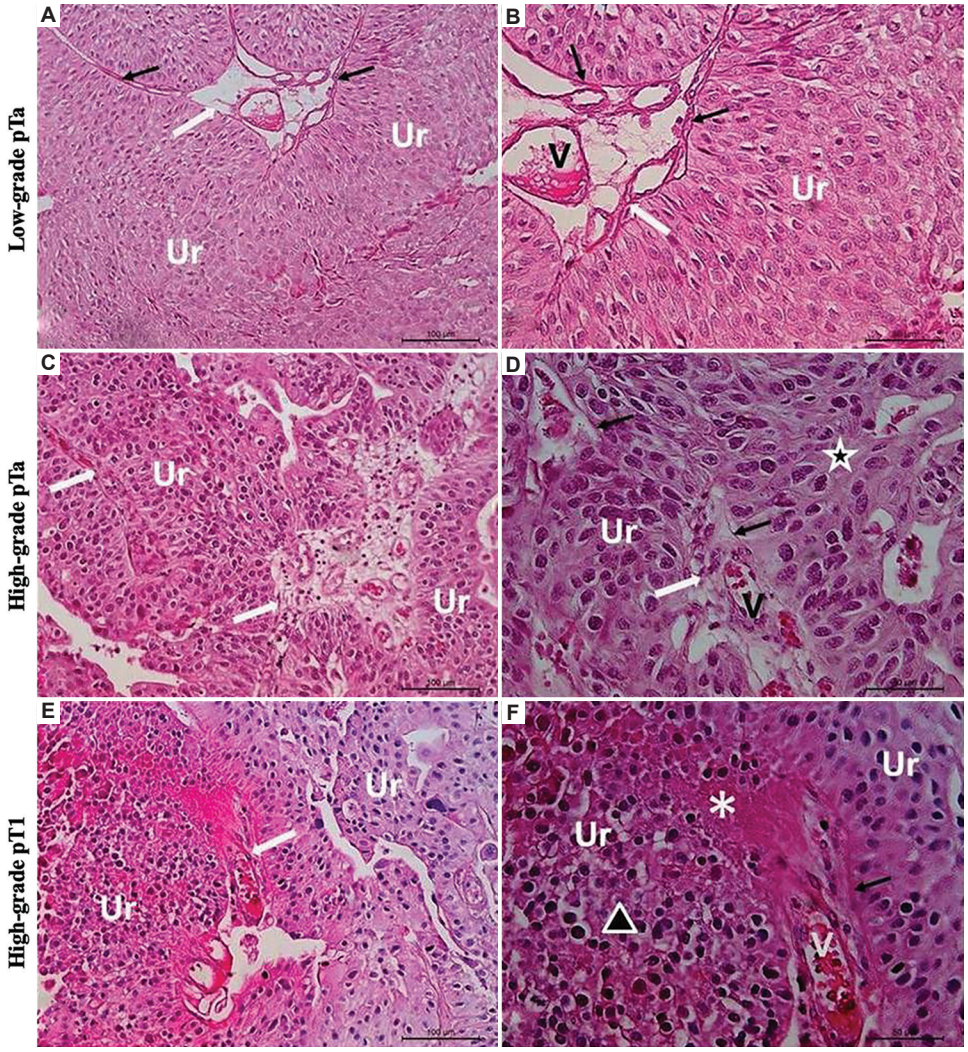

Figure 1. Urinary bladder photomicrographs of low-grade pTa group (A and B), high-grade pTa group (C and D), and high-grade pT1 group (E and F). (A and B) Urothelial cells presenting overall orderly appearance with minimal variability in architecture and cytological features, no nuclear hyperchromasia, and infrequent mitotic figures. (C and D) Significant cell pleomorphism, notable cell atypia (star), and several mitotic figures. (E and F) Basement membrane disruption (asterisk) with neoplastic cells' invasion in the lamina propria. Abbreviations and symbols: Ur: Urothelium; V: Blood vessel; white arrow, conjunctive-vascular axis; black arrow, basal membrane integrity; star, cell atypia; asterisk, basement membrane disruption. Scale bars: 100 µm (panels A, C, and E), and 50 µm (panels B, D, and F).

cohort of normal bladder tissue samples and low-grade pTa tumors, as shown in Figures 2A-D, 3A, 3D, 3G, and 3J, respectively. On the other hand, the high-grade pTa group recorded moderate immunoreactivity level for these proteins, as shown in Figure 3B, E, H, and K, whereas the pT1 group recorded weaker immunoreactivity patterns for the same set of proteins, as evidenced in Figure 3C, F, I, and L. The mean immunolabelled antigen intensities in urinary bladder samples from the normal, low-grade pTa, high-grade pTa, and high-grade pT1 groups are tabulated in Table 2.

The normal and low-grade pTa groups recorded protein levels significantly higher than those of the high-grade pTa and pT1 groups for β-F1-ATP synthase, HADHSC, and PDH, as indicated in Figure 4A-C, respectively. Interestingly, CS protein levels were significantly higher in normal group when compared to other groups (Figure 4D). Furthermore, no statistically significant differences in CS protein levels were observed among the low-grade pTa, high-grade pTa, and high-grade pT1 groups, as shown in Figure 3D.

3.3. The glycolytic pathway prevailed in high-grade pTa and high-grade pT1 bladder tumors

Intense immunoreactivity levels were observed for GLUT1 and PFK in the high-grade pTa and high-

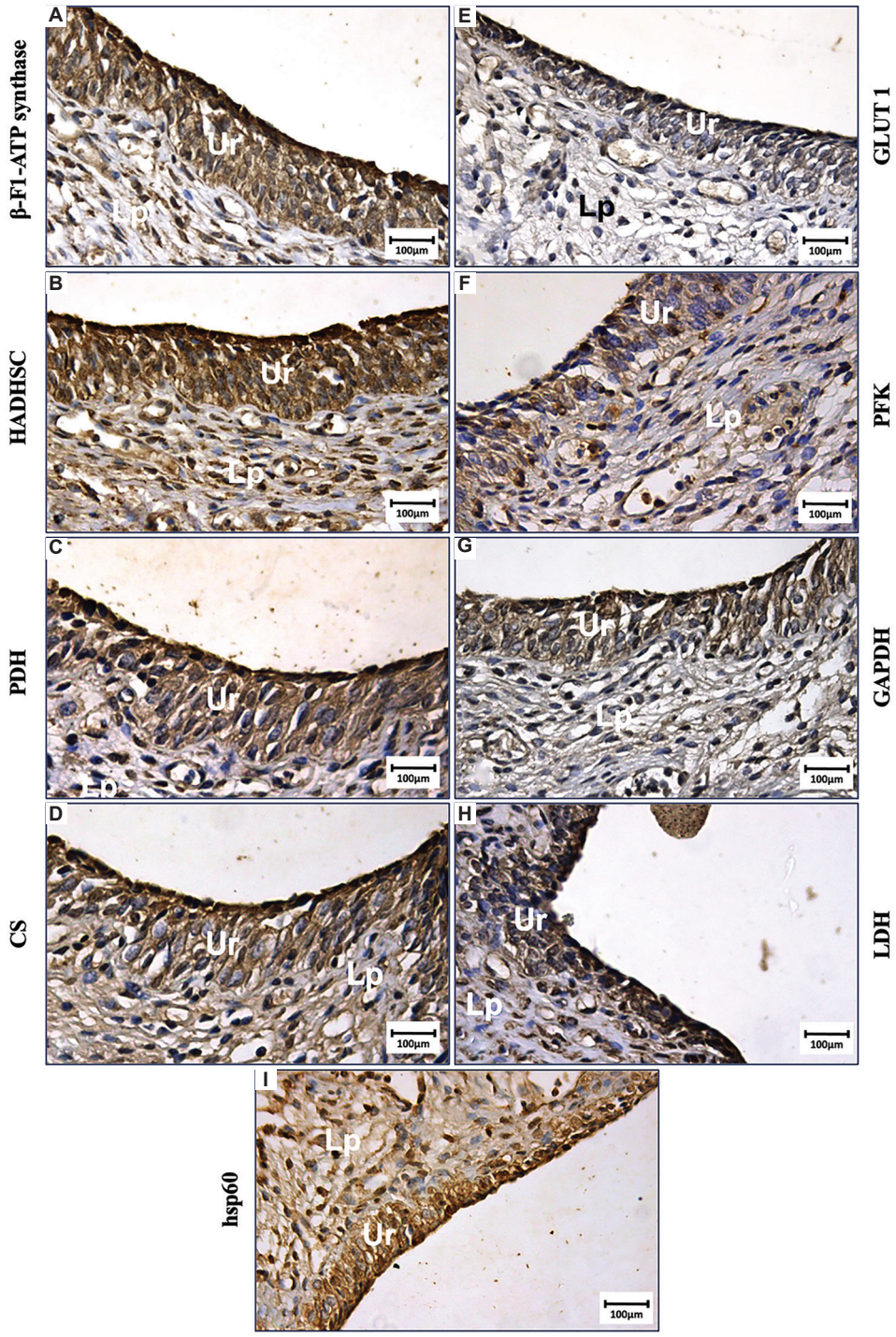

Figure 2. Immunohistochemical results of urinary bladder in normal bladder tissue group: β-F1-ATP synthase (A), HADHSC (B), PDH (C), CS (D), GLUT1 (E), PFK (F), GAPDH (G), LDH (H), and hsp60 (I). Scale bar: 100 μm.
Abbreviations: Lp: Lamina propria; Ur: Urothelium, ATP: Adenosine triphosphate; GLUT1: Glucose transporter-1; PFK: Phosphofructokinase; GAPDH: Glyceraldehyde 3-phosphate dehydrogenase; LDH: Lactate dehydrogenase; PDH: Pyruvate dehydrogenase; CS: Citrate synthase; HADHSC: Short chain 3-hydroxyacyl-CoA dehydrogenase; hsp60: Heat shock protein 60.

grade pT1 groups, as shown in Figure 5B, C, E, and F, unlike the weak immunoreactivity levels observed in the normal (Figure 2E and F) and low-grade pTa groups (Figure 5A and D), respectively (Table 2).

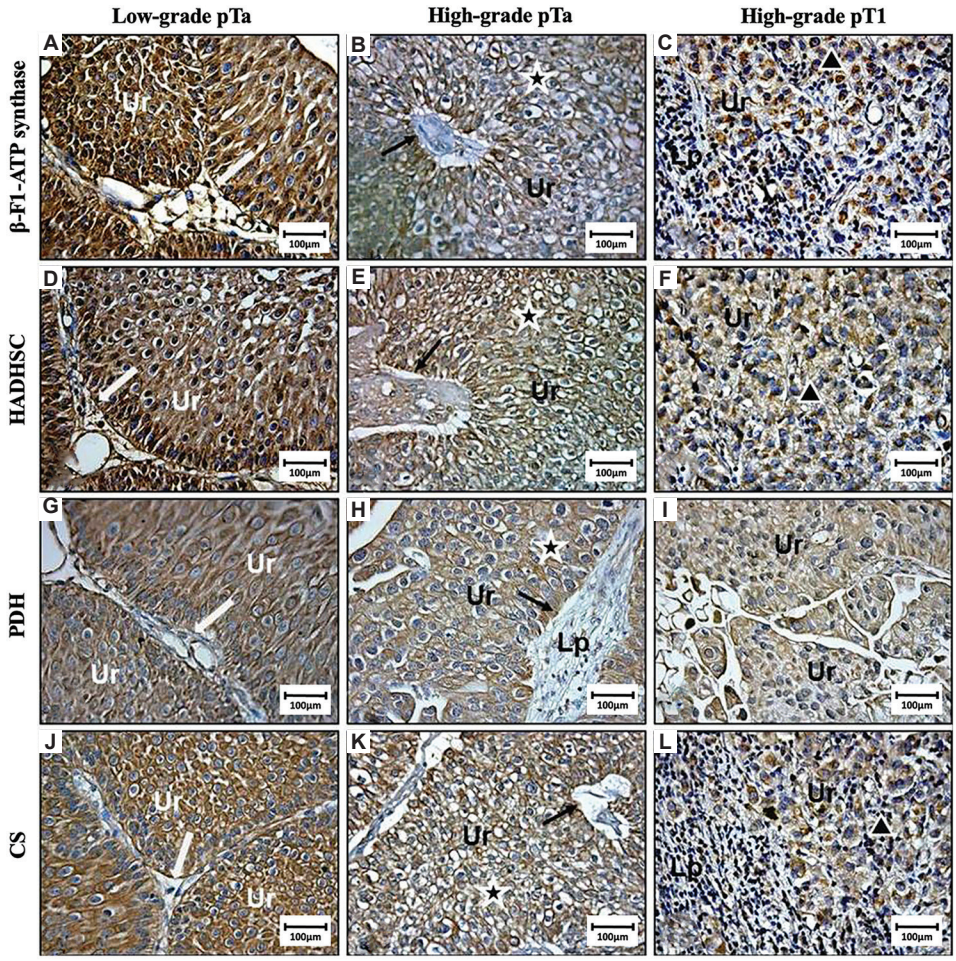

Figure 3. Immunohistochemical results of urinary bladder in low-grade pTa group (A, D, G, and J), high-grade pTa group (B, E, H, and K), and high-grade pT1 group (C, F, I, and L). Cytoplasmic immunoreactivity was observed for β-F1-ATP synthase (A, B, and C), HADHSC (D, E, and F), PDH (G, H, and I), and CS (J, K, and L) protein levels in urothelial cells. Scale bar: 100 μm.

Abbreviations and symbols: Ur: Urothelium; Lp: Lamina propria; white arrow, conjunctive-vascular axis; black arrow, basal membrane integrity; star, cell atypia; triangle, cellular cords; PDH: Pyruvate dehydrogenase; CS: Citrate synthase; HADHSC: Short chain 3-hydroxyacyl-CoA dehydrogenase; ATP: Adenosine triphosphate.

Similarly, significant increase in immunoreactivity was observed for GAPDH and LDH in both the high-grade pTa and pT1 groups, as indicated in Figure 5H, I, K and L, in comparison to the normal (Figure 2G and H) and low-grade pTa groups (Figure 5G and J), which recorded weak immunoreactivity for the same proteins (Table 2). Moreover, no statistically significant differences in immunoreactivity toward hsp60 (Figure 2I, 5M, 5N, and 5O) were observed among the groups, although all of them recorded intense immunoreactivity (Table 2).

There was significant increase in GLUT1, PFK, and GAPDH protein levels in both the high-grade pTa and pT1 groups in comparison to the normal and low-grade pTa groups, as shown in Figures 4E, 4F, and 6A. Interestingly, the pT1 group recorded the highest LDH protein levels in comparison to the other groups, as highlighted in Figure 6B. Furthermore, no statistically significant differences in LDH protein levels were found between low-grade pTa and high-grade pTa groups, which were significantly higher in relation to normal group (Figure 6B).

In addition, no statistically significant differences in hsp60 protein levels were found among the groups, as shown in Figure 6C.

3.4. IBEC was significantly lower in high-grade pTa and high-grade pT1 bladder tumors

An assessment involving the IBEC calculation was performed. Based on the results, normal bladder tissue

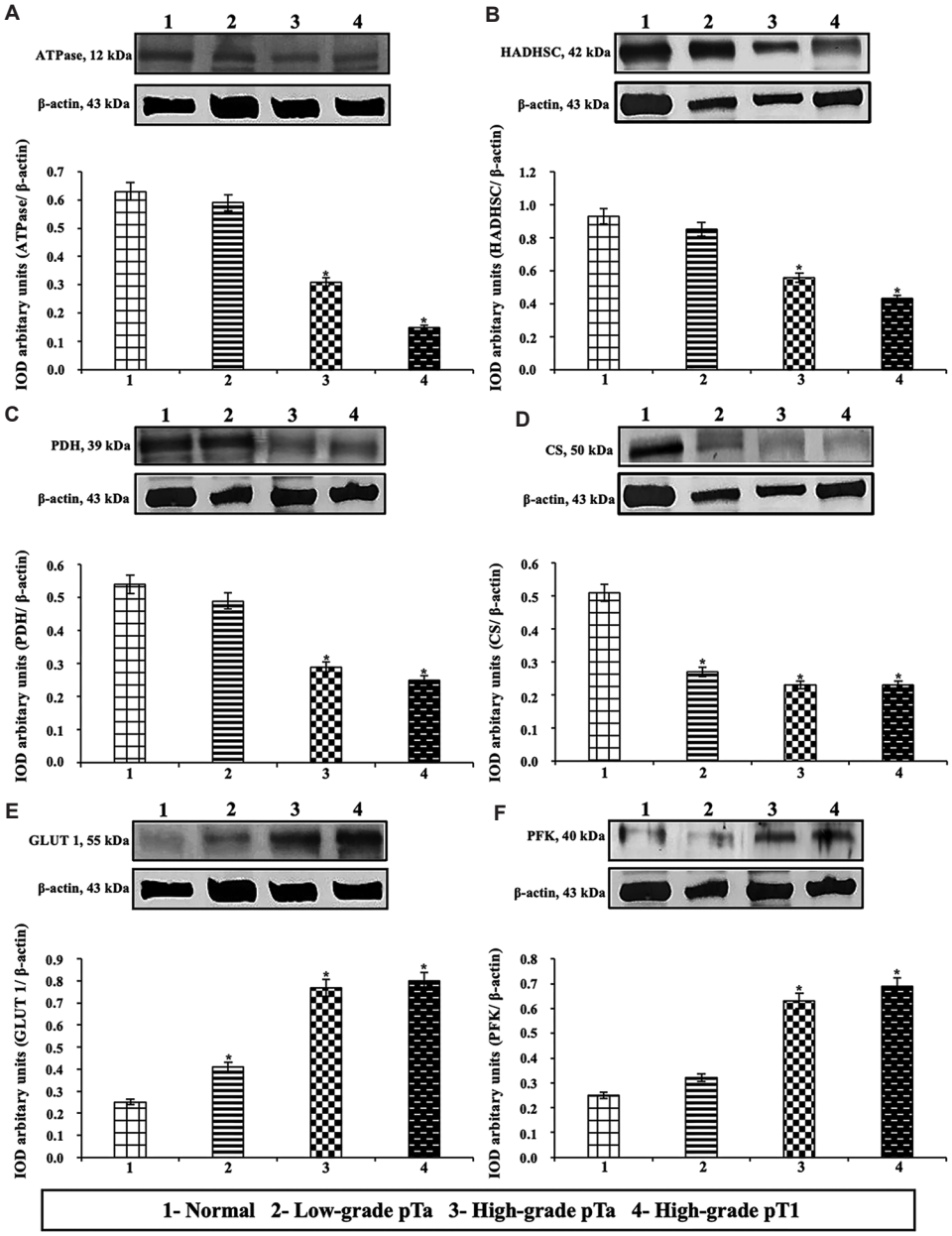

Figure 4. Representative immunoblotting analysis results and semi-quantitative determination of β-F1-ATP synthase (ATPase) (A), HADHSC (B), PDH (C), CS (D), GLUT 1 (E), and PFK (F) protein levels. Representative protein profiles pooled from ten patients per group for each repetition (duplicate). Graphs depict the relative expression of integrated optical density observed for β-F1-ATP synthase (ATPase), HADHSC, PDH, CS, GLUT 1, and PFK proteins, normalized by β-actin and expressed as mean ± standard deviation. *Significance difference ($P < 0.01$), after applying Tukey test.
Abbreviations: ATP: Adenosine triphosphate; GLUT1: Glucose transporter-1; PFK: Phosphofructokinase; PDH: Pyruvate dehydrogenase; CS: Citrate synthase; HADHSC: Short chain 3-hydroxyacyl-CoA dehydrogenase.

and low-grade pTa tumors recorded notably higher IBEC values than both high-grade pTa and pT1 tumors, as graphically represented in Figure 7.

4. Discussion

The primary treatment approach to NMIBC typically involves surgical intervention via TURBT. This procedure allows removing visible lesions and collecting tissue samples for histopathological analysis purposes, and it enables determining tumor stage and grade. Intravesical chemotherapy is often administered as adjunctive measure for NMIBC treatment within 6 h after TURBT to prevent tumor cells' post-procedure implantation and to reduce relapse rates.[24] Another adjuvant therapy option is BCG

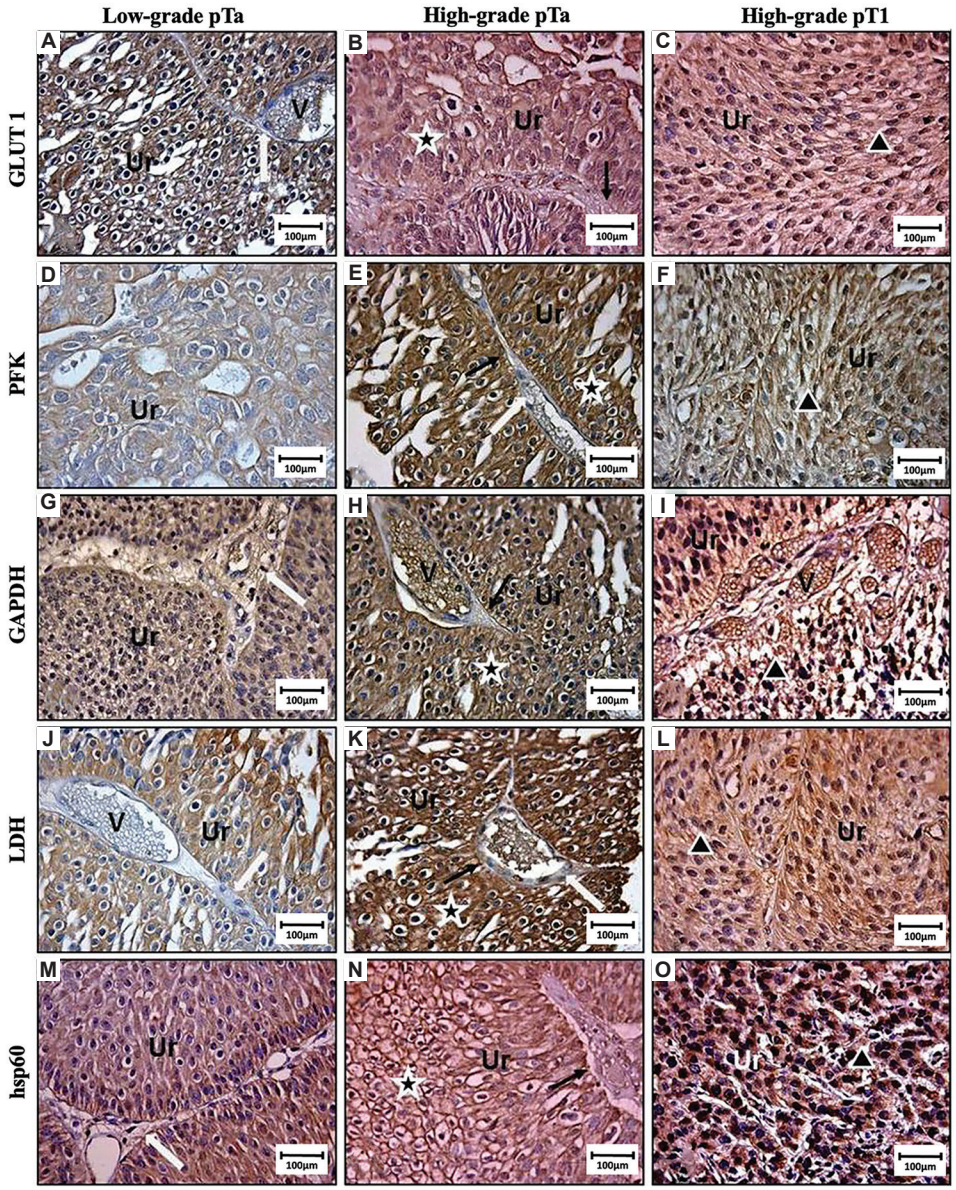

Figure 5. Immunohistochemical results of urinary bladder in low-grade pTa (A, D, G, J, and M), high-grade pTa (B, E, H, K, and N), and high-grade pT1 (C, F, I, L, and O) groups. Cytoplasmic immunoreactivity was observed for GLUT1 (A-C), PFK (D-F), GAPDH (G-I), LDH-A (J-L), and hsp60 (M-O) protein levels in urothelial cells.

Abbreviations and symbols: Ur: Urothelium; V: Blood vessel; white arrow, conjunctive-vascular axis; black arrow, basal membrane integrity; star, cell atypia; triangle, cellular cords; GLUT1: Glucose transporter-1; PFK: Phosphofructokinase; GAPDH: Glyceraldehyde 3-phosphate dehydrogenase; LDH-A: Lactate dehydrogenase A; hsp60: Heat shock protein 60.

immunotherapy, which is administered 4 to 6 weeks after TURBT application to allow resected area re-epithelialization and to minimize the risk of bacterial dissemination within the body.[6] Nowadays, BCG immunotherapy stands out as the preferred treatment to be applied to high-grade NMIBC cases, given its higher effectiveness in comparison to intravesical chemotherapy, mainly when it comes to tumor relapse and progression rates.[6,25]

However, using attenuated living organisms, such as BCG, can lead to side effects and pose challenges to predicting patient responses. Side effects occur in more than 90% of patients undergoing BCG treatment. They range from mild to moderate irritative urinary tract symptoms to severe complications, such as hemodynamic instability, persistent fever or allergic reactions that can compromise BCG usage.[25-27] Given these considerations, a

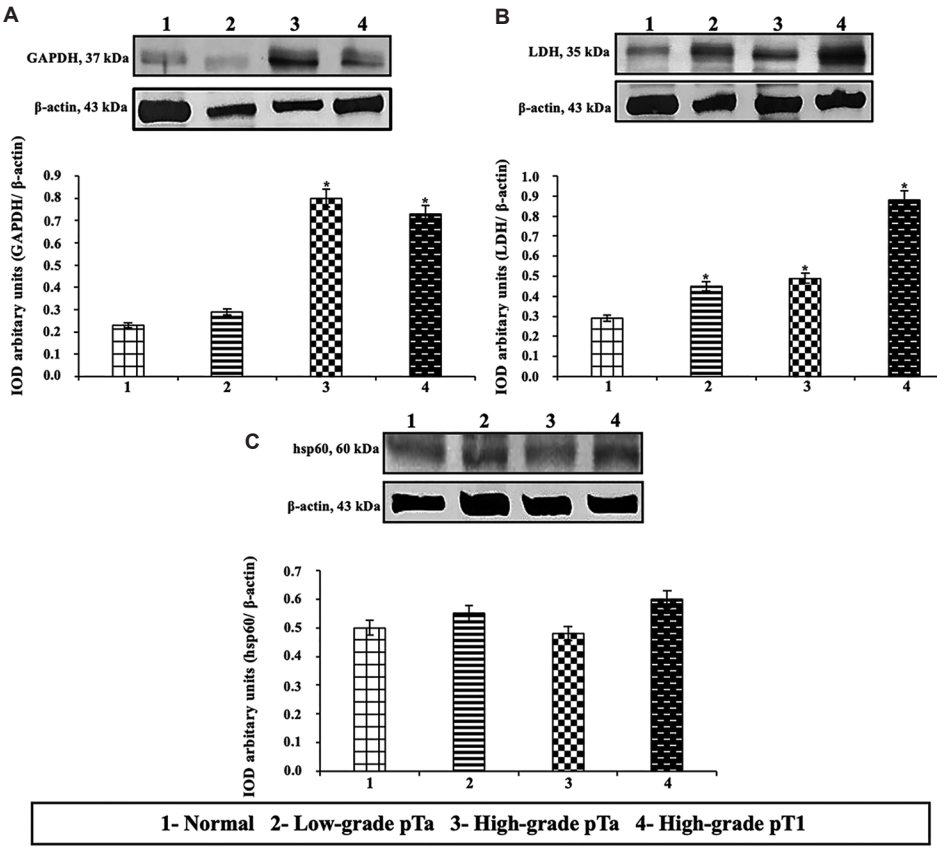

Figure 6. Representative immunoblotting analysis results and semi-quantitative determination of GAPDH (A), LDH (B), and hsp60 (C) protein levels. Representative protein profiles pooled from ten patients per group for each repetition (duplicate). Graphs depict the relative expression of integrated optical density observed for GAPDH, LDH, and hsp60 proteins, normalized by β-actin and expressed as mean ± standard deviation. *Significance difference ($P < 0.01$), after applying Tukey test.
Abbreviations: GAPDH: Glyceraldehyde 3-phosphate dehydrogenase; LDH: Lactate dehydrogenase; hsp60: Heat shock protein 60.

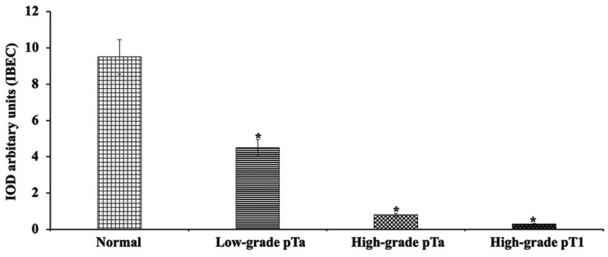

Figure 7. Bioenergetic cellular index observed for normal, low-grade pTa, high-grade pTa and high-grade pT1 groups. The presented results are expressed as mean ± standard deviation. Different lowercase letters (**A-C**) indicate significant differences ($P < 0.01$) between groups, after applying Tukey test. *Significance difference ($P < 0.01$), after applying Tukey test.

series of studies have been conducted to explore alternative therapies that can effectively eradicate NMIBC and introduce lesser detrimental effects on patients' body.

The aims of the present study were to feature and compare cell energy metabolism profiles among different histological NMIBC grades. Moreover, the IBEC was adjusted to these tumor types. Such an association between NMIBC and cell energy metabolism holds particular significance to establish clinical-pathological and prognostic criteria, as well as to further develop new, highly effective therapies targeting the metabolism of these tumor cells without causing much side effects.

Our results demonstrated notable difference in energy metabolism among normal bladder tissue, and low-grade (low-grade pTa group) and high-grade (high-grade pTa and pT1 groups) NMIBC. Normal bladder tissue and low-grade tumors showed preference for the oxidative phosphorylation pathway, whereas high-grade tumors leaned toward glycolytic metabolism. These findings were based on the analysis applied to several metabolic pathway-related proteins.

Normal bladder tissue and low-grade pTa tumors presented high IBEC due to their prevalent reliance on oxidative phosphorylation, which was evidenced by intense immunoreactivity and high β-F1-ATP synthase

Table 2. Mean immunolabelled antigen intensities in urinary bladder samples collected from normal, low-grade pTa, high-grade pTa, and high-grade pT1 groups

Antigens	Groups			
	Normal (*n*=10) (%)	Low-grade pTa (*n*=10) (%)	High-grade pTa (*n*=10) (%)	High-grade pT1 (*n*=10) (%)
β-F1-ATP synthase	3 (92.7)*	3 (86.2)*	2 (41.3)	1 (15.1)
HADHSC	3 (91.1)*	3 (90.5)*	2 (61.7)	1 (17.9)
PDH	3 (83.0)*	3 (85.9)*	2 (51.1)	1 (19.3)
CS	3 (88.4)*	3 (94.8)*	2 (52.5)	1 (23.0)
GLUT1	1 (17.3)	1 (29.7)	3 (89.9)*	3 (79.7)*
PFK	1 (24.9)	1 (32.0)	3 (94.2)*	3 (92.1)*
GAPDH	1 (19.8)	1 (29.3)	3 (85.2)*	3 (76.4)*
LDH	1 (30.2)	1 (27.4)	3 (94.7)*	3 (88.2)*
hsp60	3 (93.5)*	3 (89.2)*	3 (87.1)*	3 (81.9)*

Notes: 0, lack of immunoreactivity; 1, weak immunoreactivity (1 – 35% positive urothelial cells); 2, moderate immunoreactivity (36 – 70% positive urothelial cells); 3, intense immunoreactivity (>70% positive urothelial cells). *Statistical significance (proportion test, $P<0.0001$). Abbreviations: ATP: Adenosine triphosphate; GLUT1: Glucose transporter-1; PFK: Phosphofructokinase; GAPDH: Glyceraldehyde 3-phosphate dehydrogenase; LDH: Lactate dehydrogenase; PDH: Pyruvate dehydrogenase; CS: Citrate synthase; HADHSC: Short chain 3-hydroxyacyl-CoA dehydrogenase; hsp60: Heat shock protein 60.

protein levels, in association with weak immunoreactivity and reduced GAPDH protein levels. These tumors also presented intense immunoreactivity and high HADHSC and PDH protein levels, in addition to weak immunoreactivity and decreased GLUT1 and PFK protein levels.

Increased β-F1-ATP synthase activity indicates increased mitochondrial activity, since this protein crosses the mitochondrial inner membrane and accounts for ADP conversion into ATP. This process takes place through ADP combination to a free ionic phosphate radical, which adds another high energy phosphate bond to the molecule. The final process happens when ATP is transported by facilitated mitochondria diffusion into the cytoplasm. After the entire process, each glucose molecule generated 38 ATPs, carbon dioxide, and water.[13-16] The HADHSC protein transforms fatty acid into acetyl-coA, and PDH transforms pyruvate into acetyl-coA, and both of them transform different substrates into acetyl-coA in order to generate energy in the mitochondria. These proteins are closely related to oxidative phosphorylation, and this is the typical, normal mode of cell metabolism, since it does not deviate from the metabolic pathway to generate other substrates, as well as because it happens in an environment presenting normal oxygen levels.[13] Therefore, high IBEC in these tumors may point out good prognosis, besides helping therapeutic decision-making and these patients' follow-up.

The CS protein only recorded difference in immunoreactivity between low- and high-grade tumors, but it did not show changes in protein levels between these groups. Interestingly, CS protein levels were significantly higher in normal bladder tissue when compared to different NMIBC grades. It may have happened because this enzyme is directly linked to pathway speed, rather than to deviations in metabolic pathways. However, further studies focused on investigating the actual role played by this enzyme in NMIBC metabolism should be conducted.[28]

Immunohistochemistry and Western blotting results observed for high-grade pTa and high-grade pT1 tumors were quite consistent with each other, but they differed from those observed for normal bladder tissue and low-grade pTa tumors. The high-grade pTa and high-grade pT1 tumors manifested intense-to-moderate immunoreactivity for proteins associated with glycolytic pathway, as well as higher GLUT1, PFK, and GAPDH protein levels. They also presented weak immunoreactivity and low β-F1-ATP synthase, HADHSC, and PDH protein levels. Thus, they presented IBEC lower than that of normal bladder tissue and low-grade tumors.

Low IBEC in high-grade tumors highlights significant changes in the energy metabolism of normal cells. As previously suggested by Otto Warburg, the energy metabolic activity of malignant neoplasms is mostly concentrated in the glycolytic pathway.[13] Increased metabolism in tumor cells requires higher ATP consumption, and since the glycolytic pathway produces less ATP than oxidative phosphorylation, although much faster, some enzymes present increased activity to promptly meet the energy needs of these cells. GLUT1 belongs to the GLUT molecules' family and wields paramount importance in this scenario, since it accounts for allowing glucose to enter the cells. The literature reported increased activity of this protein in a series of neoplasms, such as pancreatic, ovarian and kidney cancer, among others.[29] This glucose avidity can be measured through positron emission tomography-computed tomography, an examination tool used to assess the metabolism of structures based on radiotracer glucose uptake determined by F18-fluorordesoxyglucose radiopharmaceutical. Lesions presenting high radiotracer glucose uptake are metabolically active. Consequently, they become more aggressive.[30] The major BC indications comprise lymph node staging, distant metastasis and relapse after definitive treatment.[30]

Cancer cells present increased glucose and glutamine uptake during cancer invasiveness progression, mostly by

increasing the expression of GLUT1 transporters on their surface.[11,12] This increased glucose uptake sets the stage for metabolic competition between effector T cells and tumor cells.[31] Notably, differentiated $CD8^+$ T cells present increased reliance on glucose-dependent metabolism in comparison to their naïve counterparts. Consequently, glucose shortage negatively impacts the effector functions of $CD8^+$ T cells, leading to compromised immune response and potentially limiting immune checkpoint therapy effectiveness.[31] Furthermore, proapoptotic Bcl-2 family members are activated and promote cell apoptosis when glucose uptake is limited.[11,32] Recent studies have suggested that limited glucose consumption in T cells can be mitigated through inosine or fatty acid metabolism modulation, although further investigations in this field should be conducted.[11,32,33]

As the active players in glycolysis, PFK and GAPDH play important role in glucose degradation and energy generation processes. LDH is another essential protein for tumor cell metabolism, since it enables pyruvate conversion into lactate, which is transported out of the cytoplasm to be used by the same cell to produce other molecules or to be used by the neighboring cells. This process ensures tumor cell energy production and substrate supply, even in hypoxic and acidic environment, due to high metabolism and low perfusion. This acidic environment protects the tumor cell from apoptosis and enables the invasion of other tissues.[34,35] LDH indices in the current study were higher in high-grade pT1 tumors than in the other types, likely because it is a more undifferentiated tumor. Thus, low IBEC in these neoplasms can be an unfavorable factor that can be used in therapeutic decision-making, mainly to indicate another TURBT (Re-TURBT) procedure or even early radical cystectomy.

There was no change in mitochondrion structure among the investigated groups, neither in immunoreactivity nor in hsp60 protein levels. This finding indicates that mitochondrial function can be restored in high-grade tumor cases showing decreased oxidative phosphorylation, as previously observed by Fantin *et al.*[36]

High-grade pTa tumors presented metabolic behavior quite similar to that of pT1 tumors, high relapse likelihood and progression to muscle-invasive disease; therefore, they must be subjected to aggressive treatment. High-grade pT1 tumors must be subjected to Re-TURBT, from 4 to 6 weeks after the first resection, mainly if there is proper muscle absence at the first resection, since this change in protocol is observed in 10 – 25% of cases.[37] Other prognostic factors that should be taken into consideration in therapeutic decision-making comprise multifocality (>3 lesions), tumors larger than 3 cm, previous treatment with BCG, and presence of associated CIS.[6,25,27] Based on a multi-institute retrospective study conducted with 2,451 high-grade pT1 patients who were analyzed after treatment with BCG, Re-TURBT was beneficial to progression-free survival, as well as to overall survival, although only in cases showing proper muscle absence after the first TURBT.[38] Results in the current study are unprecedented; thus, using IBEC in clinical practice presents a potential strategy for aiding therapeutic decision-making, mainly for high-grade pTa tumor cases, which are often not aggressively treated as pT1 tumors. Cuezva *et al.*[23] assessed IBEC in lung adenocarcinomas and observed that it was lower in large tumors (>3 cm) than in smaller tumors and than in lungs without neoplasm. IBEC was also correlated to tumor stage. IA-stage tumors recorded IBEC 2.5 times higher than IB-stage tumors, and it evidenced clear IBEC correlation to disease prognosis.

Some high-grade tumors can relapse and progress to muscle-invasive tumors during follow-up, even after aggressive local treatment application (TURBT + Re-TURBT + BCG). These patients have worse prognosis than those with muscle-invasive disease as the initial presentation. Moschini *et al.*[39] retrospectively investigated a group of 768 patients subjected to radical cystectomy due to muscle-invasive tumors (475 patients), or due to superficial tumors that had progressed to muscle-invasive stage, even after intravesical therapies, during follow-up (293 patients). They observed that the non-muscle-invasive group that had progressed during follow-up recorded worse results for progression/relapse-free survival, cancer-specific mortality, and overall mortality within 10 years, based on univariate and multivariate analyses.[39] Therefore, patients with pT1-grade NMIBC should be subjected to aggressive treatments, such as early radical cystectomy, mainly in case of BCG failure after TURBT and Re-TURBT. Since high-grade pTa tumors were metabolically similar to pT1, they should be treated in the same way as pT1, especially if they show low IBEC. Therefore, IBEC determination can be treated as an additional tool to help managing these cases, particularly under the concerns that treatments applied to them are quite aggressive and often lead to significant morbidity.

5. Conclusion

The aims of the current study were to both feature and compare cell energy metabolism profiles among normal bladder tissue and NMIBC tissues of different histological grades (such as low-grade pTa, high-grade pTa, and high-grade pT1 tumors). In addition, this study introduced the concept of IBEC, which is a new approach applicable to treat these tumors. In summary, according to the current

findings, normal bladder tissue, and low-grade pTa tumors mostly rely on oxidative phosphorylation as primary energy metabolism pathway, which contributes to high IBEC. On the other hand, high-grade pTa and high-grade pT1 tumors present prevalent glycolytic metabolism profile over oxidative phosphorylation, which leads to the lower IBEC.

In conclusion, the abnormal values of IBEC observed for NMIBC grades underscore its potential as a valuable marker in both the diagnosis and prognosis of BC patients.

Acknowledgments

The authors wish to express their gratitude for the assistance provided by the Amaral Carvalho Hospital (HAC), Jaú City, São Paulo State, Brazil, and the Program in Surgery Sciences of School of Medicine, Universidade Estadual de Campinas (UNICAMP), Campinas City, São Paulo State, Brazil.

Funding

This research was funded by the São Paulo Research Council (FAPESP grant numbers: 2014/11866-1; 2014/12047-4; 2018/10052-1; 2020/03419-6), and the Brazilian National Council for Scientific and Technological Development (CNPq grant numbers: 552120/2011-1; 312396/2021-0).

Conflict of interest

The authors declare that they have no competing interests.

Author contributions

Conceptualization: Guilherme Prado Costa, Petra Karla Böckelmann, Wagner José Fávaro

Formal analysis: Guilherme Prado Costa, Petra Karla Böckelmann, Leandro Luiz Lopes de Freitas, Gabriela Cardoso de Arruda Camargo, Gabriela de Oliveira, Bianca Ribeiro de Souza, Athanase Billis, Wagner José Fávaro

Investigation: Guilherme Prado Costa, Petra Karla Böckelmann, Renato Prado Costa, Carlos Hermann Schaal, Fernando César Sala, André Pereira Vanni, Leandro Luiz Lopes de Freitas, João Carlos Cardoso Alonso, Athanase Billis, Wagner José Fávaro

Methodology: Guilherme Prado Costa, Petra Karla Böckelmann, Leandro Luiz Lopes de Freitas, João Carlos Cardoso Alonso, Gabriela Cardoso de Arruda Camargo, Gabriela de Oliveira, Bianca Ribeiro de Souza, Athanase Billis, Wagner José Fávaro

Writing – original draft: Guilherme Prado Costa, Petra Karla Böckelmann, Wagner José Fávaro

Writing – review & editing: Guilherme Prado Costa, Wagner José Fávaro

Ethics approval and consent to participate

The study was conducted according to the guidelines of the Declaration of Helsinki and approved by the Institutional Ethics Committee of Ethics and Research Committee of Amaral Carvalho Hospital, Jaú City, São Paulo State, Brazil (CAAE number: 47475815.9.0000.5434). Informed consent was obtained from all subjects involved in the study.

Consent for publication

Written informed consent has been obtained from the patients to publish this paper.

Availability of data

The data presented in this study are available from the corresponding author on reasonable request.

References

1. Celada Luis G, Albers Acosta E, De la Fuente H, *et al*. A comprehensive analysis of immune response in patients with non-muscle-invasive bladder cancer. *Cancers* (*Basel*). 2023;15:1364.

   doi: 10.3390/cancers15051364

2. Bray F, Ferlay J, Soerjomataram I, Siegel RL, Torre LA, Jemal A. Global cancer statistics 2018: GLOBOCAN estimates of incidence and mortality worldwide for 36 cancers in 185 countries. *CA Cancer J Clin*. 2018;68:394-424.

   doi: 10.3322/caac.21492

3. Allard P, Bernard P, Fradet Y, Têtu B. The early clinical course of primary Ta and T1 bladder cancer: A proposed prognostic index. *Br J Urol*. 1998;81:692-698.

   doi: 10.1046/j.1464-410x.1998.00628.x

4. Lamm D, Persad R, Brausi M, *et al*. Defining progression in nonmuscle invasive bladder cancer: It is time for a new, standard definition. *J Urol*. 2014;191:20-27.

   doi: 10.1016/j.juro.2013.07.102

5. Babjuk M, Burger M, Capoun O, *et al*. European association of urology guidelines on non-muscle-invasive bladder cancer (Ta, T1, and carcinoma *in situ*). *Eur Urol*. 2022;81(1):75-94.

   doi: 10.1016/j.eururo.2021.08.010

6. Sylvester RJ, Van der Meijden AP, Oosterlinck W, *et al*. Predicting recurrence and progression in individual patients with stage Ta T1 bladder cancer using EORTC risk tables: A combined analysis of 2596 patients from seven EORTC trials. *Eur Urol*. 2006;49(3):466-465, discussion 475-477.

   doi: 10.1016/j.eururo.2005.12.031

7. Van Rhijn BW, Burger M, Lotan Y, *et al*. Recurrence and progression of disease in non-muscle-invasive bladder cancer: From epidemiology to treatment strategy. *Eur Urol*.

2009;56:430-442.

doi: 10.1016/j.eururo.2009.06.028

8. Cote RJ, Chatterjee SJ. Molecular determinants of outcome in bladder cancer. *Cancer J Sci Am.* 1999;5:2-15.

9. Humphrey PA, Moch H, Cubilla AL, Ulbright TM, Reuter VE. The 2016 WHO classification of tumours of the urinary system and male genital organs-part B: Prostate and bladder tumours. *Eur Urol.* 2016;70:106-119.

doi: 10.1016/j.eururo.2016.02.028

10. Kunju LP, You L, Zhang Y, Daignault S, Montie JE, Lee CT. Lymphovascular invasion of urothelial cancer in matched transurethral bladder tumor resection and radical cystectomy specimens. *J Urol.* 2008;180:1928-1932.

doi: 10.1016/j.juro.2008.07.056

11. Semeniuk-Wojtaś A, Poddębniak-Strama K, e, *et al*. Tumour microenvironment as a predictive factor for immunotherapy in non-muscle-invasive bladder cancer. *Cancer Immunol Immunother.* 2023;72(7):1971-1989.

doi: 10.1007/s00262-023-03376-9

12. Domblides C, Lartigue L, Faustin B. Control of the antitumor immune response by cancer metabolism. *Cells.* 2019;8(2):104.

doi: 10.3390/cells8020104

13. Hanahan D, Weinberg RA. Hallmarks of cancer: The next generation. *Cell.* 2011;144:646-674.

doi: 10.1016/j.cell.2011.02.013

14. DeBerardinis RJ, Lum JJ, Hatzivassiliou G, Thompson CB. The biology of cancer: Metabolic reprogramming fuels cell growth and proliferation. *Cell Metab.* 2008;7:11-20.

doi: 10.1016/j.cmet.2007.10.002

15. Vander Heiden MG, Cantley LC, Thompson CB. Understanding the Warburg effect: The metabolic requirements of cell proliferation. *Science.* 2009;324:1029-1033.

doi: 10.1126/science.1160809

16. Cairns RA, Harris IS, Mak TW. Regulation of cancer cell metabolism. *Nat Rev Cancer.* 2011;11:85-95.

doi: 10.1038/nrc2981

17. Cuezva JM, Krajewska M, De Heredia ML, *et al.* The bioenergetic signature of cancer: A marker of tumor progression. *Cancer Res.* 2002;62:6674-6681.

18. Isidoro A, Martínez M, Fernández PL, *et al*. Alteration of the bioenergetic phenotype of mitochondria is a hallmark of breast, gastric, lung and oesophageal cancer. *Biochem J.* 2004;378:17-20.

doi: 10.1042/BJ20031541

19. Vallejo CG, Cruz-Bermudez A, Clemente P, Hernandez-Sierra R, Garesse R, Quintanilla M. Evaluation of mitochondrial function and metabolic reprogramming during tumor progression in a cell model of skin carcinogenesis. *Biochimie.* 2013;95:1171-1176.

doi: 10.1016/j.biochi.2013.01.001

20. Epstein JI, Amin MB, Reuter VR, Mostofi FK. The world health organization/International society of urological pathology consensus classification of urothelial (transitional cell) neoplasms of the urinary bladder. Bladder Consensus Conference Committee. *Am J Surg Pathol.* 1998;22:1435-1448.

doi: 10.1097/00000478-199812000-00001

21. Fávaro WJ, Alonso JC, De Souza BR, *et al*. New synthetic nano-immunotherapy (OncoTherad®) for non-muscle invasive bladder cancer: Its synthesis, characterization and anticancer property. *Tissue Cell.* 2023;80:101988.

doi: 10.1016/j.tice.2022.101988

22. Reis IB, Tibo LH, Socca EA, De Souza BR, Durán N, Fávaro WJ. OncoTherad® (MRB-CFI-1) nano-immunotherapy reduced tumoral progression in non-muscle invasive bladder cancer through activation of Toll-like signaling pathway. *Tissue Cell.* 2022;76:101762.

doi: 10.1016/j.tice.2022.101762

23. Cuezva JM, Chen G, Alonso AM, *et al*. The bioenergetic signature of lung adenocarcinomas is a molecular marker of cancer diagnosis and prognosis. *Carcinogenesis.* 2004;25:1157-1163.

doi: 10.1093/carcin/bgh113

24. O'Donnell MA. Practical applications of intravesical chemotherapy and immunotherapy in high-risk patients with superficial bladder cancer. *Urol Clin North Am.* 2005;32:121-131.

doi: 10.1016/j.ucl.2005.01.003

25. Lobo N, Martini A, Kamat AM. Evolution of immunotherapy in the treatment of non-muscle-invasive bladder cancer. *Expert Rev Anticancer Ther.* 2022;22:361-370.

doi: 10.1080/14737140.2022.2046466

26. Böhle A, Brandau S. Immune mechanisms in bacillus Calmette-Guerin immunotherapy for superficial bladder cancer. *J Urol.* 2003;170:964-969.

doi: 10.1097/01.ju.0000073852.24341.4a

27. Wood D. Tumors of the bladder. In: Wein AJ, Kavoussi LR, Partin AW, Peters CA, editors. *Campbell-Walsh Urology*. 11th ed. Philadelphia, PA: Elsevier; 2016.

28. Lim HY, Ho QS, Low J, Choolani M, Wong KP. Respiratory competent mitochondria in human ovarian and peritoneal cancer. *Mitochondrion.* 2011;11:437-443.

doi: 10.1016/j.mito.2010.12.015

29. Macheda ML, Rogers S, Best JD. Molecular and cellular regulation of glucose transporter (GLUT) proteins in cancer.

J Cell Physiol. 2005;202:654-662.

doi: 10.1002/jcp.20166

30. Bouchelouche K, Choyke PL. PET/CT in renal, bladder and testicular cancer. *PET Clin.* 2015;10:361-374.

doi: 10.1016/j.cpet.2015.03.002

31. Renner K, Bruss C, Schnell A, *et al*. Restricting glycolysis preserves T cell effector functions and augments checkpoint therapy. *Cell Rep.* 2019;29:135-150.e9.

doi: 10.1016/j.celrep.2019.08.068

32. Wang T, Gnanaprakasam JN, Chen X, *et al*. Inosine is an alternative carbon source for CD8+-T-cell function under glucose restriction. *Nat Metab.* 2020;2:635-647.

doi: 10.1038/s42255-020-0219-4

33. Zhang Y, Kurupati R, Liu L, *et al*. Enhancing CD8+ T cell fatty acid catabolism within a metabolically challenging tumor microenvironment increases the efficacy of melanoma immunotherapy. *Cancer Cell.* 2017;32:377-391.e9.

doi: 10.1016/j.ccell.2017.08.004

34. Fischer K, Hoffmann P, Voelkl S, *et al*. Inhibitory effect of tumor cell-derived lactic acid on human T cells. *Blood.* 2007;109:3812-3819.

doi: 10.1182/blood-2006-07-035972

35. Swietach P, Vaughan-Jones RD, Harris AL. Regulation of tumor pH and the role of carbonic anhydrase 9. *Cancer Metastasis Rev.* 2007;26:299-310.

doi: 10.1007/s10555-007-9064-0

36. Fantin VR, St-Pierre J, Leder P. Attenuation of LDH-A expression uncovers a link between glycolysis, mitochondrial physiology, and tumor maintenance. *Cancer Cell.* 2006;9:425-434.

doi: 10.1016/j.ccr.2006.04.023

37. Kitamura H, Kakehi Y. Treatment and management of high-grade T1 bladder cancer: What should we do after second TUR? *Jpn J Clin Oncol.* 2015;45:315-322.

doi: 10.1093/jjco/hyu219

38. Gontero P, Sylvester R, Pisano F, *et al*. The impact of re-transurethral resection on clinical outcomes in a large multicentre cohort of patients with T1 high-grade/Grade 3 bladder cancer treated with bacille Calmette-Guerin. *BJU Int.* 2016;118:44-52.

doi: 10.1111/bju.13354

39. Moschini M, Sharma V, Dell'oglio P, *et al*. Comparing long-term outcomes of primary and progressive carcinoma invading bladder muscle after radical cystectomy. *BJU Int.* 2016;117:604-610.

doi: 10.1111/bju.13146

ACCSCIENCE PUBLISHING

Tumor Discovery

ORIGINAL RESEARCH ARTICLE

Unveiling the mechanism of *Buddleja officinalis* against esophageal squamous cell carcinoma through network pharmacology and molecular docking approaches

Cheng Chang[1], Zhen-Zhen Yang[2,3], Yin-Sen Song[2], Na Gao[2,3], Hao-Zhe Zhang[2,3], Xiao-Lin Zhang[2], and Tian-Li Fan[3]*

[1]Department of Medical Nursing, Zhengzhou Urban Construction Vocational College, Zhengzhou, Henan, China

[2]Translational Medicine Research Center, The Fifth Clinical Medical College of Henan University of Chinese Medicine (Zhengzhou People's Hospital), Zhengzhou, Henan, China

[3]Department of Pharmacology, Basic Medical School of Zhengzhou University, Zhengzhou, Henan, China

Abstract

In this research, we aim to explore the underlying mechanism of *Buddleja officinalis* (BO) in inhibiting esophageal squamous cell carcinoma (ESCC) by means of network pharmacology and molecular docking approaches. First, BO component targets were determined from the Traditional Chinese Medicine Systematic Pharmacology and HERB databases (known as BenCaoZuJian in Chinese transliteration), and ESCC disease targets were identified from GeneCards and DisGeNET databases. Second, the Venny 2.1 online tool was utilized to visualize the intersection targets, and shared potential targets between BO and ESCC were identified using the STRING database. Third, the component-target-pathway networks were constructed using Cytoscape software. Gene Ontology and Kyoto Encyclopedia of Genes and Genomes were utilized for further analyzing the mechanism of BO in inhibiting ESCC. Finally, molecular docking technique was employed to delineate the docking profiles of BO and determine the optimal active component, which is threonine protein kinase (AKT1). We screened six active components and 227 targets from BO, of which 24 were shared targets of ESCC and BO. The network pharmacology analysis indicated core targets with high degrees, namely, serum albumin, insulin-like growth factor 1 receptor, AKT1, estrogen receptor, and basic fibroblast growth factor receptor 1, which are the most likely binding sites for the active components in BO. The related signaling pathways underpinning the inhibition of ESCC by BO encompass MAPK signaling pathway, adhesion junction pathway, and gastric cancer pathway. Moreover, linarin was recognized as the most suitable component for AKT1. Our results revealed that BO exhibits multicomponent, multi-target, and multi-pathway characteristics, which offer a scientific foundation for elucidating its therapeutic mechanism in ESCC and present novel insights for future investigations.

Keywords: Network pharmacology; Molecular docking; *Buddleja officinalis*; Esophageal squamous cell carcinoma; Threonine protein kinase

***Corresponding author:**
Tian-Li Fan
(fantianli@zzu.edu.cn)

Citation: Chang C, Yang Z, Song Y, *et al*. Unveiling the mechanism of *Buddleja officinalis* against esophageal squamous cell carcinoma through network pharmacology and molecular docking approaches. *Tumor Discov*. 2024;3(1):2312.
https://doi.org/10.36922/td.2312

Received: November 24, 2023
Accepted: February 27, 2024
Published Online: March 20, 2024

1. Introduction

The incidence of esophageal cancer (EC), one of the most common malignancies worldwide, has dramatically increased over the past 30 years, especially in developed countries.[1-3] The primary pathological variants of EC are esophageal squamous cell carcinoma (ESCC) and adenocarcinoma, of which ESCC accounts for the vast majority (90%) of the EC cases.[4,5] Although various factors have been identified to contribute to the development of ESCC, the specific molecular mechanism of the disease remains elusive. Since obvious symptoms are hardly discoverable in the early stage, most of the ESCC cases are usually diagnosed at an advanced stage,[6,7] prompting the urgent need for effective treatments.

Buddleja officinalis (BO) is an indigenous traditional Chinese medicine (TCM) used in traditional formulations to treat inflammation, vascular disease, conjunctivitis, headache, and stroke.[8-10] For example, some studies have extensively reported the pharmacologic profiles and usage of BO in traditional recipes and demonstrated that flavonoids in BO flower buds possess anti-inflammatory and antioxidant activities.[11] In addition, aqueous extracts of BO can inhibit high glucose-induced matrix metalloproteinase activity in human umbilical vein endothelial cells.[9] Given that TCM plays a regulatory and synergistic role systematically through multi-target and multi-channel intervention strategies, it holds distinct advantages in terms of prevention and personalized treatment of ESCC. Nevertheless, the underlying mechanism by which BO exerts its effects on ESCC remains obscure.

Network pharmacology integrates multiple disciplines to establish network relationships between drugs, targets, and diseases, expanding the study of drugs from single-target research to the entire biological network, thus providing a more comprehensive understanding of drug mechanisms. This field can assist in discovering new drug candidates, optimizing drug design, and predicting drug efficacy.[12,13] The research methodology of network pharmacology conforms to the basic requirements of the holistic view of TCM, providing novel ideas and methods for TCM research.[14-16]

Herein, we used the approach of network pharmacology to investigate primary bioactive constituents, targets, and putative mechanisms of BO in inhibiting ESCC. The research flowchart is presented in Figure 1.

2. Materials and methods

2.1. Identification of dominant ingredients in BO

The dominant ingredients of BO were determined from the TCM systematic pharmacology database (TCMSP, http://tcmspw.com/tcmsp.php) and HERB database (http://herb.ac.cn). The parameters were set as follows: oral bioavailability (OB) ≥30% and drug-likeness ≥0.18.

2.2. Establishment of BO active component database

The targets were identified from the PharmMapper database (http://www.lilab-ecust.cn/pharmmapper/). The species in the PharmMapper database was set as "*Homo sapiens*" and filtered by ≥0.6 of the norm fit. The BO-associated targets were converted to standardized names shown in the UniProt database (https://www.uniprot.org/), with the status set to "reviewed" and the species set to "human."

2.3. Identification of ESCC-associated targets

The search term "esophageal squamous cell carcinoma" was used to acquire ESCC-related targets in GeneCards (https://www.genecards.org/) and DisGeNET (https://www.disgenet.org/home/).

2.4. Determination of BO-ESCC shared targets

After obtaining BO component targets (phammapper: http://www.lilab-ecust.cn/pharmmapper/), Venny 2.1 (https://bioinfogp.cnb.csic.es/tools/venny/index.html) was used to determine the common target of disease and active ingredients.

2.5. Establishing the BO-ESCC protein-protein interaction (PPI) network

The PPI network for BO-ESCC shared targets was constructed using the interaction database platform STRING v11.0 (https://cn.string-db.org/). The parameters are set as follows: the species was set to "*Homo sapiens*," with the 0.4 of confidence score cutoff.

2.6. Visualization of network analysis results

The determined BO-ESCC targets were further visualized using Cytoscape v3.9.1, and the network analysis plugin was utilized in the software, employing its statistical nodes to analyze the core targets within the network.

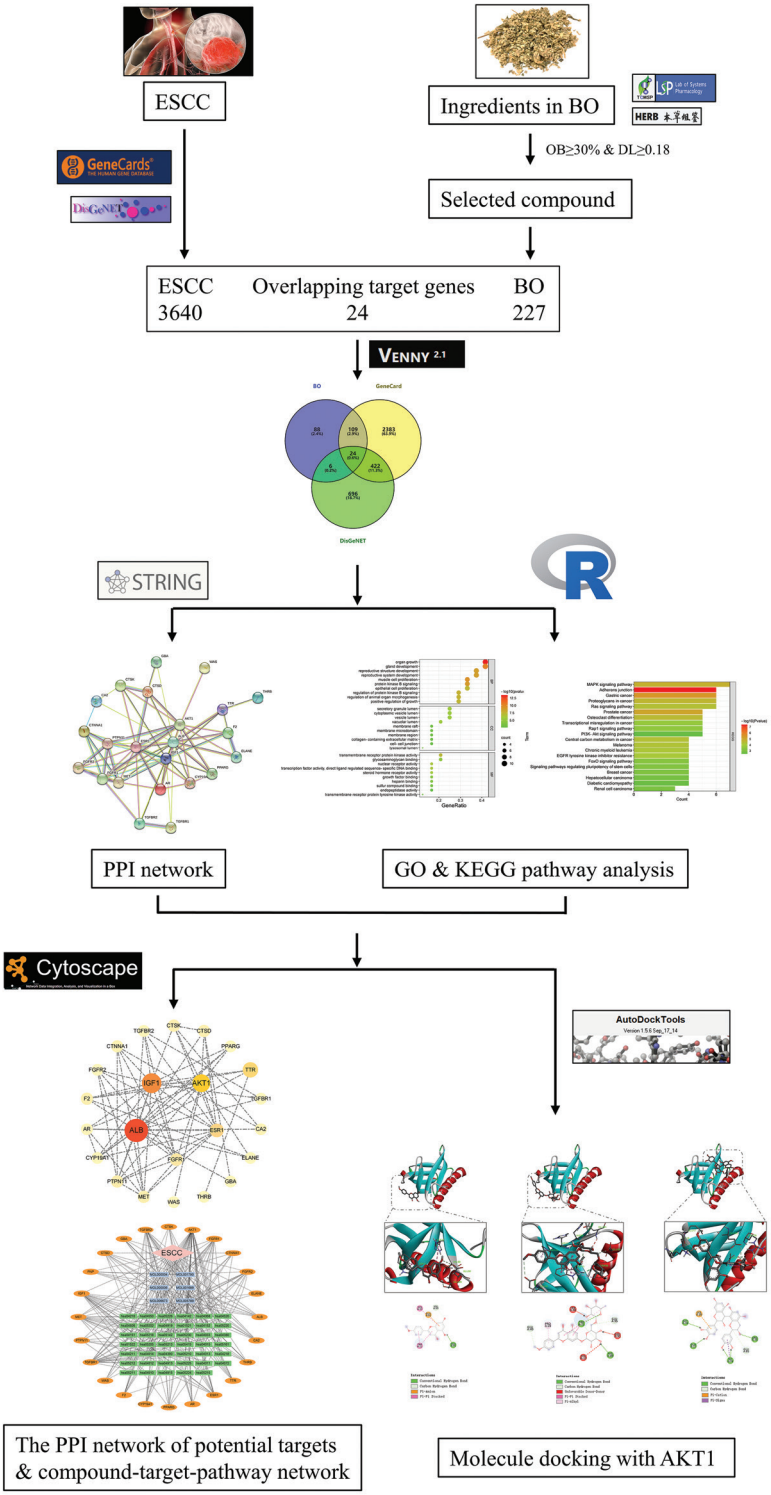

Figure 1. Flow chart of creating networks based on putative mechanisms of BO in inhibiting ESCC.
Abbreviations: BO: *Buddleja officinalis*; ESCC: Esophageal squamous cell carcinoma; GO: Gene ontology; KEGG: Kyoto encyclopedia of genes and genomes; PPI: Protein-protein interaction.

2.7. Gene Ontology (GO) and Kyoto Encyclopedia of Genes and Genomes (KEGG) pathway enrichment analysis

Initially, the potential target genes were converted to Entrez IDs using the R package ("org.Hs.eg.db, version = 3.8"). Subsequently, GO biological functions and KEGG pathway analysis were visualized by the R packages ("DOSE," "clusterProfiler," and "Pathview").

2.8. Docking for dominant ingredients

We investigated the docking of selected active components identified from the BO-ESCC PPI network onto the receptors of threonine protein kinase (AKT1) using AutoDock software. The names, molecular weights, and three-dimensional structures of BO ingredients were initially acquired from PubChem (https://pubchem.ncbi.nlm.nih.gov/). Next, the three-dimensional structure of ingredients was derived from the RCSB protein data bank (http://www.rcsb.org/). Finally, the AutoDock software was utilized to facilitate the preparation of ligands and targets essential for docking. Afterward, for the target proteins, the water molecules of the crystal structures were removed, hydrogenation was performed, amino acids were modified, energy was optimized, and the force field parameters were adjusted to satisfy the low-energy conformations of the ligand structures. Subsequently, the AKT1 and key active components were molecularly docked, with the affinity (kcal/mol) value representing the binding ability between targets and ligands. Finally, the docking results were observed and analyzed using Discovery Studio software.

3. Results

3.1. Establishment of the BO active ingredients database

Six dominant ingredients of BO were retrieved from the TCMSP and HERB databases, including acacetin, linarin, luteolin, butyrospermyl acetate, procyanidin B1, and neobyakangelicol (Table 1).

3.2. Potential targets of BO for inhibiting ESCC and visualization of PPI network

By searching the GeneCard and DisGeNET databases, a total of 3640 ESCC target genes were generated after excluding duplicates. The results of the Venny 2.1 online tool showed that 24 shared BO-ESCC targets were obtained (Figure 2A and Table 2). To further clarify the relationships among these overlapping target genes, PPI network analysis was performed, indicating that these target gene networks had 24 nodes and 73 edges, as shown in Figure 2B. The PPI network files were subsequently visualized by Cytoscape 3.9.1. NetworkAnalyzer utilized the "degrees" to highlight the importance of nodes, and the top five nodes with high degrees were considered core targets, *that is*, serum albumin (ALB), AKT1, insulin-like growth factor 1 receptor (IGF1), estrogen receptor (ESR1), and fibroblast growth factor receptor 1 (FGFR1) (Figure 2C and Table 3).

3.3. GO and KEGG analyses

To further examine whether the biological functions of the candidates are associated with ESCC, the terms subdivided in three distinct ontologies, *that is*, biological process (BP), cellular component (CC), and molecular function (MF), were enriched in GO and KEGG analyses by R programming language. In the BP group (Figure 3A), the results suggested that BO might regulate ESCC-related BPs, such as organ growth, gland development, and reproductive structure development. Subsequently, the majority of the GO terms are associated with secretory granule lumen, cytoplasmic vesicle lumen, and vesicle lumen (Figure 3B). In the BP group (Figure 3C), the GO terms mainly included transmembrane receptor protein kinase activity, glycosaminoglycan binding, and nuclear receptor activity. In addition, 41 signaling pathways were identified through KEGG pathway analysis as significantly enriched ($P < 0.05$). Figure 4 displays a bar plot showcasing the top 20 important pathways. The signaling pathways that are closely related to ESCC include MAPK signaling pathway, adhesion junction pathway, and gastric cancer pathway. The gastric cancer pathway is closely associated with the MAPK signaling pathway and is involved in processes such as activation of oncogenes, inactivation of tumor suppressor genes, dysregulation of cell cycle control, and impairment of apoptosis in gastric cancer. In addition, MAPK signaling pathway, the most relevant signaling pathway according to counting numbers, is illustrated in Figure 5. The network revealed that BO is associated with the treatment of ESCC through multiple targets and multiple pathways. Figure 6 shows a compound-target-pathway network centered on the inhibition of ESCC.

3.4. Docking of BO dominant ingredients to AKT1

The six dominant ingredients of BO can bind to AKT1 receptor proteins to varying degrees as ligands, and the lower vina scores indicate stronger and more stable binding capacity between ligands and receptors (Table 4). The vina scores of linarin, procyanidin B1, acacetin,

Table 1. Main active ingredients in BO

No.	ID	Ingredient	Molecular weight	Oral bioavailability (%)	Drug likeness	Chemical structure
1	MOL001689	Acacetin	284.26	34.97	0.24	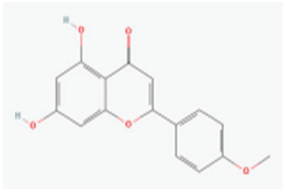
2	MOL001790	Linarin	592.5	39.84	0.71	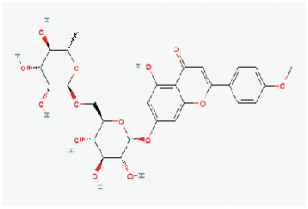
3	MOL000006	Luteolin	286.24	36.16	0.25	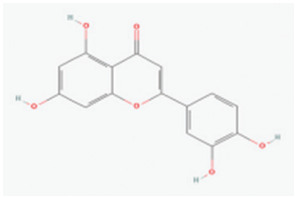
4	MOL006673	Butyrospermyl acetate	468.84	46.04	0.83	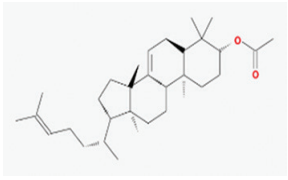
5	MOL000004	Procyanidin B1	578.5	67.87	0.66	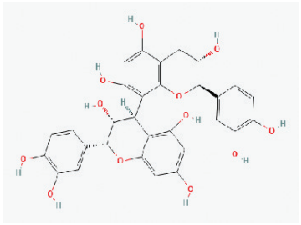
6	MOL005789	Neobyakangelicol	316.33	36.18	0.31	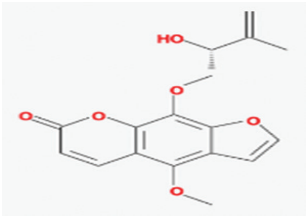

Abbreviation: BO: *Buddleja officinalis*.

luteolin, butyrospermyl acetate, and neobyakangelicol increased sequentially, with linarin expressing a strong affinity with AKT1 and engaging in the most stable binding with AKT1. It is speculated that linarin may be the most suitable natural component of AKT1 in BO. Figure 7 shows three-dimensional and two-dimensional maps of the binding of the above six components to AKT1.

4. Discussion

The mechanism of TCM treatment is complex, involving many components and targets. It is a challenge in

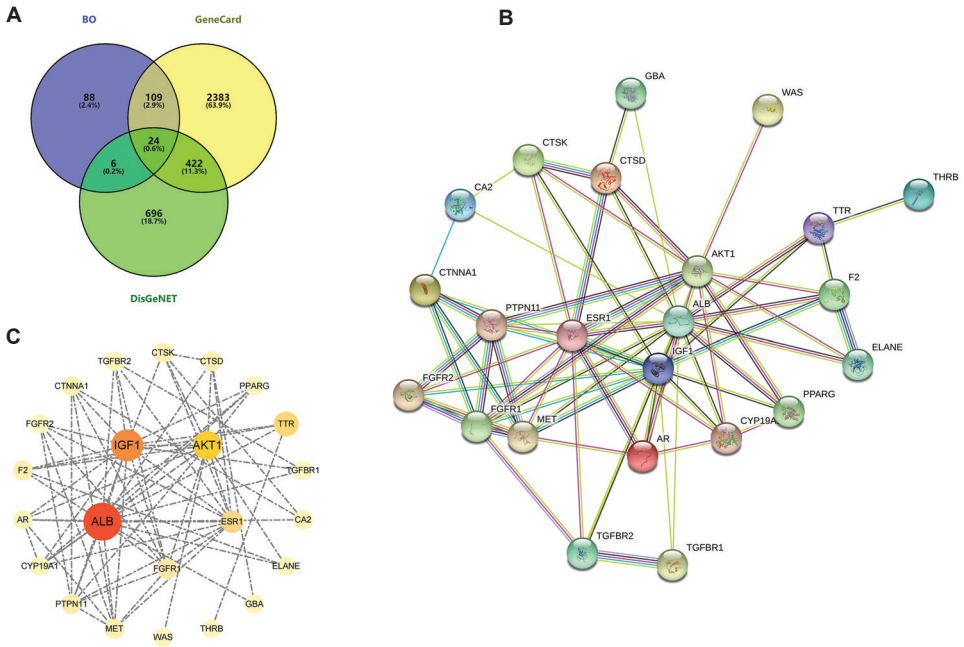

Figure 2. Putative target genes of BO for inhibiting ESCC, and PPI network. (A) The putative target genes of BO for inhibiting ESCC are shown in a Venn diagram. (B) The associations among 24 shared target genes are illustrated by a PPI network. (C) The core targets in the PPI network are visualized using Cytoscape 3.9.1 software. The node size from large to small represents the degree value from large to small. The width of the line between two nodes indicates the strength of their interaction, and the darker color indicates higher significance.
Abbreviations: BO: *Buddleja officinalis*; ESCC: Esophageal squamous cell carcinoma; PPI: Protein–protein interaction.

exploring its mechanism in treating diseases, especially when the pathogenesis remains to be clarified. Network pharmacology, an approach unifying the advantages of systematic network analysis and pharmacology, enables the comprehensive investigation for targets and the underlying pathways of drugs at the molecular level, and enhances our insights into drug mechanisms.[17,18]

According to the component-target network established in this study, six ingredients in BO were found to have multiple targets in the network, suggesting their potential therapeutic effects in the treatment of ESCC, which merit further investigation. The cancer-inhibiting effect of luteolin has been vastly reported in the literature. According to a previously published review,[19] the suppression effects of luteolin on cancer progression are mediated by inhibiting tumor cell proliferation, promoting cell cycle arrest, safeguarding cells against oncogenic stimuli, and triggering apoptosis through diverse signaling pathways. Furthermore, luteolin possesses the capability to reverse epithelial-mesenchymal transition by upregulating the expression of the epithelial biomarker E-cadherin and downregulating the mesenchymal biomarkers N-cadherin, Snail, and vimentin. Moreover, the anticancer potential of acacetin stems from multiple potential mechanisms, *for example*, inducing cytochrome c release and formation of reactive oxygen species by targeting mitochondria, inducing apoptosis, reducing matrix metalloproteinases (MMPs), inhibiting invasion and migration, and promoting cell cycle arrest and autophagy.[20] Linarin can induce apoptosis,[20] inhibit epithelial cell proliferation[21] and inhibit NF-κB activation in cancer cells to downregulate MMP-9 expression.[22] In addition, linarin can reduce phagocytosis, inhibit pro-inflammatory cytokine production, and downregulate activation marker expression in macrophages.[23] Procyanidin B1 and neobyakangelicol have rarely been covered in cancer research. Procyanidin B1 has antioxidant properties and can suppress fat accumulation[24,25] and even inhibit the migration and proliferation of liver cancer cells.[26] As one of the first furocoumarins isolated from *Angelicae dahuricae,*[27] neobyakangelicol may be associated with antioxidant activity. Despite the first investigation on this compound initiated in 1999, further explorations on its effects on cancer have been in slow progress.

Table 2. Potential targets for ESCC inhibition by BO

No.	Target	Gene symbol	Entrez ID
1	Serum albumin	*ALB*	213
2	Carbonic anhydrase 2	*CA2*	760
3	Thyroid hormone receptor beta	*THRB*	7068
4	Transthyretin	*TTR*	7276
5	Estrogen receptor	*ESR1*	2099
6	Androgen receptor	*AR*	367
7	Peroxisome proliferator-activated receptor gamma	*PPARG*	5468
8	Cytochrome P450 19A1	*CYP19A1*	1588
9	Prothrombin	*F2*	2147
10	Wiskott-Aldrich syndrome protein	*WAS*	7454
11	TGF-beta receptor type-1	*TGFBR1*	7046
12	Tyrosine-protein phosphatase non-receptor type 11	*PTPN11*	5781
13	Hepatocyte growth factor receptor	*MET*	4233
14	Insulin-like growth factor 1 receptor	*IGF1*	3479
15	Cathepsin D	*CTSD*	1509
16	Glucosylceramidase	*GBA*	2629
17	TGF-beta receptor type-2	*TGFBR2*	7048
18	Calmodulin	*CTSK*	1513
19	Threonine-protein kinase	*AKT1*	207
20	Basic fibroblast growth factor receptor 1	*FGFR1*	2260
21	Catenin alpha-1	*CTNNA1*	1495
22	Fibroblast growth factor receptor 2	*FGFR2*	2263
23	Leukocyte elastase	*ELANE*	1991

Abbreviations: BO: *Buddleja officinalis*; ESCC: Esophageal squamous cell carcinoma.

Table 3. Top five core targets with high degree

No.	Target	Gene symbol	Degree
1	Serum albumin	ALB	17
2	Insulin-like growth factor 1 receptor	IGF1	16
3	Threonine-protein kinase	AKT1	13
4	Estrogen receptor	ESR1	12
5	Basic fibroblast growth factor receptor 1	FGFR1	9

Among the 23 PPI networks of BO-ESCC interaction, the top five based on degree were ALB, IGF1, AKT1, ESR1, and FGFR1. These proteins were considered as core proteins and could potentially contribute significantly to BO's therapeutic effect on ESCC. A low ALB level is a predictor of poor survival outcomes in patients with ESCC,[28] and the status of ESR1s in ESCC is closely associated with poor prognosis and may be involved in regulating the proliferation of cancer cells.[29] Clinically, high FGFR1 amplification serves as an independent adverse prognostic factor solely for stage I–II ESCC patients,[30] and fibroblast growth factor-2-mediated FGFR1 signaling is involved in the migration and survival of ESCC cells *in vitro*.[31] The IGF1 and its receptor (insulin-like growth factor-1 receptor, IGF-1R) promote cell proliferation and inhibit apoptosis.[32] The IGF-1R can activate MAPK and PI3K/AKT signaling pathways and play an essential role in various cancer types.[33-36] The AKT is differentially expressed in various cancers and can be involved in various BPs, including cell proliferation, apoptosis, transcription, migration, invasion, and metastasis.[37-40]

To predict the underlying mechanism of therapeutic effects of BO on ESCC, we performed GO enrichment on 23 putative targets. The top 10 targets in BP was mainly enriched in organ growth, gland development, and reproductive structure development, indicating that associated targets were ESR1, AR, TGFBR1, *etc.* In

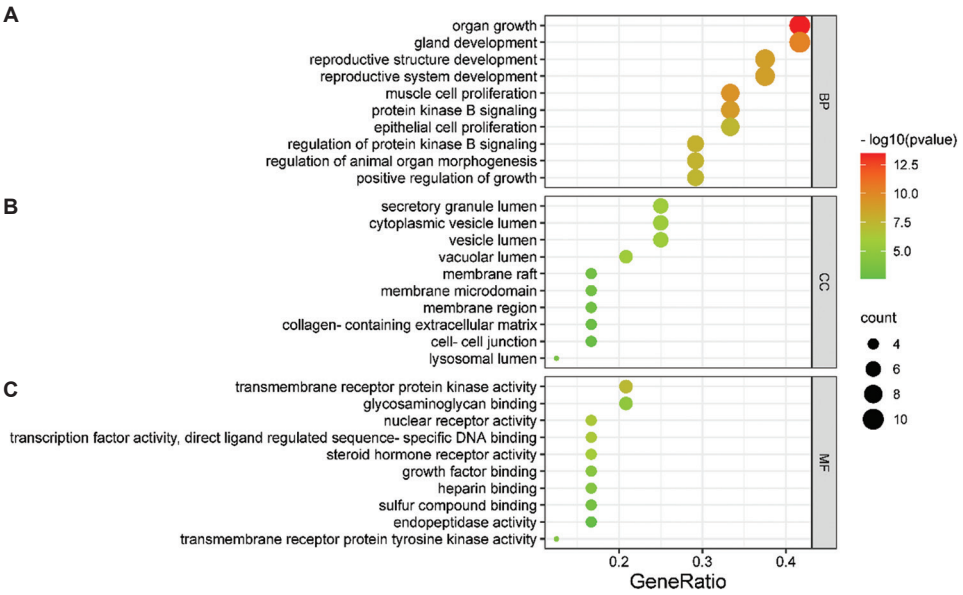

Figure 3. GO enrichment analysis of treating ESCC targets. GO analysis (including BP, CC, and MF) was visualized using the R packages "DOSE". (A) BP analysis of treating ESCC targets. (B) CC analysis of treating ESCC targets. (C) MF analysis of treating ESCC targets. Abbreviations: ESCC: Esophageal squamous cell carcinoma; GO: Gene Ontology; BP: Biological process; CC: Cellular component; MF: Molecular function.

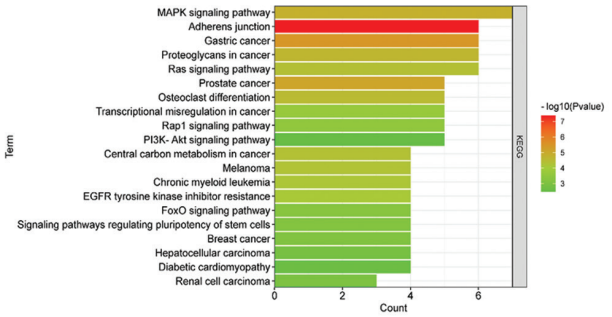

Figure 4. KEGG enrichment analysis for the signaling pathways. KEGG pathway enrichment was analyzed using the R packages "clusterProfiler".
Abbreviation: KEGG: Kyoto Encyclopedia of genes and genomes.

addition, the target enrichment of CC unveiled secretory granule lumen, cytoplasmic vesicle lumen, and vesicle lumen as the potential pathways, and revealed ALB, TTR, and IGF1 as the relevant targets. The target enrichment of MF yielded transmembrane receptor protein kinase activity and glycosaminoglycan binding, and nuclear receptor activity, and the involved targets mainly encompass TGFBR2, FGFR1, and FGFR2. Overall, these findings illuminate the complexity of ESCC pathology. To further examine the underlying mechanism by which BO acts on ESCC, we performed KEGG analysis on the targets and found that BO inhibited ESCC-related pathways, such as MAPK signaling pathway, RAS signaling pathway, and Rap1 signaling pathway.

Here, we selected the most pertinent pathway to discuss the mechanism of BO in treating ESCC. The MAPK signaling pathway is a widely prevalent cellular signaling pathway in living organisms that plays a crucial role in regulating cellular processes, *that is*, cell growth, differentiation, migration, and apoptosis. It also plays a vital role in various biological systems including neural signal transmission, inflammatory responses, and tumor development. Specifically, the MAPK signaling pathway is involved in regulating the expressions of multiple ESCC-related genes[41] and includes several regulatory components, such as extracellular signal-related kinases (ERK1/2), Jun N-terminal kinases (JNK1/2/3), p38-MAPK, and ERK5.[42] Therefore, MAPK signaling pathway is closely related to the malignant behavior of tumors and plays an indispensable role in the occurrence and development of various cancers.[43] For example, BO can inhibit high glucose-induced atherosclerosis by inhibiting p38, JNK, NF-κB and MMP signaling pathways in human aortic smooth muscle cells.[44] In the study by Oh *et al.*,[45] BO inhibited the synthesis and release of NO, iNOS, and pro-inflammatory factors by blocking ERK1/2 and NF-κB in BV-2 microglias. These findings shed light on an underlying mechanism for the anticancer effects of BO.

For the sake of further exploring the potential mechanism of BO in inhibiting ESCC, we carried out a molecular docking study on AKT1, a closely related target of ESCC, based on KEGG screening and using

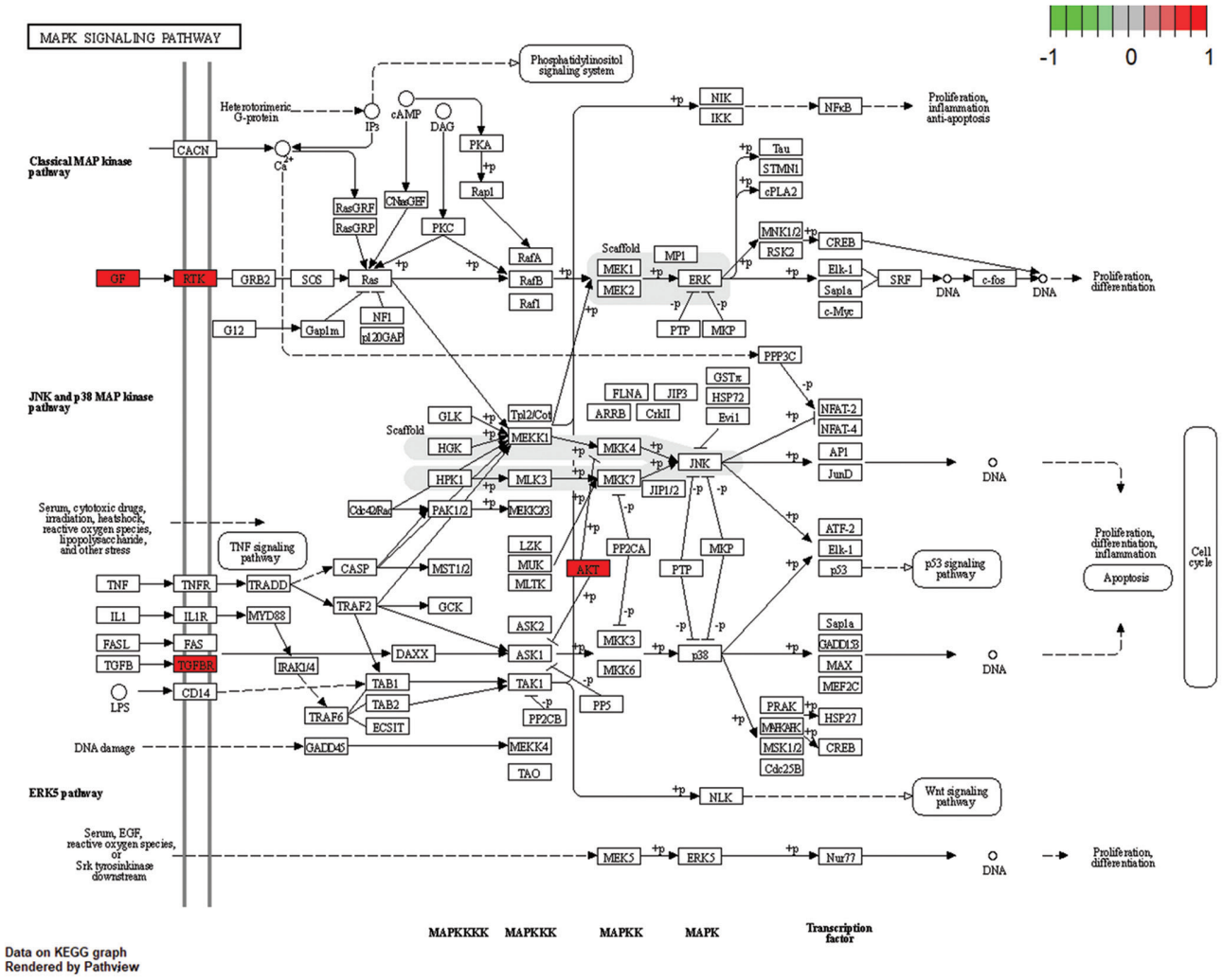

Figure 5. MAPK signaling pathway underpinning the suppression of ESCC by BO. The KEGG pathway enrichment was analyzed using the R packages "Pathview". The arrows represent the direction of regulation in which upstream genes regulate downstream genes. Targets dyed red indicate targets in the signaling network that are regulated by BO.
Abbreviations: BO: *Buddleja officinalis*; ESCC: Esophageal squamous cell carcinoma; KEGG: Kyoto encyclopedia of genes and genomes.

Table 4. Results of docking six active ingredients in BO to AKT1

No.	ID	Ingredient	Vina scores (kcal/mol)	Center*			Size#		
				x	y	z	x	y	z
1	MOL001689	Acacetin	−6.3	22.4029	15.3988	9.9840	42.8067	39.7904	49.2565
2	MOL001790	Linarin	−8.0	16.7471	15.0165	9.1125	53.3138	42.1770	50.9995
3	MOL000006	Luteolin	−6.2	16.7471	15.0165	9.1125	53.3138	42.1770	50.9995
4	MOL006673	Butyrospermyl acetate	−6.2	16.7002	15.8043	9.9840	51.0469	40.6014	49.2565
5	MOL000004	Procyanidin B1	−7.2	16.7471	15.0165	9.1125	53.3138	42.1770	50.9995
6	MOL005789	Neobyakangelicol	−6.0	16.5953	15.8043	9.1125	53.0102	40.0614	50.9995

*The center coordinates of the docking pocket between the ingredients and the target AKT1. #The size of the ingredients of the pocket with AKT1 in the x, y and z directions.
Abbreviation: BO: *Buddleja officinalis*; AKT1: Threonine protein kinase.

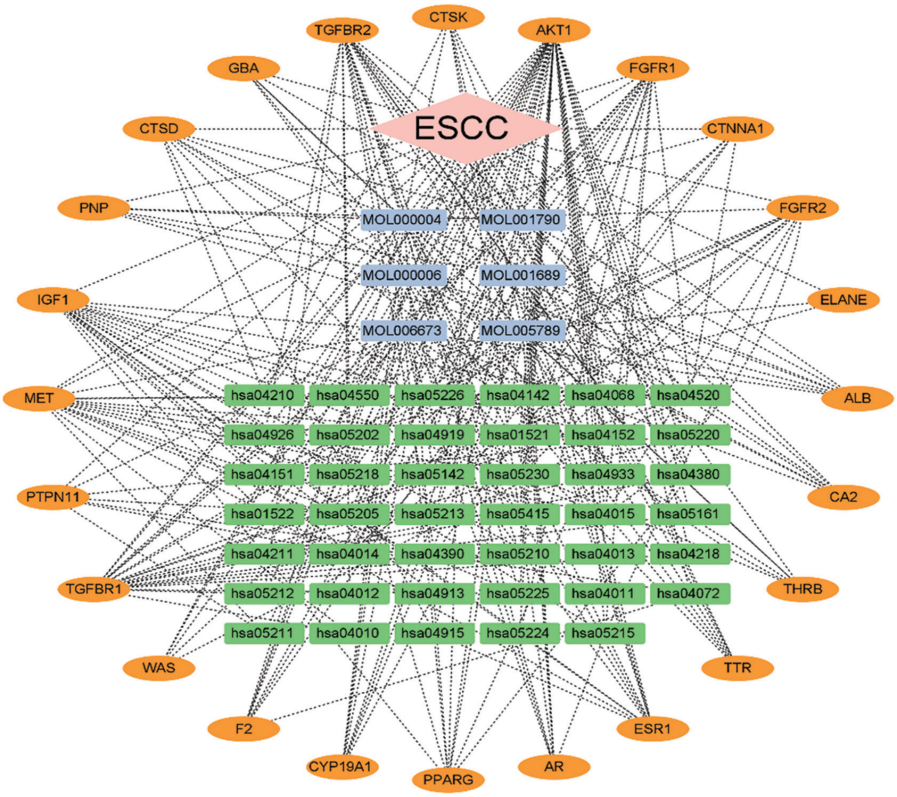

Figure 6. Compound-target-pathway network underlying the inhibition of ESCC. The map of compound-target-pathway was visualized using Cytoscape 3.9.1 software.
Abbreviation: ESCC: Esophageal squamous cell carcinoma.

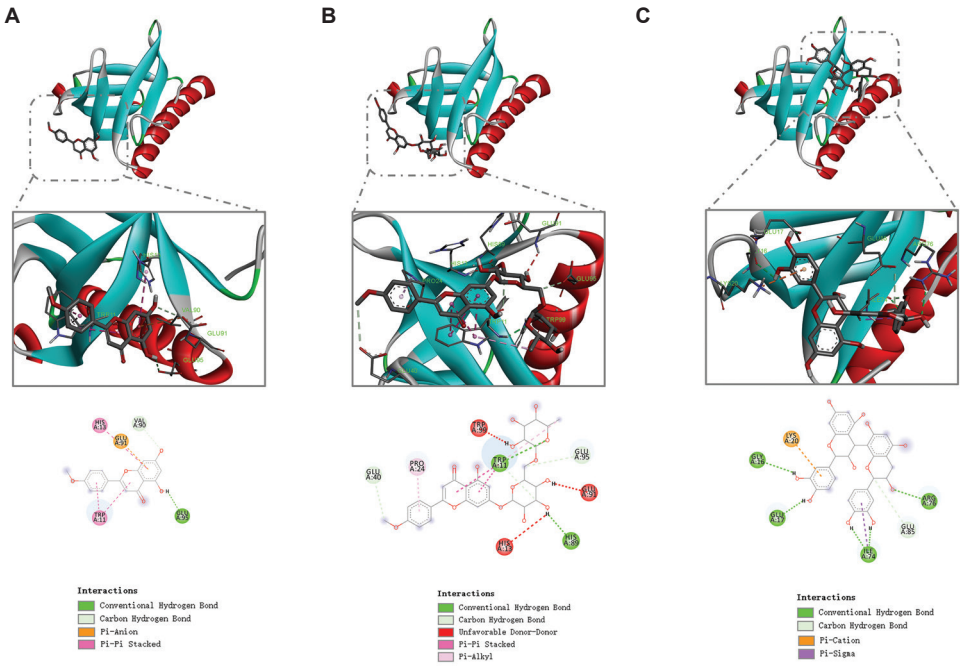

Figure 7. Three-dimensional and two-dimensional maps of the binding of acacetin, linarin, and procyanidin B1 to AKT1. AutoDock software was used to dock (A) acacetin, (B) linarin, and (C) procyanidin B1 to AKT1.
Abbreviation: AKT1: Threonine protein kinase.

key components acacetin, linarin, and procyanidin B1 as ligands. The results showed that linarin had a good binding ability to AKT1, and its interaction with AKT1 was more stable than that of acacetin or procyanidin B1. In the current study, we used a network pharmacology approach to systematically uncover the inhibitory effect of a TCM medicine on ESCC. However, several noteworthy limitations in this study are worth highlighting. For example, we did not validate target genes experimentally to eliminate irrelevant targets. Moreover, experimental validation analysis of the mechanisms was not integrated into this study; therefore, further basic or clinical studies are required to validate the molecular mechanisms by which BO inhibits ESCC.

5. Conclusion

Acacetin, linarin, luteolin, butyrospermyl acetate, procyanidin B1, and neobyakangelicol are potential active components of BO. In addition, AKT1 is a potential therapeutic target of BO, and its effects on ESCC may be mediated by MAPK signaling pathway.

Acknowledgments

None.

Funding

This research was financially supported by the Henan Province Medical Science and Technology Research Program Joint Construction Project (NO. LHGJ20210696), and General Program of Natural Science Foundation of Henan Province (NO. 212300410393).

Conflict of interest

The authors declare no conflicts of interest.

Author contributions

Conceptualization: Zhen-Zhen Yang, Na Gao, Yin-Sen Song

Formal analysis: Zhen-Zhen Yang, Na Gao

Investigation: Zhen-Zhen Yang, Na Gao, Xiao-Lin Zhang

Writing – original draft: Zhen-Zhen Yang

Writing – review & editing: Yin-Sen Song, Xiao-Lin Zhang

Data visualization: Cheng Chang, Hao-Zhe Zhang

Data analysis: Tian-Li Fan

All authors have read and agreed to the published version of the manuscript.

Ethics approval and consent to participate

Not applicable.

Consent for publication

Not applicable.

Availability of data

Data used in this work are available from the corresponding author on reasonable request.

References

1. Short MW, Burgers KG, Fry VT. Esophageal cancer. *Am Fam Physician*. 2017;95(1):22-28.
2. Domper Arnal MJ, Ferrandez Arenas A, Lanas Arbeloa A. Esophageal cancer: Risk factors, screening and endoscopic treatment in Western and Eastern countries. *World J Gastroenterol*. 2015;21(26):7933-7943.

   doi: 10.3748/wjg.v21.i26.7933
3. Huang FL, Yu SJ. Esophageal cancer: Risk factors, genetic association, and treatment. *Asian J Surg*. 2018;41(3):210-215.

   doi: 10.1016/j.asjsur.2016.10.005
4. Pan Y, Sun Z, Wang W, *et al*. Automatic detection of squamous cell carcinoma metastasis in esophageal lymph nodes using semantic segmentation. *Clin Transl Med*. 2020;10(3):e129.

   doi: 10.1002/ctm2.129
5. Hou X, Wen J, Ren Z, Zhang G. Non-coding RNAs: New biomarkers and therapeutic targets for esophageal cancer. *Oncotarget*. 2017;8(26):43571-43578.

   doi: 10.18632/oncotarget.16721
6. Zhong R, Chen Z, Mo T, Li Z, Zhang P. Potential role of circPVT1 as a proliferative factor and treatment target in esophageal carcinoma. *Cancer Cell Int*. 2019;19:267.

   doi: 10.1186/s12935-019-0985-9
7. Cao S, Chen G, Yan L, Li L, Huang X. Contribution of dysregulated circRNA_100876 to proliferation and metastasis of esophageal squamous cell carcinoma. *Onco Targets Ther*. 2018;11:7385-7394.

   doi: 10.2147/OTT.S177524
8. Houghton PJ, Mensah AY, Iessa N, Hong LY. Terpenoids in *Buddleja*: relevance to chemosystematics, chemical ecology and biological activity. *Phytochemistry*. 2003;64(2):385-393.

   doi: 10.1016/s0031-9422(03)00264-4
9. Lee YJ, Kang DG, Kim JS, Lee HS. *Buddleja officinalis* inhibits high glucose-induced matrix metalloproteinase activity in human umbilical vein endothelial cells. *Phytother Res*. 2008;22(12):1655-1659.

   doi: 10.1002/ptr.2547
10. Tai BH, Jung BY, Cuong NM, *et al*. Total peroxynitrite scavenging capacity of phenylethanoid and flavonoid

glycosides from the flowers of *Buddleja officinalis*. *Biol Pharm Bull*. 2009;32(12):1952-1956.

doi: 10.1248/bpb.32.1952

11. Huang FB, Liang N, Hussain N, *et al*. Anti-inflammatory and antioxidant activities of chemical constituents from the flower buds of *Buddleja officinalis*. *Nat Prod Res*. 2021;36:3031-3042.

doi: 10.1080/14786419.2021.1952577

12. Zhang J, Liang R, Wang L, Yang B. Effects and mechanisms of Danshen-Shanzha herb-pair for atherosclerosis treatment using network pharmacology and experimental pharmacology. *J Ethnopharmacol*. 2019;229:104-114.

doi: 10.1016/j.jep.2018.10.004

13. Chen L, Cao Y, Zhang H, *et al*. Network pharmacology-based strategy for predicting active ingredients and potential targets of Yangxinshi tablet for treating heart failure. *J Ethnopharmacol*. 2018;219:359-368.

doi: 10.1016/j.jep.2017.12.011

14. Xu J, Wang F, Guo J, *et al*. Pharmacological mechanisms underlying the neuroprotective effects of *Alpinia oxyphylla* Miq. on Alzheimer's disease. *Int J Mol Sci*. 2020;21(6):2071.

doi: 10.3390/ijms21062071

15. Ding Z, Zhong R, Yang Y, *et al*. Systems pharmacology reveals the mechanism of activity of Ge-Gen-Qin-Lian decoction against LPS-induced acute lung injury: A novel strategy for exploring active components and effective mechanism of TCM formulae. *Pharmacol Res*. 2020;156:104759.

doi: 10.1016/j.phrs.2020.104759

16. Sun PY, Wang AS, Zhang ZF, Zhang YL, Zheng X. Network pharmacology-based strategy to investigate the active ingredients and molecular mechanisms of *Scutellaria barbata* D. Don against radiation pneumonitis. *Medicine* (*Baltimore*). 2021;100(47):e27957.

doi: 10.1097/MD.0000000000027957

17. Tian Y, Tang L. Using network pharmacology approaches to identify treatment mechanisms for codonopsis in esophageal cancer. *Int J Clin Exp Pathol*. 2022;15(2):46-55.

18. Cheung MK, Yue GG, Gomes AJ, *et al*. Network pharmacology reveals potential functional components and underlying molecular mechanisms of *Andrographis paniculata* in esophageal cancer treatment. *Phytother Res*. 2022;36(4):1748-1760.

doi: 10.1002/ptr.7411

19. Imran M, Rauf A, Abu-Izneid T, *et al*. Luteolin, a flavonoid, as an anticancer agent: A review. *Biomed Pharmacother*. 2019;112:108612.

doi: 10.1016/j.biopha.2019.108612

20. Singh S, Gupta P, Meena A, Luqman S. Acacetin, a flavone with diverse therapeutic potential in cancer, inflammation, infections and other metabolic disorders. *Food Chem Toxicol*. 2020;145:111708.

doi: 10.1016/j.fct.2020.111708

21. Seo DW, Cho YR, Kim W, Eom SH. Phytochemical linarin enriched in the flower of *Chrysanthemum indicum* inhibits proliferation of A549 human alveolar basal epithelial cells through suppression of the Akt-dependent signaling pathway. *J Med Food*. 2013;16(12):1086-1094.

doi: 10.1089/jmf.2012.2674

22. Jung CH, Han AR, Chung HJ, Ha IH, Um HD. Linarin inhibits radiation-induced cancer invasion by downregulating MMP-9 expression via the suppression of NF-κB activation in human non-small-cell lung cancer A549. *Nat Prod Res*. 2019;33(24):3582-3586.

doi: 10.1080/14786419.2018.1484460

23. Kim B, Lee JH, Seo MJ, Eom SH, Kim W. Linarin down-regulates phagocytosis, pro-inflammatory cytokine production, and activation marker expression in RAW264.7 macrophages. *Food Sci Biotechnol*. 2016;25(5):1437-1442.

doi: 10.1007/s10068-016-0223-3

24. Shimada T, Tokuhara D, Tsubata M, *et al*. Flavangenol (pine bark extract) and its major component procyanidin B1 enhance fatty acid oxidation in fat-loaded models. *Eur J Pharmacol*. 2012;677(1-3):147-153.

doi: 10.1016/j.ejphar.2011.12.034

25. Li T, Li Q, Wu W, *et al*. Lotus seed skin proanthocyanidin extract exhibits potent antioxidant property via activation of the Nrf2-ARE pathway. *Acta Biochim Biophys Sin* (*Shanghai*). 2019;51(1):31-40.

doi: 10.1093/abbs/gmy148

26. Na W, Ma B, Shi S, *et al*. Procyanidin B1, a novel and specific inhibitor of Kv10.1 channel, suppresses the evolution of hepatoma. *Biochem Pharmacol*. 2020;178:114089.

doi: 10.1016/j.bcp.2020.114089

27. Piao XL, Park IH, Baek SH, Kim HY, Park MK, Park JH. Antioxidative activity of furanocoumarins isolated from *Angelicae dahuricae*. *J Ethnopharmacol*. 2004;93(2-3):243-246.

doi: 10.1016/j.jep.2004.03.054

28. Wu LL, Liu X, Huang W, *et al*. Preoperative squamous cell carcinoma antigen and albumin serum levels predict the survival of patients with stage T1-3N0M0 esophageal squamous cell carcinoma: A retrospective observational study. *J Cardiothorac Surg*. 2020;15(1):115.

doi: 10.1186/s13019-020-01163-6

29. Zuguchi M, Miki Y, Onodera Y, *et al*. Estrogen receptor α and β in esophageal squamous cell carcinoma. *Cancer Sci*. 2012;103(7):1348-1355.

doi: 10.1111/j.1349-7006.2012.02288.x

30. Song Q, Liu Y, Jiang D, *et al*. High amplification of FGFR1 gene is a delayed poor prognostic factor in early stage ESCC patients. *Oncotarget*. 2017;8(43):74539-74553.

doi: 10.18632/oncotarget.20215

31. Takase N, Koma Y, Urakawa N, *et al*. NCAM-and FGF-2-mediated FGFR1 signaling in the tumor microenvironment of esophageal cancer regulates the survival and migration of tumor-associated macrophages and cancer cells. *Cancer Lett*. 2016;380(1):47-58.

doi: 10.1016/j.canlet.2016.06.009

32. Frater J, Lie D, Bartlett P, McGrath JJ. Insulin-like growth factor 1 (IGF-1) as a marker of cognitive decline in normal ageing: A review. *Ageing Res Rev*. 2018;42:14-27.

doi: 10.1016/j.arr.2017.12.002

33. Zhou Y, Li S, Li J, Wang D, Li Q. Effect of microRNA-135a on cell proliferation, migration, invasion, apoptosis and tumor angiogenesis through the IGF-1/PI3K/Akt signaling pathway in non-small cell lung cancer. *Cell Physiol Biochem*. 2017;42(4):1431-1446.

doi: 10.1159/000479207

34. Choucair A, Pham TH, Omarjee S, *et al*. The arginine methyltransferase PRMT1 regulates IGF-1 signaling in breast cancer. *Oncogene*. 2019;38(21):4015-4027.

doi: 10.1038/s41388-019-0694-9

35. Chu PC, Lin PC, Wu HY, *et al*. Mutant KRAS promotes liver metastasis of colorectal cancer, in part, by upregulating the MEK-Sp1-DNMT1-miR-137-YB-1-IGF-IR signaling pathway. *Oncogene*. 2018;37(25):3440-3455.

doi: 10.1038/s41388-018-0222-3

36. Wang G, Lu M, Yao Y, Wang J, Li J. Esculetin exerts antitumor effect on human gastric cancer cells through IGF-1/PI3K/Akt signaling pathway. *Eur J Pharmacol*. 2017;814:207-215.

doi: 10.1016/j.ejphar.2017.08.025

37. Fresno Vara JA, Casado E, De Castro J, Cejas P, Belda-Iniesta C, Gonzalez-Baron M. PI3K/Akt signalling pathway and cancer. *Cancer Treat Rev*. 2004;30(2):193-204.

doi: 10.1016/j.ctrv.2003.07.007

38. Pal I, Mandal M. PI3K and Akt as molecular targets for cancer therapy: Current clinical outcomes. *Acta Pharmacol Sin*. 2012;33(12):1441-1458.

doi: 10.1038/aps.2012.72

39. Song M, Liu X, Liu K, *et al*. Targeting AKT with oridonin inhibits growth of esophageal squamous cell carcinoma *in vitro* and patient-derived xenografts *in vivo*. *Mol Cancer Ther*. 2018;17(7):1540-1553.

doi: 10.1158/1535-7163.MCT-17-0823

40. Li B, Xu WW, Lam AK, *et al*. Significance of PI3K/AKT signaling pathway in metastasis of esophageal squamous cell carcinoma and its potential as a target for anti-metastasis therapy. *Oncotarget*. 2017;8(24):38755-38766.

doi: 10.18632/oncotarget.16333

41. Li J, Li Z, Xu Y, Huang C, Shan B. METTL3 facilitates tumor progression by COL12A1/MAPK signaling pathway in esophageal squamous cell carcinoma. *J Cancer*. 2022;13(6):1972-1984.

doi: 10.7150/jca.66830

42. Chen S, Yang W, Zhang X, *et al*. Melamine induces reproductive dysfunction via down-regulated the phosphorylation of p38 and downstream transcription factors Max and Sap1a in mice testes. *Sci Total Environ*. 2021;770:144727.

doi: 10.1016/j.scitotenv.2020.144727

43. Shi DM, Li LX, Bian XY, *et al*. miR-296-5p suppresses EMT of hepatocellular carcinoma via attenuating NRG1/ERBB2/ERBB3 signaling. *J Exp Clin Cancer Res*. 2018;37(1):294.

doi: 10.1186/s13046-018-0957-2

44. Lee YJ, Kim JS, Kang DG, Lee HS. *Buddleja officinalis* suppresses high glucose-induced vascular smooth muscle cell proliferation: Role of mitogen-activated protein kinases, nuclear factor-kappaB and matrix metalloproteinases. *Exp Biol Med* (*Maywood*). 2010;235(2):247-255.

doi: 10.1258/ebm.2009.009222

45. Oh WJ, Jung U, Eom HS, *et al*. Inhibition of lipopolysaccharide-induced proinflammatory responses by *Buddleja officinalis* extract in BV-2 microglial cells via negative regulation of NF-kB and ERK1/2 signaling. *Molecules*. 2013;18(8):9195-9206.

doi: 10.3390/molecules18089195

ACCSCIENCE PUBLISHING

Tumor Discovery

ORIGINAL RESEARCH ARTICLE

Bioinformatics analysis of missense mutations in CXCR1 implicates altered protein stability and function

Shah Kamal[1†*], Amanullah Amanullah[1†], Qingqing Wang[1], Najeeb Ullah[1], Gohar Mushtaq[2*], Muhammad Nasir Iqbal[3], and Mohammad Amjad Kamal[4,5,6,7,8]

[1]Jiangsu Key Laboratory for Biodiversity and Biotechnology, College of Life Sciences, Nanjing Normal University, Nanjing, China

[2]Department of Biochemistry, Center for Scientific Research, Faculty of Medicine, Idlib University, Idlib, Syria

[3]Department of Bioinformatics, Faculty of Biological and Chemical Sciences, The Islamia University of Bahawalpur, Pakistan

[4]Joint Laboratory of Artificial Intelligence for Critical Care Medicine, Department of Critical Care Medicine and Institutes for Systems Genetics, West China School of Nursing, Frontiers Science Center for Disease-related Molecular Network, West China Hospital, Sichuan University, Chengdu, China

[5]King Fahd Medical Research Center, King Abdulaziz University, Jeddah, Saudi Arabia

[6]Department of Pharmacy, Faculty of Health and Life Sciences, Daffodil International University, Birulia, Savar, Dhaka, Bangladesh

[7]Centre for Global Health Research, Saveetha Medical College and Hospital, Saveetha Institute of Medical and Technical Sciences, Chennai, Tamil Nadu, India

[8]Enzymoics, 7 Peterlee Place, Hebersham, NSW, Novel Global Community Educational Foundation, Australia

[†]*These authors contributed equally to this work.*

***Corresponding authors:**
Shah Kamal
(31183001@njnu.edu.cn)
Gohar Mushtaq
(dr.goher_mushtaq@idlib-university.com)

Citation: Kamal S, Amanullah A, Wang Q, *et al*. Bioinformatics analysis of missense mutations in CXCR1 implicates altered protein stability and function. *Tumor Discov*. 2024;3(1):2512. https://doi.org/10.36922/td.2512

Received: December 22, 2023
Accepted: February 21, 2024
Published Online: March 21, 2024

Abstract

Human CXCR1 is a G-protein α subunit i (Gαi)-coupled receptor (GPCR) that plays an important role in promoting leukocyte recruitment and activation in inflammatory regions; thus, its genetic contribution to human disorders warrants further investigation. In this study, we investigated whether oncogenic missense mutations in CXCR1 would affect its activity and hinder its ability to interact with its ligand. This study utilized a bioinformatics approach and employed precise and thorough computational methods to gain insights into the molecular characteristics of mutated CXCR1 that are responsible for causing diseases. I-TASSER was used to construct a mutant model with the required mutations. Schrödinger's Desmond software was used to evaluate how mutations affect the stability and function of proteins. In this study, 299 CXCR1 missense mutations were examined; 53 of these were reported to be disease-causing, five of which were directly associated with cancer. The impact of the three cancer-causing mutations (N57D, R135C, and P302S) on protein stability and function was subsequently examined through computational analysis. Positions N57, R135, and P302 were determined to be highly conserved, and substitutions with aspartic acid (D), cysteine (C), and serine (S), respectively, could impair CXCR1 activity. Hence, our findings suggested that these mutations could alter CXCR1 ligand binding activity, lowering the risk of cancer and helping patients defend against pathogen invasion during a neutrophil-mediated innate immune response.

Keywords: CXCR1; Molecular dynamic simulation; Molecular modeling; G protein-coupled receptors

1. Introduction

CXCR1 is a rhodopsin-like (class A) G protein-coupled receptor (GPCR) that plays a crucial role in cellular signaling and is being investigated as a potential drug receptor due to its involvement in various physiological processes.[1,2] Rhodopsin is commonly used as a standard structure for mimicking GPCRs, and many rhodopsin structures have been characterized in protein databases (PDBs).[3] CXCR1 is one of two receptors that has a strong binding affinity for the CXC chemokine interleukin-8 (IL-8).[4] IL-8 is also known to regulate inflammatory and immune responses and has been linked to various diseases, including cancer.[5] On exposure to inflammatory stimuli, the chemokine IL-8 binds to the extracellular (EC) region of CXCR1.[6] Despite the physiological importance of CXCR1, the underlying molecular mechanism of its signal transduction pathway is poorly understood, primarily due to the limited availability of its structural information.[7]

GPCRs, including CXCR1, typically consist of seven transmembrane (TM) helices, four EC regions (comprising the N-terminal and three interhelical loops), and four intracellular (IC) regions (including the C-terminal and three interhelical loops).[8] Among the seven TM helices, TM3 and TM6 are regarded as pivotal elements responsible for activating switches in GPCRs, and these regions play a critical role in the transition from a partially active state to a fully activated state, particularly in the interactions between G proteins and receptors.[8,9] Crystal structures of the human adenosine A2A receptor bound to rhodopsin and agonists indicate that GPCR activation is induced by the disruption of crucial interhelical interactions.[10] Activation involves the rotation of the TM3 and TM6 domains, thereby altering the conformational structure of the receptor's G protein-interacting cytoplasmic loops to expose previously masked G protein-binding sites on the IC loops.[11] Recent advances in GPCR structural determination have studied the molecular mechanisms of GPCR activation and activity in various cellular processes, such as hormone signaling and neurotransmission.[12] The techniques used to study GPCRs involve several modifications, including making changes to the receptors themselves, adding small molecules to stabilize them, and using specialized lipid mixtures to form crystals that can be analyzed.[13,14] Activation of CXCR1 requires the involvement of both amino-terminal residues and EC loops. In this process, GPCR IC loops play a crucial role in facilitating interactions with G proteins during signaling.[4,15]

According to experimental research, charge significantly influences the interaction of CXCR1 with IL-8/CXCL8, and charged residues in the third and fourth EC loops are essential for this association.[16] Nuclear magnetic resonance spectroscopy (NMR) investigations have also reported that residues after the CXC sequence and those in the core β sheet of IL-8/CXCL8 bind directly to the N-terminus of CXCR1.[17] The ELR motif of the CXC chemokine on the N-terminus of IL-8/CXCL8 plays a role in the interaction of the chemokine with CXCR1.[18] Swapping the IC C-terminal regions consisting of 60 amino acids between CXCR1 and CXCR2 reportedly reversed the antagonistic effects of these receptors.[19] Further studies have demonstrated that the relative antagonistic effects of CXCR1 on CXCR2 were determined by a single amino acid residue: lysine 320 in CXCR2 and asparagine 311 in CXCR1.[19] The charged amino acids play a crucial role in maintaining the local structural stability required for binding in CXCR1, and mutating them disrupts this stability and prevents binding.[6] The mutations that were studied involved charged amino acids in various regions of the CXCR1 receptor, including TM helices and EC loops.[20] These mutations were predicted to alter the local structure of the receptor and potentially affect its ability to bind to other molecules. Specifically, the mutations were predicted to disrupt ion pairs, and oppositely charged amino acids would form bonds that can affect the receptor's capacity to maintain a stable structure in these regions.[21]

Identifying deleterious mutations and predicting the effects of missense mutations on protein structure and function have become important applications of computational analysis.[22] This approach can aid in the design of new drugs and therapies for treating various genetic diseases; for this reason, in the present study, we evaluated the possible consequences of mutations in the various CXCR1 domains that can affect protein function and interactions with ligands. To categorize harmful mutations, we initially used several computational algorithms, including Meta-SNP,[23] PMut,[24] and PROVEAN.[25] We also utilized the FATHMM server to detect specific genetic variants associated with carcinogenesis within disease-causing mutations.[26] Moreover, we employed mCSM,[27] SDM,[28] and DUET[29] to predict the impact of these mutations on the structure and stability of the corresponding proteins. The I-TASSER server was used to create a mutation model with the necessary missense mutation, and Schrödinger's Desmond 3D modeling software was used to explore the structural changes that affect the stability and function of the CXCR1 protein.

2. Methods

2.1. Collection of datasets

To obtain information on CXCR1 missense mutations, the study collected data from Ensembl (release 109)[30] and the Universal Protein Resource Knowledgebase (UniProtKB),

including sequence information in FASTA format (UniProt ID: P25024) from the National Centre for Biological Information (NCBI).[31,32] The structural information of CXCR1 was obtained from the Protein Data Bank (PDB) (http://www.rcsb.org/) with PDB ID: 2LNL.[33]

2.2. Computer-assisted pathogenicity analysis of the mutations

Computational techniques play a vital role in assessing the effect of mutations on proteins and distinguishing between deleterious and benign single-nucleotide variations. This capability is crucial for accurately distinguishing the impact of genetic alterations on protein function, facilitating the identification of disease-causing mutations. Meta-SNPs are web-based tools (http://snps.biofold.org/meta-snp/) that employ multiple predictive algorithms to assess the potentially detrimental effects of protein mutations.[23] The tool integrates other prediction methods, such as SNAP,[34] PhD-SNP, PANTHER,[35] and SIFT,[36] into the system, making it one of the most powerful tools for predicting the impact of mutations on protein function. Meta-SNPs utilize a random forest algorithm consisting of 100 decision trees implemented through the WEKA library.[37] This algorithm was trained on the SV-2009 dataset using a rigorous 20-fold cross-validation methodology.[23] The output of this predictor is a probability score indicating the likelihood of a mutation causing a disease, with scores <0.5 indicating a greater likelihood of the mutation being pathogenic.[38]

The PROVEAN web server applies an alignment-created scoring methodology to determine whether an amino acid replacement affects a protein's biological function.[25] In this approach, mutations with final scores <2.5 were considered harmful. The web server can be accessed at (http://provean.jcvi.org/seq_submit.php).[39]

2.3. Analysis of protein stability

Mutations in a protein can modify its stability and free energy, wherein the difference in free energy (ΔΔG) between the mutated (ΔGm) and wild-type (ΔGw) proteins reflects the effect of mutation on protein stability.[28,40] A negative ΔΔG value represents a destabilizing mutation, while a positive ΔΔG value indicates a stabilizing mutation.[28,40] Several computational approaches, including mCSM, SDM, and DUET, were used to determine the effect of mutations on protein stability.[28]

SDM2 (http://marid.bioc.cam.ac.uk/sdm2) is a computational method designed to predict the quantitative impact of mutations on protein stability.[28,41] SDM2 analyses the variation in potential amino acid substitutions within a specific structural environment tolerated by homologous proteins with known 3D structures.[42] This information is used to generate substitution probability tables, which are subsequently employed to estimate the predicted impact of a mutation on protein stability.[41]

The mCSM computational approach (http://structure.bioc.cam.ac.uk/mcsm)[27] was specifically designed to predict the effects of missense mutations on both protein stability and interactions with its corresponding ligands.[22] This prediction technique utilizes graph-based signatures to capture atom distance patterns, enabling precise evaluations of the effect of mutations on protein stability and interactions. In detail, mCSM encodes spatial relationships between atoms and provides insights into the structural consequences of genetic variations at the atomic level.[43] These signatures enable the mapping of the protein residue environment and the training of predictive models. In addition to evaluating the effect of mutations on protein stability, mCSM also takes into account possible interactions with proteins and nucleic acids. Therefore, the mCSM computational approach can provide valuable insights into how mutations might contribute to the development of various diseases.[44]

DUET (http://structure.bioc.cam.ac.uk/duet)[29] is a computational method that combines two prediction approaches, mCSM and SDM, to accurately predict the effects of missense mutations on protein stability.[29] The predictions generated by these methods are combined using support vector machines (SVMs) that have been trained with sequential minimal optimization.[45] By integrating these methods, DUET can produce a consensus prediction, offering a reliable and optimized approach for accurately predicting the effects of mutations on protein stability.[29]

2.4. Evaluation of cancer-related mutations through the FATHMM server

We utilized the FATHMM server (http://fathmm.biocompute.org.uk/cancer.html) to assess the relevance of harmful mutations to cancer. This web-based tool provides predictions that enable differentiation between cancer-causing mutations and other nonpathogenic germline polymorphisms.[46] We accurately assessed the potential role of deleterious mutations in cancer development, enhancing our understanding of the genetic basis of cancer and facilitating the identification of clinically significant mutations.[26]

2.5. Protein structure modeling of the mutation site

To construct a mutant model of CXCR1 with targeted mutations (N57D, R135C, and P302S), the crystal structure of the native protein was downloaded from PDB, and the

I-TASSER server was subsequently used with a multiple threading approach to construct the desired mutant model.[47]

2.6. Evaluation of the quality of the protein model

The CXCR1 protein is a complex molecule composed of amino acids, and its function is associated with its specific 3D structure. Understanding the structure of a protein can provide insights into its function, interactions with other molecules, and potential roles in biological processes, and the CXCR1 protein is a chemokine receptor involved in the immune system and inflammation.[48] The CXCR1 mutant and native protein models were designed through the I-TASSER server[47] and subsequently subjected to quality validation using the RAMPAGE server (https://servicesn.mbi.ucla.edu/PROCHECK).[49] The quality validation involved analyzing the stereochemical features of the models, including bond lengths, bond angles, and torsion angles, thereby ensuring that the protein models have a geometrically and chemically plausible conformation. Significant deviations in the model's stereochemical features from expected values may indicate errors in the model.[49] In addition, the protein models were compared against experimental data to evaluate their arrangement with known structural properties. This comparison aimed to validate the accuracy of the predicted models by assessing how well they aligned with the actual structure of the CXCR1 protein.

The quality of the protein models refers to their accuracy and reliability in representing the true 3D structure of the CXCR1 protein. The validation process ensures that the models have appropriate stereochemical features and are consistent with the experimental data, enhancing confidence in their utility for further research and analysis.[50] Using the RAMPAGE server, we ensured the reliability of the mutant and normal protein models by checking the stereochemical quality of the protein structure by analyzing the residue-by-residue geometry and overall structural geometry.

2.7. Molecular dynamics simulation

Molecular dynamics simulation (MDS) is a computational technique that simulates the movements and interactions of atoms and molecules over time. It provides a dynamic, detailed view of how biological molecules, such as proteins, behave at the atomic level for studying molecular structures, dynamics, and interactions, offering insights that are often challenging to obtain through experimental methods.[51] In MDS, a protein model is a 3D representation of the protein's structure that is used as the starting point for simulations.[51] The quality of the model is crucial for obtaining accurate simulation results.[52] Key factors for a high-quality protein model include an accurate representation of the native structure, compatibility with a suitable force field, inclusion of the surrounding solvent and relevant environmental factors, and the ability to undergo post-simulation analysis.[53] Ensuring these aspects enhances the reliability and biological relevance of insights gained from MDS.

The mutant and normal model structures with the highest I-TASSER score, indicating their favorable conformational arrangement, were chosen for subsequent investigation and analysis.[47] To investigate the effect of the identified mutations on the structure of CXCR1 at the mechanistic level, we conducted an MDS using Schrödinger's Desmond software.[54,55] Specifically, we analyzed the effects of the N57D, R135C, and P302S mutations on the protein structure over a simulation period of 100 ns.[56] As a critical first step, protein docking was performed before MDS, predicting the static binding position of the molecule at the active site of the protein and providing important information for the subsequent analysis of the protein's structure and function during the simulation.[55] MDS typically utilizes Newton's classical equation of motion to simulate the movements of atoms over time, providing predictions of ligand-binding status in various physiological environments.[51] By modeling the behavior of individual particles based on physical laws, MDS can provide valuable insights into the dynamic behavior and stability of proteins under diverse conditions.[54] Maestro's Protein Preparation Wizard was used to optimize, minimize, and replace missing residues in the CXCR1 receptor protein. In addition, the MDS system was constructed using the System Builder tool, where the TIP3P (Intermolecular Interaction Potential 3 Points Transferable) solvent model with 300 K temperature, 1 atm pressure, and OPLS_2005 force field was applied.[57] The models were neutralized by adding counterions and 0.15 M sodium chloride and subsequently used to simulate physiological conditions. Before simulation, the models were equilibrated, and trajectories were saved for analysis every 100 ps.[58] The stability of the simulations was assessed by calculating the root mean square deviation (RMSD) and root mean square fluctuation (RMSF) of the proteins during the simulation period.[58]

RMSD determines the average change in the distance of a set of atoms concerning a reference frame, and it is computed for each frame of trajectory.[59] The RMSD for frame x is:

$$\mathrm{RMSD}_{\mathrm{X}} = \sqrt{1/N \sum_{i=1}^{n} \left(\mathrm{r`i}(35)\right) - ri(tref))^2} \qquad \text{(I)}$$

Where N is the number of atoms in atom selection; *tref* is the reference time (typically, the first frame is used as

a reference, and time is considered as t = 0); and r is the position of selected atoms in frame x after superposition with the reference frame (frame x being recorded at time tx). The procedure was repeated for each frame in the simulation trajectory.[59]

RMSF is useful for characterizing local changes in the protein chain.[54] The RMSF for residue i is:

$$\mathrm{RMSF}_i = \sqrt{1/T\sum_{t=1}^{T} < \left(r`i(\mathrm{t})\right) - ri(tref))^2 >} \quad \text{(II)}$$

Where T is the flight path time over which the RMSF is calculated; *tref* is the reference time; *ri* is the position of residue I; r is the position of the atoms in residue I after an overlay with the reference; and the angle brackets indicate that the mean squared distance is taken over the selection of the atoms in residue I.[54]

2.8. Analysis of secondary structure changes in CXCR1 proteins

The Database of Secondary Structure in Proteins tool utilizes hydrogen bonding and other secondary structure markers to categorize protein residues and examine alterations in secondary structure patterns between wild-type and mutant CXCR1 proteins.[60] The resulting secondary structure patterns were plotted for comparison.

3. Results

This study demonstrated that missense mutations in the CXCR1 gene significantly affected the molecular structure, stability, and function of the resulting protein. This finding suggested that the altered protein could be dysfunctional and contribute to the development or progression of disease. The study utilized advanced computational methods to screen for protein stability, cancer-causing mutations, and pathogenicity.

3.1. Retrieving the dataset of missense mutations

To explore the potential effects of CXCR1 gene mutations on protein function, we acquired a comprehensive list of 299 mutations (Table S1) from a publicly available database. These mutations are distributed throughout different coding regions of the gene, allowing for a comprehensive assessment of the potential impact on protein functionality.

3.2. Analysis of missense mutations

The importance of missense mutations in amino acids can be used to assess the pathogenic implications of these mutations. PMut, PROVEAN, and Meta-SNPs (PANTHER, PhD-SNP, SIFT, and SNAP) were used to investigate the 299 missense mutations. We found that 53 mutations in CXCR1 could cause harm and disease, and these mutations were located across multiple domains of the protein (Table 1).

3.3. Prediction of the impact of mutation on CXCR1 protein stability

Three algorithms, mCSM, SDM, and DUET, were used to predict the 299 mutations and their impact on protein stability. mCSM predicted that 19 mutations would strongly destabilize protein stability, SDM predicted that 183 mutations would reduce CXCR1 protein stability, and DUET predicted that 240 amino acids would affect the stability of the CXCR1 protein (Table 2).

3.4. Identification of potential carcinogenic mutations in CXCR1

In CXCR1, 299 mutations were identified using the FATHMM server to determine their potential role in carcinogenesis. The analysis revealed five specific carcinogenic mutations (N57D, R135C, R135H, R135L, and P302S) (Table 3), and these mutations were located across different regions of CXCR1.

3.5. Conservation analysis

From the five identified carcinogenic mutations, three mutations, N57D, R135C, and P302S, were selected for further analysis. This analysis utilized the ConSurf server tool to examine the conservation and location of these three mutations.[61] The results indicated high conservation levels at these locations, with a score of 9 on the scale presented in Figure 1A-C. Based on these findings, we subsequently investigated the impact of these three mutations on protein stability and function through simulated computational analysis.

3.6. Selection of the mutant CXCR1 structure

The control model for the native protein was the 3D structure of CXCR1 (PDB ID 2LNL).[62] The I-TASSER server was used to locate template proteins with comparable folds from the PDB database and construct 10,000 conformations (decoys) from a mutant sequence.[63] I-TASSER utilized the SPICKER tool to cluster the generated conformations by performing pairwise structural alignments.[64] This process grouped similar conformations, enabling a more organized analysis of the protein structures. Consequently, five separate clusters emerged, each having a large number of models with identical structures. I-TASSER then selected a representative model from each of these clusters to construct five final models that best represented the varied conformation predictions.[64] The first model was selected for further investigation because it had the greatest confidence level (C-score).[47] Ramachandran plots were

Table 1. Predicted deleterious CXCR1 mutations using computational tools

Serial number	Mutants	Computational tool													
		PANTHER		PhD-SNP		SIFT		SNAP		Meta-SNP		PMut		PROVEAN	
		Prediction	Score	Prediction	Score	Prediction	Score	Prediction	Score	Prediction	Score	Prediction	Score	Prediction	Score
38	Y46C	Harmful	0.824	Harmful	0.916	Harmful	0.02	Harmful	0.75	Harmful	0.843	Harmful	0.77	Harmful	−7.852
39	V49G	Harmful	0.599	Harmful	0.852	Harmful	0	Harmful	0.665	Harmful	0.764	Harmful	0.9	Harmful	−6.114
42	L51P	Harmful	0.801	Harmful	0.873	Harmful	0.04	Harmful	0.72	Harmful	0.802	Harmful	0.71	Harmful	−5.374
43	L52Q	Harmful	0.805	Harmful	0.726	Harmful	0.01	Harmful	0.615	Harmful	0.74	Harmful	0.9	Harmful	−4.576
45	N57D	Harmful	0.976	Harmful	0.807	Harmful	0	Harmful	0.85	Harmful	0.886	Harmful	0.9	Harmful	−4.449
47	L59P	Harmful	0.84	Harmful	0.862	Harmful	0	Harmful	0.76	Harmful	0.835	Harmful	0.69	Harmful	−5.697
70	L78P	Harmful	0.802	Harmful	0.874	Harmful	0	Harmful	0.76	Harmful	0.838	Harmful	0.9	Harmful	−6.065
73	A82V	Harmful	0.692	Harmful	0.805	Harmful	0.04	Harmful	0.58	Harmful	0.568	Harmful	0.56	Harmful	−3.302
75	D85N	Harmful	0.702	Harmful	0.814	Harmful	0.03	Harmful	0.76	Harmful	0.64	Harmful	0.54	Harmful	−3.604
79	T91I	Harmful	0.611	Harmful	0.827	Harmful	0.03	Harmful	0.64	Harmful	0.577	Harmful	0.58	Harmful	−4.447
81	P93S	Harmful	0.99	Harmful	0.874	Harmful	0	Harmful	0.75	Harmful	0.847	Harmful	0.91	Harmful	−7.124
82	P93T	Harmful	0.992	Harmful	0.838	Harmful	0	Harmful	0.75	Harmful	0.852	Harmful	0.91	Harmful	−7.135
83	P93H	Harmful	0.996	Harmful	0.894	Harmful	0	Harmful	0.83	Harmful	0.89	Harmful	0.91	Harmful	−8.016
89	W103R	Harmful	0.994	Harmful	0.958	Harmful	0	Harmful	0.885	Harmful	0.905	Harmful	0.91	Harmful	−12.088
99	C110W	Harmful	0.999	Harmful	0.962	Harmful	0	Harmful	0.87	Harmful	0.947	Harmful	0.91	Harmful	−9.933
100	K111E	Harmful	0.973	Harmful	0.892	Harmful	0.01	Harmful	0.74	Harmful	0.787	Harmful	0.91	Harmful	−3.612
106	Y122H	Harmful	0.584	Harmful	0.797	Harmful	0.02	Harmful	0.75	Harmful	0.634	Harmful	0.69	Harmful	−3.515
107	G124D	Harmful	0.552	Harmful	0.865	Harmful	0.03	Harmful	0.725	Harmful	0.754	Harmful	0.81	Harmful	−4.345
109	L127P	Harmful	0.965	Harmful	0.879	Harmful	0.01	Harmful	0.74	Harmful	0.739	Harmful	0.91	Harmful	−5.763
111	I131T	Harmful	0.898	Harmful	0.671	Harmful	0	Harmful	0.665	Harmful	0.715	Harmful	0.91	Harmful	−4.461
113	S132N	Harmful	0.746	Harmful	0.773	Harmful	0.02	Harmful	0.635	Harmful	0.6	Harmful	0.6	Harmful	−2.684
115	D134V	Harmful	0.973	Harmful	0.934	Harmful	0.02	Harmful	0.73	Harmful	0.728	Harmful	0.85	Harmful	−7.819
116	D134G	Harmful	0.923	Harmful	0.919	Harmful	0	Harmful	0.755	Harmful	0.725	Harmful	0.91	Harmful	−5.796
117	D134E	Harmful	0.861	Harmful	0.859	Harmful	0.05	Harmful	0.68	Harmful	0.65	Harmful	0.84	Harmful	−3.479
118	R135C	Harmful	0.996	Harmful	0.898	Harmful	0.01	Harmful	0.775	Harmful	0.834	Harmful	0.91	Harmful	−6.491
119	R135L	Harmful	0.99	Harmful	0.947	Harmful	0	Harmful	0.78	Harmful	0.779	Harmful	0.91	Harmful	−5.963
120	R135H	Harmful	0.992	Harmful	0.876	Harmful	0	Harmful	0.81	Harmful	0.781	Harmful	0.89	Harmful	−4.307
122	I139T	Harmful	0.909	Harmful	0.61	Harmful	0.05	Harmful	0.59	Harmful	0.627	Harmful	0.69	Harmful	−4.734
123	V140F	Harmful	0.929	Harmful	0.866	Harmful	0.04	Harmful	0.575	Harmful	0.773	Harmful	0.74	Harmful	−4.834
136	C157F	Harmful	0.981	Harmful	0.838	Harmful	0.04	Harmful	0.705	Harmful	0.85	Harmful	0.9	Harmful	−9.54

(Cont'd...)

Table 1. *(Continued)*

Serial number	Mutants	Computational tool													
		PANTHER		PhD-SNP		SIFT		SNAP		Meta-SNP		PMut		PROVEAN	
		Prediction	Score	Prediction	Score	Prediction	Score	Prediction	Score	Prediction	Score	Prediction	Score	Prediction	Score
139	W161L	Harmful	0.997	Harmful	0.857	Harmful	0.03	Harmful	0.78	Harmful	0.824	Harmful	0.9	Harmful	−11.781
140	W161C	Harmful	0.998	Harmful	0.912	Harmful	0.01	Harmful	0.8	Harmful	0.831	Harmful	0.9	Harmful	−11.797
142	S164F	Harmful	0.88	Harmful	0.807	Harmful	0	Harmful	0.715	Harmful	0.778	Harmful	0.9	Harmful	−4.409
146	P170T	Harmful	0.776	Harmful	0.819	Harmful	0.01	Harmful	0.71	Harmful	0.689	Harmful	0.86	Harmful	−6.798
147	P170L	Harmful	0.822	Harmful	0.891	Harmful	0.04	Harmful	0.63	Harmful	0.679	Harmful	0.87	Harmful	−8.641
160	C187Y	Harmful	0.993	Harmful	0.869	Harmful	0.02	Harmful	0.88	Harmful	0.902	Harmful	0.9	Harmful	−7.963
183	F211V	Harmful	0.981	Harmful	0.901	Harmful	0.01	Harmful	0.73	Harmful	0.844	Harmful	0.9	Harmful	−6.653
185	P214L	Harmful	0.994	Harmful	0.903	Harmful	0.01	Harmful	0.665	Harmful	0.853	Harmful	0.9	Harmful	−9.694
189	Y222C	Harmful	0.998	Harmful	0.888	Harmful	0.02	Harmful	0.63	Harmful	0.852	Harmful	0.91	Harmful	−7.669
193	T225P	Harmful	0.683	Harmful	0.846	Harmful	0.01	Harmful	0.67	Harmful	0.806	Harmful	0.9	Harmful	−4.677
214	I244N	Harmful	0.82	Harmful	0.865	Harmful	0	Harmful	0.645	Harmful	0.75	Harmful	0.9	Harmful	−6.676
215	I244F	Harmful	0.627	Harmful	0.819	Harmful	0.01	Harmful	0.655	Harmful	0.658	Harmful	0.84	Harmful	−3.868
219	P257S	Harmful	1	Harmful	0.853	Harmful	0	Harmful	0.76	Harmful	0.908	Harmful	0.9	Harmful	−7.691
254	L293P	Harmful	0.843	Harmful	0.877	Harmful	0	Harmful	0.825	Harmful	0.869	Harmful	0.91	Harmful	−6.313
257	C299F	Harmful	0.976	Harmful	0.961	Harmful	0.02	Harmful	0.74	Harmful	0.849	Harmful	0.85	Harmful	−8.438
258	P302S	Harmful	1	Harmful	0.873	Harmful	0	Harmful	0.76	Harmful	0.938	Harmful	0.91	Harmful	−7.503
259	I304N	Harmful	0.776	Harmful	0.845	Harmful	0	Harmful	0.675	Harmful	0.773	Harmful	0.91	Harmful	−5.543
262	F312S	Harmful	0.998	Harmful	0.914	Harmful	0	Harmful	0.69	Harmful	0.876	Harmful	0.91	Harmful	−7.503
263	F312I	Harmful	0.998	Harmful	0.909	Harmful	0.03	Harmful	0.595	Harmful	0.861	Harmful	0.72	Harmful	−5.627
265	R313H	Harmful	0.566	Harmful	0.862	Harmful	0.03	Harmful	0.565	Harmful	0.722	Harmful	0.75	Harmful	−4.288
267	R313C	Harmful	0.795	Harmful	0.927	Harmful	0	Harmful	0.73	Harmful	0.825	Harmful	0.82	Harmful	−6.834
272	I319N	Harmful	0.855	Harmful	0.611	Harmful	0.04	Harmful	0.555	Harmful	0.701	Harmful	0.9	Harmful	−4.91
273	L320P	Harmful	0.773	Harmful	0.889	Harmful	0.01	Harmful	0.755	Harmful	0.828	Harmful	0.69	Harmful	−5.456

Table 2. Predicted CXCR1 mutations that decrease or damage protein stability using computational servers

Serial number	Computational server					
	SDM		mCSM		DUET	
	ΔΔG	Prediction of protein stability	ΔΔG	Prediction of protein stability	ΔΔG	Prediction of protein stability
1	0	Enhance	−0.8	Damaging	−0.49	Damaging
2	0	Enhance	−0.989	Damaging	−0.691	Damaging
4	0	Enhance	−0.623	Damaging	−0.253	Damaging
5	0	Enhance	−0.8	Damaging	−0.49	Damaging
6	−1.29	Decrease	−0.88	Damaging	−0.959	Damaging
7	0.02	Enhance	−0.126	Damaging	0.101	Stabilizing
8	−0.05	Decrease	−1.091	Damaging	−0.676	Damaging
9	−0.42	Decrease	−2.522	Highly damaging	−2.139	Damaging
10	−0.59	Decrease	−2.751	Highly damaging	−2.931	Damaging
11	−0.8	Decrease	−3.373	Highly damaging	−3.693	Damaging
12	−0.46	Decrease	−0.337	Damaging	−0.444	Damaging
13	−0.25	Decrease	−0.635	Damaging	−0.508	Damaging
14	−0.18	Decrease	−0.387	Damaging	−0.031	Damaging
15	0.1	Enhance	−0.375	Damaging	−0.062	Damaging
16	0.78	Enhance	−0.28	Damaging	0.24	Stabilizing
17	−0.18	Decrease	−0.543	Damaging	−0.292	Damaging
18	−0.43	Decrease	−0.295	Damaging	−0.011	Damaging
19	−0.11	Decrease	−0.573	Damaging	−0.274	Damaging
20	−0.11	Decrease	0.093	Stabilizing	0.172	Stabilizing
21	3.78	Enhance	−0.42	Damaging	0.437	Stabilizing
22	1.18	Enhance	−0.265	Damaging	0.111	Stabilizing
24	0.78	Enhance	−0.297	Damaging	0.296	Stabilizing
25	−0.29	Decrease	−0.623	Damaging	−0.456	Damaging
26	0.67	Enhance	−0.531	Damaging	−0.09	Damaging
27	0.25	Enhance	−0.6	Damaging	−0.151	Damaging
28	−0.5	Decrease	−0.125	Damaging	0.139	Stabilizing
29	0.34	Enhance	−0.048	Damaging	0.468	Stabilizing
30	−0.98	Decrease	−0.491	Damaging	−0.407	Damaging
31	−0.63	Decrease	−0.814	Damaging	−0.846	Damaging
32	0.36	Enhance	−0.299	Damaging	0.192	Stabilizing
34	0.23	Enhance	−0.398	Damaging	0.045	Stabilizing
35	−0.65	Decrease	−0.231	Damaging	0.174	Stabilizing
36	0.09	Enhance	−0.598	Damaging	−0.221	Damaging
37	−2.05	Decrease	−1.013	Damaging	−1.122	Damaging
38	−1.01	Decrease	−1.571	Damaging	−1.411	Damaging
39	−2.5	Decrease	−2.547	Highly damaging	−2.932	Damaging
40	0.64	Enhance	−1.12	Damaging	−0.806	Damaging
41	0.04	Enhance	−1.266	Damaging	−1.102	Damaging
42	−2.23	Decrease	−0.564	Damaging	−0.569	Damaging
43	−2.23	Decrease	−1.29	Damaging	−1.158	Damaging

(Cont'd...)

Table 2. ***(Continued)***

Serial number	Computational server					
	SDM		mCSM		DUET	
	ΔΔG	Prediction of protein stability	ΔΔG	Prediction of protein stability	ΔΔG	Prediction of protein stability
44	−0.67	Decrease	−1.492	Damaging	−1.302	Damaging
45	−0.62	Decrease	−2.418	Highly damaging	−2.346	Damaging
46	0.43	Enhance	−0.838	Damaging	−0.466	Damaging
47	−2.23	Decrease	−0.799	Damaging	−1.093	Damaging
48	−0.15	Decrease	−1.34	Damaging	−0.823	Damaging
49	0.11	Enhance	−0.995	Damaging	−0.382	Damaging
50	−2.23	Decrease	−0.793	Damaging	−1.086	Damaging
51	−0.2	Decrease	0.141	Stabilizing	0.532	Stabilizing
52	−1.5	Decrease	−1.928	Damaging	−2.145	Damaging
53	−0.35	Decrease	−1.305	Damaging	−1.083	Damaging
54	−0.91	Decrease	−0.095	Damaging	0.13	Stabilizing
55	−1.51	Decrease	−0.661	Damaging	−0.629	Damaging
56	0.22	Enhance	−0.199	Damaging	0.255	Stabilizing
57	−1.21	Decrease	−0.267	Damaging	−0.138	Damaging
58	−0.3	Decrease	−0.47	Damaging	−0.246	Damaging
59	−0.4	Decrease	−0.633	Damaging	−0.48	Damaging
60	−0.33	Decrease	−0.293	Damaging	−0.291	Damaging
61	0.09	Enhance	−0.657	Damaging	−0.537	Damaging
62	−0.59	Decrease	−0.984	Damaging	−0.909	Damaging
63	0.35	Enhance	−0.726	Damaging	−0.256	Damaging
64	−0.01	Decrease	−1.113	Damaging	−0.965	Damaging
65	−0.17	Decrease	−0.79	Damaging	−0.529	Damaging
66	−0.97	Decrease	−1.319	Damaging	−1.476	Damaging
67	−0.2	Decrease	−0.734	Damaging	−0.402	Damaging
68	0.11	Enhance	−1.439	Damaging	−0.979	Damaging
69	−1.35	Decrease	−2.371	Highly damaging	−2.214	Damaging
70	−2.75	Decrease	−0.963	Damaging	−1.327	Damaging
71	−0.52	Decrease	−0.638	Damaging	−0.101	Damaging
72	0.12	Enhance	−1.215	Damaging	−0.799	Damaging
73	−0.85	Decrease	−0.668	Damaging	−0.546	Damaging
74	−3.32	Decrease	−2.982	Highly damaging	−3.32	Damaging
75	0.57	Enhance	−1.063	Damaging	−0.659	Damaging
76	−0.37	Decrease	−0.994	Damaging	−0.708	Damaging
77	−1.41	Decrease	−1.807	Damaging	−1.933	Damaging
78	−2.61	Decrease	−1.29	Damaging	−1.518	Damaging
80	−1.48	Decrease	−1.249	Damaging	−1.528	Damaging
81	1.62	Enhance	−1.559	Damaging	−1.017	Damaging
82	0.34	Enhance	−1.298	Damaging	−0.848	Damaging
83	1.06	Enhance	−1.306	Damaging	−0.776	Damaging
84	−2.83	Decrease	−2.726	Highly damaging	−2.636	Damaging

(Cont'd...)

Table 2. *(Continued)*

Serial number	Computational server					
	SDM		mCSM		DUET	
	ΔΔG	Prediction of protein stability	ΔΔG	Prediction of protein stability	ΔΔG	Prediction of protein stability
85	−1.49	Decrease	−1.472	Damaging	−1.575	Damaging
86	−1.53	Decrease	−1.293	Damaging	−1.237	Damaging
87	0.65	Enhance	−0.161	Damaging	0.297	Stabilizing
88	−2.65	Decrease	−1.377	Damaging	−1.674	Damaging
89	−0.4	Decrease	−1.656	Damaging	−1.308	Damaging
90	−0.22	Decrease	−1.243	Damaging	−1.164	Damaging
91	−0.03	Decrease	−0.151	Damaging	0.239	Stabilizing
92	−1.33	Decrease	−0.923	Damaging	−0.83	Damaging
93	−0.65	Decrease	−1.619	Damaging	−1.655	Damaging
94	0.37	Enhance	−1.002	Damaging	−0.604	Damaging
95	−1.47	Decrease	−0.408	Damaging	−0.546	Damaging
96	0.64	Enhance	−0.62	Damaging	−0.322	Damaging
97	0.47	Enhance	−0.349	Damaging	0.008	Stabilizing
98	0.64	Enhance	−0.62	Damaging	−0.322	Damaging
99	−2.1	Decrease	−1.016	Damaging	−1.246	Damaging
100	0.09	Enhance	−1.65	Damaging	−1.233	Damaging
101	0.07	Enhance	−1.903	Damaging	−1.582	Damaging
102	0.18	Enhance	−1.353	Damaging	−1.029	Damaging
103	0.16	Enhance	−0.107	Damaging	0.101	Stabilizing
104	−1.65	Decrease	−0.904	Damaging	−1.041	Damaging
105	−0.53	Decrease	−1.465	Damaging	−1.453	Damaging
106	0.12	Enhance	−0.56	Damaging	−0.459	Damaging
107	−1.31	Decrease	−1.67	Damaging	−1.548	Damaging
108	0.78	Enhance	−1.844	Damaging	−1.726	Damaging
109	−2.55	Decrease	−1.164	Damaging	−1.541	Damaging
110	−4.41	Decrease	−1.686	Damaging	−2.378	Damaging
111	−2.05	Decrease	−1.481	Damaging	−1.619	Damaging
112	−3.12	Decrease	−2.55	Highly damaging	−2.883	Damaging
113	−1.12	Decrease	−0.883	Damaging	−0.605	Damaging
114	0.06	Enhance	−1.291	Damaging	−1.084	Damaging
115	0.16	Enhance	−0.467	Damaging	−0.21	Damaging
117	−0.32	Decrease	−1.154	Damaging	−1.048	Damaging
118	1.25	Enhance	−0.593	Damaging	0.048	Stabilizing
119	−0.74	Decrease	−0.781	Damaging	−0.681	Damaging
120	0.3	Enhance	−0.047	Damaging	0.352	Stabilizing
121	−0.06	Decrease	−1.476	Damaging	−1.263	Damaging
122	−2.05	Decrease	−1.446	Damaging	−1.582	Damaging
123	−1.06	Decrease	−1.247	Damaging	−1.171	Damaging
124	−0.09	Decrease	−1.191	Damaging	−1.071	Damaging
125	−0.35	Decrease	−0.029	Damaging	−0.118	Damaging
126	−0.38	Decrease	−0.181	Damaging	−0.253	Damaging

(Cont'd...)

Table 2. *(Continued)*

Serial number	Computational server					
	SDM		mCSM		DUET	
	ΔΔG	Prediction of protein stability	ΔΔG	Prediction of protein stability	ΔΔG	Prediction of protein stability
127	0.19	Enhance	−1.058	Damaging	−0.982	Damaging
128	−0.33	Decrease	−0.244	Damaging	−0.312	Damaging
129	0.42	Enhance	−0.229	Damaging	0.08	Stabilizing
130	0.27	Enhance	−0.333	Damaging	−0.096	Damaging
131	−0.19	Decrease	−0.034	Damaging	0.08	Stabilizing
132	−1.02	Decrease	−1.125	Damaging	−1.246	Damaging
133	−0.71	Decrease	−0.389	Damaging	−0.304	Damaging
134	0.65	Enhance	1.207	Stabilizing	1.307	Stabilizing
135	−0.63	Decrease	−1.173	Damaging	−1.225	Damaging
136	−0.09	Decrease	−1.133	Damaging	−1.103	Damaging
137	−1.5	Decrease	−1.281	Damaging	−1.426	Damaging
138	−0.63	Decrease	−0.974	Damaging	−0.997	Damaging
139	0.16	Enhance	−0.175	Damaging	0.345	Stabilizing
140	0.23	Enhance	−1.909	Damaging	−1.398	Damaging
141	0.08	Enhance	−1.432	Damaging	−1.007	Damaging
142	−2.23	Decrease	−0.758	Damaging	−0.987	Damaging
143	−0.2	Decrease	−1.02	Damaging	−0.766	Damaging
144	0.49	Enhance	−1.088	Damaging	−0.526	Damaging
145	0.11	Enhance	−0.405	Damaging	0.211	Stabilizing
146	0.49	Enhance	−1.618	Damaging	−1.179	Damaging
147	0.83	Enhance	−1.285	Damaging	−0.702	Damaging
149	0.11	Enhance	−1.069	Damaging	−0.916	Damaging
150	−0.65	Decrease	−2.752	Highly damaging	−2.836	Damaging
151	−1.29	Decrease	−1.693	Damaging	−2.099	Damaging
152	0.19	Enhance	−1.548	Damaging	−1.28	Damaging
153	0.25	Enhance	−2.782	Highly damaging	−2.451	Damaging
154	0.1	Enhance	−1.463	Damaging	−1.226	Damaging
155	−1.43	Decrease	−1.591	Damaging	−1.665	Damaging
156	−0.62	Decrease	0.073	Stabilizing	0.073	Stabilizing
157	0.94	Enhance	−0.824	Damaging	−0.379	Damaging
158	0.74	Enhance	−0.654	Damaging	−0.285	Damaging
159	−1.13	Decrease	−0.654	Damaging	−1.941	Damaging
160	−1.09	Decrease	−0.594	Damaging	−0.426	Damaging
161	−0.87	Decrease	−1.035	Damaging	−1.078	Damaging
162	−0.13	Decrease	−0.78	Damaging	−0.518	Damaging
163	−1.04	Decrease	−1.811	Damaging	−1.633	Damaging
164	−0.48	Decrease	−1.084	Damaging	−0.889	Damaging
165	0.84	Enhance	−0.634	Damaging	−0.28	Damaging
166	0.5	Enhance	−0.254	Damaging	0.074	Stabilizing
167	0.33	Enhance	−0.455	Damaging	−0.561	Damaging
168	−3.33	Decrease	−1.864	Damaging	−2.165	Damaging

(Cont'd...)

Table 2. ***(Continued)***

Serial number	Computational server					
	SDM		mCSM		DUET	
	ΔΔG	Prediction of protein stability	ΔΔG	Prediction of protein stability	ΔΔG	Prediction of protein stability
169	−1.16	Decrease	−0.462	Damaging	−0.005	Damaging
170	−2	Decrease	−1.04	Damaging	−1.504	Damaging
171	0.54	Enhance	−0.842	Damaging	−0.13	Damaging
172	−0.72	Decrease	−1.493	Damaging	−1.341	Damaging
173	0.84	Enhance	−1.165	Damaging	−0.552	Damaging
174	−2.59	Decrease	−2.779	Highly damaging	−3.094	Damaging
175	−0.55	Decrease	−0.853	Damaging	−0.801	Damaging
176	0.37	Enhance	−0.144	Damaging	0.025	Stabilizing
177	−0.8	Decrease	−1.71	Damaging	−1.572	Damaging
178	−1.5	Decrease	−1.578	Damaging	−1.435	Damaging
179	−2.11	Decrease	−1.044	Damaging	−1.096	Damaging
180	−0.35	Decrease	−0.933	Damaging	−0.892	Damaging
181	0.21	Enhance	−0.998	Damaging	−0.712	Damaging
182	0.1	Enhance	−1.409	Damaging	−1.197	Damaging
183	−2.05	Decrease	−0.47	Damaging	−0.695	Damaging
184	−2.67	Decrease	−0.991	Damaging	−1.342	Damaging
185	0.16	Enhance	−0.173	Damaging	0.098	Stabilizing
186	3.38	Enhance	−0.426	Damaging	0.61	Stabilizing
187	0.64	Enhance	−0.823	Damaging	−0.527	Damaging
188	0.35	Enhance	−0.51	Damaging	−0.027	Damaging
189	0.18	Enhance	−0.833	Damaging	−0.274	Damaging
190	−1.5	Decrease	−1.457	Damaging	−1.465	Damaging
191	1.07	Enhance	−0.772	Damaging	−0.327	Damaging
192	1.64	Enhance	−0.581	Damaging	0.173	Stabilizing
193	1.36	Enhance	−1.094	Damaging	−0.279	Damaging
194	−1.22	Decrease	−0.326	Damaging	−0.524	Damaging
195	−1.82	Decrease	−0.345	Damaging	−0.662	Damaging
196	−0.7	Decrease	−1.456	Damaging	−1.455	Damaging
197	−0.74	Decrease	−0.821	Damaging	−0.811	Damaging
198	−0.82	Decrease	−0.238	Damaging	−0.172	Damaging
199	0.64	Enhance	−0.865	Damaging	−0.547	Damaging
200	−0.67	Decrease	−0.378	Damaging	−0.295	Damaging
201	−0.35	Decrease	−0.688	Damaging	−0.568	Damaging
203	0.6	Enhance	−0.361	Damaging	0.179	Stabilizing
204	0.54	Enhance	0.267	Damaging	0.276	Stabilizing
205	−0.19	Decrease	0.832	Stabilizing	0.982	Stabilizing
206	0.72	Enhance	−0.394	Damaging	−0.021	Damaging
208	−0.48	Decrease	−0.79	Damaging	−0.732	Damaging
209	0.79	Enhance	−0.491	Damaging	−0.298	Damaging
210	−1.06	Decrease	−0.168	Damaging	−0.363	Damaging
211	−1.53	Decrease	−1.021	Damaging	−1.229	Damaging

(Cont'd...)

Table 2. *(Continued)*

Serial number	Computational server					
	SDM		mCSM		DUET	
	ΔΔG	Prediction of protein stability	ΔΔG	Prediction of protein stability	ΔΔG	Prediction of protein stability
212	−0.28	Decrease	−0.405	Damaging	−0.325	Damaging
213	−2.99	Decrease	−2.176	Highly damaging	−2.148	Damaging
214	−0.25	Decrease	−0.363	Damaging	0.047	Stabilizing
215	−0.86	Decrease	−1.782	Damaging	−1.638	Damaging
216	−0.3	Decrease	−1.239	Damaging	−1.197	Damaging
217	−0.84	Decrease	0.386	Stabilizing	0.671	Stabilizing
218	−0.18	Decrease	0.15	Stabilizing	0.529	Stabilizing
219	−0.53	Decrease	−0.361	Damaging	−0.323	Damaging
220	0.49	Enhance	−2.066	Highly damaging	−1.769	Damaging
221	−1.53	Decrease	−1.463	Damaging	−1.42	Damaging
222	0.03	Enhance	−1.458	Damaging	−0.939	Damaging
223	0.01	Enhance	−1.507	Damaging	−1.291	Damaging
224	−0.09	Decrease	−1.052	Damaging	−0.497	Damaging
225	−0.99	Decrease	−0.705	Damaging	−0.083	Damaging
226	0.13	Enhance	−1.026	Damaging	−0.7	Damaging
227	−0.43	Decrease	−0.757	Damaging	−0.397	Damaging
228	1.51	Enhance	−0.009	Damaging	0.775	Stabilizing
229	−0.44	Decrease	−0.52	Damaging	−0.301	Damaging
230	−0.45	Decrease	−0.405	Damaging	−0.379	Damaging
231	0.04	Enhance	−1.163	Damaging	−0.919	Damaging
232	−0.61	Decrease	−0.787	Damaging	−0.67	Damaging
233	0.09	Enhance	−0.482	Damaging	−0.088	Damaging
234	−0.15	Decrease	−0.328	Damaging	0.074	Stabilizing
235	−1.01	Decrease	0.263	Stabilizing	0.474	Stabilizing
236	−2.54	Decrease	−0.193	Damaging	−0.826	Damaging
237	−1.1	Decrease	−1.393	Damaging	−1.484	Damaging
238	−0.87	Decrease	−0.582	Damaging	−0.543	Damaging
239	−0.65	Decrease	−0.863	Damaging	−0.775	Damaging
240	0.08	Enhance	−0.095	Damaging	0.19	Stabilizing
241	−0.46	Decrease	−1.561	Damaging	−1.499	Damaging
242	−0.3	Decrease	−1.574	Damaging	−1.512	Damaging
243	−0.35	Decrease	−1.331	Damaging	−1.096	Damaging
244	0.72	Enhance	−0.648	Damaging	−0.031	Damaging
245	0.18	Enhance	−1.09	Damaging	−0.83	Damaging
246	0.49	Enhance	−0.546	Damaging	−0.449	Damaging
248	0.04	Enhance	−0.272	Damaging	−0.104	Damaging
249	−2.05	Decrease	−0.901	Damaging	−0.916	Damaging
251	−1.56	Decrease	−0.543	Damaging	−0.551	Damaging
252	2.06	Enhance	−0.959	Damaging	−0.022	Damaging
253	−1.01	Decrease	−0.282	Damaging	−0.044	Damaging
254	−2.23	Decrease	−2.109	Highly damaging	−2.322	Damaging

(Cont'd...)

Table 2. *(Continued)*

Serial number	Computational server					
	SDM		mCSM		DUET	
	ΔΔG	Prediction of protein stability	ΔΔG	Prediction of protein stability	ΔΔG	Prediction of protein stability
255	−2.23	Decrease	−1.524	Damaging	−1.886	Damaging
256	−2.51	Decrease	−1.068	Damaging	−1.314	Damaging
257	−1.48	Decrease	−1.602	Damaging	−1.8	Damaging
258	−1.2	Decrease	−1.282	Damaging	−1.375	Damaging
259	0.62	Enhance	−2.554	Highly damaging	−2.103	Damaging
260	−1.37	Decrease	−2.77	Highly damaging	−2.94	Damaging
261	−2.75	Decrease	−0.921	Damaging	−1.194	Damaging
262	−0.6	Decrease	−1.188	Damaging	−1.162	Damaging
263	−1.8	Decrease	−2.268	Highly damaging	−2.523	Damaging
264	−0.25	Decrease	−1.212	Damaging	−1.028	Damaging
265	0.08	Enhance	−0.499	Damaging	−0.179	Damaging
266	−1.1	Decrease	−1.912	Damaging	−1.991	Damaging
267	−0.77	Decrease	−1.415	Damaging	−1.386	Damaging
269	0.39	Enhance	−0.398	Damaging	−0.124	Damaging
270	1.73	Enhance	−1.155	Damaging	−0.344	Damaging
271	−0.37	Decrease	−0.609	Damaging	−0.29	Damaging
272	−0.98	Decrease	−1.443	Damaging	−1.302	Damaging
273	−2.78	Decrease	−1.231	Damaging	−1.766	Damaging
274	−1.59	Decrease	−1.302	Damaging	−1.54	Damaging
275	−1.29	Decrease	0.235	Stabilizing	0.407	Stabilizing
276	−0.5	Decrease	−0.018	Damaging	0.31	Stabilizing
277	−0.85	Decrease	−0.131	Damaging	−0.098	Damaging
278	−0.3	Decrease	−0.162	Damaging	−0.04	Damaging
279	−0.46	Decrease	0.152	Stabilizing	0.096	Stabilizing
280	−0.31	Decrease	−0.642	Damaging	−0.45	Damaging
281	0.22	Enhance	−0.481	Damaging	−0.154	Damaging
283	−0.7	Decrease	−0.927	Damaging	−0.935	Damaging
284	−0.52	Decrease	0.043	Stabilizing	0.025	Stabilizing
285	−0.13	Decrease	−1.119	Damaging	−0.996	Damaging
286	−0.8	Decrease	−0.131	Damaging	−0.21	Damaging
287	−1.24	Decrease	0.335	Stabilizing	0.197	Stabilizing
288	−0.45	Decrease	−0.863	Damaging	−0.798	Damaging
289	−0.5	Decrease	−0.369	Damaging	−0.14	Damaging
290	−1.19	Decrease	−0.442	Damaging	−0.65	Damaging
291	0.86	Enhance	−1.18	Damaging	−0.745	Damaging
292	0.52	Enhance	−1.572	Damaging	−1.227	Damaging
293	0.58	Enhance	−0.397	Damaging	−0.006	Damaging
294	−0.5	Decrease	−1.064	Damaging	−1.231	Damaging
295	−0.44	Decrease	−1.581	Damaging	−1.556	Damaging
296	−0.71	Decrease	−1.476	Damaging	−1.407	Damaging
297	0.59	Enhance	−1.611	Damaging	−1.089	Damaging
298	−1.7	Decrease	−2.091	Highly damaging	−2.354	Damaging
299	−0.51	Decrease	−1.611	Damaging	−1.737	Damaging

Abbreviation: ΔΔG: Difference in free energy between the mutant and wild−type proteins.

Table 3. Predicted cancer-associated CXCR1 mutations using the FATHMM server

Serial number	Mutation	Prediction
44	R135C	Cancer
45	R135L	Cancer
46	R135H	Cancer
95	N57D	Cancer
208	P302S	Cancer

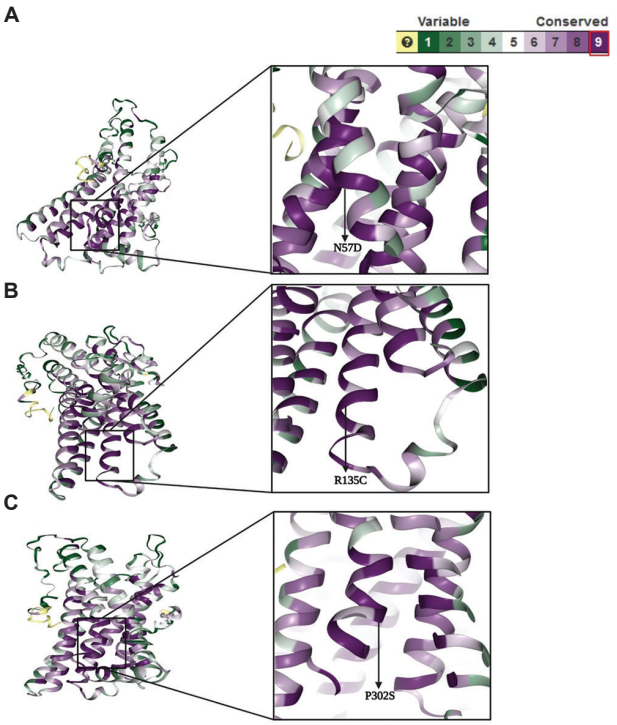

Figure 1. Residue conservation analysis of the N57D, R135C, and P302S residues of CXCR1 using the ConSurf server. (A) respresent that residues mutations N57D, (B) represent R135C, and (C) represent that P302S lyes in most consered regin of CXCR1 protein structure.

used to measure the model's quality.[65] The data revealed that 76.7% of the residues in the model were in the favored region of the native CXCR1 structure (Figure 2).

3.7. Molecular dynamic simulation of CXCR1

To understand the conformational changes caused by the N57D, R135C, and P302S mutations in the CXCR1 protein, a 100 ns MDS was performed. Various structural parameters, such as secondary structure elements (SSEs), were used to monitor the protein's behavior during the simulation.

The RMSD value can provide insight into the stability of protein structures. In this study, the RMSD was calculated for the backbone residues of the native and mutant CXCR1 proteins by comparing them with their original structures. As displayed in Figure 3A and C, the RMSD values for the mutant proteins (N57D, R135C, and P302S) were found to be highly unstable compared to those of the native protein. While the native protein remained stable during simulation, the mutant proteins took a longer time to stabilize. The RMSD values for the mutant proteins continuously increased from 25 to 45 ns, whereas the RMSD values for the native CXCR1 remained stable. These findings indicate that these mutations adversely affected protein stability and function. The RMSD for the mutant CXCR1 was approximately 8 Å (Figure 3C), while that for the native CXCR1 was approximately 4.4 Å (Figure 3A).

Next, we calculated the RMSF of the Cα atom to investigate the effect of mutated CXCR1 proteins on residue dynamics, i.e., protein stability and function. The RMSF values of the mutant structures were reportedly greater than those of the native structures, particularly for residues located between positions 150 and 200 (7.7 RMSF Å fluctuation) and between positions 300 and 350 (8 and 11 RMSF Å fluctuation) (Figure 4A and B).

3.8. Protein secondary structure elements

The SSE algorithm was used to investigate the structural flexibility of CXCR1 proteins.[60] Figure 5 displays the data on SSEs over time, allowing for a comparison of the structural changes between the native and mutant CXCR1 proteins. Both the native and mutant forms of the protein exhibited coils, α-helices, turns, bends, and β-sheets during the simulation. In contrast, the mutant protein displayed a significant rise in residues forming α-helices (Figure 5B), while the native protein exhibited a decrease in both loops and β-strands forming residues (Figure 5A).

3.9. Effects of mutant CXCR1 on protein secondary/tertiary structure elements

For homology modeling of normal and mutant CXCR1, the I-TASSER modeled structure was evaluated using UCSF Chimera calculations.[66] We performed homology modeling of the normal and mutant CXCR1 structures to assess the spatial arrangement of the conserved amino acids asparagine (N57), arginine (R135), and proline (P302), while the mutant amino acids included aspartic acid (57D), cysteine (135C), and serine (302S). This investigation was prompted by the observation of the highest sequence similarity and conserved sequence of CXCR1. We selected the structures of asparagine (N57), arginine (R135), and proline (P302), while the aspartic acid (57D), cysteine (135C), and serine (302S) mutants were used to generate a 3D model of CXCR1 using the I-TASSER online tool based on high C-scores. Notably, the C-score of the CXCR1

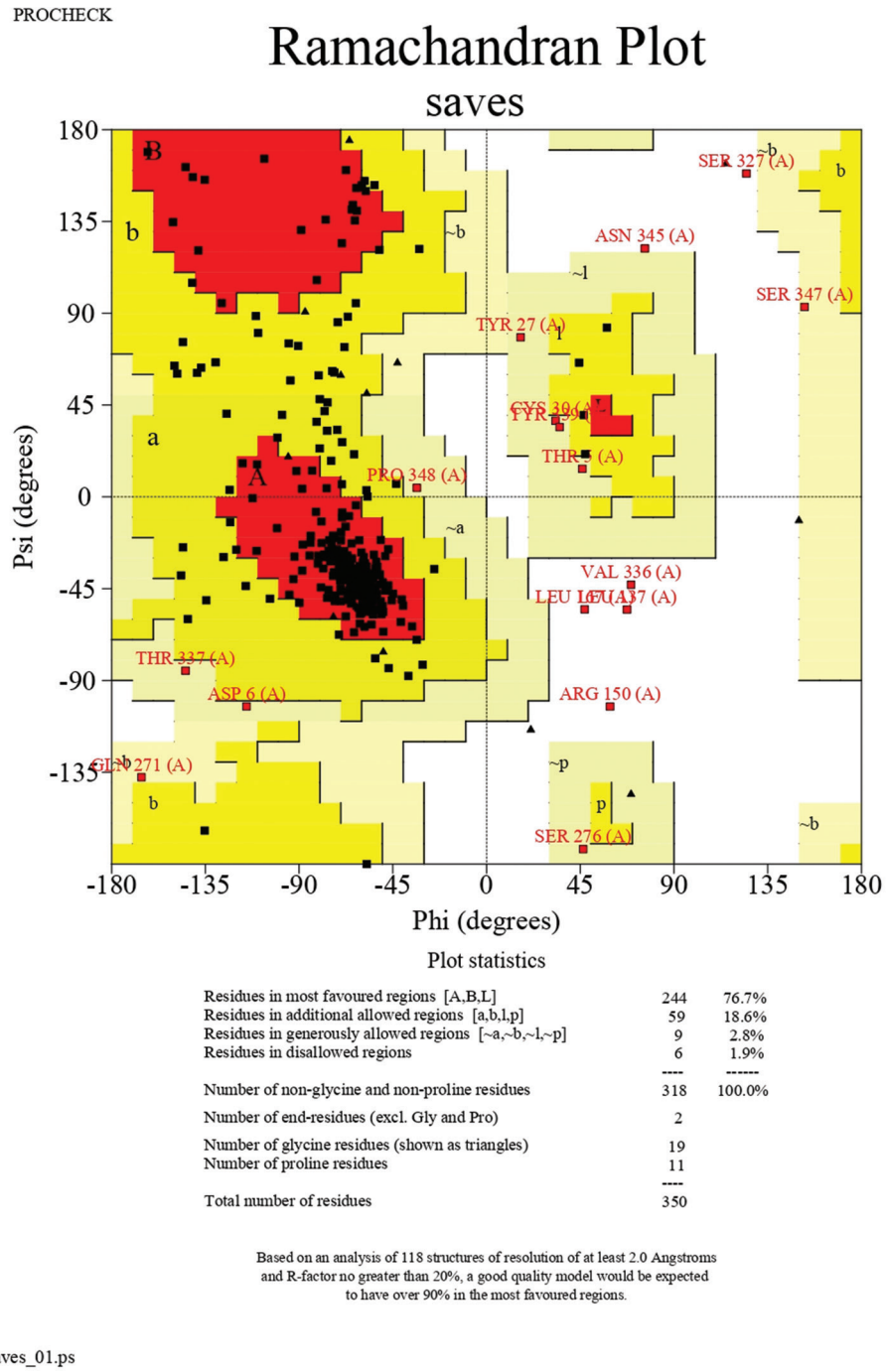

Figure 2. Ramachandran plot analysis to assess the quality of both native and mutant CXCR1 protein structures with a focus on the distribution of residues in the plot. The plot is displayed in a colored format to enable easier visualization.

normal line was -1.20, the template modeling score (TMS) was 0.56 ± 0.15, and the RMSD was 6.4 ± 3.9 Å, while the C-score of the CXCR1 mutant was -1.10, the TM-score was 0.54 ± 0.14, and the RMSD was 6.2 ± 3.7 Å.

The mutation of asparagine (N) to aspartic acid (D) in a protein induces changes in both secondary and tertiary structures. This difference is attributed to the distinct side-chain properties of the amino acids, facilitating local interactions and potentially altering the hydrogen bonding networks. The influence of mutations on electrostatic interactions and hydrophobic forces can further contribute to modifications in the overall folding and stability of

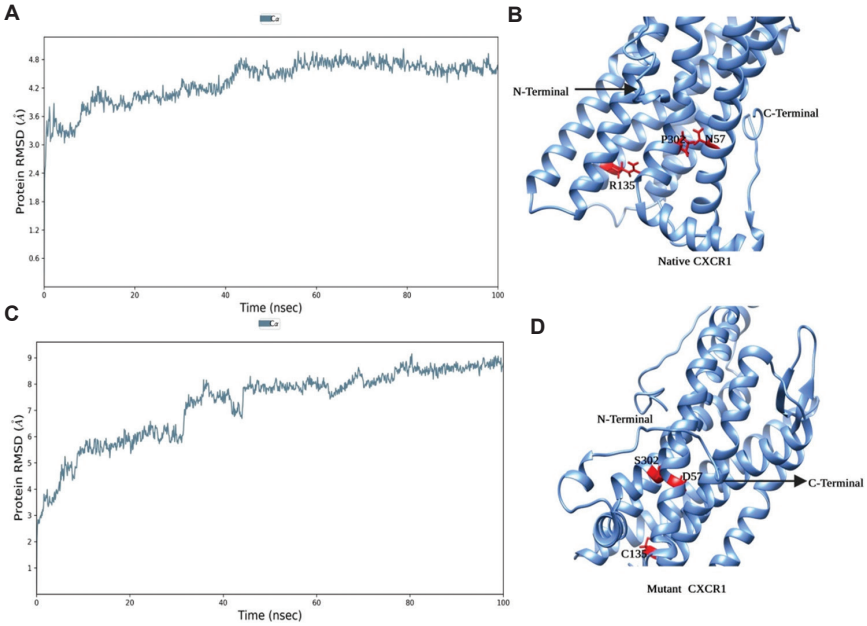

Figure 3. Molecular dynamic simulations of the native and mutant CXCR1 proteins over 100 ns and the backbone root-mean-square deviation (RMSD) of the two structures. (A) shows native protein remained stable during simulation with RMSD value of 4.4 Å. (B) represent normal 3D structure of CXCR1 with no effect on structure stability. (C) The RMSD values for mutant proteins N57D, R135C, and P302S, at 8 Å, indicate significant instability. (D) structure of CXCR1, post-point mutation, shows notable alterations, affecting protein stability and function.

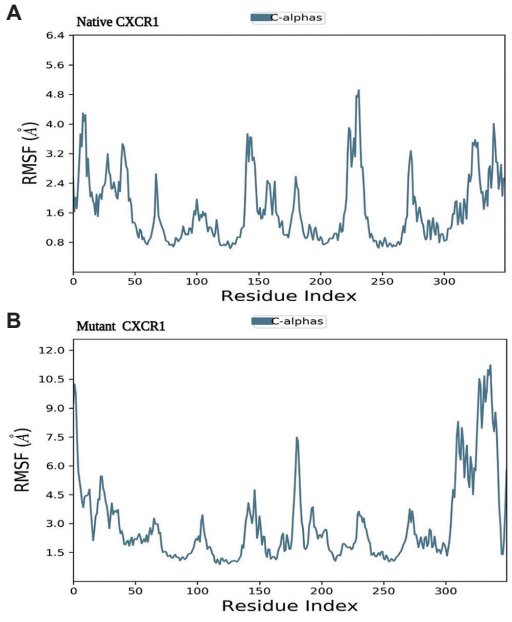

Figure 4. Analysis of the native CXCR1 protein structure following a molecular dynamic simulation. In terms of the root-mean-square fluctuation (RMSF) of the backbone alpha carbon (Cα) atoms over the simulation period. The y-axis of the plot represents the RMSF values, and the x-axis of the plot corresponds to each atom in the protein structure. (A) Represents lower RMSF values (4 Å fluctuation) notably for residues between positions 150 and 200, with values at positions 300 and 350 measuring 3.8 Å. (B) Shows higher RMSF values for mutant structures compared to native structures, with residues between positions 150 and 200 fluctuating at 7.7 Å and between positions 300 and 350 fluctuating at 8 and 11 Å, respectively.

proteins.[67] The changes in amino acid distances in the structure of the CXCR1 normal N57 and G56 amino acids was 5.9 Å, that of N57 and S58 was 10.4 Å, that of the D57 and G56 amino acids was 6.8 Å, and that of D57 with S58 was 9.7 Å (Figure 6A). The asparagine (N) at position 57 was likely involved in hydrogen bonding due to its polar nature. Substituting asparagine with aspartic acid (D) would introduce a negative charge. This change could disrupt hydrogen bonding interactions in the region, potentially affecting the local structure.

A point mutation of arginine (R) with cysteine (C) in a protein has notable effects on the secondary and tertiary structures. The differing side chain properties, including charge and length, disrupt local interactions, affecting the stability of secondary structures such as α-helices and β-sheets. In addition, this substitution can influence the overall 3D folding of the protein, altering its electrostatic interactions and potentially impacting its functional conformation.[68] In our study, the length of the normal CXCR1 R135 with D134 was 6.5 Å, the length of the R135 with the amino acid Y136 was 11.8 Å, the length of the C135 with D134 was 7.6 Å, and the length of the C135 with Y136 was 11 Å (Figure 6B). Arginine (R) at position 135 is a positively charged amino acid that may be involved in electrostatic interactions. Substituting arginine with cysteine (C) eliminates the positive charge and disrupts the protein's electrostatic interactions. In addition, cysteine

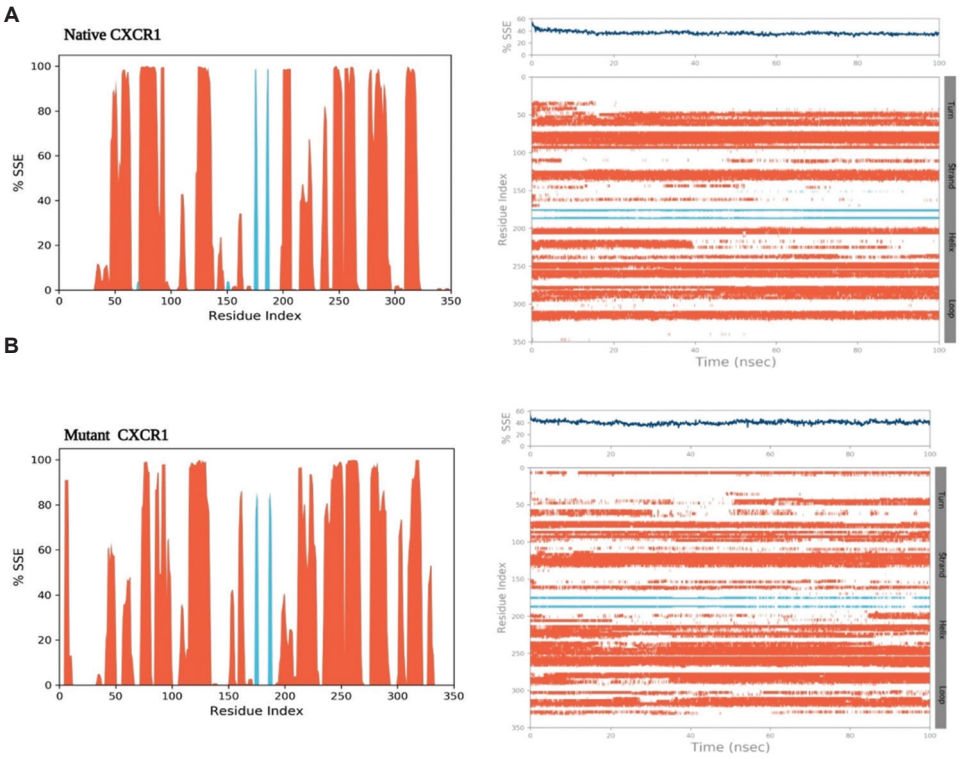

Figure 5. Time-dependent changes in the secondary structural element classification for both the native and mutant protein structures a 100-ns period. (A) Demonstrated a decrease in the residues forming both loops and β-strands. (B) Indicates a significant increase in residues forming α-helices.

can form disulfide bonds that can potentially alter the overall protein structure.

Substitution of proline (P) with serine (S) in a protein induces notable effects on both secondary and tertiary structures. When the cyclic, rigid side chain of proline is replaced with the flexible, hydroxyl-containing side chain of serine, the substitution disrupts the local conformations and regular secondary structures such as α-helices. At the tertiary level, the unique structural constraints imposed by proline are altered, influencing the overall 3D folding pattern of the protein.[69] In this study, the amino acid distances of the normal CXCR1 P302 amino acid with amino acids N301 and I303 were 6.7Å and 6.9Å, respectively (Figure 6C). In contrast, the amino acid distances of mutant CXCR1 S302 with N301 and I303 were 7.2Å and 8.9Å, respectively (Figure 6C). Nonetheless, structural variations were observed in terms of distance measurements and C-scores (Figure 6). These findings provided critical insights into the structural disparities and corresponding functional implications of CXCR1 among proteins and critical mutations.

4. Discussion

CXCR1 interacts with CXCL8 through its N-terminal β-strand.[17] The tertiary structures of the CXCL8 dimers were simulated in the present study. The CXCL8-CXCR1/2 signaling axis is implicated in the pathophysiology of various disorders, including chronic obstructive pulmonary disease (COPD), asthma, cystic fibrosis, and cancer. The interaction of CXCL8, which is released by some cancer cells, with CXCR1/2 in the tumor microenvironment is crucial in carcinogenesis and cancer metastasis.[6] Recent advancements in computational biology enabled the visualization of the disease status and genotype–phenotype association.[70] The integration of various bioinformatics approaches can identify potential missense mutations in genes that may have functional implications. This comprehensive methodology enables the exploration and detection of genetic variations that could impact the function and behavior of specific genes, thereby contributing to our understanding of their role in biological processes and disease development.[71] This study employed several bioinformatics methods to identify mutations in the CXCR1 gene that may be harmful and contribute to carcinogenesis. Through various analyses, we aimed to understand how these mutations could impact protein stability and function.

In the present study, by computational tools, 53 of the 299 mutations extracted from the public database were predicted to be deleterious (Table 1). Five mutations were

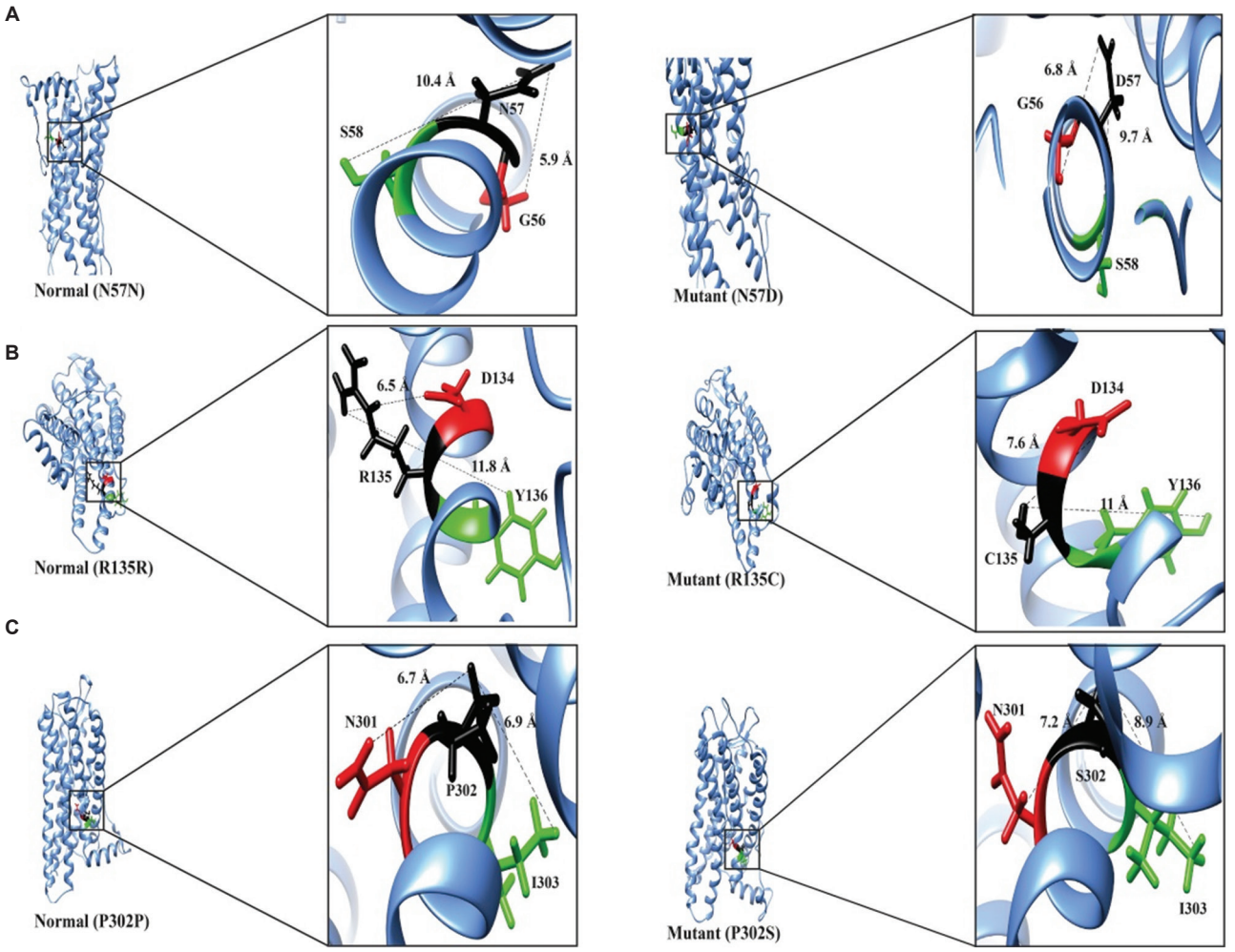

Figure 6. The structural impact of mutations on CXCR1, focusing on the conserved amino acids (N57, R135, and P302). (A) The asparagine (N) to aspartic acid (D) mutation at position 57 induced changes in amino acid distances, with N57–G56 at 5.9 Å and N57–S58 at 10.4 Å in the normal protein and D57–G56 at 6.8 Å and D57–S58 at 9.7 Å in the mutant protein. (B) The R-to-C mutation at position 135 exhibited alterations in bond distances, with R135–D134 at 6.5 Å and R135–Y136 at 11.8 Å in the normal protein and C135–D134 at 7.6 Å and C135–Y136 at 11 Å in the mutant protein. (C) The proline (P) to serine (S) mutation at position 302 exhibited variations in amino acid distances, with P302–N301 at 6.7 Å and P302–I303 at 6.9 Å in the normal protein and S302–N301 at 7.2 Å and S302–I303 at 8.9 Å in the mutant protein.

identified by FATHMM analysis as carcinogenic mutations (Table 3). We selected N57D, R135C, and P302S among the five mutations and conducted a conservation analysis that revealed the high conservation of the N57, R135, and P302 positions, with a conservation score of 9 (Figure 1A-C). A previous study revealed that the double mutants R199H/D265H and R203H/D265H, as well as the triple mutant R199H/R203H/D265H in CXCR1, failed to trigger an IL-8-dependent calcium response.[72] Interestingly, this mutation appears in the DRY motif and mostly resides in the TM region of CXCR1 for interaction with its ligands; it is also found at the IC end of TM3 in CXCR1, and it is also a highly conserved motif. The arginine residue (R) is conserved in 96% of receptors in this class.[73] The highly conserved DRY motif in CXCR1, particularly the conserved arginine residue (R), the TMs, TM1, TM3, and TM7, present promising opportunities for in-depth research to fully comprehend the influence of this motif on the structure, stability, and functionality of the protein.[74] Further investigations could shed light on how this motif contributes to the overall function of CXCR1.

Identifying the specific locus of the mutated amino acid can provide insight into how the mutation may alter the protein's overall structure and function. Numerous studies have examined how the location of mutations within a protein structure can affect its function. The relationships between mutation location and effects on protein structure, stability, and function have been investigated in

these studies to gain insights into disease development and progression.[23,75] Using I-TASSER, we modeled the native and mutant CXCR1 protein structures (Figure 3B and D) for MDS analysis to explore the structural consequences of the mutation on the protein structure. This approach allowed us to investigate the effect of the mutation on the overall structure of the protein. The RMSD data obtained from the simulations indicated that the mutant CXCR1 protein displayed a distinct and noticeable pattern of deviation throughout the entire simulation duration compared to the behavior observed for the native protein (Figure 3A and C). This finding suggested that the mutation significantly destabilized the CXCR1 protein, leading to structural alterations that are different from those observed in the native protein. The RMSF data provided additional evidence to corroborate the hypothesis that the mutation disrupts the stability of the protein structure (Figure 4A and B). The data revealed that the level of variation at the residue level was significantly greater in the mutant protein than in the wild-type protein, indicating that the mutation significantly altered the protein conformation and increased its flexibility. The SSE analysis indicated that the mutant protein exhibited a distinct alteration in the protein conformation, transitioning from an α-helix to a coil form, unlike the native protein (Figure 5A and B). This finding suggested that the mutation-induced changes in the protein's secondary structure, leading to a shift in its overall conformation. The observed conformational changes in our analysis offer compelling evidence that the substitution of amino acids in the mutant protein resulted in substantial alterations to its overall structure. These alterations resulted in mutant proteins that are less stable, more flexible, and less tightly packed than the native protein. Taken together, our results strongly indicated that the mutation had a significant and profound influence on both the structure and stability of the protein.

Previous studies have demonstrated the complementary nature of *in silico* approaches and wet laboratory experiments in understanding biological phenomena. The integration of computational methods with experimental techniques has proven to be a powerful tool for predicting and validating hypotheses in a range of biological systems.[70,76] The combination of computational mutation predictions with MDS analysis has been instrumental in identifying disease-causing mutations.[77] This approach has enabled the identification of the most deleterious mutations from a large pool of mutations, providing valuable insights into the molecular basis of various diseases.[78] Computational methods play a vital role in establishing the groundwork for genetic research aimed at comprehending the molecular foundations of diseases.[79] These methods facilitate the detection of mutations that contribute to diseases and assist in the exploration of potential therapeutic strategies. Moreover, such computational methods can assist in the clinical assessment of genetic variants,[70,76] enabling more informed and effective treatment decisions.

5. Conclusion

In silico investigations of the TM domains of CXCR1 (TM1, TM3, and TM7) revealed N57D, R135C, and P302S point mutations as potential carcinogenic variants. In addition, MDS analysis indicated that these mutations lead to changes in the structural stability of the protein, including increased flexibility and reduced compactness. The structural instability of the mutant protein could lead to an inability to interact with the CXCL8 ligand and other associated proteins, which may have implications for cancer development. The molecular understanding attained through this study could serve as a foundation for *in vitro* and *in vivo* experiments investigating the effect of N57D, R135C, and P302S mutations on the interaction of CXCR1 with its ligand and its association with disease development.

Acknowledgments

None.

Funding

This work was supported by the National Natural Science Foundation of China (32270438, 32170498, 31970388), National Key Research and Development Program of China (2021YFF0702000, 2018YFD0900602), 1.3.5 Project for Disciplines of Excellence by the West China Hospital, Sichuan University (ZYJC21050), Science and Technology Department of Sichuan Province (2022YFH0116), Priority Academic Program Development of Jiangsu Higher Education Institutions (PAPD), and the National Clinical Research Center for Geriatrics, West China Hospital, Sichuan University (Z2023JC003).

Conflict of interest

The authors declare no conflict of interest.

Author contributions

Conceptualization: Shah Kamal, Gohar Mushtaq, Muhammad Nasir Iqbal

Formal analysis: Shah Kamal, Amanullah Amanullah, Qingqing Wang, Najeeb Ullah, Muhammad Nasir Iqbal

Writing – original draft: Shah Kamal, Gohar Mushtaq, Mohammad Amjad Kamal

Writing – review & editing: Gohar Mushtaq, Mohammad Amjad Kamal, Najeeb Ullah

Ethics approval and consent to participate

Not applicable.

Consent for publication

Not applicable.

Availability of data

All datasets generated for this study are available on request from the corresponding authors.

References

1. Yang D, Zhou Q, Labroska V, *et al*. G protein-coupled receptors: Structure-and function-based drug discovery. *Signal Transduct Target Ther.* 2021;6(1):7.

   doi: 10.1038/s41392-020-00435-w

2. Katritch V, Cherezov V, Stevens RC. Diversity and modularity of G protein-coupled receptor structures. *Trends Pharmacol Sci.* 2012;33(1):17-27.

   doi: 10.1016/j.tips.2011.09.003

3. Berman HM, Westbrook J, Feng Z, *et al*. The protein data bank. *Nucleic Acids Res.* 2000;28(1):235-242.

   doi: 10.1093/nar/28.1.235

4. Rajagopalan L, Rajarathnam K. Ligand selectivity and affinity of chemokine receptor CXCR1. Role of N-terminal domain. *J Biol Chem.* 2004;279(29):30000-30008.

   doi: 10.1074/jbc.M313883200

5. Holmes WE, Lee J, Kuang WJ, Rice GC, Wood WI. Structure and functional expression of a human interleukin-8 receptor. Science. 1991;253(5025):1278-1280. *J Immun.* 2009;183(5):2895-2897.

   doi: 10.1126/science.1840701

6. Ha H, Debnath B, Neamati N. Role of the CXCL8-CXCR1/2 axis in cancer and inflammatory diseases. *Theranostics.* 2017;7(6):1543-1588.

   doi: 10.7150/thno.15625

7. Park SH, Das BB, Casagrande F, *et al*. Structure of the chemokine receptor CXCR1 in phospholipid bilayers. *Nature.* 2012;491(7426):779-783.

   doi: 10.1038/nature11580

8. Sojka AC, Brennan KM, Maizels ET, Young CD. The science behind g protein-coupled receptors (GPCRs) and their accurate visual representation in scientific research. *J Biocommun.* 2017;41(1):e6.

   doi: 10.5210/jbc.v41i1.7309

9. Hofmann KP, Scheerer P, Hildebrand PW, *et al*. A G protein-coupled receptor at work: The rhodopsin model. *Trends Biochem Sci.* 2009;34(11):540-552.

   doi: 10.1016/j.tibs.2009.07.005

10. Park JH, Scheerer P, Hofmann KP, Choe HW, Ernst OP. Crystal structure of the ligand-free G-protein-coupled receptor opsin. *Nature.* 2008;454(7201):183-187.

    doi: 10.1038/nature07063

11. Vauquelin G, Van Liefde I. G protein-coupled receptors: A count of 1001 conformations. *Fundam Clin Pharmacol.* 2005;19(1):45-56.

    doi: 10.1111/j.1472-8206.2005.00319.x

12. Rosenbaum DM, Rasmussen SGF, Kobilka BK. The structure and function of G-protein-coupled receptors. *Nature.* 2009;459(7245):356-363.

    doi: 10.1038/nature08144

13. Rosenbaum DM, Cherezov V, Hanson MA, *et al*. GPCR engineering yields high-resolution structural insights into beta2-adrenergic receptor function. *Science.* 2007;318(5854):1266-1273.

    doi: 10.1126/science.1150609

14. Landau EM, Rosenbusch JP. Lipidic cubic phases: A novel concept for the crystallization of membrane proteins. *Proc Natl Acad Sci U S A.* 1996;93(25):14532-14535.

    doi: 10.1073/pnas.93.25.14532

15. Oldham WM, Hamm HE. Heterotrimeric G protein activation by G-protein-coupled receptors. *Nat Rev Mol Cell Biol.* 2008;9(1):60-71.

    doi: 10.1038/nrm2299

16. Leong SR, Kabakoff RC, Hébert CA. Complete mutagenesis of the extracellular domain of interleukin-8 (IL-8) type A receptor identifies charged residues mediating IL-8 binding and signal transduction. *J Biol Chem.* 1994;269(30):19343-19348.

17. Skelton NJ, Quan C, Reilly D, Lowman H. Structure of a CXC chemokine-receptor fragment in complex with interleukin-8. *Structure.* 1999;7(2):157-168.

    doi: 10.1016/S0969-2126(99)80022-7

18. Hébert CA, Vitangcol RV, Baker JB. Scanning mutagenesis of interleukin-8 identifies a cluster of residues required for receptor binding. *J Biol Chem.* 1991;266(28):18989-18994.

19. Nicholls DJ, Tomkinson NP, Wiley KE, *et al*. Identification of a putative intracellular allosteric antagonist binding-site in the CXC chemokine receptors 1 and 2. *Mol Pharmacol.* 2008;74(5):1193-1202.

    doi: 10.1124/mol.107.044610

20. Han X, Feng Y, Chen X, Gerard C, Boisvert WA. Characterization of G protein coupling mediated by the conserved D134(3.49) of DRY motif, M241(6.34), and F251(6.44) residues on human CXCR1. *FEBS Open Bio.* 2015;5:182-190.

    doi: 10.1016/j.fob.2015.03.001

21. Huynh N, Mallik B, Zhang L, Martins-Green M, Morikis D. Computational studies of CXCR1, the receptor of IL-8/CXCL8, using molecular dynamics and electrostatics. *Biopolymers.* 2008;89(1):52-61.

doi: 10.1002/bip.20851

22. Pandurangan AP, Blundell TL. Prediction of impacts of mutations on protein structure and interactions: SDM, a statistical approach, and mCSM, using machine learning. *Protein Sci.* 2020;29(1):247-257.

doi: 10.1002/pro.3774

23. Capriotti E, Altman RB, Bromberg Y. Collective judgment predicts disease-associated single nucleotide variants. *BMC Genomics.* 2013;14(Suppl 3):S2.

doi: 10.1186/1471-2164-14-S3-S2

24. López-Ferrando V, Gazzo A, de la Cruz X, Orozco M, Gelpí JL. PMut: A web-based tool for the annotation of pathological variants on proteins, 2017 update. *Nucleic Acids Res.* 2017;45(W1):W222-W228.

doi: 10.1093/nar/gkx313

25. Choi Y, Chan AP. PROVEAN web server: A tool to predict the functional effect of amino acid substitutions and indels. *Bioinformatics.* 2015;31(16):2745-2747.

doi: 10.1093/bioinformatics/btv195

26. Rogers MF, Shihab HA, Mort M, Cooper DN, Gaunt TR, Campbell C. FATHMM-XF: Accurate prediction of pathogenic point mutations via extended features. *Bioinformatics.* 2018;34(3):511-513.

doi: 10.1093/bioinformatics/btx536

27. Pires DE, Ascher DB, Blundell TL. mCSM: Predicting the effects of mutations in proteins using graph-based signatures. *Bioinformatics.* 2014;30(3):335-342.

doi: 10.1093/bioinformatics/btt691

28. Worth CL, Preissner R, Blundell TL. SDM--a server for predicting effects of mutations on protein stability and malfunction. *Nucleic Acids Res.* 2011;39:W215-222.

doi: 10.1093/nar/gkr363

29. Pires DE, Ascher DB, Blundell TL. DUET: A server for predicting effects of mutations on protein stability using an integrated computational approach. *Nucleic Acids Res.* 2014;42:W314-W319.

doi: 10.1093/nar/gku411

30. Martin FJ, Amode MR, Aneja A, *et al.* Ensembl 2023. *Nucleic Acids Res.* 2023;51(D1):D933-D941.

doi: 10.1093/nar/gkac958

31. Sherry ST, Ward MH, Kholodov M, *et al.* dbSNP: The NCBI database of genetic variation. *Nucleic Acids Res.* 2001;29(1):308-311.

doi: 10.1093/nar/29.1.308

32. UniProt Consortium. UniProt: A hub for protein information. *Nucleic Acids Res.* 2015;43:D204-D212.

doi: 10.1093/nar/gku989

33. Goodsell DS, Zardecki C, Di Costanzo L, *et al.* RCSB protein data bank: Enabling biomedical research and drug discovery. *Protein Sci.* 2020;29(1):52-65.

doi: 10.1002/pro.3730

34. Hecht M, Bromberg Y, Rost B. Better prediction of functional effects for sequence variants. *BMC Genomics.* 2015;16(Suppl 8):S1.

doi: 10.1186/1471-2164-16-S8-S1

35. Mi H, Lazareva-Ulitsky B, Loo R, *et al.* The PANTHER database of protein families, subfamilies, functions and pathways. *Nucleic Acids Res.* 2005;33:D284-D288.

doi: 10.1093/nar/gki078

36. Ng PC, Henikoff S. SIFT: Predicting amino acid changes that affect protein function. *Nucleic Acids Res.* 2003;31(13):3812-3814.

doi: 10.1093/nar/gkg509

37. Bendl J, Stourac J, Salanda O, *et al.* PredictSNP: Robust and accurate consensus classifier for prediction of disease-related mutations. *PLoS Comput Biol.* 2014;10(1):e1003440.

doi: 10.1371/journal.pcbi.1003440

38. Pejaver V, Mooney SD, Radivojac P. Missense variant pathogenicity predictors generalize well across a range of function-specific prediction challenges. *Hum Mutat.* 2017;38(9):1092-1108.

doi: 10.1002/humu.23258

39. Ghosh M, Sodhi SS, Sharma N, *et al.* An integrated *in silico* approach for functional and structural impact of non-synonymous SNPs in the MYH1 gene in Jeju Native Pigs. *BMC Genet.* 2016;17:35.

doi: 10.1186/s12863-016-0341-1

40. Vila JA. Proteins' evolution upon point mutations. *ACS Omega.* 2022;7(16):14371-14376.

doi: 10.1021/acsomega.2c01407

41. Pandurangan AP, Ochoa-Montaño B, Ascher DB, Blundell TL. SDM: A server for predicting effects of mutations on protein stability. *Nucleic Acids Res.* 2017;45(W1):W229-W235.

doi: 10.1093/nar/gkx439

42. Choudhury A, Mohammad T, Anjum F, *et al.* Comparative analysis of web-based programs for single amino acid substitutions in proteins. *PLoS One.* 2022;17(5):e0267084.

doi: 10.1371/journal.pone.0267084

43. AlAjmi MF, Khan S, Choudhury A, *et al.* Impact of deleterious mutations on structure, function and stability of serum/glucocorticoid regulated kinase 1: A gene to diseases correlation. *Front Mol Biosci.* 2021;8:780284.

doi: 10.3389/fmolb.2021.780284

44. Rodrigues CHM, Myung Y, Pires DEV, Ascher DB. mCSM-PPI2: Predicting the effects of mutations on protein-protein interactions. *Nucleic Acids Res.* 2019;47(W1):W338-W344.

doi: 10.1093/nar/gkz383

45. Mutlu G, Acı Çİ. SVM-SMO-SGD: A hybrid-parallel support vector machine algorithm using sequential minimal optimization with stochastic gradient descent. *Parallel Comput.* 2022;113:102955.

doi: 10.1016/j.parco.2022.102955

46. Shihab HA, Gough J, Cooper DN, Day INM, Gaunt TR. Predicting the functional consequences of cancer-associated amino acid substitutions. *Bioinformatics.* 2013;29(12):1504-1510.

doi: 10.1093/bioinformatics/btt182

47. Zhang Y. I-TASSER server for protein 3D structure prediction. *BMC Bioinformats.* 2008;9:40.

doi: 10.1186/1471-2105-9-40

48. Ishimoto N, Park JH, Kawakami K, *et al*. Structural basis of CXC chemokine receptor 1 ligand binding and activation. *Nat Commun*. 2023;14(1):4107.

doi: 10.1038/s41467-023-39799-2

49. Lovell SC, Davis IW, Arendall WB 3rd, *et al*. Structure validation by Calpha geometry: Phi,psi and Cbeta deviation. *Proteins*. 2003;50(3):437-450.

doi: 10.1002/prot.10286

50. Kc DB. Recent advances in sequence-based protein structure prediction. *Brief Bioinform.* 2017;18(6):1021-1032.

doi: 10.1093/bib/bbw070

51. Hollingsworth SA, Dror RO. Molecular Dynamics Simulation for All. *Neuron.* 2018;99(6):1129-1143.

doi: 10.1016/j.neuron.2018.08.011

52. Muhammed MT, Aki-Yalcin E. Homology modeling in drug discovery: Overview, current applications, and future perspectives. *Chem Biol Drug Des*. 2019;93(1):12-20.

doi: 10.1111/cbdd.13388

53. Brooks BR, Brooks CL 3rd, Mackerell AD Jr, *et al*. CHARMM: The biomolecular simulation program. *J Comput Chem.* 2009;30(10):1545-1614.

doi: 10.1002/jcc.21287

54. Rasheed MA, Iqbal MN, Saddick S, *et al*. Identification of lead compounds against Scm (fms10) in *Enterococcus faecium* using computer aided drug designing. *Life (Basel).* 2021;11(2):77.

doi: 10.3390/life11020077

55. Hildebrand PW, Rose AS, Tiemann JKS. Bringing molecular dynamics simulation data into view. *Trends Biochem Sci.* 2019;44(11):902-913.

doi: 10.1016/j.tibs.2019.06.004

56. Ferreira LG, Dos Santos RN, Oliva G, Andricopulo AD. Molecular docking and structure-based drug design strategies. *Molecules.* 2015;20(7):13384-13421.

doi: 10.3390/molecules200713384

57. Shivakumar D, Williams J, Wu Y, Damm W, Shelley J, Sherman W. Prediction of absolute solvation free energies using molecular dynamics free energy perturbation and the OPLS force field. *J Chem Theory Comput.* 2010;6(5):1509-1519.

doi: 10.1021/ct900587b

58. Huang Y, Li Z, Hong Q, *et al*. A stepwise docking molecular dynamics approach for simulating antibody recognition with substantial conformational changes. *Comput Struct Biotechnol J.* 2022;20:710-720.

doi: 10.1016/j.csbj.2022.01.012

59. Hung LH, Guerquin M, Samudrala R. GPU-Q-J, a fast method for calculating root mean square deviation (RMSD) after optimal superposition. *BMC Res Notes.* 2011;4:97.

doi: 10.1186/1756-0500-4-97

60. Carter P, Andersen CAF, Rost B. DSSPcont: Continuous secondary structure assignments for proteins. *Nucleic Acids Res.* 2003;31(13):3293-3295.

doi: 10.1093/nar/gkg626

61. Ashkenazy H, Abadi S, Martz E, *et al*. ConSurf 2016: An improved methodology to estimate and visualize evolutionary conservation in macromolecules. *Nucleic Acids Res.* 2016;44(W1):W344-W350.

doi: 10.1093/nar/gkw408

62. Wang Y, Park JH, Lupala CS, *et al*. Computer aided protein engineering to enhance the thermo-stability of CXCR1-T4 lysozyme complex. *Sci Rep.* 2019;9(1):5317.

doi: 10.1038/s41598-019-41838-2

63. Yang J, Zhang Y. Protein structure and function prediction using I-TASSER. *Curr Protoc Bioinformatics.* 2015;52:5.8.1-5.8.15.

doi: 10.1002/0471250953.bi0508s52

64. Roy A, Kucukural A, Zhang Y. I-TASSER: A unified platform for automated protein structure and function prediction. *Nat Protoc.* 2010;5(4):725-738.

doi: 10.1038/nprot.2010.5

65. Sobolev OV, Afonine PV, Moriarty NW, *et al*. A global Ramachandran score identifies protein structures with unlikely stereochemistry. *Structure.* 2020;28(11):1249-1258.e2.

doi: 10.1016/j.str.2020.08.005

66. Guzzi AF, Oliveira FSL, Amaro MMS, Tavares-Filho PF, Gabriel JE. *In silico* prediction of the functional and structural consequences of the non-synonymous single nucleotide polymorphism A122V in bovine CXC chemokine receptor

type 1. *Braz J Biol.* 2020;80(1):39-46.

doi: 10.1590/1519-6984.188655

67. Kato K, Nakayoshi T, Kurimoto E, Oda A. Mechanisms of deamidation of asparagine residues and effects of main-chain conformation on activation energy. *Int J Mol Sci.* 2020;21(19):7035.

doi: 10.3390/ijms21197035

68. Chakkalakal SA, Heilig J, Baumann U, Paulsson M, Zaucke F. Impact of arginine to cysteine mutations in collagen II on protein secretion and cell survival. *Int J Mol Sci.* 2018;19(2):541.

doi: 10.3390/ijms19020541

69. Ganguly HK, Basu G. Conformational landscape of substituted prolines. *Biophys Rev.* 2020;12(1):25-39.

doi: 10.1007/s12551-020-00621-8

70. Zaki OK, Krishnamoorthy N, El Abd HS, *et al*. Two patients with Canavan disease and structural modeling of a novel mutation. *Metab Brain Dis.* 2017;32(1):171-177.

doi: 10.1007/s11011-016-9896-9

71. Agrahari AK, Kumar A, Siva R, Zayed H, Doss CGP. Substitution impact of highly conserved arginine residue at position 75 in GJB1 gene in association with X-linked Charcot-Marie-tooth disease: A computational study. *J Theor Biol.* 2018;437:305-317.

doi: 10.1016/j.jtbi.2017.10.028

72. Suetomi K, Rojo D, Navarro J. Identification of a signal transduction switch in the chemokine receptor CXCR1. *J Biol Chem.* 2002;277(35):31563-31566.

doi: 10.1074/jbc.M204713200

73. Mirzadegan T, Benkö G, Filipek S, Palczewski K. Sequence analyses of G-protein-coupled receptors: Similarities to rhodopsin. *Biochemistry.* 2003;42(10):2759-2767.

doi: 10.1021/bi027224+

74. Rovati GE, Capra V, Neubig RR. The highly conserved DRY motif of class A G protein-coupled receptors: Beyond the ground state. *Mol Pharmacol.* 2007;71(4):959-964.

doi: 10.1124/mol.106.029470

75. Arshad M, Bhatti A, John P. Identification and *in silico* analysis of functional SNPs of human TAGAP protein: A comprehensive study. *PLoS One.* 2018;13(1):e0188143.

doi: 10.1371/journal.pone.0188143

76. Mosaeilhy A, Mohamed MM, Doss CGP, *et al*. Genotype-phenotype correlation in 18 Egyptian patients with glutaric acidemia type I. *Metab Brain Dis.* 2017;32(5):1417-1426.

doi: 10.1007/s11011-017-0006-4

77. Zhao F, Zheng L, Goncearenco A, Panchenko AR, Li M. Computational approaches to prioritize cancer driver missense mutations. *Int J Mol Sci.* 2018;19(7):2113.

doi: 10.3390/ijms19072113

78. Chun S, Fay JC. Identification of deleterious mutations within three human genomes. *Genome Res.* 2009;19(9):1553-1561.

doi: 10.1101/gr.092619.109.

79. Li J, Wei Z, Hakonarson H. Application of computational methods in genetic study of inflammatory bowel disease. *World J Gastroenterol.* 2016;22(3):949-960.

doi: 10.3748/wjg.v22.i3.949

ACCSCIENCE PUBLISHING

Tumor Discovery

ORIGINAL RESEARCH ARTICLE

Matrix metalloproteinase-1 as a potential biomarker for early gastric cancer detection and its effect on gastric cancer cell proliferation and migration

Ke Yi[1†], Yan Hu[1†], Xiaoli Zhu[2†], and Qing Li[2*]

[1]Central Laboratory, The First People's Hospital of Taicang, Soochow Medical College of Soochow University, Taicang Affiliated Hospital of Soochow University, Suzhou, China

[2]Department of Gastroenterology, The First People's Hospital of Taicang, Soochow Medical College of Soochow University, Taicang Affiliated Hospital of Soochow University, Suzhou, China

Abstract

The present study aimed to investigate the association between matrix metalloproteinase-1 (MMP-1) and early gastric cancer (EGC), while also evaluating the effect of MMP-1 on gastric cancer cell proliferation and migration. Transcriptome RNA sequencing and database analysis were conducted to assess the relationship between MMP-1 expression and EGC. Differences in MMP-1 expression between clinical EGC samples and paracancerous tissues were detected using fluorescence quantitative polymerase chain reaction (PCR). In N87 gastric cancer cells, changes in proliferation- and migration-related indicator expression were determined. Gene sequencing revealed differential expression of MMP-1 in early and advanced gastric cancers. Furthermore, enhanced MMP-1 expression was observed in early and advanced gastric cancer tissues, exhibiting a positive correlation with the malignant phenotype in gastric cancer cell lines. Fluorescence quantitative PCR revealed considerably higher MMP-1 expression in EGC tissues than in paracancerous tissues. CCK8 and EdU assays demonstrated a significant increase in N87 cell proliferation on MMP-1 upregulation and a decrease on its downregulation. The scratch assay results demonstrated a corresponding enhancement in N87 cell migratory capacity with MMP-1 upregulation, which was attenuated on its downregulation. Western blot experiments revealed a decrease in the expression of the epithelial-mesenchymal transition-related protein E-cadherin after MMP-1 upregulation, while vimentin expression significantly increased. Conversely, the downregulation of MMP-1 led to opposite outcomes. Overall, MMP-1 emerges as a potential biomarker for EGC diagnosis and plays a crucial role in the regulation of N87 gastric cancer cell proliferation and migration.

Keywords: Proliferation; Gastric cancer; MMP-1; Early diagnosis; Migration

1. Introduction

Gastric cancer is among the most prevalent cancers worldwide, ranking as the third most common cancer after breast and lung cancers, and represents the second leading cause of

†*These authors contributed equally to this work.*

***Corresponding author:**
Qing Li
(liqing66878@suda.edu.cn)

Citation: Yi K, Hu Y, Zhu X, Li Q. Matrix metalloproteinase-1 as a potential biomarker for early gastric cancer detection and its effect on gastric cancer cell proliferation and migration. *Tumor Discov*. 2024;3(1):1973.
https://doi.org/10.36922/td.1973

Received: September 28, 2023
Accepted: January 12, 2024
Published Online: March 26, 2024

cancer-related deaths in Asia.[1] Gastric cancer encompasses two main classifications: early and advanced stages. In early gastric cancer (EGC), lesions are confined to the mucosal and submucosal layers of the gastric wall. EGC patients typically exhibit a 5-year survival rate exceeding 90%, whereas, for advanced gastric cancer patients, this rate drops below 30%. The incidence rate of gastric cancer increases progressively with age, with a median age of 70 years at diagnosis, and the prognosis is usually poor. Approximately 10% of gastric cancers are detected in patients aged 45 years or younger. Therefore, early diagnosis of gastric cancer plays a vital role in improving patient prognosis and reducing mortality, which are keys to improving survival rates.[2,3]

Matrix metalloproteinases (MMPs), produced by both tumor cells and normal cells, are also known as interstitial collagenases. Among the MMPs, matrix metalloproteinase-1 (MMP-1) is one of the most commonly expressed types. The overexpression of MMP-1 is correlated with metastasis, inflammation, and tumor invasion,[4,5] highlighting its significant role in the pathogenesis of gastric cancer.[6,7] A comprehensive study involving 1,377 cases and 1,543 controls showed that the MMP1-1607 1G > 2G polymorphism was associated with a significantly elevated risk of gastric cancer.[8] Furthermore, in tumors, MMP-1 overexpression has been reported to be correlated with increased invasive and migratory capacities of hepatocellular carcinoma cells.[9]

In the present study, gene sequencing revealed that the enhanced expression of MMP-1 is correlated with the malignant properties of gastric cells in both early and advanced gastric cancer. Furthermore, an analysis of 20 pairs of EGC and paracancerous tissue samples demonstrated that elevated MMP-1 expression levels exhibited high sensitivity and specificity in identifying EGC. Therefore, MMP-1 holds promise as a potential diagnostic marker for EGC and plays a regulatory role in gastric cancer cells.

2. Materials and methods

2.1. Materials

The NCI-N87 human gastric cancer cell line utilized in the present research was purchased from the Shanghai Cell Bank of the Chinese Academy of Sciences, China. The human-derived MMP-1 gene shRNA downregulation vector, overexpression vector, and pLent-U6-GFP-Puro negative control plasmid with a nonsense sequence were constructed by Shandong WZ Biosciences Inc., China. The specific shRNA sequences used were as follows: sh1: 5'-GCTAGCTCAGGATGACATTGATT C A A G A G A T C A A T G T C A T C C T G A G C T A G CTTTTTT-3' and sh2:5'-GCGTGTG ACAGTAAGCTA A C C T T C A A G A G A G G T T A G C T T A C T G T C A CACGCTTTTTT-3'. Other reagents employed in this study included: 1640 medium (Hyclone, USA); fetal bovine serum (BI, Zhejiang Sorfa Life Science Research Co., Ltd., China); Lipofectamine 3000 (Thermo Fisher Scientific, USA); Penicillin-Streptomycin solution (Shanghai Beyotime Biotechnology Co., Ltd., China); trypsin ((Shanghai Beyotime Biotechnology Co., Ltd., China); SDS-PAGE assay kit (Shanghai Beyotime Biotechnology Co., Ltd., China); ECL assay kit ((Shanghai Beyotime Biotechnology Co., Ltd., China); RIPA lysis buffer (Shanghai Beyotime Biotechnology Co., Ltd., China); BCA assay kit (Shanghai Beyotime Biotechnology Co., Ltd., China); CCK8 assay kit (MCE, China); and an EDU assay kit (Guangzhou RiboBio Co., Ltd., China).

2.2. Cell culture, cell transfection, and grouping

The 1640 culture medium, consisting of 10% fetal bovine serum and 1% double antibodies, was used to culture NCI-N87 human gastric cancer cells (hereafter referred to as N87) under culture conditions of 5% CO_2 at 37°C. During the logarithmic growth phase, good-condition N87 cells were cultured into 6-well plates and transfected when they reached an approximately 70% growth rate. The MMP-1-overexpression plasmid (Ad-MMP-1), two RNA-interference plasmids, and corresponding controls were transfected using Lipofectamine 3000, and the cells were further cultured.

2.3. Cell proliferation

Transfected N87 cells were inoculated into 96-well plates at a density of 5000 cells/well, with each well containing 100 μL of medium. Six replicate wells were prepared for each experiment to ensure experimental accuracy.

2.3.1. CCK8 assays

After incubation for 24, 48, and 72 h, 10 μL of CCK8 reagent was added to each well and incubated for an hour. The optical density values were measured at 450 nm using a multifunction microplate reader, and the data were subsequently analyzed.

2.3.2. EdU assays

After 24 h of incubation, the cells were treated with the EdU reagent and incubated for an additional 2 h for labeling. Subsequently, the cells were fixed with 4% paraformaldehyde and treated with 0.5% Triton X-100, followed by Apollo dye for 30 min. Cells were washed three times with PBS and then stained with Hoechst nuclear dye at a ratio of 1:100 for 10 min. After washing, cells were imaged and counted for further analysis.

2.4. Cell migration

During the logarithmic growth phase, N87 cells were inoculated into a 6-well plate. When the cell growth rate reached 80%, Ad-MMP-1, the two interference plasmids and the corresponding controls were transfected with Lipofectamine 3000 at specific concentrations. Subsequently, a 200-μL pipette tip was used to make scratches, and the medium was replaced with a new medium containing 1% serum. Images were captured to document the initial (0-h) scratch data. Following incubation under low-serum culture conditions for 48 h, the scratch was imaged to record the 48-h data. The changes in the scratch-wound area and the differences between the groups were calculated and compared using the ImageJ software.

2.5. Western blotting

Total protein was extracted from transfected N87 cells using RIPA lysis buffer, and their concentrations were measured using a BCA kit. Then, the cells were mixed with SDS buffer for 5 min at 100°C to prepare the samples. After SDS-PAGE electrophoresis, the proteins were transferred to polyvinylidene difluoride membranes using electrophoresis equipment. Immunoreactivity was measured after blocking with 5% skim milk. Images were captured using a chemiluminescence imaging system, and any differences observed were analyzed.

2.6. Statistical methods

GraphPad 9.0 software was utilized to conduct all statistical analyses of the data. The mean values of the two groups were compared using an independent-sample *t*-test. A $P < 0.05$ indicated a significant difference.

3. Results

3.1. MMP-1 as the potential diagnostic marker for EGC

After whole-transcriptome RNA sequencing and subsequent bioinformatics analysis, three pairs of early and advanced gastric cancer cells, along with their paracancerous tissues, were derived using clinical endoscopy. Pathological examination confirmed the samples, which were then subjected to analysis. Nearly 1,831 differentially expressed coding genes were present in advanced gastric cancer, whereas there were only 121 differentially expressed coding genes in EGC (Figure 1A). A heat map revealed 44 differentially expressed genes in both early and advanced gastric cancer, of which 17 were upregulated, including *MMP-1* (Figure 1B). The membrane surface protein molecule, MMP-1, was initially screened due to its higher expression levels in both early and advanced gastric cancer tissues. Its expression level was correlated with the malignant phenotype of gastric cancer cell lines (Figure 1). A search of The Cancer Genome Altlas database revealed the presence of enhanced MMP-1 expression or mutations in various malignancies. Based on 170 gastric cancer-related studies involving 4067 patients, MMP-1 polymorphisms were found to be associated with gastric cancer. Previous studies have linked elevated MMP-1 expression levels with patient prognosis across different malignancies (Figure 2A). In the present study, fluorescence quantitative polymerase chain reaction (PCR) assays were performed on collected EGC and control tissue samples. MMP-1 expression was significantly higher in EGC tissues than in their paracancerous counterparts (Figure 2B). Further analysis indicated that high MMP-1 expression has a sensitivity and specificity of 0.67 and 0.8, respectively, for detecting EGC, suggesting its potential as a biomarker for EGC diagnosis (Figure 2C).

3.2. Effect of MMP-1 on gastric cancer cell proliferation

The upregulation of MMP1 in N87 cells was verified by western blotting (Figure 3A). EdU experiments were performed on N87 cells transfected with Ad-MMP-1 and the respective control groups. The ratio of EdU-positive cells was significantly higher in the MMP-1 overexpression group than in the control group (Figure 3B), indicating a significant improvement in the proliferative ability of N87 cells by MMP-1 overexpression. In addition, MMP1 downregulation was verified by western blot analysis (Figure 4A). Simultaneously, N87 cells with MMP-1 knockdown were examined using EdU experiments, revealing a decreased proportion of EdU-positive cells and a significantly diminished proliferative ability, particularly evident in the sh2 group ($P < 0.05$; Figure 4B).

3.3. Effect of MMP-1 on gastric cancer cell migration

Results of the scratch experiment analysis revealed that the scratch wound area of N87 cells with upregulated MMP-1 expression was reduced by 62.3% compared to the initial scratch area at 48 h. This represented a significant increase compared to that in the control group; specifically, a 44% reduction in the scratch wound area was observed with a *P*-value of 0.0047 (Figure 5A). In contrast, the scratch wound areas in the sh1 and sh2 (RNA interference) groups were reduced by 46.8% and 48.6%, respectively. This represented a significant decrease compared with the percentage reduction in the corresponding control group (60.6%). These differences were statistically significant, with *P*-values of 0.0009 and 0.004, respectively (Figure 5B), suggesting that MMP-1 promoted cell migration.

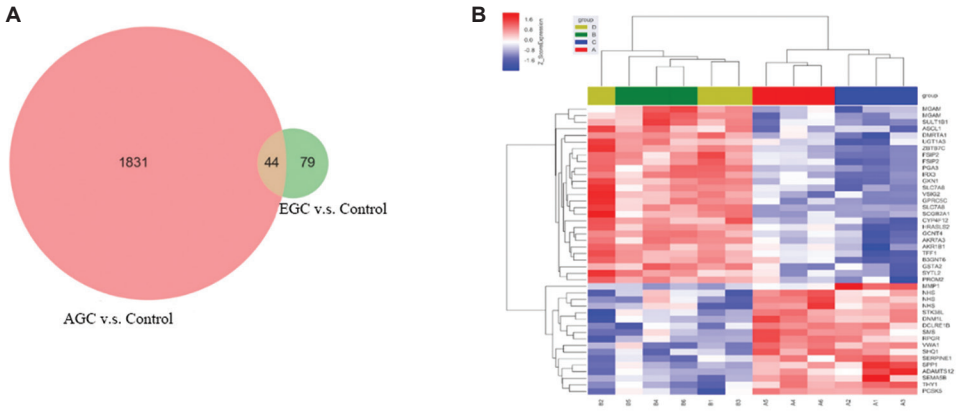

Figure 1. Results related to whole transcriptome sequencing of early gastric cancer/paracancerous tissues and advanced gastric cancer/paracancerous tissues: (A) Differentially expressed coding genes in early gastric cancer (EGC) and advanced gastric cancer (AGC); (B) Heatmap of 44 differentially expressed genes shared by both EGC and AGC.

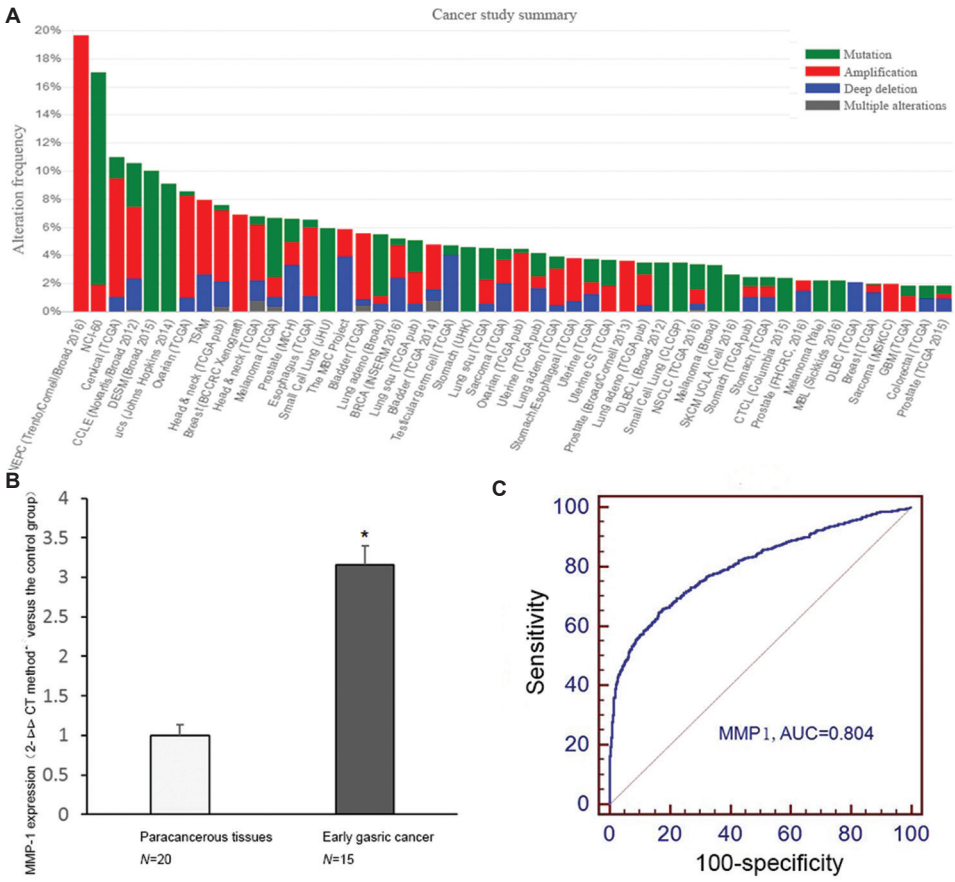

Figure 2. MMP-1 as a potential diagnostic marker for early gastric cancer: (A) A search of TCGA database revealed that high expression of or mutations in MMP-1 was present in a variety of malignancies, and MMP-1 polymorphisms were found to be associated with gastric cancer in gastric cancer-related studies; (B) MMP-1 expression in early cancer and paracancerous tissues was detected by fluorescence quantitative PCR. *$P < 0.05$; (C) Receiver operating characteristic curve (ROC) analysis was performed using SPSS software.
Abbreviations: AUC: Area under the curve; PCR: Polymerase chain reaction; TGCA: The Cancer Genome Atlas; MMP-1: Matrix metalloproteinase-1.

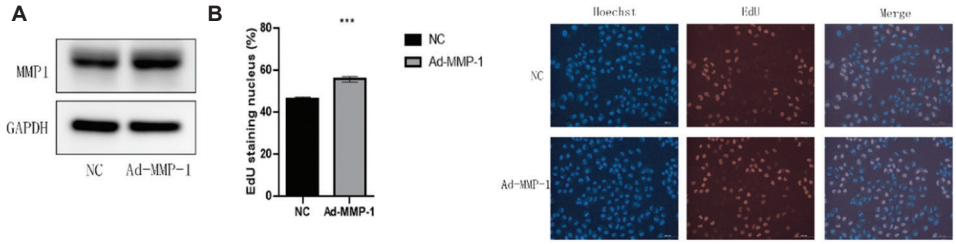

Figure 3. Effect of MMP-1 overexpression on the proliferative ability of gastric cancer cells: (A) Western blot validation of the upregulation of MMP-1 expression; (B) Percentage of EdU-positive cells.
Note: *$P < 0.05$; **$P < 0.01$; ***$P < 0.001$; ****$P < 0.0001$
Abbreviations: Ad-MMP-1: MMP-1-overexpression plasmid; NC: Negative control; MMP-1: Matrix metalloproteinase-1.

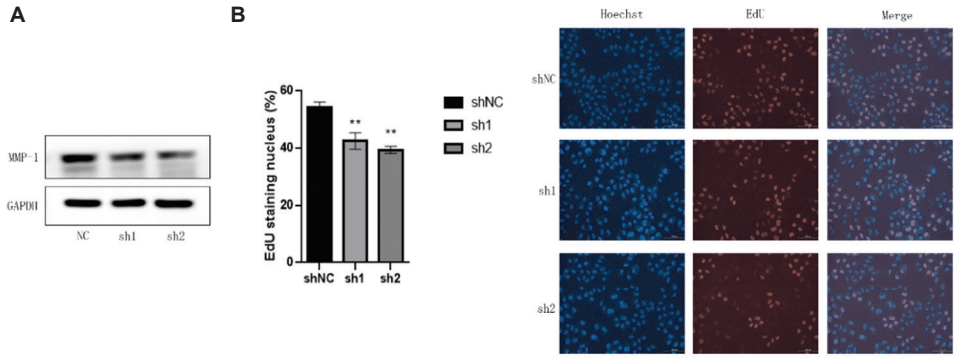

Figure 4. Effect of MMP-1 disruption on the proliferative ability of gastric cancer cells: (A) Western blot validation of MMP-1 disruption and (B) statistics of the percentage of EdU-positive cells.
Note: *$P < 0.05$; **$P < 0.01$; ***$P < 0.001$; ****$P < 0.0001$
Abbreviation: NC: Negative control; MMP-1: Matrix metalloproteinase-1.

3.4. Effect of MMP-1 on the epithelial-mesenchymal transition (EMT)-related protein expression in gastric cancer cells

Analysis of the MMP-1 effect on EMT-related protein expression in gastric cancer cells revealed significantly increased vimentin expression, whereas a lower expression of E-cadherin was observed with the overexpression of MMP-1. Similarly, following the downregulation of MMP-1, a significant decrease in vimentin expression and an increase in E-cadherin expression were observed in N87 cells (Figure 6).

4. Discussion

Matrix metalloproteinases are secreted by many cells and are involved in various physiological processes, such as angiogenesis[10] and embryogenesis.[11] They also play a role in many pathological conditions, including myocardial infarction,[12] fibrotic diseases,[13] osteoarthritis,[14,15] and cancer.[16,17] At least 11 MMPs function within cells, including MMP-1, MMP-3, MMP-7, MMP-8, MMP-9, MMP-10, MMP-11, MMP-12, MMP-14, MMP-23, and MMP-26.[18,19] MMPs can disrupt the histologically observed barrier in tumor cells. These enzymes are essential for tumor infiltration and metastasis. Moreover, MMPs such as MMP-1, MMP-2, and MMP-9[20-22] are involved in tumor EMT by interacting with each other.[9,23]

Differentially expressed genes were identified using BioGRID, STRING, GO, and KEGG pathway analyses, revealing that MMP-1 expression was considerably upregulated in gastric cancer tissues and cells, as well as in clinical serum samples, based on tissue protein assays.[23-27] Similar findings were reported for esophageal carcinoma, demonstrating that MMP-1 functions as an oncogene and the high expression of MMP-1 in esophageal cancer was closely associated with lymph node metastasis, microvascular density, and advanced TNM (tumor, node, and metastasis) staging.[28-30] A combination of 19 serum proteins was reported to act as a diagnostic marker to distinguish patients with TNM Stages I-II, with MMP-1 being the best in terms of performance. These outcomes suggest that MMP-1 could be a potential biomarker for the early diagnosis and prevention of gastric cancer.[31] In colorectal cancer, *in vivo* and *ex vivo* experiments confirmed that the expression of MMP-1 was higher than

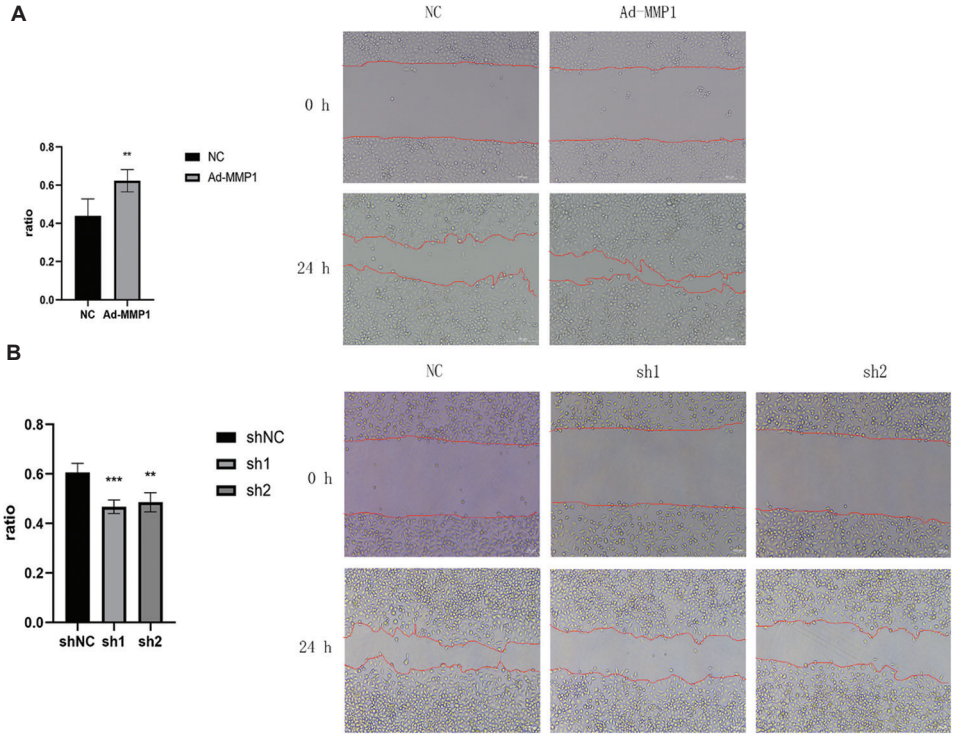

Figure 5. Effect of MMP-1 on the migration of gastric cancer cells detected by scratch healing assay: (A) Effect of upregulation of MMP-1 expression on the migration of gastric cancer cells and (B) effect of downregulation of MMP-1 expression on the migration of gastric cancer cells.
Abbreviations: Ad-MMP-1: MMP-1-overexpression plasmid; NC: Negative control.

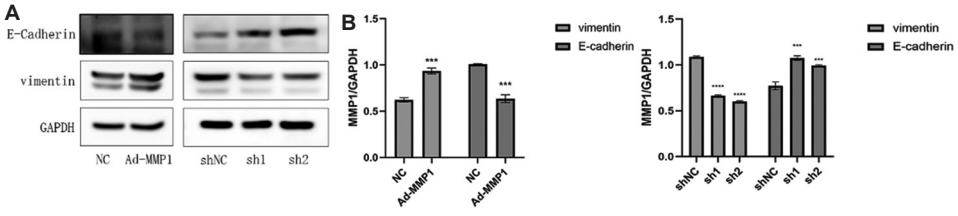

Figure 6. Effect of MMP-1 on the expression of epithelial-mesenchymal transition-related proteins in gastric cancer cells, as detected by western blotting: (A) Western blot detection of related protein expression and (B) grayscale value comparisons of differences in related protein expression levels.
Abbreviations: Ad-MMP-1: MMP-1-overexpression plasmid; NC: Negative control.

that of matched paraneoplastic non-cancerous tissues, and its high expression was significantly associated with lymphatic metastasis as well as TNM staging.[32] An association between polymorphisms in the MMP-1 promoter and the risk of gastric cancer, particularly in conjunction with smoking behavior and *Helicobacter pylori* infection, has been reported in Taiwan, potentially useful in the early detection and prevention of gastric cancer.[4] This conclusion was drawn from a survey involving 121 gastric cancer patients and 363 matched healthy volunteers, supported by literature evidence.[33] Effective screening methods for early detection can facilitate the timely treatment of patients and improve their chances of survival.[34-37]

The low survival rate of numerous stomach cancer patients is due to the fact that the tumor is often detected in the middle or late stages.[38,39] Timely and comprehensive treatment is crucial for a better prognosis.[40-43] The diagnosis of gastrointestinal tumors still relies on invasive upper gastrointestinal endoscopy.[44,45] However, noninvasive tests and highly specific biomarkers can provide valuable data for gastric cancer screening and diagnosis. For instance, peripheral blood,[46,47] urine,[48,49] and body fluids such as saliva,[50,51] gastric lavage,[52] and gastric juices[53,54] can serve as good sources.[55] Population-based surveillance programs have been effective in reducing gastric cancer-related morbidity and mortality in several countries.[56,57] Therefore, early diagnosis strategies are crucial for providing timely treatment

to improve patient prognosis and survival. In addition, medical imaging and mathematical modeling techniques have been used to diagnose gastric cancer at an early stage.[58-62] Bioinformatics methods have shown that ITGAX, CCL14, ADHFE1, and HOXB13 are expressed at significantly higher levels in gastric cancer tumor tissues than in adjacent normal tissues.[63] Furthermore, immunohistochemistry was employed to study the low expression of MLL2 in tissue microarrays of 529 cases of human gastric cancer and its correlation with early-stage cancer.[64] These genes may serve as gastric cancer marker genes, providing ideas for future experimental studies, and similar stories abound.

Metastasis is a leading contributor to cancer morbidity and mortality, resulting in approximately 90% of cancer-related deaths. The biochemical events and parameters involved in the metastatic process and tumor microenvironment have been targeted or can be potential targets for metastasis prevention and inhibition.[65-67] Epithelial-mesenchymal transition is a process that is required for the progression of many types of malignant tumors.[68-72] Matrix metalloproteinases are involved in various essential functions, including cell regeneration, programmed cell death, and angiogenesis, as well as normal developmental and pathological processes such as EMT.[73] MMP-1 is a critical factor in the development of several tumors, and several articles have reported that MMP-1 is involved in EMT-associated processes, including hepatocellular carcinoma,[9] head-and-neck cancer,[74] cervical cancer,[75] and colorectal cancer.[76] Furthermore, increased expression levels of MMP-1 have been observed in the tumor cells and tumor-associated stroma of breast cancer individuals with EMT markers present in the peripheral blood compared to those without EMT markers. In addition, tumor grade is independently correlated with MMP-1 expression in cancer cells,[77,78] suggesting that MMP-1 plays an essential role in tumor EMT and staging.

5. Conclusion

This study demonstrated that MMP-1 holds promise as a specific diagnostic marker for EGC. In addition, it illustrated the effects of MMP-1 modulation on the proliferation and migration of gastric cancer cells, a finding that has not been reported previously. Therefore, these findings provide important insights for setting future research directions.

Acknowledgments

None.

Funding

This study was supported by the guiding projects of the Suzhou Science and Technology Bureau (SYSD2019036), the Taicang Science and Technology Bureau (TC2019JCYL18), and the Taicang Science and Technology Bureau (TC2018JCYL20).

Conflict of interest

The authors declare that they have no competing interests.

Author contributions

Conceptualization: Qing Li, Ke Yi
Data analysis: Xiaoli Zhu
Formal analysis: Ke Yi
Investigation: Ke Yi
Methodology: Yan Hu
Writing – original draft: Ke Yi
Writing – review & editing: Xiaoli Zhu, Qing Li

Ethics approval and consent to participate

Not applicable.

Consent for publication

Not applicable.

Availability of data

The datasets analyzed in the current study are available from the corresponding author on reasonable request.

References

1. Rahman R, Asombang AW, Ibdah JA. Characteristics of gastric cancer in Asia. *World J Gastroenterol*. 2014;20(16):4483-4490.

   doi: 10.3748/wjg.v20.i16.4483

2. Machlowska J, Baj J, Sitarz M, Maciejewski R, Sitarz R. Gastric cancer: Epidemiology, risk factors, classification, genomic characteristics and treatment strategies. *Int J Mol Sci*. 2020;21(11):4012.

   doi: 10.3390/ijms21114012

3. Van Cutsem E, Sagaert X, Topal B, Haustermans K, Prenen H. Gastric cancer. *Lancet*. 2016;388(10060):2654-2664.

   doi: 10.1016/s0140-6736(16)30354-3

4. Yang MD, Lin KC, Lu MC, *et al*. Contribution of matrix metalloproteinases-1 genotypes to gastric cancer susceptibility in Taiwan. *BioMedicine* (*Taipei*). 2017;7(2):10.

   doi: 10.1051/bmdcn/2017070203

5. Cui N, Hu M, Khalil RA. Biochemical and biological attributes of matrix metalloproteinases. *Prog Mol Biol Transl Sci*. 2017;147:1-73.

   doi: 10.1016/bs.pmbts.2017.02.005

6. Tsai CW, Chang WS, Gong CL, *et al*. Contribution of

matrix metallopeptidase-1 genotypes, smoking, alcohol drinking and areca chewing to nasopharyngeal Carcinoma susceptibility. *Anticancer Res*. 2016;36(7):3335-3340.

7. Zhao S, Yu M. Identification of MMP1 as a potential prognostic biomarker and correlating with immune infiltrates in cervical squamous cell carcinoma. *DNA Cell Biol*. 2020;39(2):255-272.

   doi: 10.1089/dna.2019.5129

8. Peng Q, Xu Y. Association between promoter polymorphisms of matrix metalloproteinase-1 and risk of gastric cancer. *Onco Targets Ther*. 2015;8:2519-2526.

   doi: 10.2147/ott.S83004

9. Scheau C, Badarau IA, Costache R, *et al*. The role of matrix metalloproteinases in the epithelial-mesenchymal transition of hepatocellular carcinoma. *Anal Cell Pathol* (*Amst*). 2019;2019:9423907.

   doi: 10.1155/2019/9423907

10. Wang X, Khalil RA. Matrix metalloproteinases, vascular remodeling, and vascular disease. *Adv Pharmacol*. 2018;81:241-330.

    doi: 10.1016/bs.apha.2017.08.002

11. Moracho N, Learte AIR, Muñoz-Sáez E, *et al*. Emerging roles of MT-MMPs in embryonic development. *Dev Dyn*. 2022;251(2):240-275.

    doi: 10.1002/dvdy.398

12. Kassiri Z, Khokha R. Myocardial extra-cellular matrix and its regulation by metalloproteinases and their inhibitors. *Thromb Haemost*. 2005;93(2):212-219.

    doi: 10.1160/th04-08-0522

13. Craig VJ, Zhang L, Hagood JS, Owen CA. Matrix metalloproteinases as therapeutic targets for idiopathic pulmonary fibrosis. *Am J Respir Cell Mol Biol*. 2015;53(5):585-600.

    doi: 10.1165/rcmb.2015-0020TR

14. Grillet B, Pereira RVS, Van Damme J, Abu El-Asrar A, Proost P, Opdenakker G. Matrix metalloproteinases in arthritis: Towards precision medicine. *Nat Rev Rheumatol*. 2023;19(6):363-377.

    doi: 10.1038/s41584-023-00966-w

15. Nissinen L, Kähäri VM. Matrix metalloproteinases in inflammation. *Biochim Biophys Acta*. 2014;1840(8):2571-2580.

    doi: 10.1016/j.bbagen.2014.03.007

16. Xie J, Zhou X, Wang R, *et al*. Identification of potential diagnostic biomarkers in MMPs for pancreatic carcinoma. *Medicine (Baltimore)*. 2021;100(23):e26135.

    doi: 10.1097/md.0000000000026135

17. Lopez-Navarro ER, Gutierrez J. Metalloproteinases and their inhibitors in neurological disease. *Naunyn Schmiedebergs Arch Pharmacol*. 2022;395(1):27-38.

    doi: 10.1007/s00210-021-02188-x

18. Bassiouni W, Ali MAM, Schulz R. Multifunctional intracellular matrix metalloproteinases: Implications in disease. *FEBS J*. 2021;288(24):7162-7182.

    doi: 10.1111/febs.15701

19. Kapoor C, Vaidya S, Wadhwan V, Hitesh, Kaur G, Pathak A. Seesaw of matrix metalloproteinases (MMPs). *J Cancer Res Ther*. 2016;12(1):28-35.

    doi: 10.4103/0973-1482.157337

20. Jiang H, Li H. Prognostic values of tumoral MMP2 and MMP9 overexpression in breast cancer: A systematic review and meta-analysis. *BMC Cancer*. 2021;21(1):149.

    doi: 10.1186/s12885-021-07860-2

21. Shakery T, Safari F. Downregulation of PINKBAR/pAKT and MMP2/MMP9 expression in MDA-MB-231 breast cancer cells as potential targets in cancer therapy by hAMSCs secretome. *Cells Tissues Organs*. 2023;212(2):155-163.

    doi: 10.1159/000520370

22. Wang X, Wang B, Xie J, Hou D, Zhang H, Huang H. Melatonin inhibits epithelialtomesenchymal transition in gastric cancer cells via attenuation of IL1β/NFκB/MMP2/MMP9 signaling. *Int J Mol Med*. 2018;42(4):2221-2228.

    doi: 10.3892/ijmm.2018.3788

23. Rani V, Yadav D, Atale N. Matrixmetalloproteinase inhibitors: Promising therapeutic targets against cancer. *Curr Pharm Des*. 2021;27(45):4557-4567.

    doi: 10.2174/1381612827666210830103059

24. Yang C, Gong A. Integrated bioinformatics analysis for differentially expressed genes and signaling pathways identification in gastric cancer. *Int J Med Sci*. 2021;18(3):792-800.

    doi: 10.7150/ijms.47339

25. Xu J, Changyong E, Yao Y, Ren S, Wang G, Jin H. Matrix metalloproteinase expression and molecular interaction network analysis in gastric cancer. *Oncol Lett*. 2016;12(4):2403-2408.

    doi: 10.3892/ol.2016.5013

26. Cai QW, Li J, Li XQ, Wang JQ, Huang Y. Expression of STAT3, MMP-1 and TIMP-1 in gastric cancer and correlation with pathological features. *Mol Med Rep*. 2012;5(6):1438-1442.

    doi: 10.3892/mmr.2012.849

27. Chen YJ, Liang L, Li J, *et al*. IRF-2 inhibits gastric cancer invasion and migration by down-regulating MMP-1. *Dig Dis Sci*. 2020;65(1):168-177.

    doi: 10.1007/s10620-019-05739-8

28. Liu M, Hu Y, Zhang MF, *et al*. MMP1 promotes tumor growth and metastasis in esophageal squamous cell

carcinoma. *Cancer Lett*. 2016;377(1):97-104.

doi: 10.1016/j.canlet.2016.04.034

29. Peng HH, Zhang X, Cao PG. MMP-1/PAR-1 signal transduction axis and its prognostic impact in esophageal squamous cell carcinoma. *Braz J Med Bioll Res*. 2012;45(1):86-92.

doi: 10.1590/s0100-879x2011007500152

30. Zhou J, Xu M, Tan J, Zhou L, Dong F, Huang T. MMP1 acts as a potential regulator of tumor progression and dedifferentiation in papillary thyroid cancer. *Front Oncol*. 2022;12:1030590.

doi: 10.3389/fonc.2022.1030590

31. Shen Q, Polom K, Williams C, *et al*. A targeted proteomics approach reveals a serum protein signature as diagnostic biomarker for resectable gastric cancer. *EBioMedicine*. 2019;44:322-333.

doi: 10.1016/j.ebiom.2019.05.044

32. Wang K, Zheng J, Yu J, *et al*. Knockdown of MMP1 inhibits the progression of colorectal cancer by suppressing the PI3K/Akt/cmyc signaling pathway and EMT. *Oncol Rep*. 2020;43(4):1103-1112.

doi: 10.3892/or.2020.7490

33. Kumar P, Sebastian A, Verma K, *et al*. mRNA expression analysis of E-cadherin, VEGF, and MMPs in gastric cancer: A pilot study. *Indian J Surg Oncol*. 2021;12(Suppl 1):85-92.

doi: 10.1007/s13193-020-01096-5

34. Matsuoka T, Yashiro M. Biomarkers of gastric cancer: Current topics and future perspective. *World J Gastroenterol*. 2018;24(26):2818-2832.

doi: 10.3748/wjg.v24.i26.2818

35. Sun Y, Jin J, Jing H, *et al*. ITIH4 is a novel serum biomarker for early gastric cancer diagnosis. *Clin Chim Acta*. 2021;523:365-373.

doi: 10.1016/j.cca.2021.10.022

36. Wu D, Zhang P, Ma J, *et al*. Serum biomarker panels for the diagnosis of gastric cancer. *Cancer Med*. 2019;8(4):1576-1583.

doi: 10.1002/cam4.2055

37. Guo X, Peng Y, Song Q, *et al*. A liquid biopsy signature for the early detection of gastric cancer in patients. *Gastroenterology*. 2023;165(2):402-413.e13.

doi: 10.1053/j.gastro.2023.02.044

38. Zheng L, Wu C, Xi P, *et al*. The survival and the long-term trends of patients with gastric cancer in Shanghai, China. *BMC Cancer*. 2014;14:300.

doi: 10.1186/1471-2407-14-300

39. Yang J, Bo L, Han T, Ding D, Nie M, Yin K. Pathway-and clinical-factor-based risk model predicts the prognosis of patients with gastric cancer. *Mol Med Rep*. 2018;17(5):6345-6356.

doi: 10.3892/mmr.2018.8722

40. Chrom P, Stec R, Szczylik C. Second-line treatment of advanced gastric cancer: Current options and future perspectives. *Anticancer Res*. 2015;35(9):4575-4583.

41. Wang X, Deng J, Liang H. Well differentiated carcinoma with a poor prognosis: A retrospective analysis of papillary gastric adenocarcinoma. *Surg Today*. 2021;51(8):1387-1396.

doi: 10.1007/s00595-021-02289-3

42. Digklia A, Wagner AD. Advanced gastric cancer: Current treatment landscape and future perspectives. *World J Gastroenterol*. 2016;22(8):2403-2414.

doi: 10.3748/wjg.v22.i8.2403

43. Wei R, Du X, Wang J, *et al*. Risk and prognosis of subsequent primary gastric cancer. *Oncol Res Treat*. 2022;45(4):186-196.

doi: 10.1159/000521846

44. Chang JY, Shim KN, Tae CH, *et al*. Comparison of clinical outcomes after endoscopic submucosal dissection and surgery in the treatment of early gastric cancer: A single-institute study. *Medicine (Baltimore)*. 2017;96(30):e7210.

doi: 10.1097/md.0000000000007210

45. Kumar S, Katona BW, Long JM, *et al*. Endoscopic ultrasound has limited utility in diagnosis of gastric cancer in carriers of CDH1 mutations. *Clin Gastroenterol Hepatol*. 2020;18(2):505-508.e1.

doi: 10.1016/j.cgh.2019.04.064

46. Wang F, Hu D, Lou X, *et al*. BNIP3 and DAPK1 methylation in peripheral blood leucocytes are noninvasive biomarkers for gastric cancer. *Gene*. 2024;898:148109.

doi: 10.1016/j.gene.2023.148109

47. Hu D, Lou X, Meng N, *et al*. Peripheral blood-based DNA methylation of long non-coding RNA H19 and metastasis-associated lung adenocarcinoma transcript 1 promoters are potential non-invasive biomarkers for gastric cancer detection. *Cancer Control*. 2021;28:10732748211043667.

doi: 10.1177/10732748211043667

48. Fan H, Li X, Li ZW, *et al*. Urine proteomic signatures predicting the progression from premalignancy to malignant gastric cancer. *EBioMedicine*. 2022;86:104340.

doi: 10.1016/j.ebiom.2022.104340

49. Kao HW, Pan CY, Lai CH, *et al*. Urine miR-21-5p as a potential non-invasive biomarker for gastric cancer. *Oncotarget*. 2017;8(34):56389-56397.

doi: 10.18632/oncotarget.16916

50. Hoshino I. The usefulness of microRNA in urine and saliva as a biomarker of gastroenterological cancer. *Int J Clin Oncol*. 2021;26(8):1431-1440.

doi: 10.1007/s10147-021-01911-1

51. Miyamoto S, Watanabe Y, Oikawa R, *et al*. Analysis of helicobacter pylori genotypes in clinical gastric wash samples. *Tumour Biol*. 2016;37(8):10123-10132.

doi: 10.1007/s13277-016-4886-4

52. Chae HD, Kim IH. Prognostic significance of CEA expression by RT-PCR in peritoneal wash from patients with gastric cancer: Result of a 5-year follow-up after curative resection. *Scand J Gastroenterol*. 2016;51(8):956-960.

doi: 10.3109/00365521.2016.1172339

53. Zhou X, Liu J, Meng A, *et al*. Gastric juice piR-1245: A promising prognostic biomarker for gastric cancer. *J Clin Lab Anal*. 2020;34(4):e23131.

doi: 10.1002/jcla.23131

54. Pan Y, Zheng Y, Yang J, *et al*. A new biomarker for the early diagnosis of gastric cancer: Gastric juice-and serum-derived SNCG. *Future Oncol*. 2022;18(28):3179-3190.

doi: 10.2217/fon-2022-0253

55. Lopes C, Chaves J, Ortigão R, Dinis-Ribeiro M, Pereira C. Gastric cancer detection by non-blood-based liquid biopsies: A systematic review looking into the last decade of research. *United European Gastroenterol J*. 2023;11(1):114-130.

doi: 10.1002/ueg2.12328

56. Enríquez-Sánchez LB, Gallegos-Portillo LG, Camarillo-Cisneros J, *et al*. Cost-benefit of serum pepsinogen screening for gastric adenocarcinoma in the Mexican population. *Rev Gastroenterol Mexico (Eng Ed)*. 2022;87(3):285-291.

doi: 10.1016/j.rgmxen.2021.11.002

57. Machii R, Takahashi H. Japanese cancer screening programs during the COVID-19 pandemic: Changes in participation between 2017-2020. *Cancer Epidemiol*. 2023;82:102313.

doi: 10.1016/j.canep.2022.102313

58. Cesaretti M, Bian AZL. *In vivo* medical imaging technologies: New possibility in diagnosis of gastric cancer. *Minerva Chir*. 2016;71(4):270-277.

59. Zhu SL, Dong J, Zhang C, Huang YB, Pan W. Application of machine learning in the diagnosis of gastric cancer based on noninvasive characteristics. *PLoS One*. 2020;15(12):e0244869.

doi: 10.1371/journal.pone.0244869

60. Thapa S, Fischbach LA, Delongchamp R, Faramawi MF, Orloff MS. Using machine learning to predict progression in the gastric precancerous process in a population from a developing country who underwent a gastroscopy for dyspeptic symptoms. *Gastroenterol Res Pract*. 2019;2019:8321942.

doi: 10.1155/2019/8321942

61. Leja M, Linē A. Early detection of gastric cancer beyond endoscopy-new methods. *Best Pract Res Clin Gastroenterol*. 2021;50-51:101731.

doi: 10.1016/j.bpg.2021.101731

62. Qian Z, Wang J. Application of computed tomography imaging in diagnosis of endocrine nerve of gastric cancer and nursing intervention effect. *World Neurosurg*. 2021;149:341-351.

doi: 10.1016/j.wneu.2020.10.005

63. Rezaei Z, Ranjbaran J, Safarpour H, *et al*. Identification of early diagnostic biomarkers via WGCNA in gastric cancer. *Biomed Pharmacother*. 2022;145:112477.

doi: 10.1016/j.biopha.2021.112477

64. Numakura S, Uozaki H. Low MLL2 protein expression is associated with fibrosis in early stage gastric cancer. *In Vivo*. 2021;35(1):603-609.

doi: 10.21873/invivo.12297

65. Guan X. Cancer metastases: Challenges and opportunities. *Acta Pharm Sin B*. 2015;5(5):402-418.

doi: 10.1016/j.apsb.2015.07.005

66. Fu BM. Tumor metastasis in the microcirculation. *Adv Exp Med Biol*. 2018;1097:201-218.

doi: 10.1007/978-3-319-96445-4_11

67. Guo S, Huang J, Li G, Chen W, Li Z, Lei J. The role of extracellular vesicles in circulating tumor cell-mediated distant metastasis. *Mol Cancer*. 2023;22(1):193.

doi: 10.1186/s12943-023-01909-5

68. Burr R, Gilles C, Thompson EW, Maheswaran S. Epithelial-mesenchymal plasticity in circulating tumor cells, the precursors of metastasis. *Adv Exp Med Biol*. 2020;1220:11-34.

doi: 10.1007/978-3-030-35805-1_2

69. Pastushenko I, Blanpain C. EMT transition states during tumor progression and metastasis. *Trends Cell Biol*. 2019;29(3):212-226.

doi: 10.1016/j.tcb.2018.12.001

70. Fiori ME, Di Franco S, Villanova L, Bianca P, Stassi G, De Maria R. Cancer-associated fibroblasts as abettors of tumor progression at the crossroads of EMT and therapy resistance. *Mol Cancer*. 2019;18(1):70.

doi: 10.1186/s12943-019-0994-2

71. Zhang Y, Weinberg RA. Epithelial-to-mesenchymal transition in cancer: Complexity and opportunities. *Front Med*. 2018;12(4):361-373.

doi: 10.1007/s11684-018-0656-6

72. Phillips RM, Lam C, Wang H, Tran PT. Bittersweet tumor development and progression: Emerging roles of epithelial plasticity glycosylations. *Adv Cancer Res*. 2019;142:23-62.

doi: 10.1016/bs.acr.2019.01.002

73. Bakir B, Chiarella AM, Pitarresi JR, Rustgi AK. EMT,

MET, plasticity, and tumor metastasis. *Trends Cell Biol*. 2020;30(10):764-776.

doi: 10.1016/j.tcb.2020.07.003

74. Zhang W, Huang X, Huang R, *et al*. MMP1 overexpression promotes cancer progression and associates with poor outcome in head and neck carcinoma. *Comput Math Methods Med*. 2022;2022:3058342.

doi: 10.1155/2022/3058342

75. Tian R, Li X, Gao Y, Li Y, Yang P, Wang K. Identification and validation of the role of matrix metalloproteinase-1 in cervical cancer. *Int J Oncol*. 2018;52(4):1198-1208.

doi: 10.3892/ijo.2018.4267

76. Du L, Liu N, Jin J, *et al*. ZNF3 regulates proliferation, migration and invasion through MMP1 and TWIST in colorectal cancer. *Acta Biochim Biophys Sin* (*Shanghai*). 2022;54(12):1889-1896.

doi: 10.3724/abbs.2022187

77. Cierna Z, Mego M, Janega P, *et al*. Matrix metalloproteinase 1 and circulating tumor cells in early breast cancer. *BMC Cancer*. 2014;14:472.

doi: 10.1186/1471-2407-14-472

78. Zhu Y, Tao Z, Chen Y, *et al*. Exosomal MMP-1 transfers metastasis potential in triple-negative breast cancer through PAR1-mediated EMT. *Breast Cancer Res Treat*. 2022;193(1):65-81.

doi: 10.1007/s10549-022-06514-6

ACCSCIENCE PUBLISHING

Tumor Discovery

CASE REPORT

Compressive neuropathy of the branch of the posterior interosseous nerve with isolated paralysis of the extensor digitorum longus muscle: A case report

Balaji Zacharia[1]*, Puneeth K. Pai[2], and Vishnu Unnikrishnan[2]

[1]Department of Orthopedics, Government Medical College, Kannur, Pariyaram, Kerala, India

[2]Department of Orthopedics, Government Medical College, Kozhikode, Kerala, India

Abstract

Compressive neuropathies occur when a nerve is compressed in a closed osteofibrous tunnel. Here, we report a case of isolated paralysis of the extensor digitorum longus muscle due to compression of a branch of the posterior interosseous nerve (PIN) in the proximal forearm in a 56-year-old man presented with progressive weakness of the left hand over 18 months. During the first time of clinical consultation, we found a swelling in the extensor aspect of the left proximal forearm, and a firm, non-tender, mobile swelling located deep in the extensor muscles, without other muscle involvement. The sensation was intact. An ultrasound scan and magnetic resonance imaging scan confirmed the diagnosis of an intramuscular lipoma, which was further confirmed with histopathologic examination. The patient was treated with an excision of the lipoma and decompression of the nerve. Post-operatively, the patient was given regular physiotherapy, through which he achieved improvement in his finger extension within a year. This is an extremely rare case of isolated paralysis of the extensor digitorum longus due to compression of the branch of the PIN by an intermuscular lipoma in the forearms.

Keywords: Posterior interosseous nerve palsy; Finger drop; Extensor digitorum longus paralysis; Intramuscular lipoma

***Corresponding author:**
Balaji Zacharia
(balaji.zacharia@gmail.com)

Citation: Zacharia B, Pai PK, Unnikrishnan V. Compressive neuropathy of the branch of the posterior interosseous nerve with isolated paralysis of the extensor digitorum longus muscle: A case report. *Tumor Discov.* 2023;3(1):1585.
https://doi.org/10.36922/td.1585

Received: August 11, 2023
Accepted: November 15, 2023
Published Online: December 1, 2023

1. Background

Compressive neuropathies are caused by increased pressure in the nerves as the nerve pass through a closed osteofibrous tunnel, whose capacity is not commensurate with the content. In most cases, compressive neuropathies are idiopathic. The peripheral nerve is usually resistant to acute microvascular compressive changes due to low pressure. Prolonged compression of the nerve can cause increased intracellular permeability, leading to interfascicular edema and a delay in nerve conduction. Large-diameter nerve fibers are more susceptible to compression. Friction and traction can also cause nerve ischemia. Compressive neuropathies rarely occur in radial nerve[1].

Compressive neuropathies may occur as a result of neural sheath tumors and non-neural sheath tumors. Ganglioma, lymphangioma, hemangioma, myeloblastoma,

and lipoma are some of the non-neural sheath tumors that induce compressive neuropathy, with lipoma being regarded as the most common cause. Lipomas are benign soft-tissue tumors arising from adipose tissue. They are also called universal tumors because they can occur in any part of the body[2]. According to histopathological findings, lipomas are divided into lipoblastoma (immature fat cells), hibernomas (mature brown fat cells), and lipomas (mature white fat cells). Lipomas can cause neuropathy in four different ways: (i) Extrinsic compression by solitary lipoma, (ii) intrinsic compression by encapsulated lipoma, (iii) compression on the nerves by the fibrofatty masses of lipofibromatous hamartomas, and (iv) compression by macrodystrophia lipomatosa, causing localized gigantism of the extremities, especially toes and fingers. Solitary lipoma is the most common type of lipoma that produces nerve lesions. A solitary lipoma can compress a nerve located at superficial or deep locations[3]. On the other hand, intramuscular lipomas are very rare, and they are located deep within the muscle fibers[4].

The occurrence of nerve palsy caused by lipoma is rare. The majority of publications about lipoma causing compressive neuropathies are either case reports or small case series. There are few reports of lipoma causing posterior interosseous nerve (PIN) palsy[4]. Here, we report a case of isolated paralysis of the extensor digitorum longus due to compression of the PIN by an intermuscular lipoma in the proximal part of the left forearm.

2. Case presentation

A 56-year-old man presenting with progressive weakness in his left hand for 18 months approached us in December 2019. During the first time of clinical consultation, we found a 5 × 2.5 × 2 cm soft swelling over the proximal part of the left forearm. There was a drop in the middle and ring fingers (Figure 1). The extension of the wrist and metacarpophalangeal joints of the thumb and other fingers was unaffected. There was no sensory involvement. Radiograms of the neck and forearm showed normal results. Magnetic resonance imaging revealed a 2.2 × 2.4 × 5.2 cm lesion in the extensor compartment of the left forearm. It appeared hyperintense on T1-weighted and T2-weight images, suppressed on short tau inversion recovery images with no diffusion restrictions, and blooming on gradient echo sequences or post-contrast enhancement. The lesion extends to the flexor compartment over the superior interosseous membrane. The lesion closely abutted and compressed the PIN just after exiting from the supinator muscle. Given these findings, the lesion was diagnosed as an intermuscular lipoma (Figure 2A).

After obtaining his informed consent, the patient was treated with excision of the lipoma and decompression

Figure 1. The dropping of the middle and ring finger and normal extension of other fingers of the left hand.

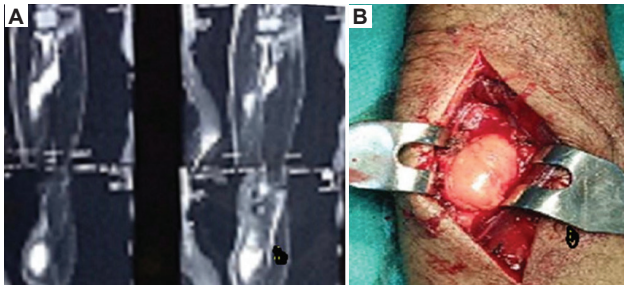

Figure 2. (A) Magnetic resonance imaging scan showed a 2.2 × 2.4 × 5.2 cm lesion in the extensor compartment of the left forearm. It appeared hyperintense on the T1-weighted and T2-weighted images. (B) Intraoperative photograph showed that the tumor was lying beneath the extensor carpi ulnaris muscle over the supinator.

of the PIN. The procedure was performed under a supraclavicular block. A 10 cm long curvilinear incision was made in the proximal forearm dorsally. The tumor was located beneath the extensor carpi ulnaris muscle over the supinator (Figure 2B). The lipoma was removed completely. Upon inspection, the PIN was found to be intact. A gross examination of the tumor demonstrated a well-circumscribed yellow mass consistent with lipoma. The patient was given a long arm slab until suture removal. The sutures were removed after 10 days. The diagnosis of lipoma was also corroborated by histopathological approaches (Figure 3A and B). Thereafter, he was prescribed regular physiotherapy and electrical stimulation from the physical medicine and rehabilitation center. His finger extension improved considerably after a year.

3. Discussion

The PIN originates as a continuation of the deep branch of the radial nerve. After piercing the lateral intermuscular

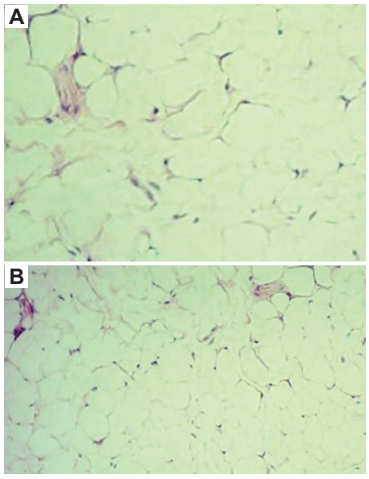

Figure 3. Hematoxylin-eosin-stained specimens showed mature adipocytes without atypia and a uniform distribution of vacuoles in the cytoplasm. (A) Low power ×10; (B) high power ×40.

septum at approximately 10 cm above the lateral epicondyle, the radial nerve traverses between the brachialis muscle medially and the extensor carpi radialis longus muscle laterally. The lateral epicondyle branches into superficial and deep branches, and the superficial branch continues as a sensory branch through the flexor compartment of the forearm. The deep branch of the radial nerve innervates the extensor carpi radialis brevis and supinator muscle before it enters the supinator between its two heads. Then, it winds around the neck of the radius to reach the posterior compartment of the forearm. From here onward, it is known as the PIN.

After exiting the supinator, the main trunk of the PIN gives three branches to extensor digitorum longus, extensor digiti minimi, and extensor carpi ulnaris. Then, it divides into a long branch which innervates extensor pollicic longus and extensor indicis and a short branch innervating abductor pollicic longus and extensor pollicis brevis. There are many variations in the origin of the branch to the extensor carpi radialis brevis. It can originate from the radial nerve, the superficial branch of the radial nerve, or the PIN[5]. The clinical manifestations of PIN palsy vary according to the site of involvement. The long radial extensors are usually spared in typical PIN palsy. Usually, the ulnar extensor and long extensor of fingers will be affected. When the patient is attempting to extend the wrist, there is a radial deviation due to the unopposed action of the extensor carpi radialis longus. There will not be any associated deep tendon reflex or sensory abnormalities in PIN palsy[6].

PIN syndrome may result in finger and thumb drops. This is due to the entrapment of the deep branch of the radial nerve between the two heads of the supinator. The common causes for this entrapment are fracture dislocation of the proximal radius and rheumatoid arthritis. The milder form of radial tunnel syndrome resembles the tennis elbow. The main structures causing entrapment of the deep branch of the radial nerve in the tunnel are the capsule-tendon-aponeurotic complex in the anterior aspect of the radiohumeral joint, the vascular arcade formed by the recurrent branch of the radial artery, and the arcade formed by the medial edge of the extensor carpi radialis brevis and the arcade of Frohse[7].

Compressive neuropathies of PIN may remain undiagnosed for long. Sometimes, it may mimic tennis elbow[8]. The first case of parosteal lipoma surrounding the neck of the radius causing weakness of finger extensors was reported by Richmond in 1953[9]. In an analysis of 31 cases of non-traumatic PIN palsies, 14 patients had entrapment of nerves within the supinator. The most common cause of compression in their series was the ganglion, followed by lipoma[10]. Another case showed that the excision of soft-tissue chondroma led to a complete resolution of symptoms of PIN palsy[11].

The anterior and posterior approaches to the proximal radius can injure the PIN. The anterior approach requires more muscle retraction but is relatively safer. Besides, Monteggia fracture can produce PIN palsy either at the time of injury or occur during treatment of neglected Monteggia fractures[12,13]. van den Bogaerde and Shin reported a case of PIN palsy due to nerve incarceration with EndoButton during the repair of distal biceps rupture[14]. Of note, inflammatory myofibroblastic pseudotumors, rheumatoid arthritis, false aneurysm, and psoriatic arthritis rarely cause compressive neuropathy of the PIN[15-18].

In our case, the patient developed isolated paralysis of the extensor digitorum longus of the left forearm and had difficulty extending the metacarpophalangeal joint of the middle and ring fingers. We believe that this is due to the peculiar anatomy of the PIN. After winding around the neck of the radius, the main trunk of the nerve splits into three independent branches innervating extensor digitorum longus, extensor digiti minimi, and extensor carpi ulnaris. Compression only occurred to the branch innervating extensor digitorum longus, sparing branches to the extensor indicis, and extensor digiti minimi.

4. Conclusion

Isolated muscle weakness due to compressive neuropathy of the PIN is extremely rare. This is a rare case of isolated paralysis of extensor digitorum longus due to

the compression of a branch of PIN by an intermuscular lipoma.

Acknowledgments

None.

Funding

None.

Conflict of interest

The authors have no conflict of interest in publishing this report.

Author contributions

Conceptualization: Balaji Zacharia
Investigation: All authors
Methodology: Balaji Zacharia, Puneeth K. Pai
Formal analysis: All authors
Writing – original draft: All authors
Writing – review & editing: All authors

Ethics approval and consent to participate

According to the institutional policy, case reports are exempted from IRB clearance.

Consent for publication

We have obtained informed written consent from the patient for publication of this report.

Availability of data

Data can be obtained from the corresponding author upon reasonable request.

References

1. Helfenstein Júnior M, 2020, Uncommon compressive neuropathies of upper limbs. *Best Pract Res Clin Rheumatol*, 34(3): 101516.

   https://doi.org/10.1016/j.berh.2020.101516

2. Heidari N, Kraus T, Weinberg AM, *et al*., 2011, The risk injury to the posterior interosseous nerve in standard approaches to the proximal radius: A cadaver study. *Surg Radiol Anat*, 33(4): 353–357.

   https://doi.org/10.1007/s00276-010-0718-1

3. Flores LP, Carneiro JZ, 2007, Peripheral nerve compression secondary to adjacent lipomas. *Surg Neurol*, 67(3): 258–262.

   https://doi.org/10.1016/j.surneu.2006.06.052

4. Colasanti R, 2016, Delayed diagnosed intermuscular lipoma causing a posterior interosseous nerve palsy in a patient with cervical spondylosis: The "priceless" value of the clinical examination in the technological era. *G Chir*, 37: 42–45.

   https://doi.org/10.11138/gchir/2016.37.1.042

5. Abrams RA, Ziets RJ, Lieber RL, *et al*., 1997, Anatomy of the radial nerve motor branches in the forearm. *J Hand Surg*, 22(2): 232–237.

   https://doi.org/10.1016/s0363-5023(97)80157-8

6. Mcgann SA, Flores RH, Nashel DJ, 2011, Entrapment Neuropathies and Compartment Syndromes. Philadelphia, PA: Mosby. p783–796.

   https://doi.org/10.1016/b978-0-323-06551-1.00078-6

7. Bonfiglioli R, Mattioli S, Violante FS, 2015, Occupational Mononeuropathies in Industry. Netherlands: Elsevier. p411–426.

   https://doi.org/10.1016/b978-0-444-62627-1.00021-4

8. Werner P, Furtner M, Loscher WN, *et al*., 2007, A case of posterior interosseous nerve palsy: Good recovery despite diagnostic delay. *J Neurol Neurosurg Psychiatry*, 78(12): 1408–1409.

   https://doi.org/10.1136/jnnp.2007.126896

9. Fitzgerald A, Anderson W, Hooper G, 2002, Posterior interosseous nerve palsy due to parosteal lipoma. *J Hand Surg*, 27(6): 535–537.

   https://doi.org/10.1054/jhsb.2002.0783

10. Hashizume H, Nishida K, Nanba Y, *et al*., 1996, Non-traumatic paralysis of the posterior interosseous nerve. *J Bone Joint Surg Br*, 78(5): 771–776.

    https://doi.org/10.1302/0301-620x.78b5.0780771

11. Madhavan P, leslie IJ, 1998, Intracapsular chondroma of the elbow producing a posterior interosseous nerve palsy. *J Hand Surg*, 23(1): 107–108.

    https://doi.org/10.1016/s0266-7681(98)80235-0

12. Di Gennaro GL, Martinelli A, Bettuzzi C, *et al*., 2015, Outcomes after surgical treatment of missed Monteggia fractures in children. *Musculoskelet Surg*, 99(S1): S75–S82.

    https://doi.org/10.1007/s12306-015-0362-3

13. Hackl W, Gabl M, Gadner K, *et al*., 2002, Delayed radial paresis after monteggia fracture? A case report. *Accident Surg*, 105(6): 569–571.

    https://doi.org/10.1007/s00113-002-0414-7

14. Van den Bogaerde J, Shin E, 2015, Posterior interosseous nerve incarceration with endobutton repair of distal biceps. *Orthopedics*, 38(1): e68–e71.

    https://doi.org/10.3928/01477447-20150105-92

15. Fernandez AM, Tiku ML, 1994, Posterior interosseous nerve entrapment in rheumatoid arthritis. *Semin Arthritis Rheum*, 24(1): 57–60.

    https://doi.org/10.1016/0049-0172(94)90100-7

16. Ali R, Yang LJS, Henning PT, 2014, Posterior interosseus nerve palsy resulting from inflammatory myofibroblastic pseudotumor: Case presentation. *PM R*, 6(7): 659–661.

https://doi.org/10.1016/j.pmrj.2013.12.016

17. Ali E, Colaço R, Gillespie P, *et al*., 2011, Inflammatory posterior interosseous nerve palsy in a patient with psoriatic arthropathy. *J Plast Reconstr Aesthet Surg*, 64(8): e205–e207.

https://doi.org/10.1016/j.bjps.2011.03.039

18. Weinstein RN, 1996, False aneurysm presenting as delayed posterior interosseus nerve palsy. *J Orthop Trauma*, 10(8): 583–585.

https://doi.org/10.1097/00005131-199611000-00015

ACCSCIENCE PUBLISHING

Tumor Discovery

CASE REPORT

Odontogenic myxofibroma arising in the mandibular angle of a child with long-term follow-up: A case report

Momoko Yoshikawa[1,2], Takeshi Karube[1], Hiroki Nagamine[1], Wataru Muraoka[1,3], Hideki Kizu[1,4], Hiromasa Kawana[1,5], Taneaki Nakagawa[1], and Seiji Asoda[1]*

[1]Department of Dentistry and Oral Surgery, School of Medicine, Keio University, Tokyo, Japan

[2]Department of Dentistry and Oral Surgery, National Hospital Organization, Murayama Medical Center, Tokyo, Japan

[3]Department of Dentistry and Oral Surgery, Kawasaki Municipal Ida Hospital, Kawasaki, Japan

[4]Department of Dentistry and Oral Surgery, Federation of National Public Service Personnel Mutual Aid Associations, Tachikawa Hospital, Tokyo, Japan

[5]Department of Oral and Maxillofacial Implantology, Kanagawa Dental University, Yokosuka, Japan

Abstract

Odontogenic myxofibroma of the jawbone is a rarity in children, and there are few reports of cases with long-term follow-up, which mainly describe the growth process of odontogenic myxofibroma. We herein report a case of odontogenic myxofibroma that arose in the mandibular angle of a pediatric patient with a long-term follow-up of more than 14 years. The patient, when he was 10-years-old, first approached us with a complaint of painless swelling in the right mandibular angle that was palpable and showed bone-like hardness. Computed tomography revealed an ill-defined bone defect measuring 20 mm in diameter with bone protrusion in the margin. A biopsy was performed to differentiate the mass from osteosarcoma, giving a preliminary diagnosis of odontogenic myxofibroma or chondromyxofibroma. Therefore, tumorectomy was performed under general anesthesia. We curetted the bone surrounding the tumor and filled defect with iliac cancellous bone. The final diagnosis was odontogenic myxofibroma. At present, 14 years after the surgery, the patient had experienced an uneventful post-operative course without recurrence.

Keywords: Odontogenic myxofibroma; Pediatric tumor; Long-term follow-up

***Corresponding author:**
Seiji Asoda
(asoda@keio.jp)

Citation: Yoshikawa M, Karube T, Nagamine H, *et al*. Odontogenic myxofibroma arising in the mandibular angle of a child with long-term follow-up: A case report. *Tumor Discov*. 2024;3(1):2096. https://doi.org/10.36922/td.2096

Received: October 24, 2023
Accepted: January 11, 2024
Published Online: March 19, 2024

1. Background

Odontogenic myxofibroma of the jawbone is a relatively rare disease with very few reports regarding its occurrence in children under 10 years of age.[1-3] In most cases, the lesion extends to the alveolar region and is accompanied by some dental symptoms such as tooth deviation and movement.[4] In addition, radiographic images may show significant bone destruction, resorption, and protrusion, which are features requiring differentiation from malignant diseases such as osteosarcoma.[5,6] Although post-operative recurrence has been reported to be common,[7,8] cases reporting long-term follow-up of the growth process remain scarce.

We herein report a pediatric case of odontogenic myxofibroma confined to the mandibular angle, who had experienced an uneventful postoperative course with no recurrence after more than 14 years of follow-up.

2. Case presentation

In June 2009, a 10-year-old Japanese boy presented to our department following a complaint of a painless swelling in the right mandibular angle. The pediatric patient had no remarkable personal or family medical history. Clinical findings included a palpable bone-like hard swelling in the right mandibular angle, but there were no abnormal findings in the oral cavity.

Panoramic X-ray and computed tomography (CT) scan revealed an ill-defined radiolucent image measuring 20 mm in diameter with an indistinct border, featuring a bone-like protrusion in the right mandibular angle (Figures 1 and 2). Magnetic resonance imaging revealed low signal intensity on T1-weighted imaging and high signal intensity on T2-weighted short inversion time inversion-recovery imaging with a partially irregular border with the surrounding bone (Figure 3). Because the possibility of a malignant tumor could not be ruled out merely based on the imaging findings, a biopsy was performed, and a histological evaluation of the biopsied sample rule out a diagnosis of osteosarcoma in our patient. The histopathological findings demonstrated fibrous proliferation with bland spindle cells, and the immunostaining showed negative expression of AE1/AE2 and desmin, and positive expression of SMA and bcl2. The diagnosis was deemed to be odontogenic myxofibroma or chondromyxofibroma.

Figure 1. A panoramic X-ray scan. An ill-defined bone defect with cortical bone resorption and the outward protrusion of the surrounding cortical bone-like spicules could be seen in the right mandibular angle (arrows).

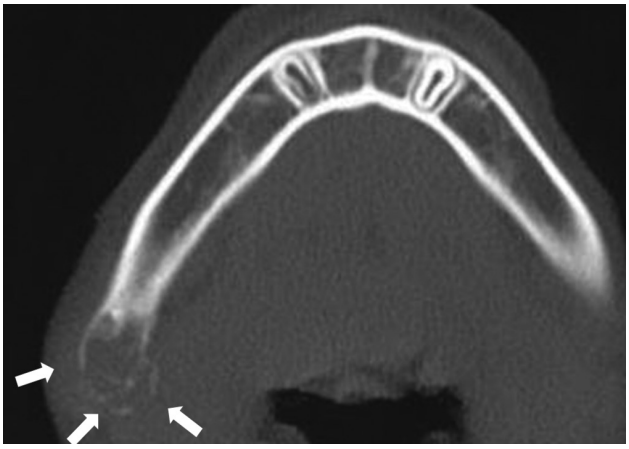

Figure 2. Computed tomography image obtained in the axial plane. A bone-like spicule was observed around the cortical bone defect with an unclear border (arrows).

In October 2009, the patient underwent tumorectomy and grafting of iliac cancellous bone under general anesthesia (Figure 4). A surgery was operated on the submandibular lesion, and the tumor was enucleated in one lump. Although the border between the tumor and bone was relatively clear, the bony surface exposed after tumorectomy was curetted in one layer with a rounded carbide bur. An absorbable plate was applied to give the mandibular angle morphology, and the gap between the plate and defect was filled with iliac cancellous bone. Macroscopically, the tumor was an elastic, soft lesion measuring 17 × 15 × 10 mm in size with a glossy surface and translucent white color (Figure 5).

Histopathologically, there was no obvious odontogenic epithelium, and spindle-shaped cells with little atypia were found to have proliferated in the mucous-like matrix. Immunostaining showed that AE1/AE2, desmin, and S-100 were negative, while SMA was positive. These findings support a final diagnosis of odontogenic myxofibroma (Figure 6).

Panoramic X-ray at 8 years postoperatively showed that the grafted bone had been integrated with the residual bone, without obvious difference in mandibular growth between the left and right sides (Figure 7). More than 14 years since the surgery had passed, the post-operative course for the patient had been uneventful without recurrence.

Figure 3. Magnetic resonance imaging. (A) T1-weighted image (axial plane). (B) T2-weighted short inversion time inversion-recovery image (axial plane). T1-weighted image showed a low signal intensity (arrows), and T2-weighted image showed a high signal intensity with a partially irregular border with the surrounding bone (arrows).

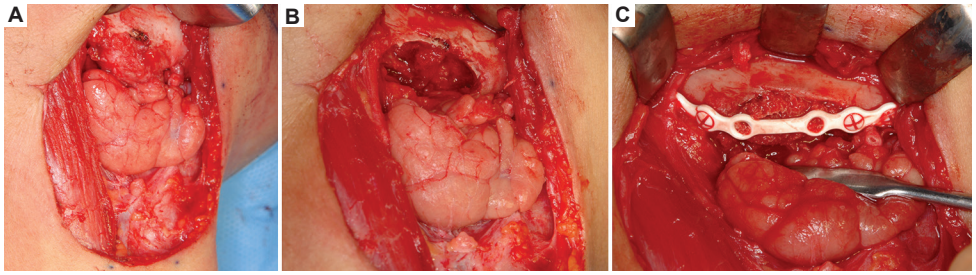

Figure 4. Intraoperative findings. (A) Surgical exposure of the lesion. (B) The lesion after tumorectomy. (C) The lesion after iliac cancellous bone grafting. An absorbable plate was applied to give the mandibular angle morphology, and the gap between the plate and defect was filled with iliac cancellous bone.

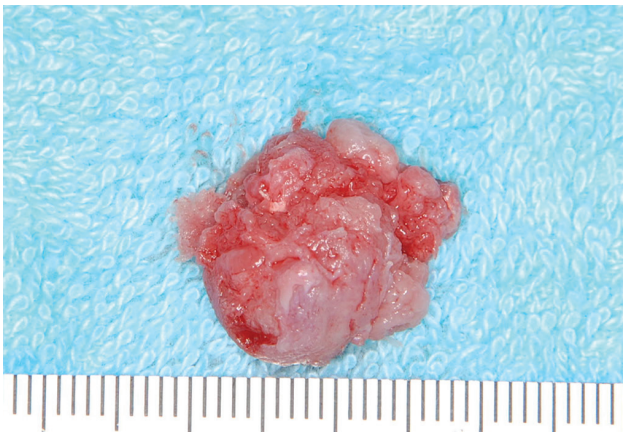

Figure 5. Enucleated specimen. The enucleated specimen, with a glossy surface and translucent white color, measures 17 × 15 × 10 mm in size.

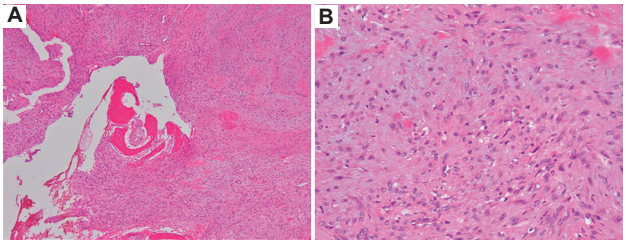

Figure 6. (A and B) Histopathological findings (hematoxylin-eosin stain). Both the image at different magnification showed. spindle-shaped cells with little atypia had proliferated in the mucous-like matrix, and the presence of odontogenic epithelium was unclear.

3. Discussion

Odontogenic myxofibromas are relatively rare tumors that occur in the jawbone intraosseously. In the 2017 World Health Organization classification of odontogenic tumors,[9] benign odontogenic tumors are classified into three categories: Benign epithelial odontogenic tumors, benign mixed epithelial-mesenchymal odontogenic tumors, and benign mesenchymal odontogenic tumors. Odontogenic myxofibroma is categorized as a benign mesenchymal odontogenic tumor, like odontogenic myxoma. Among odontogenic myxomas, those with a lot of fibrous formation

Figure 7. A panoramic X-ray scan at 8-year postoperatively. The grafted bone at the right mandibular angle had been integrated with the existing bone, and the mandibular angle morphology was found to be under recovery (arrows).

in the mucous-like matrix are specifically diagnosed as odontogenic myxofibromas. Typically, lesions that occur in the jawbone are defined as odontogenic, but such a definition does not extend to the presence or absence of an odontogenic epithelial mass while making a diagnosis.[1,4,10] Indeed, many cases have actually been reported in which no odontogenic epithelium is found, as in our present case (Tables 1 and 2).

The incidence of both odontogenic myxoma and odontogenic myxofibroma is estimated to be 3.3 – 15.7% among odontogenic tumors in Europe and the US.[5,7] The incidence in children under 10 years of age is 0.7 – 3.5%, which is lower than that in adults.[1-3] In Japan, the incidence of odontogenic myxoma and myxofribroma is 1.6 – 2.7%, which is lower than that in other countries.

Since statistics on odontogenic myxofibromas alone are not widely available, we performed a clinical statistical analysis of 46 cases of odontogenic myxofibromas of the mandible occurring in Japan from 1970 to 2023. The patient age ranged from 3 to 64 years old, and 38 cases (82.6%) were ≥11 years old (Table 1), while 8 (17.4%) were ≤10 years old (Table 2). There was a slight preponderance of female patients in the cases, with 17 male cases (44.7%) and 21 female cases

Table 1. Reports of odontogenic myxofibroma in the mandible angle in Japanese cases aged ≥11 years old

Case	Authors	Year	Age (years)	Gender	Radiographic findings				Localization	Treatment	Odontogenic epithelium	Follow-up time (months)
					Features	Maximum diameter of lesion (mm)	Alveolar bone invasiveness	Unerupted impacted tooth				
1	Momiyama *et al.*[11]	1970	13	F	Honeycomb	80	Yes	Yes	The right mandibular first premolar~second molar	Enucleation and curettage	No	Unknown
2	Masuda *et al.*[12]	1971	36	F	Multilocular; clear border	50	Yes	No	The left mandibular canine~third molar	Partial mandibulectomy	No	51
3	Watanabe *et al.*[13]	1971	25	M	Multilocular; dendriform	30	Yes	No	The left mandibular first premolar~first molar	Enucleation and curettage	No	5
4	Okayama *et al.*[14]	1973	27	F	Honeycomb; dendriform; unclear border	50	Yes	Yes	The right mandibular first molar~the right mandibular ramus	Enucleation and curettage	No	Unknown
5	Sakai *et al.*[15]	1976	28	M	Unknown	Unknown	Unknown	No	The right mandibular canine~the left second premolar	Unknown	Unknown	Unknown
6			35	F	Unknown	Unknown	Unknown	No	The right mandibular second molar	Unknown	Unknown	Unknown
7			38	F	Unknown	Unknown	Unknown	No	The right mandibular second premolar~third molar	Unknown	Unknown	Unknown
8			44	M	Unknown	Unknown	Unknown	No	The left mandibular first molar	Unknown	Unknown	Unknown
9			27	F	Unknown	Unknown	Unknown	No	The right mandibular first molar	Unknown	Unknown	Unknown
10			43	F	Unknown	Unknown	Unknown	No	The right mandibular second premolar~second molar	Unknown	Unknown	Unknown
11	Okui *et al.*[16]	1976	32	F	Multilocular; clear border	20	Yes	No	The right mandibular central incisor~canine	Enucleation and curettage	No	Unknown
12	Izumi *et al.*[17]	1977	49	M	Dendriform	15	Yes	No	Unknown	Enucleation and curettage	No	72
13	Kurachi *et al.*[18]	1977	29	F	Multilocular; clear border	35	Yes	No	The right mandibular lateral incisor~the left mandibular canine	Partial mandibulectomy	No	48
14	Nishijima *et al.*[19]	1978	26	F	Multilocular; Dendriform; clear border	40	Yes	Yes	Unknown	Enucleation and curettage	No	24
15	Nishijima *et al.*[20]	1978	34	F	Multilocular; clear border	40	No	No	The left mandibular central incisor~second molar	Hemi-mandibulectomy	No	Unknown

(Cont'd...)

Table 1. *(Continued)*

Case	Authors	Year	Age (years)	Gender	Radiographic findings				Localization	Treatment	Odontogenic epithelium	Follow-up time (months)
					Features	Maximum diameter of lesion (mm)	Alveolar bone invasiveness	Unerupted impacted tooth				
16	Osaki *et al.*[21]	1978	48	M	Multilocular; clear border	20	Yes	No	The right mandibular first premolar~the left mandibular first premolar	Enucleation and curettage	No	9
17	Furuta *et al.*[22]	1979	17	M	Ground glass appearance; slightly unclear border	Unknown	Yes	No	The right mandibular ramus	Enucleation and curettage	No	24
18	Abe *et al.*[23]	1979	44	F	Multilocular; clear border	43	Yes	No	The right mandibular canine~the left mandibular first premolar	Enucleation and curettage	Yes	6
19	Miyake *et al.*[24]	1981	35	F	Multilocular; clear border	30	Yes	No	The right mandibular first molar~the right mandibular ramus	Partial mandibulectomy	No	30
20	Tanaka *et al.*[25]	1983	64	M	Multilocular	90	Yes	No	The left mandibular first molar~third molar	Hemi-mandibulectomy PCBM grafts (plate reconstruction)	No	13
21	Futenma *et al.*[26]	1984	16	M	Clear border	65	Yes	Yes	The left mandibular first premolar~first molar	Enucleation and curettage	Yes	28
22	Osuga *et al.*[27]	1985	43	M	Multilocular; Dendriform; unclear border	77	Yes	No	The left mandibular canine~the left mandibular notch, condylar process	Segmental mandibulectomy PCBM grafts (plate reconstruction)	No	30
23	Nomura *et al.*[28]	1987	29	F	Multilocular; dendriform; slightly unclear border	50	Yes	No	The left mandibular second premolar~third molar	Enucleation and curettage	No	15
24			43	F	Multilocular; partially irregular border	25	Yes	No	The right mandibular canine~second molar	Enucleation and curettage	No	10
25	Ohshima *et al.*[29]	1987	25	M	Sun-ray appearance; partially clear border	20	Yes	No	The left mandibular first premolar~second molar	Enucleation and curettage	Yes	8
26	Yasukawa *et al.*[30]	1988	15	F	Multilocular; dendriform; unclear border	70	Yes	Yes	The right mandibular first premolar~first molar	Segmental mandibulectomy PCBM grafts (plate reconstruction)	No	About 48
27			43	M	Bilocular; clear border	20	Yes	No	The left mandibular first premolar~first molar	Enucleation and curettage PCBM grafts	No	17

(Cont'd...)

Table 1. *(Continued)*

Case	Authors	Year	Age (years)	Gender	Radiographic findings				Localization	Treatment	Odontogenic epithelium	Follow-up time (months)
					Features	Maximum diameter of lesion (mm)	Alveolar bone invasiveness	Unerupted impacted tooth				
28			24	F	Dendriform; clear border	60	Yes	Yes	The right mandibular second premolar~the right mandibular ramus	Segmental mandibulectomy PCBM grafts (plate reconstruction)	No	27
29	Ishihara *et al.*[31]	1989	26	M	Unilocular; clear border	30	Yes	No	The right mandibular first premolar~first molar	Enucleation and curettage	No	24
30	Okada *et al.*[32]	1990	26	M	Unilocular; clear border	30	Yes	Yes	Unknown	Enucleation and curettage	Yes	18
31	Nakagawa *et al.*[33]	1998	37	M	Multilocular; clear border	80	Yes	Yes	The right mandibular second premolar~the right mandibular ramus	Segmental mandibulectomy	Yes	8
32	Suzuki *et al.*[34]	1999	24	F	Soap bubble appearance	44	Yes	No	The right mandibular first premolar~the left mandibular lateral incisor	Enucleation and curettage	Yes	12
33	Shimizu *et al.*[35]	2004	61	F	Multilocular; clear border	30	Yes	No	The left mandibular second premolar~third molar	Segmental mandibulectomy PCBM grafts (plate reconstruction)	No	16
34	Yagishita *et al.*[36]	2007	41	M	Multilocular; clear border	40	Yes	No	The left mandibular median~the left mandibular coronoid process	Enucleation and curettage	No	17
35	Kadono *et al.*[37]	2009	41	M	Multilocular; dendriform; clear border	60	Yes	Yes	Unknown	Enucleation and curettage	Yes	18
36	Suwa *et al.*[38]	2013	20	F	Multilocular; clear border	10	Yes	No	The right mandibular lateral incisor~second premolar	Enucleation and fenestration	No	24
37	Ohta *et al.*[39]	2015	36	F	Clear border	Unknown	Yes	No	The right mandibular second premolar~the right mandibular ramus	Segmental mandibulectomy; mandibular reconstruction using PCBM grafts with titanium mesh tray	No	72
38	Sato *et al.*[40]	2018	22	M	Unilocular; clear border	30	Yes	No	The left mandibular third molar~the left condyle	Zygomatic osteotomy; segmental mandibulectomy; plate reconstruction	No	84

Abbreviations: M: Male; F: Female; PCBM: Particulate cancellous bone and marrow.

Table 2. Reports of odontogenic myxofibroma in the mandible angle in Japanese cases aged ≤10 years old

Case	Authors	Year	Age (y)	Gender	Radiographic findings				Localization	Treatment	Odontogenic epithelium	Follow-up time (months)
					Features	Maximum diameter of lesion (mm)	Alveolar bone invasiveness	Unerupted impacted tooth				
1	Ito *et al.*[41]	1973	10	M	Unilocular clear border	80	Yes	Yes	The left mandibular second molar~the left mandibular ramus	Enucleation and curettage PCBM grafts	No	8
2	Inoue *et al.*[42]	1979	7	F	Unilocular	43 and 20 Two lesions	Yes	Yes	The left mandibular second primary molar~the left mandibular ramus	Enucleation and curettage	Yes	24
3	Osuga *et al.*[27]	1985	8	F	Dendriform; honeycomb; clear border	27	Yes	No	The right mandibular second primary molar	Enucleation and curettage	No	20
4	Sato *et al.*[43]	2017	8	M	Unilocular; clear border	20	Yes	Yes	The right mandibular second molar	Enucleation and curettage	Yes	42
5	Kanda *et al.*[44]	2018	6	M	Unilocular; clear border	25	Yes	Yes	The left mandibular second primary molar~first molar	Enucleation and fenestration	Yes	24
6	Oda *et al.*[45]	2020	8	M	Unilocular; clear border	Unknown	Yes	Yes	The right mandibular first molar~the right mandibular ramus	First biopsy: fenestration; second biopsy: enucleation and curettage	No	44
7	Kanoh *et al.*[46]	2021	3	F	Unilocular; clear border	16	No	No	The right mandibular angle	Enucleation and curettage	No	84
8	The current case	2023	10	M	Unilocular; unclear border	17	No	No	The right mandibular angle	Enucleation and curettage PCBM grafts (plate reconstruction)	No	168

Abbreviations: M: Male; F: Female; PCBM: Particulate cancellous bone and marrow.

(55.3%), which is consistent with previous reports.[4,8] However, among children ≤10 years of age, 5 (62.5%) were boys and 3 (37.5%) were girls, highlighting a slight preponderance of male patients. In general, the lesions invade into the alveolar bone and are often accompanied by root resorption and deviation of adjacent teeth. Only three cases (6.5%), including our own, were reported to be localized in the mandibular angle and not associated with teeth.

Differential diagnoses include ameloblastoma, myxoid nerve sheath tumors, chondromyxoid fibroma, low-grade myxofibrosarcoma,[9] and osteosarcoma. Among them, differentiation from malignancy is of significant clinical relevance. The radiographic and CT findings in myxofibromas are often uni- or multi-locular radiolucent images showing unclear borders, and the cortical bone around the lesion is usually bulging and thinning.[47] In the present case, the radiographic and CT images showed a unilocular radiolucent image with unclear borders accompanied by cortical bone resorption and protrusion. This finding was similar to the characteristic of osteosarcoma of the jaw, such as osteoid protrusion (spicula) and reactive trabecular bone formation (sun-ray image), which made differentiation difficult.[6] In some cases of osteosarcoma of the jawbone, radiographic findings have shown a radiolucent image with a clear border, such as a cyst, which reportedly hampered differentiation from benign diseases.[48,49] Therefore, making a careful diagnosis is critical.

Radical resection or conservative surgery is the most common method of treatment, and Meleti *et al.*[8] stated that the rates were 26.09% and 73.91%, respectively. In the present analysis of 46 cases in Japan, radical resection was performed in 12 cases (26.1%) and conservative surgery in 28 cases (60.9%), with the approach unknown in 6 cases (13.0%), a trend similar to that reported in Europe and the US.[8] There are differences of opinion concerning the selection of surgical procedure, with some reports supporting the choice of radical resection in cases of large lesions or recurrence, considering the local invasiveness of the tumor.[1,50,51] However, extensive jaw resection in children may induce aesthetic issues and psychological suffering due to hindered growth of the maxillofacial region and a deformed facial appearance. Therefore, it is suggested that benign mandibular tumors in young patients first be treated with enucleation and curettage, even if the tumor is large enough to be considered for jaw resection. In fact, in the eight pediatric cases ≤10 years of age assessed in this analysis, enucleation and curettage or enucleation and fenestration were selected, and conservative surgery was performed in 100% of these cases. In contrast, in 38 adult cases, conservative treatment was applied in only 20 cases (52.6%), suggesting that conservative surgery was more commonly performed in children than in adults. In this case study, we performed enucleation and curettage, considering the site of origin, age, growth, and post-operative appearance. The patient had been well without recurrence for 14 years since the surgery. Until now, there have been no functional or aesthetic issues reported by the patient.

Odontogenic myxofibromas may show invasive growth into bone, and there are reports of recurrence in 9.5% of patients over 3 years of follow-up.[8,52] In children, 20% of myxomas and myxofibromas in patients under 16 years of age recurred within 1 year after surgery.[7] There were no reports of recurrence among the 46 Japanese cases we analyzed. However, the mean post-operative observation period of the 45 patients, excluding our own case, was only 2 years and 3 months (ranging from 5 months to 7 years), and data on post-operative observation period were not described for 10 cases. In addition, the follow-up period of the six pediatric cases ranged from 8 months to 7 years, and none of the cases had a long-term follow-up period as long as 14 years like ours. Thus, the actual recurrence rate of odontogenic myxofibromas in the long term is unknown. A large-scale study of the long-term prognosis should be conducted to investigate the appropriateness of conservative surgery. In addition, given that studying post-operative growth is taken into account in pediatric cases, we consider that long-term follow-up is necessary to evaluate the functional and esthetic effect of the procedure.

4. Conclusion

We report a case of odontogenic myxofibroma that arose in the mandibular angle of a pediatric patient with a long-term follow-up of more than 14 years. The occurrence of odontogenic myxofibromas in the jawbone of children has been rarely reported.[53] This case report and literature statistics will provide helpful information for the diagnosis and determining treatment strategies for odontogenic myxofibroma in children with growth process.

Acknowledgments

None.

Funding

None.

Conflict of interest

The authors declare no conflicts of interest.

Author contributions

Conceptualization: Momoko Yoshikawa, Takeshi Karube, Seiji Asoda

Data curation: Momoko Yoshikawa, Takeshi Karube, Hiroki Nagamine, Wataru Muraoka, Hideki Kizu

Investigation: Momoko Yoshikawa, Takeshi Karube, Hiroki Nagamine, Wataru Muraoka, Hideki Kizu

Supervision: Seiji Asoda, Hiromasa Kawana, Taneaki Nakagawa

Writing – original draft: Momoko Yoshikawa Seiji Asoda

Writing – review & editing: Momoko Yoshikawa, Takeshi Karube, Seiji Asoda

Ethics approval and consent to participate

An explicit permission or consent of the case subject described in this case report had been obtained before their participation.

Consent for publication

Informed consent has been obtained from the patient for publication of this case report.

Availability of data

The data can be requested from the corresponding author following reasonable request.

References

1. Haser GC, Su HK, Hernandez-Prera JC, *et al.* Pediatric odontogenic fibromyxoma of the mandible: Case report and review of the literature. *Head Neck*. 2016;38(1):E25-E28.

   doi: 10.1002/hed.24090

2. Mortellaro C, Berrone M, Turatti G, *et al.* Odontogenic tumors in childhood: A retrospective study of 86 treated cases. Importance of a correct histopathologic diagnosis. *J Craniofac Surg*. 2008;19(4):1173-1176.

   doi: 10.1097/SCS.0b013e31805151d3

3. Guerrisi M, Piloni MJ, Keszler A. Odontogenic tumors in children and adolescents. A 15-year retrospective study in Argentina. *Med Oral Patol Oral Cir Bucal*. 2007;12(3):E180-E185.

4. Chrcanovic BR, Gomez RS. Odontogenic myxoma: An updated analysis of 1,692 cases reported in the literature. *Oral Dis*. 2019;25(3):676-683.

   doi: 10.1111/odi.12875

5. Kansy K, Juergens P, Krol Z, *et al.* Odontogenic myxoma: Diagnostic and therapeutic challenges in paediatric and adult patients--a case series and review of the literature. *J Craniomaxillofac Surg*. 2012;40(3):271-276.

   doi: 10.1016/j.jcms.2011.04.009

6. Malik F, Gleysteen JP, Agarwal S. Osteosarcoma of the jaw: Report of 3 cases (including the rare epithelioid variant) with review of literature. *Oral Surg Oral Med Oral Pathol Oral Radiol*. 2021;131(3):e71-e80.

   doi: 10.1016/j.oooo.2020.03.044

7. Keszler A, Dominguez FV, Giannunzio G. Myxoma in childhood: An analysis of 10 cases. *J Oral Maxillofac Surg*. 1995;53(5):518-521.

   doi: 10.1016/0278-2391(95)90062-4

8. Meleti M, Giovannacci I, Corradi D, *et al.* Odontogenic myxofibroma: A concise review of the literature with emphasis on the surgical approach. *Med Oral Patol Oral Cir Bucal*. 2015;20(1):e1-e6.

   doi: 10.4317/medoral.19842

9. El-Naggar AK, Chan JKC, Grandis JR, Takata T, Slootweg PJ. *WHO Classification of Head* and *Neck Tumours*. 4th ed. Lyon: IARC Press; 2017. p. 229-230.

10. Buchner A, Odell E. Odontogenic myxoma/myxofibroma. In: Barnes L, Eveson JW, Reichart P, Sidransky D, editors. *World Health Organization Classification of Tumours: Pathology* and *Genetics Head* and *Neck Tumours*. Lyon: IARC Press; 2005. p. 316-317.

11. Momiyama M, Kawarada K, Sugiyama T, *et al*. Myxoma of the jaw cases and review of the Japanese Literature. *J Jpn Stomatol Soc*. 1970;19:957-965.

12. Masuda M, Murase H, Kawachi S, *et al*. Two cases of the central myxofibroma. *Jpn J Oral Maxillofac Surg*. 1971;18:432-437.

13. Watanabe K, Mushimoto K, Yamamoto S, *et al*. A case of myxofibroma in the mandible. *J Jpn Stomatol Soc*. 1971;20:795-800.

14. Okayama H, Ito T, Higa R, Seguchi Y, Yoshimoto M. Myxofibroma of the mandible. Report of a case with special reference to electron microscopic observation. *Nihon Koku Geka Gakkai Zasshi*. 1973;19:491-495.

   doi: 10.5794/jjoms.19.491

15. Sakai Y, Horiuchi H, Takahashi S. Eight cases of myxofibroma in the oral cavity. *J Tokyo Dent Coll Soc*. 1976;10:1471-1477.

16. Okui K, Nagahata H, Shimosato T, *et al*. Myxomatous change in central fibroma: An electron microscopic study. *Jpn J Oral Maxillofac Surg*. 1976;22:805-811.

17. Izumi H, Oikawa T, Iwasaki O, *et al*. Clinicopathological studies on myxoma of the jaw in Japan. *Nihon Univ J Oral Sci*. 1977;3:114-127.

18. Kurachi Y, Nagumo M, Enomoto S, *et al*. Three cases of myxoma of the jaw. *Jpn J Oral Maxillofac Surg*. 1977;23:631-636.

19. Nishijima K, Ishida T, Okamoto Y, *et al*. A case of myxofibroma in the area of the anterior mandible. *Jpn J Oral*

Maxillofac Surg. 1978;24:94-98.

20. Nishijima K, Nagahata S, Okamoto Y, *et al*. A case of myxofibroma in the area of the right mandible ramus. *Jpn J Oral Maxillofac Surg*. 1978;24:1127-1131.
21. Osaki T, Kotani H, Ogawa T, *et al*. Myxofibroma of the mandible and the cheek: Report of two cases. *Jpn J Oral Maxillofac Surg*. 1978;24:1202-1206.
22. Furuta N, Kaneko K, Hasegawa A, *et al*. Surgical treatment and that postoperative course for mandibular nonmalignant tumors of young patients by enucleation of tumor and removal of circumferential bone. *Jpn J Oral Maxillofac Surg*. 1979;25:345-352.
23. Abe N, Sakamoto S, Kameyama Y, *et al*. A case of odontogenic myxo-fibroma. *J Matsumoto Dent Univ Soc*. 1979;5:45-52.
24. Miyake M, Iwanari S, Daito Y, *et al*. A study on a case of epulis-like myxofibroma in mandibula. *Nihon Univ Dent J*. 1981;55:936-942.
25. Tanaka T, Mimura T, Oheda N, *et al*. Reconstruction after the hemimandibulectomy on the patient with widespread myxoma: Report of a case. *Jpn J Oral Maxillofac Surg*. 1983;29:591-596.
26. Futenma C, Matsuda K, Igari T, *et al*. Odontogenic myxofibroma with peculiar calcareous Substances: Report of a case. *Jpn J Oral Maxillofac Surg*. 1984;30:1494-1500.
27. Osuga T, Kinoshita F, Shionoya N, *et al*. Clinical study of odontogenic myxofibroma--report of 2 cases and literature review. *Josai Shika Daigaku Kiyo*. 1985;14(1):103-114.
28. Nomura J, Tagawa T, Hirano Y, *et al*. Two cases of myxofibroma in the jaw and discussion based on references in Japan. *J Jpn Stomatol Soc*. 1987;36:226-238.
29. Ohshima T, Takai Y, Mori K, *et al*. A case of odontogenic myxofibroma of the mandible. *Jpn J Oral Maxillofac Surg*. 1987;33:117-122.
30. Yasukawa K, Kobayashi N, Asano S, *et al*. Myxofibroma of the mandible: Report of three cases. *Jpn J Oral Maxillofac Surg*. 1988;34:558-564.
31. Ishihara A, Matsumoto S, Kaneko M, *et al*. A case of myxofibroma in the area of the anterior mandible. *Jpn J Oral Maxillofac Surg*. 1989;35:1922-1928.
32. Okada T, Saito K, Kataoka R, *et al*. A case of odontogenic myxofibroma of the mandible. *Jpn J Oral Maxillofac Surg*. 1990;36:695-699.
33. Nakagawa A, Suzuki Y, Tojima H, *et al*. A case of odontogenic myxofibroma of the mandible. *Otolaryngol Head Neck Surg*. 1998;70:907-919.
34. Suzuki T, Tsurusako S, Hattori H, *et al*. A case of odontogenic myxofibroma occurring from anterior teeth to premolar area of mandible. *Jpn Stomatol Soc*. 1999;48:83-86.
35. Shimizu M, Tahima T, Tatsuta Y, *et al*. A case of myxofibroma of the mandible. *Jpn J Oral Diag*. 2004;17:124-130.
36. Yagishita Y, Shigematsu H, Hori T, *et al*. A case of central odontogenic myxofibroma managed by conservative surgery. *Jpn J Oral Diag*. 2007;20:120-129.
37. Kadono S, Yohida H, Sakata T, *et al*. A case of odontogenic myxofibroma in the mandible. *Jpn J Oral Diag*. 2009;22:299-302.
38. Suwa H, Kawarada K, Atsuzi K, *et al*. a case of myxofibroma in the mandible. *J Gifu Dent Soc*. 2013;40:159-163.
39. Ohta K, Takechi M, Shigeishi H, Okumura T, Miyauchi M, Takata T. A case of implant treatment and mandibular reconstruction using titanium mesh tray and autogenous iliac particulate cancellous bone in a patients with odontogenic myxofibroma. *J Jpn Stomatol Soc*. 2015;64:269-275.

    doi: 10.11277/stomatology.64.269
40. Sato H, Asoda S, Muraoka W, *et al*. Large odontogenic mixofibroma of the mandible excised without visible scar: A case report. *J Oral Maxillofac Surg Med Pathol*. 2018;30:272-277.

    doi: 10.1016/j.ajoms.2018.02.002
41. Ito T, Soga K, Tsuboguchi T, *et al*. A case of odonotogenic myxofibroma of the left mandible. *Jpn J Oral Maxillofac Surg*. 1973;19:365-368.
42. Inoue Y, Ishikawa K, Jinno T, *et al*. A case of odontgenic myxofibroma. *Aichi Gakuin J Dent Sci*. 1979;17:87-93.
43. Sato H, Yasui T, Karube T, *et al*. A case of odontogenic myxofibroma in the mandible of a child. *Jpn J Oral Maxillofac Surg*. 2017;63:467-471.
44. Kanda T, Nobumoto T, Hamada A, *et al*. A case of pediatric odontogenic myxofibroma of the mandible. *J Hiroshima Univ Dent Soc*. 2018;50:77-83.
45. Oda S, Mori M, Harada H. A case of odontogenic myxofibroma arising in the mandible of a child. *J Jpn Oral Med*. 2020;26:31-35.
46. Kanoh Y, Yamaguchi S, Ohbuchi Y, Yamamoto T, Miyabe S, Shimozato K. A case of odontogenic myxofibroma arising in the inferior border of the mandible of a 3-year-old girl. *Jpn J Oral Maxillofac Surg*. 2021;67:188-193.

    doi: 10.5794/jjoms.67.188
47. Alhousami T, Sabharwal A, Gupta S, Aguirre A, Park E, Kramer JM. Fibromyxoma of the jaw: Case report and review of the literature. *Head Neck Pathol*. 2018;12(1):44-51.

    doi: 10.1007/s12105-017-0823-0
48. Delgado R, Maafs E, Alfeiran A, *et al*. Osteosarcoma of the jaw. *Head Neck*. 1994;16(3):246-252.

    doi: 10.1002/hed.2880160307
49. Vege DS, Borges AM, Aggrawal K, Balasubramaniam G, Parikh DM, Bhaser B. Osteosarcoma of the craniofacial bones. A clinico-pathological study. *J Craniomaxillofac Surg*. 1991;19(2):90-93.

doi: 10.1016/s1010-5182(05)80614-6

50. Infante-Cossío P, Martínez-de-Fuentes R, García-Perla-García A, Jiménez-Castellanos E, Gómez-Izquierdo L. Myxofibroma of the maxilla. Reconstruction with iliac crest graft and dental implants after tumor resection. *Med Oral Patol Oral Cir Bucal*. 2011;16(4):e532-e536.

doi: 10.4317/medoral.16.e532

51. Lahey E, Woo SB, Park HK. Odontogenic myxoma with diffuse calcifications: A case report and review of the literature. *Head Neck Pathol*. 2013;7(1):97-102.

doi: 10.1007/s12105-012-0387-y

52. Abiose BO, Ajagbe HA, Thomas O. Fibromyxomas of the jawbones--a study of ten cases. *Br J Oral Maxillofac Surg*. 1987;25(5):415-421.

doi: 10.1016/0266-4356(87)90093-3

53. Santarelli A, Mascitti M, Capocasale G, *et al.* Odontogenic myxofibroma in a paediatric patient: Case report and review of the literature. *Glob J Oral Sci.* 2015;1:23-28.

doi: 10.30576/2414-2050.2015.01.5

ACCSCIENCE PUBLISHING

Tumor Discovery

CASE SERIES

Inflammatory disease of the orbit: A case series

Meliani Kaoutar[1]*, Rhandour Widad[1], Bouardi Nizar[2], Maaroufi Mustapha[2], Khammar Zineb[1†], and Berrady Rhizlane[1†]*

[1]Department of Internal Medicine and Onco Hematology, CHU Hassan II Fez, Fez, Morocco

[2]Department of Radiology, Chu Hassan II Fez, Fez, Morocco

Abstract

Inflammatory orbital pseudotumors are a heterogeneous group of diseases characterized by their sensitivity to corticosteroid treatment regardless of the underlying etiology. Histological examination is generally performed following a lack of response to steroids, progressive neurological involvement, or suspicion of malignancy on radiological imaging. Herein, we report three clinical cases presented to our internal medicine department. The first case underscores the need for enucleation of the orbit due to the aggressiveness of orbital pseudotumors. This first case revealed Takayasu disease in a 39-year-old patient. Following the failure of corticosteroid therapy, favorable progression was achieved with adalimumab. Our second case concerns a 49-year-old woman presenting with exophthalmos, demonstrating rapid improvement in both clinical and biological parameters on corticosteroid administration. However, despite clinical amelioration, the partial radiological persistence of the orbital tumor prompted a positron emission tomography scan, revealing intense metabolic activity in the orbit despite the absence of clinical symptoms. Given the impracticability of biopsy, treatment with anti-CD20 was proposed, yielding a favorable radiological response. The third case describes an inflammatory orbital pseudotumor revealed by hemolytic anemia, with improved clinical and biological parameters observed over a 6-month period.

Keywords: Inflammatory disease of the orbit; Orbital inflammatory syndrome; Orbital pseudotumor; Vasculitis; Hemolytic anemia

†These authors contributed equally to this work.

***Corresponding authors:**
Meliani Kaoutar
(kaoutar.meliani@usmba.ac.com)
Berrady rhizlane
(Rhizberr@yahoo.fr)

Citation: Kaoutar M, Widad R, Nizar B, Mustapha M, Zineb K, Rhizlane B. Inflammatory disease of the orbit: A case series. *Tumor Discov.* 2024;3(1):1792. https://doi.org/10.36922/td.1792

Received: September 11, 2023
Accepted: December 28, 2023
Published Online: March 28, 2024

1. Introduction

Inflammatory disease of the orbit (IDO) is a disease that affects all elements of the orbit and its appendages. It was first described by Gleason[1] and subsequently elaborated by other researchers.[2]

IDO affects individuals across all age groups, representing up to 6% of orbital disorders and frequently necessitating orbital biopsy procedures.[3] Its differential diagnosis encompasses a variety of disorders, including tumors, infections, congenital deformities, trauma, and systemic or local inflammatory diseases.[4] Several systemic inflammatory disorders are associated with IDO, including giant cell arteritis, Churg-Strauss syndrome, Erdheim-Chester disease, histiocytosis X, autoimmune thyroid disease, sarcoidosis, granulomatosis with polyangiitis, Crohn's disease, systemic lupus erythematosus, and other connective tissue diseases.[5]

Congenital lesions, particularly lymphangiomas and dermoid cysts, may exhibit sporadic symptoms that resemble IDO or develop an inflammatory component.[6] In addition, the extra-scleral expansion of primary eye tumors, such as malignant melanomas, can trigger a subsequent orbital inflammatory response.[7]

Inflammatory elements can present in both primary and metastatic tumors within the orbit, with rhabdomyosarcoma notably exhibiting features resembling an inflammatory disorder. Patients with IDO should undergo thorough evaluation for secondary infectious disorders stemming from bacteria, viruses, fungi, and parasites, as these infections can precipitate severe inflammatory diseases.[8]

The diagnosis of IDO relies on clinical and paraclinical assessments. Despite the aggressiveness observed in certain cases, IDO typically remains a benign condition, although it can pose a threat to orbital function and may lead to oculomotor dysfunction. Histologically, IDO is characterized by chronic inflammation without obvious local cause. In this case series, we presented the clinical, radiological, and evolutionary profiles of three clinical cases of IDO.

2. Case presentation

2.1. Case 1

A 38-year-old woman with a history of pelvic fracture was admitted to the internal medicine department for management of an evolving orbital mass over the past year.

On clinical examination, the patient presented with a painful exophthalmos on the right eye accompanied by inflammatory characteristics, chemosis, periorbital edema, lacrimation, and visual acuity of 4/10. In addition, ocular hypertonia with blurred papillary edges in the temporal region of the eye was noted. The cardiovascular examination also revealed a decreased right radial pulse and a supraclavicular murmur.

Orbital magnetic resonance imaging (MRI) revealed an extra conical intra-orbital lesion process involving the superior rectus and external rectus muscles, in contact with the lacrimal gland, with mass effect and responsible for a grade II exophthalmos, demonstrating hypointensity on both T1 and T2 imaging, with homogeneous and diffuse enhancement (Figure 1A).

A thoracic-abdominal-pelvic scan revealed bilateral lobar retractile parenchymal micronodules, with some exhibiting a budded tree morphology. In addition, diffuse inflammatory thickenings of the aorta and the right common carotid artery (Figure 1B) were observed, along with extensive stenosis of the superior mesenteric artery >15 mm and stenosis of the left renal artery, accompanied by asymmetry of kidney size of 8.5 cm on the left and 11.5 cm on the right.

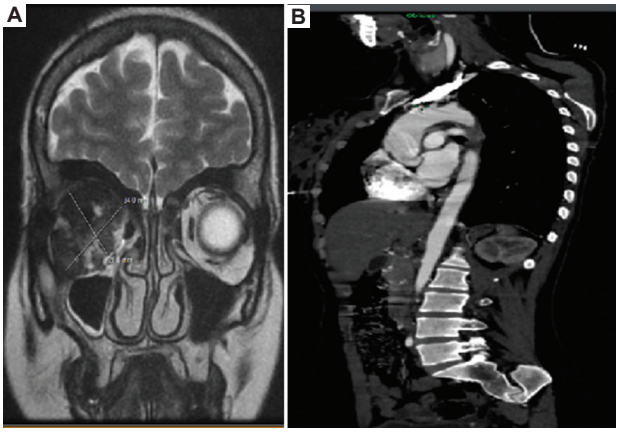

Figure 1. Imaging results of Case 1. (A) Coronal section in T2 sequence, revealing a T2-hyposignal right orbital intra- and extra-cone infiltrate. The infiltrate appears poorly defined and not centered on a particular organ, with weak enhancement after causal contrast, indicative of grade II exophthalmos. (B) Diffuse aortitis indicative of Takayasu disease.

The biological analysis revealed an inflammatory syndrome, while thyroid function tests were within normal limits. Liver and kidney function evaluations showed no abnormalities. Serological test for hepatitis, human immunodeficiency virus, syphilis, cytomegalovirus, toxoplasmosis, and rubella yielded negative results. Levels of angiotensin-converting enzyme and IgG4 were within normal ranges. The lipid profile was within acceptable parameters. *Mycobacterium tuberculosis* (MB) was identified in bronchoscopy through genetic analysis, with the presence of MB also confirmed in the pleural fluid. Subsequently, the patient was initiated on anti-tuberculosis medications (isoniazid, rifampicin, pyrazinamide, and ethambutol for the initial 2 months, followed by a continuation regimen of rifampicin and isoniazid for the subsequent 4 months).

A cardiac ultrasound revealed no abnormalities, with a good systolic ejection fraction.

Following multiple biopsies, the external orbitotomy revealed fat tissue interspersed with numerous vessels featuring congestive walls. Lymphocytic cellularity without atypia was observed, indicative of chronic and fibrous inflammatory remodeling without granulomatous lesions.

A bolus of corticosteroid therapy, administered under antibiotic cover, transiently reduced local inflammatory signals and improved clinical symptoms.

The progression was marked by the rapid resolution of superinfection in the orbit, alongside continued clinical progression of the orbital mass and persistence of the apoplexy syndrome, requiring analgesic treatment.

The ophthalmologists opted for enucleation, accompanied by several muscle and conjunctival biopsies,

due to the unique characteristics of the intraorbital tumor, which exhibited a solid and adherent consistency reminiscent of cartilage. The sole concern was to eliminate an underlying neoplastic process.

The final histological examination confirmed the pseudotumor nature of the inflammatory process. It revealed the presence of lymphoid cells and scattered T-phenotype cells expressing CD3 alongside CD20 expression by numerous well-defined nodules lacking expansive characteristics. In addition, a KI-67 proliferation index of 10% was noted, particularly accentuated in the clear germinal centers, along with vascular lesions. Furthermore, polyclonal rearrangement of the heavy and light kappa chains of immunoglobulins was observed, definitively ruling out the hypothesis of hemopathy or a solid tumor.

It was concluded that the patient had Takayasu disease, as evidenced by a pseudo-orbital tumor in conjunction with pulmonary tuberculosis. The diagnosis was based on the fulfillment of four diagnostic criteria: age, decreased right brachial pulse, supraclavicular murmur, and radiological lesions consistent with diffuse thickenings of the aorta and common carotid artery, as well as stenosis of the superior mesenteric and left renal arteries. Following successful anti-tuberculosis treatment, the patient was commenced on infliximab therapy. Subsequently, there was a resolution of clinical complaints and normalization of inflammatory signals after 1 month of treatment. At the 6-month follow-up, a positron emission tomography (PET) scan revealed a slight residual hypermetabolism localized to the orbital mass, with no hypermetabolism elsewhere.

2.2. Case 2

A 49-year-old woman, mother of four children, with a history of hysterectomy for a benign pelvic mass 4 years ago, presented with a capricious, non-painful orbital mass evolving over 2 years. Clinical examination revealed an irreducible, painful, and non-pulsatile axial exophthalmos, which did not worsen in the forward-leaning position or with the Valsalva maneuver. Visual acuity was 8/10, with no oculomotor abnormalities. Scans and MRI revealed a process of right ocular lesion, extended to the posterior pole with invasion of the optic nerve and involvement of the superior and external rectus muscle (Figure 2A-C).

Biological analysis showed evidence of an inflammatory syndrome, along with negative serologies (serology hepatitis, human immunodeficiency virus, syphilis, and toxoplasmosis). Intradermal tuberculin test and MB sputum test results were negative. Anti-neutropohil cytoplasmic antibodies test was negative, while levels of angiotensin-converting enzyme were within normal limits. Renal and hepatic functions were normal, as were the

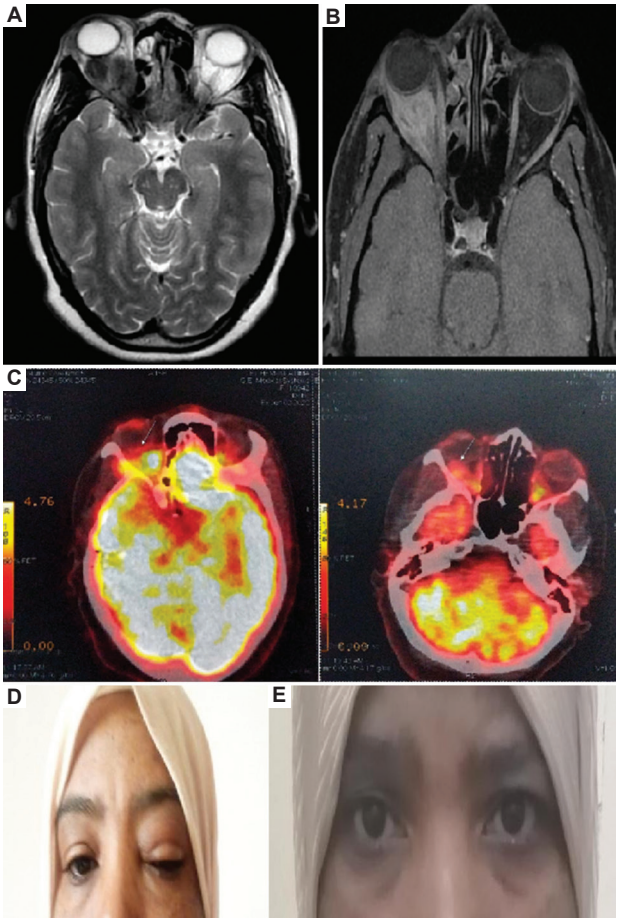

Figure 2. Medical examinations of Case 2. (A) Magnetic resonance imaging of the orbit. (B) Axial and coronal section in T2 sequence, demonstrating a T2-hyposignal, poorly defined right orbital intraconal infiltrate, not centered on a particular organ, and exhibiting weak enhancement after contrast administration, consistent with grade I exophthalmos. (C) Positron emission tomography scan obtained after 1 month of CD20 monoclonal antibodies (rituximab) treatment, demonstrating regression of metabolic activity. External photographs of the patient, captured before (D) and after (E) treatment.

results of the IgG4 assay. A salivary gland biopsy yielded normal findings, with a focus score of 0.

The diagnosis of idiopathic orbital pseudotumor was established based on clinical and radiological criteria. The patient was initially treated with bolus corticosteroids followed by oral corticosteroids at a dosage of 1 mg/kg/day, resulting in favorable clinical progression. Notably, there was a complete resolution of exophthalmos and restoration of visual acuity to 10/10 within the 1st week of treatment (Figure 2C and E). A follow-up imaging study conducted after 3 months of treatment demonstrated a 50% improvement in the inflammatory process (Figure 2D). However, a PET scan revealed persistent disease activity in the right orbital mass, prompting a therapeutic switch to weekly

CD20 monoclonal antibodies (rituximab 375 mg/m^2). A subsequent PET scan after 1 month of rituximab therapy demonstrated a decrease in metabolic activity (Figure 2D). A radiological follow-up was planned after 6 months of treatment, with maintenance therapy using rituximab.

2.3. Case 3

A 58-year-old man with a history of bilateral cataracts for 1 year presented with an alteration in his general condition. General examination revealed an anemic syndrome, splenomegaly with a 6 cm costal margin, hepatomegaly, a solid, and non-pulsatile left orbital tumor (Figure 3A), accompanied by conjunctival jaundice. Orbital MRI revealed a well-defined oval lesion formation in the left palpebral region with regular hyposignal contours on T1 and T2 sequences, without extension into the end orbit (Figure 3C). In addition, scans indicated hepatosplenomegaly measuring 24 cm, with the spleen also measuring 24 cm.

Biological findings revealed profound anemia, characterized by a hemoglobin level of 4 g/dl. In addition, leukopenia was observed with a leukocyte count of 2264/mm^3, along with lymphopenia (lymphocyte count at 765/mm^3) and thrombocytopenia (platelet count at 9000/mm^3). A regenerative reticulocyte count was noted, along with a positive indirect Coombs test. The phospho-calcium balance was within normal limits. Inflammatory markers showed a positive polyclonal profile on protein electrophoresis, with a C-reactive protein level of 85 mg/L. Renal function tests yielded normal results, as did the thyroid test. Furthermore, serological tests indicated a history of successfully treated chronic hepatitis B with an undetectable viral load. Serological tests for hepatitis C, human immunodeficiency virus, syphilis, and toxoplasmosis returned negative results. In addition, the tuberculosis screening was negative.

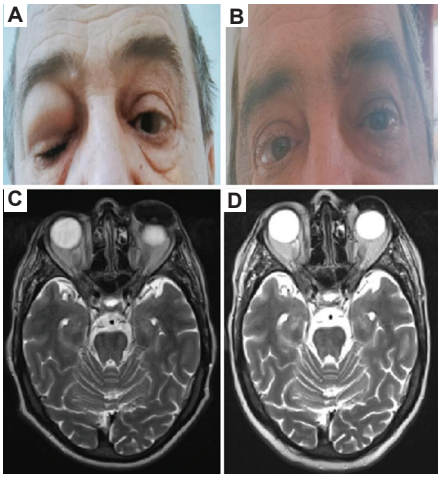

Figure 3. Clinical presentations of Case 3. (A) External photograph of the patient displaying exophthalmos, which developed over 3 months along with hemolytic anemia and tumor syndrome. (B) Complete clinical improvement observed. (C) Axial scan revealing a well-defined oval-shaped lesion in the left upper palpebral region, exhibiting hypo T1 and T2 signals with mild contrast enhancement. (D) Treatment with corticosteroids resulted in partial regression of the left upper palpebral mass, as observed in the hyposignal T2, with slight enhancement after contrast administration in the axial sequence.

The bone marrow biopsy revealed high cellularity indicative of a regenerating marrow. However, immunohistochemistry results (CD20, CD3, CD34, CD15, CD68, and CD30) were inconclusive, failing to definitely rule out a tumoral origin. Subsequently, the patient was initiated on corticosteroid therapy at a dose of 1 mg/kg/day. Based on the remarkable clinical improvement observed (Figure 3B), including weight regain, alleviation of asthenia, and resolution of the orbital mass, a diagnosis of inflammatory orbital pseudotumor with associated hemolytic anemia was established. Notably, normalization of abnormal blood counts and resolution of the inflammatory syndrome were observed as early as 3 weeks into treatment. Follow-up imaging at 2 months revealed partial remission of the condition (Figure 3D), while scans at 6 months indicated complete resolution of hepatomegaly and splenomegaly. Although a palpebral biopsy was proposed, the patient was lost to follow-up.

3. Discussion

Inflammatory diseases of the orbit remain poorly defined in terms of etiology and pathogenesis. Various factors such as infection, immune response, post-traumatic conditions, or molecular mimicry have been proposed as potential causes.[1] The administration of steroids and immunosuppressants is often considered favorable, given the observed increase in inflammation cytokines.

It is important to note the potential diagnostic challenges posed by persistent and progressive tumors resistant to corticosteroid treatment, as observed in Case 1. Such cases raise concerns regarding the presence of an underlying aggressive neoplastic pathology.[9] Bilateralization of the inflammatory process, occurring in 8 – 20% of cases,[10] and exaggerated edema and incoercible periorbital inflammation, led to exenteration. To the best of our knowledge, Case 1 represents the first case of an orbital pseudotumor revealing Takayasu vasculitis of the large trunk.

However, Case 2 illustrates the favorable (essentially clinical) evolution of idiopathic pseudo-orbital tumors, as observed in 70% of cases under corticosteroid treatment.[11] Nonetheless, the persistence of radiological abnormalities required additional therapeutic measurements. The management strategies for refractory cases remain undefined. However, the etiological investigation should

always be thorough to eliminate any plausible association with systemic or other diseases.

Fine-needle aspiration biopsies are used in cases of suspected metastases, although larger fragments are preferred for lymphoma studies, limiting the applicability of this method. Histology remains the gold standard in paraclinical explorations. However, its indications remain limited to cases with progressive neurological deficits, lack of response to steroids, or persistent imaging abnormalities.

In Case 2, the ophthalmologists refrained from performing an orbital tumor biopsy due to its close relationship with the optic nerve.

Furthermore, to the best of our knowledge, the association between hemolytic anemia and an inflammatory orbital pseudotumor has been described in only one case.[12] The clinical and radiological response to corticosteroid therapy after 6 months was favorable.

In general, imaging modalities (PET scan and MRI) reveal different types of involvement, encompassing structures such as lacrimal glands, oculomotor muscles, optic nerve, sclera, episclera, Tenon's capsule, uvea, and orbital fat. In addition, extensions into intracranial structures through the cavernous sinus and the middle cranial fossa represent the two most common locations. This distinction aids in categorizing the disease as localized or diffuse. Our three cases reflect the different involvement of the orbital structures.

Mombaerts cases reflect the different ins used to describe the different histological forms of IDO.[13] The classic form is characterized by polymorphic inflammation and a polymorphic infiltrate comprising lymphocytes, plasma cells, macrophages, eosinophils, and neutrophils. Multinucleated giant cells with foreign bodies are infrequently observed.

The sclerosing form is characterized by extensive fibrosis and a paucity of inflammatory cells, while the granulomatous form is characterized by the presence of histiocytes and multinucleated cells, suggestive of a sarcoid reaction. The final form presents as small-vessel vasculitis. Classical and sclerotic forms are the most prevalent. This classification holds prognostic significance, with classical forms generally exhibiting a better prognosis than sclerotic forms. However, research by Swamy *et al.*[14] demonstrated a recurrence rate of 0.3 per patient-year in classical forms versus 0.15 per patient-year in sclerotic forms. In the classic form, T-lymphocytes outnumber B-lymphocytes, with helper T-lymphocytes surpassing suppressor T-lymphocytes.[15] The proportion of fibrovascular stroma increases in both subacute and chronic forms, leading to fibrosis formation that fixes muscle structures by destroying fatty tissue. The inflammatory infiltrate is believed to stem from local fat necrosis of the ischemic type.[16] In cases of resistance or recurrence, a repeat anatomopathological examination is warranted, as certain forms may transition to lymphoma.[17]

The therapeutic approaches for IDO are diverse and well-documented in published series. Steroids are the mainstay of treatment, offering an excellent response. However, despite the success of low-dose radiation therapy in managing recurrent myositis and optic nerve decompression, documented recurrences underscore its limitations. Calcineurin inhibitors such as cyclosporine or tacrolimus have demonstrated efficacy, with cyclosporine emerging as a viable option for corticosteroid-intolerant diabetic patients. Antimetabolites (cyclophosphamide, azathioprine, and methotrexate) have proven effective in several published series, although requiring regular biological monitoring to monitor side effects.[18] Monoclonal antibodies have also shown promise. Infliximab, when used alone or in combination with methotrexate, yielded favorable results.[19] Rituximab, administered either intravenous weekly at a dosage of 375 mg/m^2 or at 1000 mg on days 0 and 15, has exhibited efficacy in refractory cases unresponsive to steroids, radiosurgery, or conventional treatments, resulting in positive clinical responses.[20] While tocilizumab has demonstrated effectiveness in the treatment of systemic juvenile idiopathic arthritis and rheumatoid arthritis, its use in IDO lacks published evidence.[21]

4. Conclusion

Inflammatory diseases of the orbit are a highly heterogeneous group requiring meticulous clinical examination and thorough investigation to guide therapeutic management. Knowledge of the physiopathology is paramount in effectively utilizing the available therapeutic options. Despite the generally benign nature of the lesions, they pose a significant threat to the functional prognosis of the orbit. This complexity underscores the need for further experimental work to refine global management protocols, particularly considering the variability in histological lesions such as sclerosis, fibrosis, inflammation, myositis, and granuloma.

Acknowledgments

None.

Funding

None.

Conflict of interest

The authors declare that they have no competing interest.

Author contributions

Conceptualization: Meliani Kaoutar, Rhandour Widad
Investigation: Meliani Kaoutar
Visualization: Bouardi Nizar
Writing – original draft: Meliani Kaoutar
Writing – review & editing: Meliani Kaoutar, Maaroufi Mustapha, Khammar Zineb, Berrady Rhizlane

Ethics approval and consent to participate

Informed consent was obtained from participants.

Consent for publication

Publication consent was obtained from the patients included in the study.

Availability of data

Data used in this work are available from the corresponding author on reasonable request.

References

1. Gleason JE. Idipathetic myositis involving the extraocular muscles. *Ophthalmol Rec*. 1903;12:471-478.
2. Jackson H. Pseudo-tumor of the orbit. *Br J Ophthalmol*. 1958;42(4):212-224.

   doi: 10.1136/bjo.42.4.212
3. Shields JA, Shields CL, Scartozzi R. Enququz auprru de 1 264 patients atteints de tumeurs orbitaires et de let de simulées: The 2002 Montgomery Lecture, partie 1. *Ophthalmology*. 2004;111:997-1008.

   doi: 10.1016/j.ophtha.2003.01.002
4. Kennerdell JS, Dresner SC. Les syndromes inflammatoires orbitaires non spon spres. *Surv Ophthalmol*. 1984;29:93-103.

   doi: 10.1016/0039-6257(84)90166-8
5. McCluskey P, Powell RJ. L', P dans les maladies inflammatoires systtmmatoi. *Lancet*. 2004;364:2125-2133.
6. Colombo F, Holbach LM, Naumann GO. Inflammation chronique des kystes dermoo de: Une éne o clinicopathologique de 115 patients (Chronic inflammation in dermoid cysts: A clinicopathologic study of 115 patients). *Orbite*. 2000;19:97-107. [Article in French]
7. Foley MR, Moshfeghi DM, Wilson MW, Haik BG, Pappo AS, Hill DA. Les syndromes inflammatoires orbitaires avec atteinte systémique peuvent ressembler à une maladie métastatique (Orbital inflammatory syndromes with systemic involvement may resemble metastatic disease). *Ophthalmol Plast Reconstr Surg*. 2003;19:324-327. [Article in French]
8. Carvounis PE, Mehta AP, Gesist CE. Orbital myositis associated with *Borrelia burgdorferi* (Lyme disease) infection. *Ophthalmology*. 2004;111(5):1023-1028.

   doi: 10.1016/j.ophtha.2003.08.032
9. Birch-Hirschfeld A. Handbuch der Gesamten Augenheilkunde. Vol. 9. Berlin: Julius Springer; 1930. p. 251-253.
10. Ghribi M, Derbel A, Frikha F, *et al*. Idiopathic inflammatory pseudotumors of the orbit: A rare pathology that should not be overlooked. Rev Med Interne. 2021;42:A177.
11. Gordon L. Orbital inflammatory disease: A diagnostic and therapeutic challenge. *Eye*. 2006;20:1196-1206.

    doi: 10.1038/sj.eye.6702383
12. Ye.1038/YS, GYS, G AK. Idiopathic orbital inflammation: Review of the literature and new advances. *Middle East Afr J Ophthalmol*. 2018;25(2):71-80.

    doi: 10.4103/meajo
13. Mombaerts I, Goldschmeding R, Schlingemann R, Koorneef L. What isan orbital pseudotumor? A clinical pathological review. *Surv Ophtalmol*. 1996a;41:67-78.

    doi: 10.1016/s0039-6257(97)81996-0
14. Swamy BN, McCluskey P, Nemet A, *et al*. Idiopathic orbital inflammatory syndrome: Clinical features and treatment outcomes. *Br J Ophthalmol*. 2007;91:1667-1670.

    doi: 10.1136/bjo.2007.124156
15. Adenis JP, Salomon JL, Franco JL. Inflammations subaiguat ou chroniques (Pseudotumeurs inflammatoires). In: Adenis JP, Morax S, editors. *Pathologie Orbito Palpébrale*. Netherlands: Masson, Elsevier; 1998. p. 436-444.
16. Herrmann B, Rozot P, Baylac F, Civit T, Reynal C, Ketema MA. Lipogranulome de l'orbite. À propos d'un cas (Lipogranuloma of the orbit. Apropos of a case). *J Fr Ophtalmol*. 1996;19:780-784. [Article in French]
17. Civit T, Colnat-Coulbois S, Joud A. Inflammation orbitaire subaiguë ou chronique (pseudotumeurs inflammatoires). *Neurochirurgie*. 2010;56:192-196.
18. Chundury A, Espinoza G, Chundury R, *et al*. *EyeWiki, American Academy of Ophthalmology*; 2022. Available from: https://eyewiki.aao.org/nonspecific_orbital_inflammation_(idiopathic_orbital_inflammation,_orbital_inflammatory_syndrome,_orbital_pseudotumor)
19. Sahlin S, Lignell B, Williams M, Dastmalchi M, Orrego A. Treatment of idiopathic sclerosing inflammation of the orbit (myositis) with infliximab. *Acta Ophthalmol*. 2009;87:906-908.

    doi: 10.1111/j.1755-3768.2008.01320.x
20. Sur A, Hirschbien M, Williams H, Karesh J. CyberKnife radiosurgery and rituximab in the successful management of idiopathic sclerosing orbital inflammatory disease. *Ophthalm Plas Reconstr Surg*. 2006;22:395-397.

    doi: 10.1097/01.iop.0000231549.24125.7a
21. Ibrahim I, Barton A, Ibrahim A, Ho P. Idiopathic orbital inflammation successfully treated with rituximab in a patient with rheumatoid arthritis. *J Rheumatol*. 2012;39(7):1485-1486.

    doi: 10.3899/jrheum.111230

Our Journals

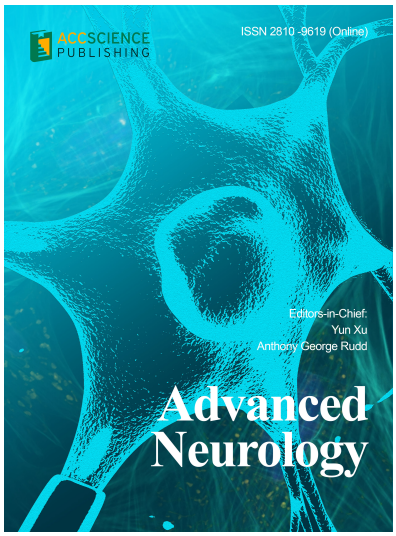

Advanced Neurology is a peer-reviewed and open-access journal that aims to publish and disseminate novel research in the breadth of neurology and neuroscience. The journal aims to advance our understanding in the nervous system and provide a platform to neuroscientists and physicians to showcase their findings in original fundamental and clinical research as well as to present new ideas that highlight the changes in the neurological clinical practice.

Advanced Neurology covers subject areas, including but not limited to the following:

- Neurological disorders
- Neurodegenerative disease
- Cerebrovascular disease
- Epilepsy and movement disorders
- Neuroimmune disease
- Neurological infections
- Muscle disease
- Molecular and cellular neuroscience
- Systems neuroscience
- Cognitive neuroscience
- Computational modeling of nervous system

Global Translational Medicine is a quarterly journal that focuses on medicine, biological sciences, and biomaterials engineering. The goal of *Global Translational Medicine* is to provide a platform to researchers for showcasing their latest research works in translational medicine so as to advance the field towards the betterment of human health. Despite the advancement of omics and new technologies, the process of transforming these technologies and scientific research results into effective therapies and putting them into clinical use still has a long way to go. *Global Translational Medicine* provides a platform to fill the gaps in preclinical and inter-disciplinary research, to promote clinical translation of scientific research results, and to contribute to the conception of new and improved preventive measures as well as diagnostic and therapeutic techniques of diseases.

Global Translational Medicine covers the following themes: cardiovascular disease, metabolism/diabetes/obesity, neuroscience/neurology, cancer, biomaterials and their applications in medicine, proteomics/metabolomics, pharmacogenomics, biomarkers, bioinformatics and data mining, animal and clinical research, and medical methods arising from interdisciplinary crossover.

Start a new journal

Write to us via email if you are interested to start a new journal with AccScience Publishing. Please attach your CV, professional profile page and a brief pitch proposal in your email. We shall inform you of our decision whether we are interested to collaborate in starting a new journal.

Contact: info@accscience.com

https://accscience.com/journal/TD

Contact

www.accscience.com

8 Burn Road, #15-03 Trivex, Singapore 369977

Email: editorial@accscience.com

Phone: +65 8182 1586